

Copyright

by

Peter Thompson Frailie, II

2014

The Dissertation Committee for Peter Thompson Frailie, II Certifies that this is the approved version of the following dissertation:

**Modeling of Carbon Dioxide Absorption/Stripping by Aqueous
Methyldiethanolamine/Piperazine**

Committee:

Gary Rochelle, Supervisor

Michael Baldea

Chau-Chyun Chen

Eric Chen

Gyeong Hwang

**Modeling of Carbon Dioxide Absorption/Stripping by Aqueous
Methyldiethanolamine/Piperazine**

by

Peter Thompson Frailie, II, B.S. CH.E.

Dissertation

Presented to the Faculty of the Graduate School of

The University of Texas at Austin

in Partial Fulfillment

of the Requirements

for the Degree of

Doctor of Philosophy

The University of Texas at Austin

May 2014

Dedication

To my family

Acknowledgements

The past six years in Austin, TX have brought with them many opportunities for personal and professional growth, and I feel fortunate to have shared them with friends, family, and friends-who-I-consider-family. When I first moved away from home my roommates Marty Gran, Tom Murphy, and Mark Pond showed me around the city and introduced me to some of my closest friends including Dan Miller, Justin Harris, Doug French, Jen Pai, Norman Horn, Grant Offord, Adam Stephens, Aimee Faucett, Maggie Gran, and Helen Murphy. Having spent the first twenty-three years of my life in Kentucky, I anticipated that the move to Texas would be rather difficult. Marty, Tom, and Mark made the transition a surprisingly easy one.

I would also like to acknowledge all members of the Rochelle group past and present for helping me complete my studies, but I would especially like to thank Fred Closmann, Stephanie Freeman, Jason Davis, Ross Dugas, Bob Tsai, Andrew Sexton, Jorge Plaza, David Van Wagener, Xi Chen, Qing Xu, Lynn Li, Stephen Fulk, Omkar Namjoshi, Darshan Sachde, Tarun Madan, Stuart Cohen, Brent Sherman, Nathan Fine, and Alex K. Voice. We climbed mountains in Wyoming and Norway, sand boarded in Dubai, and enjoyed karaoke in Kyoto, Japan. I'm certain that this will only be the beginning of our adventures.

My family has always been a great source of support, encouragement, and guidance in all aspects of my life. Mom, Dad, Tyler, Uncle Don, and Mary Beth are always looking for ways to brighten my day, remind me of the great times we've spent together, and plan future family outings. Family has always been and will always be the most important thing in my life, and I am blessed to have been born into a great one.

For their financial support during my studies I would like to thank Luminant Energy, the Texas Carbon Management Program, and the Thrust 2000 Uniden Endowed Graduate Fellowship in Engineering.

Staff members in the department of chemical engineering, especially Randy Rife and Maeve Cooney, have always been quick to offer invaluable assistance. Randy Rife expeditiously addressed every technical problem regardless of its complexity. Maeve Cooney kept me on track for paper/quarterly report submissions, juggled countless schedules to maximize the utilization of Dr. Rochelle's time, and reminisced about the horse farms back in my old Kentucky home.

Finally, I would like to thank my advisor Dr. Gary T. Rochelle for his professional and personal guidance. His humility, faith, and joy are inspirational to say the least, and I look forward to continuing our friendship long after I have left The University of Texas at Austin.

Modeling of Carbon Dioxide Absorption/Stripping by Aqueous Methyldiethanolamine/Piperazine

Peter Thompson Frailie, II, Ph.D.

Supervisor: Gary T. Rochelle

Rigorous thermodynamic and kinetic models were developed in Aspen Plus[®] Rate Sep[™] for 8 m PZ, 5 m PZ, 7 m MDEA/2 m PZ, and 5 m MDEA/5 m PZ. Thermodynamic data was regressed using a sequential regression methodology, and incorporated data for all amine, amine/water, and amine/water/CO₂ systems. The sensitivity of CO₂ absorption rate was determined in a wetted wall column simulation in Aspen Plus[®], and the results were used in Microsoft Excel to determine the optimum reaction rates, activation energies, and binary diffusivities. Density, viscosity, and binary diffusivity are calculated using user-supplied FORTRAN subroutines rather than built-in Aspen Plus[®] correlations.

Three absorber configurations were tested: adiabatic, in-and-out intercooling, and pump-around intercooling. The two intercooled configurations demonstrated comparable improvement in capacity and packing area, with the greatest improvement in 8 m PZ occurring between lean loadings of 0.20 and 0.25 mol CO₂/mol alkalinity. The effects of absorber temperature and CO₂ removal were tested in the adiabatic and in-and-out intercooled configurations. For 7 m MDEA/2 m PZ at a lean loading of 0.13 mol CO₂/mol alkalinity reducing the absorber temperature from 40 °C to 20 °C increases capacity by 64% without an appreciable increase in packing area. Increasing CO₂

removal from 90% to 99% does not double the packing area due to favorable reaction rates at the lean end of the absorber.

Two stripper configurations were tested: the simple stripper and the advanced flash stripper. For all amines, absorber configurations, and lean loadings the advanced flash stripper demonstrated the better energy performance, with the greatest benefit occurring at low lean loadings.

An economic estimation method was developed that converts purchased equipment cost and equivalent work to \$/MT CO₂. The method is based on economic factors proposed by DOE-NETL and IEAGHG. The total cost of CO₂ decreases as lean loading decreases for all amines and configurations. Increasing CO₂ removal from 90% to 99% results in a 1% increase in the total cost of CO₂ capture. Decreasing absorber temperature for 7 m MDEA/2 m PZ from 40 °C to 20 °C decreases total cost of CO₂ capture by up to 9.3%.

Table of Contents

List of Tables	xiii
List of Figures	xvii
Chapter 1: Introduction	1
Chapter 2: Modeling CO ₂ Capture Using MDEA/PZ.....	6
2.1 RATIONALE FOR PZ ACTIVATED MDEA.....	6
2.2 THERMODYNAMIC MODELING	8
2.3 ABSORBER AND KINETIC MODELING	10
2.4 STRIPPER CONFIGURATIONS	16
2.5 OVERALL PROCESS OPTIMIZATION	17
Chapter 3: Thermodynamic Modeling.....	19
3.1 INTRODUCTION	19
3.2 LITERATURE REVIEW	20
3.3 MODEL DESCRIPTION	22
3.3.1 Equilibrium Constant Calculations in Aspen Plus®	22
3.3.2 Activity Coefficient Calculation in Aspen Plus®	24
3.3.3 Vapor-Liquid Equilibrium Calculation in Aspen Plus®	27
3.4 OPERATING RANGES OF MODELS	27
3.4.1 Temperature	27
3.4.2 Loading	28
3.4.3 Amine Concentration.....	29
3.5 SEQUENTIAL REGRESSION METHODOLOGY	29
3.6 MODEL REGRESSION.....	32
3.6.1 Amine/H ₂ O	32
3.6.2 MDEA/H ₂ O/CO ₂ Regression.....	38
3.6.3 PZ/H ₂ O/CO ₂ Regression.....	43
3.6.4 MDEA/PZ/H ₂ O/CO ₂ Regression.....	51
3.6.5 Generic Amines	61

3.7	CONCLUSIONS.....	64
Chapter 4: Kinetic Modeling		66
4.1	INTRODUCTION	66
4.2	LITERATURE REVIEW	66
4.3	METHODOLOGY	67
4.3.1	Hydraulic Properties	67
4.3.2	Reactions and Reaction Rate Constants.....	74
4.3.3	Sensitivity Analysis	78
4.3.4	Mass Transfer Correlations.....	79
4.3.5	Loading Adjustment.....	81
4.4	RESULTS	83
4.4.1	Reaction Constants and Binary Diffusivity	83
4.4.2	Stability Analysis	90
4.4.3	Generic Amines	91
4.4.4	Rate-Based Stripper Modeling.....	95
4.5	CONCLUSIONS.....	98
Chapter 5: Process Modeling		100
5.1	INTRODUCTION	100
5.2	LITERATURE REVIEW	100
5.3	METHODOLOGY	102
5.3.1	Aspen Plus [®] Thermodynamic and Kinetic Framework.....	102
5.3.2	Absorber Configurations.....	106
5.3.2.1	Adiabatic Absorber	107
5.3.2.2	In-and-Out Intercooling.....	109
5.3.2.3	Pump-Around Intercooling	109
5.3.3	Stripper Configurations.....	110
5.3.3.1	Simple Stripper.....	111
5.3.3.2	Advanced Flash Stripper	114
5.3.4	L/L _{min} Analysis	117
5.4	RESULTS	119

5.4.1	L/L _{min}	119
5.4.2	Intercooling Configurations	123
5.4.3	Stripper Configurations.....	126
5.4.4	Absorber Temperature	131
5.4.5	CO ₂ Removal	139
5.5	CONCLUSIONS.....	145
Chapter 6:	Process Economics.....	146
6.1	INTRODUCTION	146
6.2	METHODS	146
6.2.1	Scaling.....	146
6.2.2	Derating.....	147
6.2.3	Scaling Purchased Equipment Cost to 2010 DOE Cost and Performance Baseline	149
6.3	CALCULATING PEC.....	149
6.3.1	Absorber.....	150
6.3.2	Cross Exchangers.....	151
6.3.3	Reboiler or Steam Heater.....	152
6.3.4	Compressor	153
6.3.5	All Other Process Units	153
6.4	ADVANCED FLASH STRIPPER WITH INTERCOOLED ABSORBER	154
6.4.1	Intercooled Absorber Optimization	156
6.4.2	Advanced Flash Stripper Design and Optimization.....	157
6.5	CALCULATING COST OF CO ₂ AVOIDED.....	158
6.6	RESULTS AND DISCUSSION.....	159
6.6.1	Minimum W _{EQ} Design Configuration	159
6.6.2	Scaling.....	170
6.6.2.1	Derating Summary	170
6.6.2.2	Scaling Purchase Equipment Cost (PEC) to 2010 DOE Cost and Performance Baseline.....	171
6.6.3	CAPEX Summary.....	174

6.6.4 Absorber Configuration	175
6.6.5 Effect of Absorber Temperature	177
6.6.6 CO ₂ Removal	179
6.6.7 Sensitivity Analysis	181
6.7 CONCLUSIONS.....	182
Chapter 7: Conclusions and Recommendations	184
7.1 CONCLUSIONS.....	184
7.2 RECOMMENDATIONS.....	186
Appendix A: 5deMayo Thermodynamics.....	189
Appendix B: Guy Fawkes Model	204
Appendix C: Density and Viscosity Data	234
References.....	236
Vita.....	242

List of Tables

Table 2-1: Comparing 7m MDEA/2m PZ to 8m PZ and 7m MEA.....	8
Table 3-1: Parameters used for MDEA/H ₂ O and MDEA/H ₂ O/CO ₂ regressions	31
Table 3-2: Regression results for MDEA/H ₂ O, PZ/H ₂ O, and MDEA/PZ/H ₂ O	.33
Table 3-3: Data sources for Amine/H ₂ O regression.....	33
Table 3-4: Regression results for MDEA/H ₂ O/CO ₂	38
Table 3-5: Data sources for MDEA/H ₂ O/CO ₂ regression.....	39
Table 3-6: Regression results for activity coefficient of CO ₂ in MDEA/H ₂ O/CO ₂	42
Table 3-7: Regression results for PZ/H ₂ O/CO ₂	44
Table 3-8: Data sources for PZ/H ₂ O/CO ₂ regression	44
Table 3-9: Slopes of speciation curves for 8 m PZ at 40 °C and 150 °C.....	47
Table 3-10: Regression results for activity coefficient of CO ₂ in PZ/H ₂ O/CO ₂ ..	50
Table 3-11: Regression results for MDEA/PZ/H ₂ O/CO ₂	51
Table 3-12: Data sources for MDEA/PZ/H ₂ O/CO ₂ regression	51
Table 3-13: Slopes of speciation curves for 7 m MDEA/2 m PZ at 40 °C and 120 °C for CO ₂ -containing species, MDEA, and PZ	57
Table 3-14: Empirical expression and model predicted capacities of 8 m PZ, 7 m MDEA/2 m PZ, and 5 m MDEA/5 m PZ between 500 and 5,000 Pa equilibrium partial pressure of CO ₂ at 40 °C.....	58
Table 4-1: Regression results for MDEA, PZ, and MDEA/PZ density	69
Table 4-2: Data sources for MDEA, PZ, and MDEA/PZ density	69
Table 4-3: Regression results for MDEA, PZ, and MDEA/PZ viscosity.....	70
Table 4-4: Data sources for MDEA, PZ, and MDEA/PZ viscosity	71

Table 4-5:	Regression results for MDEA, PZ, and MDEA/PZ viscosity.....	83
Table 4-7:	Stability analysis for regressed kinetic parameters and parameters defining the binary diffusivity of CO ₂	91
Table 4-8:	Comparison between PZ and MDEA/PZ on the basis of heat of absorption, CO ₂ absorption rate, and capacity.....	93
Table 5-1:	Operating conditions regressed into Independence model kinetics	106
Table 5-2:	Configuration comparison at lean loadings of 0.23, 0.26, and 0.32 mol CO ₂ /mol alkalinity for 8 m PZ at 40 °C and 90% removal from an inlet stream with 12% CO ₂ and a CO ₂ flow rate of 130 kg/s and a liquid flow rate that is 1.2 times the minimum.....	125
Table 5-3:	Adiabatic absorbers at temperatures of 40 °C, 30 °C, and 20 °C and lean loadings of 0.13, 0.19, and 0.25 mol CO ₂ /mol alkalinity for 7 m MDEA/2 m PZ with a liquid flow rate that is 1.2 times the minimum	134
Table 5-4:	Comparison of adiabatic and intercooled absorbers with 90% and 99% CO ₂ capture for 7 m MDEA/2 m PZ with a lean loading of 0.07 mol CO ₂ /mol alkalinity at 40 °C and 1.2 times the minimum liquid flow rate	143
Table 6-1:	Stream table for optimized advanced flash stripper with intercooled absorber	163
Table 6-2:	Stream table for optimized advanced flash stripper with intercooled absorber	164
Table 6-3:	Stream table for optimized advanced flash stripper with intercooled absorber	165
Table 6-4:	Equipment table for advanced flash stripper with intercooled absorber	166

Table 6-5:	Equipment table for advanced flash stripper with intercooled absorber	167
Table 6-6:	Equipment table for short stripper with intercooled absorber	168
Table 6-7:	Equipment table for short stripper with intercooled absorber	169
Table 6-8:	Derating summary for the four cases considered in this study and the 2012 DOE NETL Report	170
Table 6-9:	Prices of unit operations for PZ-SS, MEA-SS, and PZ-AFS assuming 593 MW _e	173
Table 6-10:	PEC for capture and compression equipment for all four cases scaled to 550 MW _e net power production.....	174
Table 6-11:	CO ₂ avoided for all four cases on the basis of 550 MW _e net power produced.....	175
Table 6-12:	Cost of CO ₂ captured for each absorber configuration with 8 m PZ and lean loadings of 0.20, 0.29, and 0.35 mol CO ₂ /mol alkalinity, 40 °C vapor and liquid feed, L/L _{min} =1.2, and 90% removal.....	177
Table 6-13:	Cost of CO ₂ captured for each absorber temperature with 7 m MDEA/2 m PZ and lean loadings of 0.13, 0.19, and 0.22 mol CO ₂ /mol alkalinity, 90% removal, L/L _{min} =1.2, and in-and-out intercooling.....	179
Table 6-14:	Cost of CO ₂ captured for 7 m MDEA/2 m PZ and 8 m PZ with 90% and 99% removal with L/L _{min} =1.2, in-and-out intercooling, 40 °C vapor and liquid feed, and a lean loading corresponding to a CO ₂ equilibrium partial pressure of 75 Pa.....	180
Table 6-15:	Sensitivity of total cost of CO ₂ capture to αβ and COE	181
Table A-1:	Regression results for PZ/H ₂ O.....	189
Table A-2:	Regression results for PZ/H ₂ O/CO ₂ Density and Viscosity	190

Table A-3: Regression results for PZ/H ₂ O/CO ₂	195
Table A-4: Regression results for activity coefficient of CO ₂	202
Table B-1: Regression results for PZ/H ₂ O.....	204
Table B-2: Regression results for PZ/H ₂ O/CO ₂ Density (Reference Equation B-1)	205
Table B-3: Regression results for PZ/H ₂ O/CO ₂ Density (Reference Equation B-2)	208
Table B-4: Regression results for PZ/H ₂ O/CO ₂	210
Table B-6: Regression results for activity coefficient of CO ₂	217
Table B-7: Regression results for MDEA/H ₂ O.....	218
Table B-8: Regression results for MDEA/H ₂ O/CO ₂ Density and Viscosity	220
Table B-9: Regression results for MDEA/H ₂ O/CO ₂	221
Table B-10: Regression results for MDEA/PZ/H ₂ O and MDEA/PZ/H ₂ O/CO ₂	224
Table B-11: Regression results for MDEA/PZ/H ₂ O/CO ₂ Density (Reference Equation 4-1)	224
Table B-12: Regression results for MDEA/PZ/H ₂ O/CO ₂ Density (Reference Equation 4-2)	225
Table C-1: Density of 7 m MDEA/2 m PZ and 5 m MDEA/5 m PZ from 20-60 °C.	234
Table C-2: Viscosity of 7 m MDEA/2 m PZ and 5 m MDEA/5 m PZ from 20-60 °C.	235

List of Figures

- Figure 2-1: Chemical structures of all relevant amine species in MDEA/PZ.....7
- Figure 2-2: Partial pressure of CO₂ as a function of loading for 7 m MDEA/2 m PZ from 30–120 °C.....14
- Figure 3-1: Experimental data (points) and model predictions (lines) for unloaded amine volatility as a function of temperature for 7 m MDEA/2 m PZ35
- Figure 3-2: Experimental data (points) and model predictions (lines) for unloaded amine heat capacity as a function of temperature for 7 m MDEA/2 m PZ, 5 m MDEA/5 m PZ, 50 wt % PZ, and 50 wt % MDEA36
- Figure 3-3: Experimental data (points) and model predictions (lines) for unloaded MDEA/H₂O heat capacity as a function of MDEA mole fraction at 25 °C (blue), 40 °C (red), 70 °C (green), and 95 °C (purple)37
- Figure 3-4: Experimental data (points) and model predictions (lines) for unloaded PZ/H₂O heat capacity as a function of temperature for 2 m (blue), 3.6 m (red), and 8 m (green) PZ.....37
- Figure 3-5: Experimental data (points) and model predictions (line) for the dissociation constant of MDEA as a function of temperature40
- Figure 3-6: Experimental data (points) and model predictions (lines) for partial pressure of CO₂ as a function of loading for 50 wt % MDEA41
- Figure 3-7: Experimental data (points; Rinker, 1997) and Aspen Plus[®] predictions (lines) for the activity coefficient of CO₂ in 50 wt % MDEA42
- Figure 3-8: Experimental data (points; Dugas, 2009; Xu, 2011) and Aspen Plus[®] predictions (lines) for the partial pressure of CO₂ divided by the loading squared as a function of loading for 8 m PZ.....45

Figure 3-9: Experimental data (points; Nguyen, 2012) and Aspen Plus [®] predictions (lines) for speciation of 8 m PZ at 40 °C	46
Figure 3-10: Experimental data at 40 °C (points) Aspen Plus [®] predictions for the mole fraction of HCO ₃ ⁻ (blue) and PZ(COO) ₂ ²⁻ (purple) as a function of loading at 40 °C (solid lines) and 150 °C (dotted lines).....	46
Figure 3-11: Experimental data (points; Freeman, 2011) and Aspen Plus [®] predictions (lines) for the heat of CO ₂ absorption for 8 m PZ as a function of loading from 40-140 °C	48
Figure 3-12: Experimental data (points) and Aspen Plus [®] predictions (lines) for activity coefficient of CO ₂ from 25-160 °C	50
Figure 3-13: Activity coefficient of CO ₂ as a function of loading for 7 m MDEA/2 m PZ from 40-160 °C.....	52
Figure 3-14: Heat of CO ₂ absorption for 7 m MDEA/2 m PZ as a function of loading from 40-120 °C. Solid lines are predicted by Aspen Plus [®] , dotted line is result of empirical expression (Xu, 2011).....	53
Figure 3-15: Experimental data (dashed lines; Kierzkowska-Pawlak, 2007) and Aspen Plus [®] predictions (lines) for the differential heat of CO ₂ absorption for 50 wt % MDEA as a function of loading from 40-120 °C.....	54
Figure 3-16: Experimental data (points; Chen, 2011; Xu, 2011; Li, 2011) and Aspen Plus [®] model predictions (lines) for partial pressure of CO ₂ divided by the loading squared as a function of loading for 5 m MDEA/5 m PZ from 10-120 °C	55
Figure 3-17: Experimental data (points; Nguyen, 2012) and Aspen Plus [®] predictions (lines) for speciation of 7 m MDEA/ 2m PZ at 40 °C as a function of loading.....	56

Figure 3-18: Solubility constant, K_{sp} , as a function of inverse temperature for loaded and unloaded 3-7 m (purple), 8 m (red), 9 m (blue), and 10 m (green) PZ	58
Figure 3-19: Aspen Plus [®] predictions for the activity coefficient of H_2O , $PZCOO^-$, PZH^+ , and MDEA in 7 m MDEA/2 m PZ at 40 °C	59
Figure 3-20: Aspen Plus [®] predictions for the activity coefficient of $MDEAH^+$, PZ, CO_3^{2-} , HCO_3^- , H^+PZCOO^- , and $PZ(COO)_2^{2-}$ in 7 m MDEA/2 m PZ at 40 °C as a function of loading.....	60
Figure 3-21: Heat of CO_2 absorption (blue) at 40 °C (solid line) and 120 °C (dotted line) and capacity (red) with (solid line) and without (dotted line) a viscosity correction at 40 °C for 50 wt % amine MDEA/PZ mixtures as a function of wt % PZ divided by wt % amine.....	62
Figure 3-22: Heat of CO_2 absorption (blue) at 40 °C (solid line) and 120 °C (dotted line) and capacity (red) with (solid line) and without (dotted line) a viscosity correction at 40 °C for PZ as a function of wt % PZ.	63
Figure 4-1: Density of 5 m MDEA/5 m PZ experimental data (points; This Work) and Aspen Plus [®] predictions (lines).....	72
Figure 4-2: Viscosity of 5 m MDEA/5 m PZ experimental data (points, This Work) and Aspen Plus [®] predictions (lines).....	72
Figure 4-3: Process flow diagram for the wetted wall column Aspen Plus [®] simulation.....	76
Figure 4-4: Experimental values (points and solid line) and Aspen Plus [®] predictions (dotted line) for 7 m MDEA/2 m PZ at a loading of 0.21 mol CO_2 /mol alkalinity at 40 °C (Chen, 2011)	82

Figure 4-5: Sensitivity of k_g' to diffusion (blue) and reaction (red) control for 8 m PZ from 40-100 °C.....	85
Figure 4-6: Experimental data (points) and Aspen Plus [®] predictions (lines) for k_g'	86
Figure 4-7: Flux _{PRED} /Flux _{EXP} for 8 m PZ and 5 m PZ from 40-100 °C	88
Figure 4-8: Flux _{PRED} /Flux _{EXP} for 7 m MDEA/2 m PZ and 5 m MDEA/5 m PZ from 10-100 °C	88
Figure 4-10: Aspen Plus [®] predictions for k_g' (blue), viscosity normalized capacity (red solid line) and heat of CO ₂ absorption (red dotted line) at 40 °C for MDEA/PZ with 50 wt % amine.....	93
Figure 4-11: Aspen Plus [®] predictions for k_g' (blue), viscosity-normalized capacity (red solid line) and heat of CO ₂ absorption (red dotted line) at 40 °C for MDEA/PZ in the ratio of 35 wt % to 15 wt %.....	95
Figure 4-12: Fractional contribution of k_g , k_g'' , and k_L/m to the overall mass transfer resistance in a simple stripper with 8 m PZ	97
Figure 4-13: K_{EQ} calculated from Gibbs energy (solid lines) and k_f/k_r predictions (dotted lines) for PZCOO ⁻ , PZ(COO) ₂ ²⁻ , and HCO ₃ ⁻ forming reactions	98
Figure 5-1: Base case process cycle for 90% CO ₂ capture from coal-fired power plant using 5 m MDEA/5 m PZ	103
Figure 5-2: Process cycles for 90% CO ₂ capture from coal-fired power plant using 5 m MDEA/5 m PZ assuming 40 °C (red) and 20 °C (blue) absorber.....	104
Figure 5-3: Process cycles for 90% (red) and 99% (green) CO ₂ capture from coal-fired power plant using 5 m MDEA/5 m PZ assuming 40 °C absorber.....	105

Figure 5-4: Bulk liquid temperature profile for adiabatic absorber using 8 m PZ with lean loading of 0.32 mol CO ₂ /mol alkalinity for (L/G) _{mol} = 16 (blue), (L/G) _{mol} = 8 (purple), and (L/G) _{mol} = 7 (red).....	108
Figure 5-5: Process flow diagram for absorber with pump-around intercooling	110
Figure 5-6: Process flow diagram for simple stripper	112
Figure 5-7: Temperature profiles for the main cross exchanger modeled as one (dotted lines) and two (solid lines) sets of Heater blocks for 7 m MDEA/2 m PZ with a lean loading of 0.13 mol CO ₂ /mol alkalinity and LMTD = 5 K.	114
Figure 5-8: Process flow diagram for advanced flash stripper	115
Figure 5-9: Minimum (L/G) _{mol} for an absorber with in-and-out intercooling (blue) and pump-around intercooling (green) and without intercooling (red) at 40 °C for 7 m MDEA/2 m PZ at 90% CO ₂ capture from coal-fired power plant flue gas.	118
Figure 5-10: Capacity for 8 m PZ in an adiabatic absorber and liquid flow rates corresponding to 1.0, 1.1, 1.2, and 1.3 times the minimum.....	120
Figure 5-11: Mass transfer area (solid lines) and equivalent work (dotted lines) for 8 m PZ in an adiabatic absorber with a simple stripper and liquid flow rates corresponding to 1.1, 1.2, and 1.3 times the minimum, 90% removal, 40 °C, 12% CO ₂	120
Figure 5-12: Temperature profiles for 8 m PZ in adiabatic absorbers at a liquid flow rate corresponding to 1.1 times the minimum liquid flow rate and lean loadings of 0.2 (red), 0.26 (green), and 0.35 (blue) mol CO ₂ / mol alkalinity, 90% removal, 40 °C inlet gas and liquid.	121

Figure 5-13: Normalized packing area (blue) and capacity (red) as a function of lean loading for 8 m PZ at 40 °C with an adiabatic absorber (dashed lines), in-and-out intercooling (dotted lines), and pump-around intercooling (solid lines) with a liquid flow rate that is 1.2 times the minimum and 90% removal.	124
Figure 5-14: W_{EQ} (blue) and rich loading (red) 8 m PZ with a liquid flow rate equal to 1.2 times the minimum for a simple stripper with rich solutions from an adiabatic absorber (solid lines), in-and-out intercooling (dashed lines), and pump-around intercooling (dotted lines).....	127
Figure 5-15: Heat of desorption for 8 m PZ at 140 °C (blue) and 150 °C (red). Temperatures correspond to feed and product temperatures for simple stripper. Vertical lines at 0.29 and 0.37 mol CO ₂ /mol alkalinity correspond to rich and lean loadings, respectively, for adiabatic absorber with a liquid rate equal to 1.2 times the minimum.	128
Figure 5-16: Heat of CO ₂ Desorption (green), steam losses (red), and sensible heat losses (blue) for a simple stripper with 8 m PZ and an adiabatic absorber (solid lines), absorber with in-and-out intercooling (dashed lines), and absorber with pump-around intercooling (dotted lines) and a liquid flow rate equal to 1.2 times the minimum absorbed at 40 °C.	129
Figure 5-17: Equivalent work for 8 m PZ with a simple stripper (blue) and advanced flash stripper (red) using rich solutions generated by an adiabatic absorber (solid lines), in-and-out intercooling (dashed lines), and pump-around intercooling (dotted lines).....	131

Figure 5-18: Normalized packing area (blue) and solvent capacity (red) for 7 m MDEA/2 m PZ at 40 °C (solid lines), 30 °C (dashed lines), and 20 °C (dotted lines) and a liquid flow rate equal to 1.2 times the minimum and 90% removal for an adiabatic absorber.	132
Figure 5-19: Normalized packing area (blue) and solvent capacity (red) for 7 m MDEA/2 m PZ at 40 °C (solid lines), 30 °C (dashed lines), and 20 °C (dotted lines) and a liquid flow rate equal to 1.2 times the minimum and 90% removal for an adiabatic absorber.	135
Figure 5-20: Equivalent work for 7 m MDEA/2 m PZ with a simple stripper (red) and advanced flash stripper (blue) and an adiabatic absorber at 40 °C, 30 °C, and 20 °C and a liquid flow rate equal to 1.2 times the minimum and 90% removal.	136
Figure 5-21: Operational loadings for adiabatic absorbers at 40 °C and the minimum liquid flow rates.	137
Figure 5-22: CO ₂ solubility at 40 °C for 8 m PZ, 7 m MDEA/2 m PZ, and 5 m MDEA/5 m PZ.	138
Figure 5-23: Minimum (L/G) _{mol} for 7 m MDEA/2 m PZ at 40 °C in adiabatic (solid lines) and intercooled (dotted lines) absorbers with 90% (red) and 99% (green) capture from the flue gas of a coal-fired power plant	139
Figure 5-24: Normalized mass transfer area and equivalent work for 7 m MDEA/2 m PZ with an adiabatic absorber at 40 °C and simple stripper.	140

Figure 5-25: Bulk liquid temperature and CO ₂ flux normalized to CO ₂ partial pressure for 7 m MDEA/2 m PZ with a lean loading of 0.07 mol CO ₂ /mol alkalinity in adiabatic absorbers with 90% (solid lines) and 99% (dashed lines) CO ₂ removal rates. Absorber position refers to the 99% removal case.....	141
Figure 5-26: Bulk liquid temperature and CO ₂ flux normalized to CO ₂ partial pressure for 7 m MDEA/2 m PZ with a lean loading of 0.07 mol CO ₂ /mol alkalinity in in-and-out intercooled absorbers with 90% (solid lines) and 99% (dashed lines) CO ₂ removal rates. Absorber position refers to the 99% removal case.	142
Figure 5-27: Normalized mass transfer area and equivalent work for 8 m PZ with an adiabatic absorber at 40 °C and a liquid flow rate equal to 1.2 times the minimum with 90% and 99% removal.	144
Figure 6-1: Process flow diagram for proposed advanced flash stripper with intercooled absorber.....	155
Figure 6-2: Total cost of CO ₂ capture for adiabatic, in-and-out intercooled, and pump-around intercooled configurations with 8 m PZ, 90% removal, and the advanced flash stripper. $\alpha\beta=1$ and COE=\$0.10/kWh.....	176
Figure 6-3: Total cost of CO ₂ capture for 7 m MDEA/2 m PZ with in-and-out intercooling, the advanced flash stripper, and a variable absorber temperature. $\alpha\beta=1$ and COE=\$0.10/kWh.....	178
Figure 6-4: Total cost of CO ₂ capture at 90% and 99% removal for 7 m MDEA/2 m PZ and 8 m PZ at 40 °C with an absorber with in-and-out intercooling and the advanced flash stripper. $\alpha\beta=1$ and COE=\$0.10/kWh.....	180

Figure A-1: Experimental data (points, Dugas 2009; Xu 2011) and model predictions (lines) for PZ volatility in 2-10 m PZ. High temperature data was omitted from the regression due to incompatibility.....	189
Figure A-2: Experimental data (points, Hilliard 2008) and model predictions (lines) for the heat capacity of 2 m PZ and 3.6 m PZ.	190
Figure A-3: Density of loaded 5 m PZ from 20-60 °C.	191
Figure A-4: Viscosity of loaded 5 m PZ from 20-60 °C.....	191
Figure A-5: Density of loaded 7 m PZ from 20-60 °C.	192
Figure A-6: Viscosity of loaded 7 m PZ from 20-60 °C.....	192
Figure A-7: Density of loaded 8 m PZ from 20-60 °C.	193
Figure A-8: Viscosity of loaded 8 m PZ from 20-60 °C.....	193
Figure A-9: Density of loaded 9 m PZ from 20-60 °C.	194
Figure A-10: Viscosity of loaded 9 m PZ from 20-60 °C.....	194
Figure A-11: Experimental data (points; Dugas 2009) and model predictions (lines) for CO ₂ solubility in 2 m PZ from 40-100 °C.....	196
Figure A-12: Experimental data (points; Dugas 2009) and model predictions (lines) for CO ₂ solubility in 5 m PZ from 40-100 °C.....	196
Figure A-13: Experimental data (points; Dugas 2009; Xu 2011) and model predictions (lines) for CO ₂ solubility in 8 m PZ from 40-160 °C.....	197
Figure A-14: Experimental data (points; Dugas 2009; Xu 2011) and model predictions (lines) for CO ₂ solubility in 12 m PZ from 40-160 °C.....	197
Figure A-15: Experimental data (points; Hilliard 2008) and model predictions (lines) for heat capacity of 2 m PZ at loadings of 0.16 and 0.27 mol CO ₂ /mol alkalinity.	198

Figure A-16: Experimental data (points; Hilliard 2008) and model predictions (lines) for heat capacity of 3.6 m PZ at loadings of 0.16 and 0.375 mol CO ₂ /mol alkalinity.	198
Figure A-17: Experimental data (points; Freeman 2011) and model predictions (lines) for heat capacity of 8 m PZ at loadings of 0.21, 0.29 and 0.4 mol CO ₂ /mol alkalinity.	199
Figure A-18: Experimental data (points; Freeman 2011) and model predictions (lines) for heat capacity of 10 m PZ at a loading of 0.31 mol CO ₂ /mol alkalinity and 12 m PZ at a loading of 0.29 mol CO ₂ /mol alkalinity.	199
Figure A-19: Experimental data (points; Nguyen 2012) and model predictions (lines) for PZ volatility in loaded 8 m PZ from 40-60 °C.	200
Figure A-20: Experimental data (points; Nguyen 2012) and model predictions (lines) for PZ volatility in loaded 10 m PZ from 40-60 °C.	200
Figure A-21: Experimental data (points; Hetzer 1968) and model predictions (lines) for PZ pKa.	201
Figure A-22: Experimental data (points; Freeman 2010) and model predictions (lines) for heat of CO ₂ absorption in 8 m PZ from 40—160 °C.	201
Figure A-23: Model predictions for liquid mole fraction in 8 m PZ at 40 °C.	202
Figure A-24: Experimental data (points; Svendsen 2010) and model predictions (lines) for the activity coefficient of CO ₂ from 25-80 °C.	203
Figure B-1: Experimental data (points, Dugas 2009; Xu 2011) and model predictions (lines) for PZ volatility in 2-10 m PZ. High temperature data was omitted from the regression due to incompatibility.	204
Figure B-2: Experimental data (points, Hilliard 2008) and model predictions (lines) for the heat capacity of 2 m PZ and 3.6 m PZ.	205

Figure B-3: Density of loaded 5 m PZ from 20-60 °C.	206
Figure B-4: Density of loaded 7 m PZ from 20-60 °C.	206
Figure B-5: Density of loaded 8 m PZ from 20-60 °C.	207
Figure B-6: Density of loaded 9 m PZ from 20-60 °C.	207
Figure B-7: Viscosity of loaded 5 m PZ from 20-60 °C.	208
Figure B-8: Viscosity of loaded 7 m PZ from 20-60 °C.	209
Figure B-9: Viscosity of loaded 8 m PZ from 20-60 °C.	209
Figure B-10: Viscosity of loaded 9 m PZ from 20-60 °C.	210
Figure B-11: Experimental data (points; Dugas 2009) and model predictions (lines) for CO ₂ solubility in 2 m PZ from 40-100 °C.	211
Figure B-12: Experimental data (points; Dugas 2009) and model predictions (lines) for CO ₂ solubility in 5 m PZ from 40-100 °C.	211
Figure B-13: Experimental data (points; Dugas 2009; Xu 2011) and model predictions (lines) for CO ₂ solubility in 8 m PZ from 40-160 °C.	212
Figure B-14: Experimental data (points; Dugas 2009; Xu 2011) and model predictions (lines) for CO ₂ solubility in 12 m PZ from 40-160 °C.	212
Figure B-15: Experimental data (points; Hilliard 2008) and model predictions (lines) for heat capacity of 2 m PZ at loadings of 0.16 and 0.27 mol CO ₂ /mol alkalinity.	213
Figure B-16: Experimental data (points; Hilliard 2008) and model predictions (lines) for heat capacity of 3.6 m PZ at loadings of 0.16 and 0.375 mol CO ₂ /mol alkalinity.	213
Figure B-17: Experimental data (points; Freeman 2011) and model predictions (lines) for heat capacity of 8 m PZ at loadings of 0.21, 0.29 and 0.4 mol CO ₂ /mol alkalinity.	214

Figure B-18: Experimental data (points; Freeman 2011) and model predictions (lines) for heat capacity of 10 m PZ at a loading of 0.31 mol CO ₂ /mol alkalinity and 12 m PZ at a loading of 0.29 mol CO ₂ /mol alkalinity.	214
Figure B-19: Experimental data (points; Nguyen 2012) and model predictions (lines) for PZ volatility in loaded 8 m PZ from 40-60 °C.	215
Figure B-20: Experimental data (points; Nguyen 2012) and model predictions (lines) for PZ volatility in loaded 10 m PZ from 40-60 °C.	215
Figure B-21: Experimental data (points; Hetzer 1968) and model predictions (lines) for PZ pKa.	216
Figure B-22: Experimental data (points; Freeman 2010) and model predictions (lines) for heat of CO ₂ absorption in 8 m PZ from 40—160 °C.	216
Figure B-23: Model predictions for liquid mole fraction in 8 m PZ at 40 °C.	217
Figure B-24: Experimental data (points; Svendsen 2010) and model predictions (lines) for the activity coefficient of CO ₂ from 25-80 °C.	218
Figure B-25: Experimental data (Nguyen, 2012) and model predictions (lines) for MDEA volatility in 7 m and 8.4 m MDEA.	219
Figure B-26: Experimental data (Zhang, 2002) and model predictions (lines) for MDEA heat capacity from 25-95 °C.	219
Figure B-27: Experimental data (Weiland, 1998) and model predictions (lines) for loaded MDEA density at 25 °C.	220
Figure B-28: Experimental data (Weiland, 1998) and model predictions (lines) for loaded MDEA viscosity at 25 °C.	221
Figure B-29: Experimental data (Jou, 1982) and model predictions (lines) for solubility of CO ₂ in 50 wt % MDEA from 25-120 °C.	222

Figure B-30: Experimental data (Jou, 1993) and model predictions (lines) for solubility of CO ₂ in 4.5 MDEA from 40-120 °C.	222
Figure B-31: Experimental data (Weiland, 1997) and model predictions (lines) for heat capacity of loaded 30-60 wt % MDEA at 25 °C.	223
Figure B-32: Experimental data (Kierzkowska-Pawlak, 2007) and model predictions (lines) for heat of CO ₂ absorption in 50 wt % MDEA from 40-120 °C.	223
Figure B-33: Experimental data (Hamborg, 2007) and model predictions (line) for MDEA pKa from 20-150 °C.	224
Figure B-34: Experimental data (This Work) and model predictions (lines) for loaded 7 m MDEA/2 m PZ density from 20-60 °C.	225
Figure B-35: Experimental data (This Work) and model predictions (lines) for loaded 5 m MDEA/5 m PZ density from 20-60 °C.	226
Figure B-36: Experimental data (This Work) and model predictions (lines) for loaded 7 m MDEA/2 m PZ viscosity from 20-60 °C.	226
Figure B-37: Experimental data (This Work) and model predictions (lines) for loaded 5 m MDEA/5 m PZ viscosity from 20-40 °C.	227
Figure B-38: Experimental data (Nguyen, 2012) and model predictions (lines) for unloaded amine volatility in 7 m MDEA/2 m PZ from 40-70 °C...	227
Figure B-39: Experimental data (Nguyen, 2012) and model predictions (lines) for unloaded amine volatility in 5 m MDEA/5 m PZ from 40-70 °C...	228
Figure B-40: Experimental data (Nguyen, 2012) and model predictions (lines) for heat capacity of 7 m MDEA/2 m PZ and 5 m MDEA/5 m PZ from 40-120 °C.	228

Figure B-41: Experimental data (Chen, 2011; Xu, 2011) and model predictions (lines) for solubility of CO ₂ in 7 m MDEA/2 m PZ from 40-160 °C.....	229
Figure B-42: Experimental data (Chen, 2011; Xu, 2011) and model predictions (lines) for solubility of CO ₂ in 7 m MDEA/2 m PZ from 40-160 °C.....	229
Figure B-43: Experimental data (Nguyen, 2012) and model predictions (lines) for heat capacity of 7 m MDEA/2 m PZ from 40-120 °C.....	230
Figure B-44: Experimental data (Nguyen, 2012) and model predictions (lines) for heat capacity of 5 m MDEA/5 m PZ from 40-120 °C.....	230
Figure B-45: Model predictions for heat of CO ₂ absorption in 7 m MDEA/2 m PZ from 40-160 °C.	231
Figure B-46: Model predictions for heat of CO ₂ absorption in 5 m MDEA/5 m PZ from 40-160 °C.	231
Figure B-47: Predictions for liquid mole fraction in 7 m MDEA/2 m PZ at 40 °C.	232
Figure B-48: Predictions for liquid mole fraction in 5 m MDEA/5 m PZ at 40 °C.	232
Figure B-49: Parity plot comparing experimental flux (Dugas, 2009; Chen, 2011) and predicted flux for 8 m PZ, 7 m MDEA/2 m PZ, and 5 m MDEA/5 m PZ from 40-100 °C.	233
Figure B-50: Experimental (Dugas, 2009; Chen, 2011) and predicted (lines) k _g ' for 8 m PZ, 7 m MDEA/2 m PZ, and 5 m MDEA/5 m PZ from 40-100 °C.	233

Chapter 1: Introduction

Highly publicized reports such as that compiled by the Intergovernmental Panel on Climate Change (IPCC, 2007) have increased public concern over greenhouse gas spurring a global debate over the feasibility of regulating carbon emissions. While there is not an overwhelming consensus as to how these regulations should be implemented, most groups agree that any legislation will significantly increase the cost of energy. Seventy percent of the electricity generated in the United States is derived from carbon-emitting fossil fuels (USEIA, 2011). Replacing this infrastructure with renewable energy would require not only several years and hundreds of billions of dollars, but also significant advances in technology to improve reliability. This prospect has incentivized research groups to develop cost-effective technologies that significantly reduce the carbon emitted by existing plants. This study focuses on such a technology: retrofit amine scrubbing systems for the removal of CO₂ from the flue gas of coal-fired power plants.

If the goal is to significantly reduce total carbon emissions at a relatively low price, coal-fired power plants are an attractive CO₂ source for several reasons. First of all, they generate forty-five percent of the electricity in the United States (USEIA, 2011) and about seventy-seven percent of the CO₂ (IEA, 2011). On a per kWh basis coal emits more than twice as much CO₂ (900 g/kWh) as its chief competitor: natural gas (387 g/kWh). Therefore, the marginal benefit of fitting a MW of coal-fired capacity with a

CO₂ scrubbing system is greater than that of fitting a MW of natural gas capacity. Secondly, coal is likely to be a significant energy source for decades to come. In addition to an extensive existing coal-burning infrastructure, the United States has a huge domestic supply of coal. It is estimated that the United States has approximately 4 trillion tons of coal (USEIA, 2010), half of which has already been identified. At 2008 energy consumption rates (100×10^{15} BTU per year; USDOE, 2008), identified coal reserves could produce all of the energy in the United States for the next 150 years. Of course this estimate assumes that energy demand will not go up, which is an indefensible position to take. However, even if the United States energy demand grows by 3.8% per year and every BTU consumed in the country is supplied by coal, identified domestic coal reserves will last about 50 years. Finally, coal-fired flue gas has a relatively high concentration of CO₂. As the concentration of a component increases the cost of extracting it decreases. Because the concentration of CO₂ in coal-fired flue gas is about four times that of natural gas flue gas, the cost of mitigation should be lower.

Academic and industrial research groups are currently considering several methods for removing CO₂ from flue gas. At the 10th International Conference on Greenhouse Gas Technologies there were several presentations given on adsorbents, oxy-fuel combustion, and membranes, each of which has the potential to capture CO₂ at a reasonable price from large point sources, eventually. If cost-effective technology is going to be deployed in the near future, a more established separation technique will have to be employed. The removal of CO₂ from process gases using amine scrubbing has been extensively studied for several solvents and solvent blends, and it is currently being

applied in several industrial applications. This familiarity will facilitate immediate deployment of large scale amine scrubbing, making it the choice technology for achieving near-term reductions in CO₂ emissions.

The ostensible mission of the Rochelle group is to rip apart the “art” of amine scrubbing, make a science out of it, and put it back together in a consistent manner. Modeling efforts tend to focus on the latter two steps of this process. This work improves on previous work on thermodynamic modeling (Hilliard, 2008) kinetic modeling (Plaza, 2011) and process design (Van Wagener, 2011) to continue innovating process configurations for piperazine (PZ) and expand modeling activities to include mixtures of methyldiethanolamine (MDEA) and PZ. Blending MDEA and PZ has the potential to combine the high CO₂ capacity of MDEA and the favorable kinetics of PZ. To compare these amines on an economic basis three tools were developed: (1) a thermodynamic model, (2) a kinetics model, and (3) an economic evaluation method.

This work also expands temperature, amine concentration, and CO₂ loading ranges that can be accurately modeled in Aspen Plus[®], which enables the testing of a greater variety of process configurations such as colder absorbers and greater CO₂ removal rates. To compare process configurations the conditions must be simulated using a consistent thermodynamic and kinetic framework. This requires a robust model capable of simulating a much wider set of conditions than any model previously constructed at UT-Austin.

The following is a summary of the completed work in each of the modeling areas.

Thermodynamic and Kinetic Modeling

Heat capacity, loaded and unloaded amine volatility, CO₂ solubility, NMR, CO₂ activity coefficient, density, viscosity, heat of absorption, and CO₂ absorption rate data were used to construct thermodynamically consistent amine models in Aspen Plus[®] for PZ (2—12 m), MDEA (2.8—8.4 m), 7 m MDEA/2 m PZ, and 5 m MDEA/5 m PZ.

Efforts focused on the following objectives:

- Regressed thermodynamic data for PZ (2—12 m)
- Regressed thermodynamic data for MDEA (2.8—8.4 m)
- Regressed thermodynamic data for 7 m MDEA/2 m PZ and 5 m MDEA/5 m PZ within the MDEA and PZ framework
- Incorporated wetted wall column CO₂ absorption rate data for 8 m PZ, 5 m PZ, 7 m MDEA/2 m PZ, and 5 m MDEA/5 m PZ

Absorber Modeling

Several absorber configurations were tested using 8 m PZ, 7 m MDEA/2 m PZ, and 5 m MDEA/ 5 m PZ. Configurations are compared on the basis of solvent capacity predicted using Aspen Plus[®] RateSep[™]. Efforts focused on the following objectives:

- Developed a rate-based absorber
- Developed a method for optimizing absorber size
- Tested novel intercooled configurations

Stripper Configurations

Several stripper configurations were tested using 8 m PZ, 7 m MDEA/2 m PZ, and 5 m MDEA/ 5 m PZ. Configurations are compared on the basis of equivalent work predicted using Aspen Plus[®]. Efforts focused on the following objectives:

- Developed rate-based stripper models for established configurations such as the simple stripper, two-stage flash, and advanced flash stripper
- Developed rate-based stripper models for novel configurations utilizing features such as a rich solvent bypass, multi-temperature vessels, and multi-pressure vessels

Overall Process Optimization

The interactions between absorber and stripper process configurations are tested, as well as their effect on operating and capital costs. Efforts focused on the following objectives:

- Determined effect of CO₂ removal (e.g. 90% vs. 99%) on process performance and optimum configuration
- Developed a pricing model for the comparison of operating and capital costs

Chapter 2: Modeling CO₂ Capture Using MDEA/PZ

2.1 RATIONALE FOR PZ ACTIVATED MDEA

Figure 2-1 depicts the chemical structures of MDEA, PZ, and all amine species derived from their reaction with CO₂. PZ is a cyclic diamine capable of forming PZ carbamate (PZCOO⁻), PZ dicarbamate (PZ(COO)₂²⁻), protonated PZ (PZH⁺), and protonated PZ carbamate (H⁺PZCOO⁻). It should be noted that it is possible to form diprotonated PZ (PZH₂²⁺), but the relevant pH ranges for this study are too high for this species to be present at an appreciable concentration. MDEA is a tertiary amine only capable of accepting a proton to form protonated MDEA (MDEAH⁺). When PZ reacts with CO₂, one nitrogen covalently bonds to the CO₂ molecule, and another nitrogen accepts the proton replaced by CO₂. Therefore, every mole of absorbed CO₂ consumes two moles of alkalinity. MDEA simply accepts the proton generated when CO₂ reacts with water to form the bicarbonate molecule, thus consuming one mole of alkalinity per mole of CO₂.

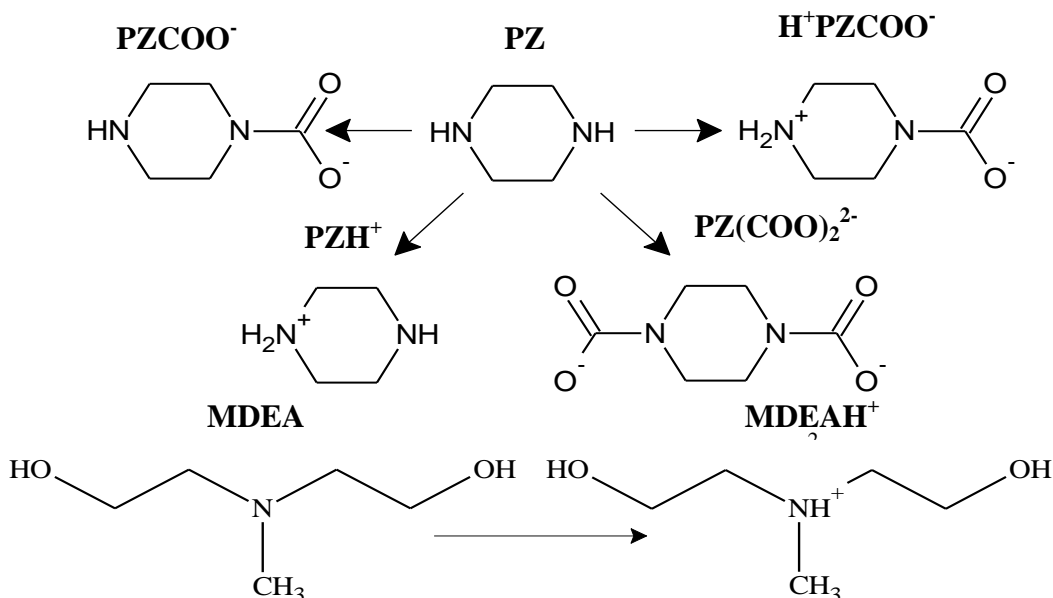


Figure 2-1: Chemical structures of all relevant amine species in MDEA/PZ.

The reaction between PZ and CO₂ is very fast, but the stoichiometry limits solvent capacity. MDEA has an excellent capacity, but the absorption rate is limited by the slow bicarbonate forming reaction. A blend of MDEA and PZ has the potential to combine the high capacity of MDEA with the attractive kinetics of PZ. Table 2-1 compares 7m MDEA/2m PZ to 8m PZ and 7m MEA on the basis of capacity, CO₂ absorption rate (k_g ; Dugas, 2009), and heat of absorption. Aside from the heat of absorption of MEA (Kim, 2008), which continues to be the best in the industry, the blend is better than or competitive with both of the benchmark amines in every category. Another less obvious advantage of the blend is that, unlike PZ, it is not limited by amine solubility. At low temperature and loading 8m PZ precipitates (Freeman, 2010), an event that would be difficult if it ever occurred in an industrial operation. While this does not preclude the viability of PZ as an amine for CO₂ capture from coal-fired power plants, its operating

ranges are more limited than amines such as 7m MDEA/2m PZ, which do not form precipitates.

Table 2-1: Comparing 7m MDEA/2m PZ to 8m PZ and 7m MEA

Amine	Capacity (mol CO₂/kg solvent)	k_g'@40 °C and 5kPa (kmol/m².kPa.s)	ΔH_{ABS} (kJ/mol CO₂)
7m MDEA/2m PZ	0.83	4.7x10 ⁻⁷	68
8m PZ	0.76	4.7x10 ⁻⁷	65
7m MEA	0.50	3x10 ⁻⁷	84

Several mixtures of MDEA and PZ are currently being used in industrial applications. BASF patented a PZ activated MDEA solvent for the removal of CO₂, H₂S, and/or COS from natural gas, coke-oven gas, and various synthesis gases (Appl, 1982). Dow Chemical Company, UOP LLC, and Huntsman Corporation are all very familiar with the properties and application of blended amines such as MDEA/PZ (Kohl, 1997). Because major industrial players have experience with it, MDEA/PZ will have less resistance to application than other solvents.

2.2 THERMODYNAMIC MODELING

Several previous studies have modeled amine thermodynamics. An early FORTRAN model developed by Austgen (1989) used Electrolyte-NRTL and UNIFAC methodology to predict CO₂ solubility and speciation data for various amine/H₂O/CO₂ systems. This FORTRAN framework was later modified by Bishnoi (2000) and Cullinane (2005) to include kinetic rate data for several more amines and blended amines. Two MDEA/PZ models have been developed in the past couple years: (1) a UNIQUAC-based thermodynamic model developed by Ermatchkov (2011) and (2) a COMSOL-based thermodynamic and kinetic model developed by Edali (2010). Though all of these

models accurately predict selected sets of experimental data, their scope and thermodynamic consistency are practically inadequate for this study.

All of these models calculate equilibrium constants using a polynomial expression rather than thermodynamically significant quantities such as ΔG_f° , ΔH_f° , and C_P° . There are two equations that may be used to calculate equilibrium constants in Aspen Plus[®]: (1) a temperature-dependent polynomial and (2) an expression based on $\Delta G_{f,rxn}^\circ$, $\Delta H_{f,rxn}^\circ$, and $\Delta C_{P,rxn}^\circ$. These expressions are shown below as Equations 2-1 and 2-2, respectively. The major disadvantage of using Equation 2-1 is that it does not maintain consistency between speciation and the thermodynamic properties calculated from speciation. A simulation using Equation 2-1 will calculate equilibrium constants at the operating temperature, solve the system of equations to determine speciation, and use the resulting speciation to calculate properties such as enthalpy and heat capacity. The constants in Equation 2-1 correspond to terms in Equation 2-2, and, thus, these constants can be used to calculate ΔG_f° , ΔH_f° , and C_P° values for every species in the system. Therefore, models using Equation 2-1 use one set of ΔG_f° , ΔH_f° , and C_P° parameters to calculate thermodynamic properties and, effectively, another set of ΔG_f° , ΔH_f° , and C_P° parameters to calculate equilibrium constants. If these two sets of parameters do not match up, the model contains a thermodynamic inconsistency. Using Equation 2-2 avoids this problem by using the same set of ΔG_f° , ΔH_f° , and C_P° parameters to calculate both equilibrium constants and thermodynamic properties.

$$\ln K_{eq} = A + \frac{B}{T} + C \ln T + DT \quad \text{Equation 2-1}$$

$$-\ln K_{eq} = \frac{\Delta G^o}{RT} = \frac{\Delta G_0^o - \Delta H_0^o}{RT_0} + \frac{\Delta H_0^o}{RT} + \frac{1}{T} \int_{T_0}^T \frac{\Delta C_P^o}{R} dT - \int_{T_0}^T \frac{\Delta C_P^o}{R} dT \quad \text{Equation 2-2}$$

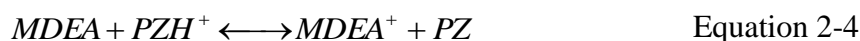
In addition to having a thermodynamic inconsistency, models developed during earlier studies are based on a limited set of experimental data. Heat capacity, amine volatility, and CO₂ activity coefficient data, all of which are excluded from these early models, are very important when optimizing a rate-based absorption/stripping operation. Activity-based models developed by Hilliard (2008) and Dugas (2009) in Aspen Plus[®] sought to correct these inadequacies, but they were unable to do so for the amines and concentration ranges relevant to this work. The Aspen Plus[®] models developed in this study will utilize sequential regression methodology to predict experimental data for amine dissociation constant (Hamborg, 2007; Hetzer, 1968) CO₂ solubility (Bishnoi, 2000; Chen, 2011; Dugas, 2009; Jou 1993), amine volatility (Nguyen, 2011), heat capacity (Hilliard, 2008), activity coefficient of CO₂ (Rinker, 1997; Svendsen, 2009), and speciation (Ermatchkov, 2003) over operationally significant temperature, loading, and amine concentration ranges using thermodynamically consistent methods.

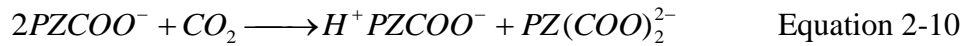
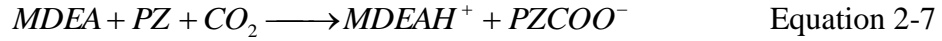
2.3 ABSORBER AND KINETIC MODELING

Recent studies on absorber modeling have focused on the development and validation of rate-based simulations of pilot plant campaigns (Dugas, 2008; Liu, 2006; Plaza, 2008). At absorber conditions it cannot be assumed that reactions reach equilibrium. The rate at which the system approaches equilibrium is affected by several

parameters including CO₂ loading, temperature, vapor and liquid diffusivities, vapor and liquid concentration profiles, and heats of reaction. This study seeks to continue the refinement of rate-based models developed at The University of Texas at Austin to include more complex sets of kinetic reactions and a more useful treatment of ion diffusivities.

The most complex set of amine kinetics relevant to this study was developed by Bishnoi (2000) for a specific blend (7.7 m MDEA/1.1 m PZ). Recently collected wetted wall column data concerning CO₂ solubility and absorption rate make it possible to expand the range of amine mixtures to include 7 m MDEA/2 m PZ, 5 m MDEA/5 m PZ, and concentrated (8 m) PZ. Because these solvents use progressively more PZ, a new set of kinetic reactions will have to be used to model the absorption of CO₂ in which MDEA and PZ are both potential catalysts for the formation of carbamate species (i.e. PZCOO⁻, PZ(COO)₂²⁻, H⁺PZCOO⁻). In MDEA/PZ blends containing very little PZ there is not an appreciable amount of free PZ over the operational loading range. Solvents like 5 m MDEA/5 m PZ and 8 m PZ have a significant amount of free PZ at lean loading conditions, and, thus, PZ catalyzed reactions must be considered. Equations 2-3 through 2-10 were determined from speciation data (experimental and model-predicted) to be the most complete set of kinetic and equilibrium reactions for modeling the absorption of CO₂ by MDEA, PZ, and MDEA/PZ.





Aspen Plus[®] calculates ion diffusivities using the Nernst-Hartley Equation, which is a function of temperature (T), charge (z_i), Faraday's number (F), the gas constant (R), two regressed parameters ($l_{1,i}$ and $l_{2,i}$), and mole fraction of non-ionic species (x_k).

$$D_i = \left(\frac{RT}{z_i F^2} \right) (l_{1,i} + l_{2,i} T) \sum_k x_k \quad \text{Equation 2-11}$$

A notable omission to this equation is mixture viscosity, which has been shown to correlate very strongly with diffusivity (Derks, 2008; Samanta, 2007; Dugas, 2009). This study will calculate ion diffusivities using Equation 2-12, and the values of D_0 , α , and β will be adjusted to fit CO_2 absorption rates at higher temperatures (80 °C—100 °C).

$$D_i = D_0 T^\beta \mu^\alpha \quad \text{Equation 2-12}$$

The rate-based Aspen Plus[®] model has been used to determine the performance of several absorber configurations. Intercooling has already been shown to improve solvent capacity for MEA, AMP, and PZ-promoted potassium carbonate (Plaza, 2009; Sipocz, 2011; Tobiesen, 2007). Because less amine is needed to capture the same amount of CO_2 , less amine must be pumped, heated, and cooled, thus reducing the equivalent work.

This study will seek to quantify the operational benefit of intercooling, as well as expand the set of evaluated amines to include the MDEA/PZ blends.

Another process configuration that was evaluated concerns the use of a colder absorber. Lowering the absorber temperature has the potential to improve process efficiency by increasing both the capacity and the partial pressure of CO₂ being fed into the compressor. Both of these improvements may be attributed to the effect depicted in Figure 2-2. Assuming that the operational loading range always corresponds to equilibrium partial pressures of 0.5 and 5 kPa at the lean and rich ends, respectively, decreasing the absorber temperature from 40 °C to 30 °C both increases the capacity of 7 m MDEA/2 m PZ from 0.76 mol CO₂/ kg H₂O + amine to 0.88 mol CO₂/kg H₂O + amine and increases the partial pressure of CO₂ at 120 °C from 550 kPa to 800 kPa. Both of these benefits may be attributed to the upward shift in the operational loading range. The effect on partial pressure of CO₂ is trivial; the effect on capacity is a little more complex. PZ is a much stronger base than MDEA. When the first molecule of CO₂ is absorbed by unloaded MDEA/PZ, PZ is much more likely than MDEA to catalyze the reaction. Therefore, low loading amine properties (e.g. capacity) are dictated by PZ. Shifting to a higher operational loading range implies shifting from a PZ-dominated system towards a MDEA-dominated system. Because MDEA exhibits a greater capacity than PZ, lowering the temperature of activated MDEA solvents has the potential to increase capacity.

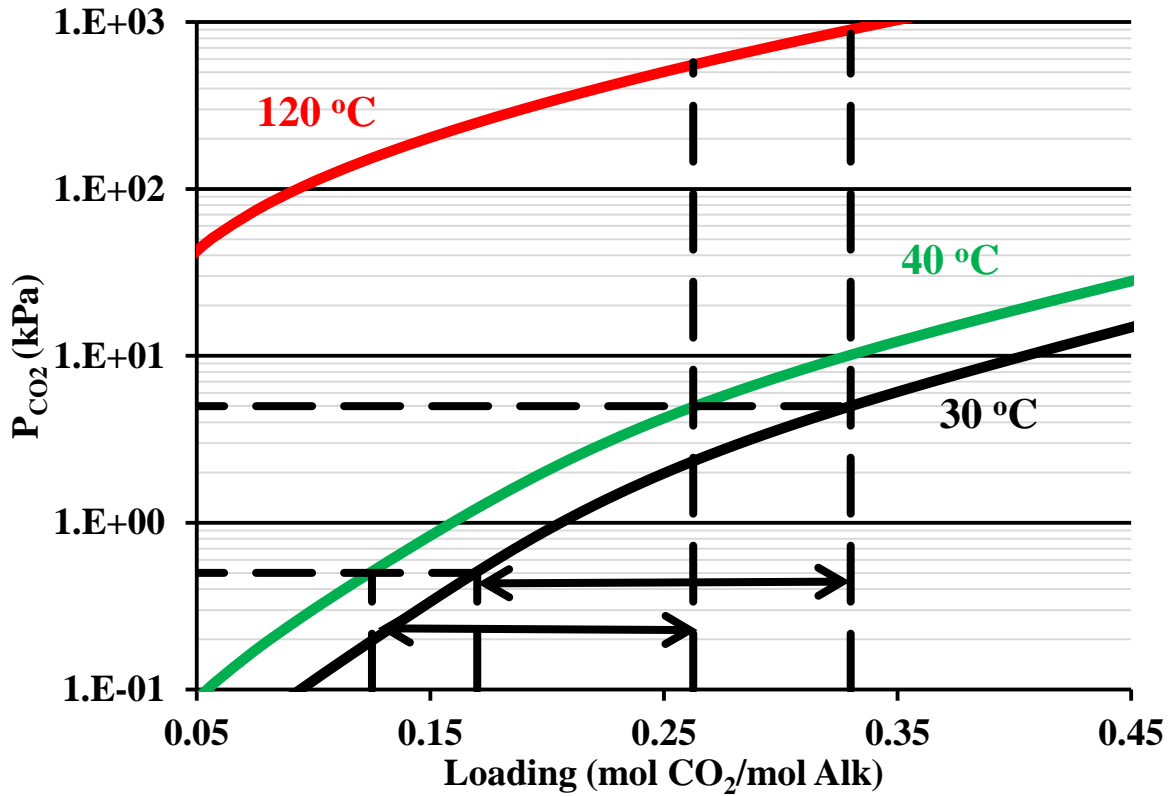


Figure 2-2: Partial pressure of CO₂ as a function of loading for 7 m MDEA/2 m PZ from 30–120 °C.

Despite the potential advantages of using a colder absorber there are very few references to it in literature. Dugas (2009) hints at its advantages, but provides no results or recommendations as to how it could be implemented. Outside of the chilled ammonia process, which must cool the solvent to combat high amine volatility, there is only one study examining the effect of absorber temperature on process efficiency (Kvamsdal, 2010). There are several possible reasons for this lack of interest. A major deterrent is that adequate heat sinks must be readily available to cool the inlet vapor and liquid streams. Also, colder operating temperatures are perceived as detrimental to CO₂ absorption rate. Both reaction rates and diffusion coefficients decrease as temperature

decreases, suggesting that a much larger absorber would be needed to remove the same amount of CO₂. A less obvious potential disadvantage is that lowering the absorber temperature could cause the solvent to precipitate in the column. This is not a major issue with most solvents, but PZ, which precipitates at higher loadings, could not be used to capture CO₂ from coal-fired flue gas at these temperatures.

These perceived disadvantages do not preclude the usefulness of quantifying the relationship between absorber temperature and process performance. Lower temperatures are not as detrimental to the absorption rate of CO₂ as one might think. The concentration of amine is approximately constant across the liquid boundary layer, allowing the pseudo-first order assumption to be applied to absorber kinetics. Under this assumption the liquid side mass transfer coefficient, k_g' , may be expressed as a function (Equation 2-13) of amine concentration ([Am]), a second order reaction rate constant (k_2), diffusivity of CO₂ (D_{CO_2}), and the Henry's constant of CO₂ (H_{CO_2}).

$$k_g' \approx \frac{\sqrt{D_{CO_2} [Am] k_2}}{H_{CO_2}} \quad \text{Equation 2-13}$$

Because D_{CO_2} , k_2 , and H_{CO_2} exhibit similar temperature dependences, k_g' has a negligible dependence on temperature. Preliminary results show that for each degree centigrade that the absorber temperature is lowered there is marginal improvement in operating cost and a marginal increase in capital cost. Depending on the relative magnitudes of these costs, there exists an optimum absorber temperature for a given set of economic constraints that might be easily accommodated by available heat sinks. If

this optimization is ever to be attempted, the effect of absorber temperature on equivalent work and absorber height must be established.

2.4 STRIPPER CONFIGURATIONS

Most stripper models generate predictions using equilibrium-based calculations. At stripper temperatures (100—150 °C) the rate of desorption of CO₂ is not appreciably limited by reaction rate, but it is limited by mass transfer rate. Chemical reactions proceed quickly enough to reach equilibrium, but reactants and products must diffuse to and from the reaction boundary layer for the entire system to be considered at equilibrium. The diffusion rate of reactants and products is strongly influenced by both hydraulic properties such as viscosity, density, and diffusion coefficients and process parameters such as packing type, liquid holdup, and liquid velocity. This study will implement correlations that have been developed by Tsai (2010) and Wang to calculate interfacial area and mass transfer coefficients as functions of these parameters for rate-based simulations in Aspen Plus[®].

Previous work on advanced stripper configurations (Leites et al., 2003; Oyenekan, 2007; Van Wagener, 2011) has focused on one tradeoff: improving process reversibility (operating cost) in exchange for process complexity (capital cost). By operating several columns and vessels at several temperatures and pressures, the desorption of CO₂ can be accomplished with much smaller driving forces, thus improving process reversibility. Van Wagener (2011) simulated several process configurations for MEA and PZ including multi-stage flash, interheated column, and cold-rich bypass. Relative to the simple stripper, each of these configurations applies heat and/or strips CO₂ in more steps using

smaller heat and material driving forces. The relative advantages of these configurations varied from one amine to another, suggesting that a relationship may be established between amine bulk properties and the potential advantages of particular process configurations. This study expands the set of amines tested in these advanced configurations and develops an advanced flash stripper configuration that improves process reversibility.

2.5 OVERALL PROCESS OPTIMIZATION

When modeling an absorber and stripper separately, communication between the process units tends to be unidirectional. The rich solution being fed into a stripper may have been generated using an optimized absorber design, but the optimum lean solution generated by the stripper is not fed back to the absorber. In practice the lean solution exiting the stripper must be identical to the lean solution entering the absorber, but that is not always applied as a constraint. Modeling an absorber and stripper together both improves the accuracy of process performance estimates and allows for the design and optimization of much more complex process configurations in which several variable heat and material streams flow between the absorber and stripper.

This capability will be useful for determining the relationship between removal rate and process performance. Removal rate significantly influences operational loading ranges. Typically processes are designed to remove 90% of the CO₂. The quasi-quantitative reasoning behind this number is that removing less than 90% would not justify the construction of a billion dollar plant but the marginal benefits of removing more than 90% are significantly less than the marginal costs of larger process units. If

the removal rate is increased to 99%, the operational loading range has the potential to double. A larger loading range implies a larger variety of relevant chemical reactions, especially in amine blends where there are several possible catalysts. Because both absorber sizing and stripper design depend heavily on solvent capacity and operational loading range, both process units must be modeled to determine the effect of removal rate on process performance. This study establishes this relationship, focusing on the potential benefit of higher removal rates.

The true costs and benefits of process configurations cannot be determined without a thorough economic analysis. Process reversibility can always be improved by adding more flash vessels, larger heat exchangers, and taller columns, but eventually the marginal improvements in efficiency are dwarfed by the marginal cost of purchasing new equipment. A few attempts have been made to quantify the impact of CO₂ scrubbing on the cost of electricity (Desideri, 1999; Alie, 2005, Rochelle, 2005; Abu-Zahra, 2007), but these studies tend to focus on one amine or one process configuration. A global optimization requires the examination of several amines and process configurations. The economic analysis in this work will focus on establishing the relationships between bulk amine properties, amine chemical structure, and the overall cost of advanced process configurations. By simulating several process configurations with an adequate array of amines, the costs and benefits of solvent capacity, CO₂ absorption rate, and heat of absorption can be quantified.

Chapter 3: Thermodynamic Modeling

3.1 INTRODUCTION

Before modeling amine kinetics or process performance a thermodynamic framework must be developed that accurately and precisely predicts equilibrium conditions for all relevant amines and amine blends over operationally significant temperature, loading, and amine concentration ranges. The model presented in this study predicts equilibrium conditions for methyldiethanolamine (MDEA), piperazine (PZ), and MDEA/PZ at operating conditions relevant to CO₂ capture from large point sources such as coal-fired power plants (12 mol %), natural gas combined cycle power plants (3-4 mol-%), steel mills (20 mol %), and cement plants (20 mol %). Experimental data for amine volatility (loaded and unloaded), heat capacity (loaded and unloaded), CO₂ solubility, and CO₂ activity coefficient were regressed with Aspen Plus[®] DRS and Microsoft Excel[™]. NMR, heat of absorption, and solid solubility data were also checked to validate model predictions. The final activity-based Aspen Plus[®] thermodynamic model uses seventy-four adjusted parameters to predict all amine, amine/H₂O, and amine/H₂O/CO₂ data using activity coefficients calculated by the electrolyte non-random two liquid (eNRTL) method. In addition to accurate predictions of the directly regressed experimental data, the model predicts a heat of fusion for PZ·6H₂O of 48 kJ/mol, solvent capacities that are comparable to simpler empirical models, and heats of CO₂ absorption for PZ (75 kJ/mol CO₂), MDEA (55 kJ/mol CO₂), and MDEA/PZ (~65 kJ/mol CO₂).

3.2 LITERATURE REVIEW

Several previous studies have modeled the thermodynamics of MDEA, PZ, and MDEA/PZ in CO₂ capture. An early activity-based FORTRAN model developed by Austgen (1989) used Electrolyte-NRTL and UNIFAC methodology to predict CO₂ and H₂S solubility and speciation data for various amines and amine blends including 25-50 wt % MDEA. This FORTRAN framework was later modified by Bishnoi (2002) to include MDEA/PZ thermodynamic and kinetic data at absorber conditions (40-70 °C) and low concentrations of PZ (<5 wt %). Aspen Technology, Inc. (2011) developed rate-based models for CO₂ capture using MDEA and MDEA/PZ blends. The MDEA model focuses on a natural gas treating plant in North Carolina, Canada (Ralf, 2004), and the MDEA/PZ model is based on work by Bishnoi (2000), Hilliard (2008), and Austgen (1989). Cullinane (2005) expanded the PZ concentration range to include up to 25 wt % PZ solutions as well as K₂CO₃/PZ blends. The first Aspen Plus[®] thermodynamic model for concentrated PZ was developed by Hilliard (2008) to predict CO₂ solubility, amine volatility, heat capacity, heat of absorption, and speciation data over operationally significant temperature and loading ranges. Two MDEA/PZ models have been developed recently: (1) a UNIQUAC-based thermodynamic model developed by Ermachkov (2011) and (2) a COMSOL-based thermodynamic and kinetic model developed by Edali (2010). Though all of these models accurately predict selected sets of experimental data, their scope and thermodynamic consistency are practically inadequate for this study.

All of these models calculate equilibrium constants using a polynomial expression rather than thermodynamically significant quantities such as ΔG_f° , ΔH_f° , and C_P° . There are two equations that may be used to calculate equilibrium constants in Aspen Plus[®]: (1) a temperature-dependent polynomial and (2) an expression based on $\Delta G_{f,rxn}^\circ$, $\Delta H_{f,rxn}^\circ$, and $\Delta C_{P,rxn}^\circ$. These expressions are shown below as Equations 3-1 and 3-2, respectively. The major disadvantage of using Equation 3-1 is that it does not maintain consistency between speciation and the thermodynamic properties calculated from speciation.

$$\ln K_{eq} = A + \frac{B}{T} + C \ln T + DT \quad \text{Equation 3-1}$$

$$-\ln K_{eq} = \frac{\Delta G^\circ}{RT} = \frac{\Delta G_0^\circ - \Delta H_0^\circ}{RT_0} + \frac{\Delta H_0^\circ}{RT} + \frac{1}{T} \int_{T_0}^T \frac{\Delta C_P^\circ}{R} dT - \int_{T_0}^T \frac{\Delta C_P^\circ}{R} dT \quad \text{Equation 3-2}$$

In addition to having a thermodynamic inconsistency, models developed during earlier studies are based on a limited set of experimental data. Heat capacity, amine volatility, and CO₂ activity coefficient data, all of which are excluded from these early models, are very important when optimizing a rate-based absorption/stripping operation. Activity-based models developed by Hilliard (2008) and Dugas (2009) in Aspen Plus[®] sought to correct these inadequacies, but they were unable to do so for the amines and concentration ranges relevant to this work. The Aspen Plus[®] models developed in this study will utilize sequential regression methodology to predict experimental data for amine dissociation constant (Hamborg, 2007; Hetzer, 1968), CO₂ solubility (Bishnoi, 2000; Chen, 2011; Dugas, 2009; Jou, 1993), amine volatility (Nguyen, 2012), heat capacity (Hilliard, 2008), activity coefficient of CO₂ (Rinker, 1997; Svendsen, 2009), and

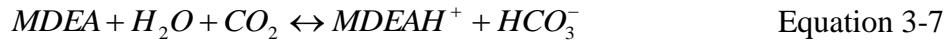
speciation (Ermatchkov, 2003) over operationally significant temperature, loading, and amine concentration ranges using thermodynamically consistent methods.

3.3 MODEL DESCRIPTION

The model presented here is the third iteration of an MDEA/PZ thermodynamic framework developed during this study. The previous two versions, 5deMayo and GuyFawkes, are documented in Appendices A and B, respectively.

3.3.1 Equilibrium Constant Calculations in Aspen Plus[®]

The models in this study calculate equilibrium constants using Equation 3-2 for each of the chemical reactions listed below.



The species in Equations 3-3 to 3-8 can be separated into three distinct groups: (1) molecular (PZ, MDEA, CO₂, and H₂O), (2) ionic (PZH⁺, PZCOO⁻, PZ(COO)₂²⁻, MDEAH⁺, HCO₃⁻, and CO₃²⁻), and (3) zwitterion (H⁺PZCOO⁻). The Gibbs energy of formation (ΔG_f^0) for each group is calculated at process conditions from a designated reference state. The reference state for each group is different, and, therefore, different parameters are required to calculate ΔG_f^0 .

All molecular species, with the exception of H₂O, are designated Henry's components with an ideal gas reference state. Liquid phase ΔG_f° , ΔH_f° , and C_P° are calculated by first calculating the vapor phase properties at the given temperature and pressure. The relationship between the liquid and vapor phase properties is given by the Henry's constant of species i in solvent A, H_{iA} , which is calculated by Equation 3-9.

$$\ln H_{iA}(T) = a_{iA} + \frac{b_{iA}}{T} + c_{iA} \ln T + d_{iA} T + \frac{e_{iA}}{T^2} \quad \text{Equation 3-9}$$

Equations 3-2 and 3-9 are very similar in form. Appreciating the similarities can be helpful when regressing amine volatility and unloaded heat capacity data. The constant a_{iA} in Equation 3-9 corresponds to ΔG_f° in 3-2, b_{iA} corresponds to ΔH_f° , and the remaining parameters correspond to the C_P° calculation. Ideal gas properties and the parameters of Equation 3-9 are used to regress experimental data concerning the liquid phase, and, thus, the mathematical relationships between the above mentioned parameters should be considered when interpreting regression results.

Ionic species are referenced to infinite dilution in water. Because ionic species cannot enter vapor or solid phases, the calculation of ΔG_f° , ΔH_f° , and C_P° is simple and straightforward.

The zwitterion is modeled as a Henry's component with an ideal gas reference state. Hilliard (2008) modeled the zwitterion as an ionic species with a charge of 10^{-5} . This approach introduced two major errors: (1) at high CO₂ loadings where the concentration of zwitterion is particularly high the solution is not in charge balance, and (2) the diffusion coefficient is five orders of magnitude larger than that of other ionic

species. Because the zwitterion is assumed to be a non-volatile species, the Henry's constant of H^+PZCOO^- in water is fixed at e^{-20} , which is on the order of 2×10^{-9} . All liquid phase properties for zwitterions are calculated by the same equations and methods used to calculate the properties of molecular species.

3.3.2 Activity Coefficient Calculation in Aspen Plus[®]

Activity coefficients for ionic species are calculated using the electrolyte non-random two liquid (eNRTL) method. The activity coefficient is defined as the partial excess Gibbs energy of a component in a mixture (Equation 3-10).

$$\ln \gamma_i = \frac{G_m^{*E}}{RT} = \left[\frac{\delta(nG_m^{*E} / RT)}{\delta n_i} \right] \quad \text{Equation 3-10}$$

The eNRTL method assumes that there are three contributions to the activity coefficient: (1) the Pitzer-Debye-Huckel long-range interaction, (2) the Born correction for the infinite dilution aqueous reference state, and (3) local contributions.

The long-range interaction is calculated by Equation 3-11, where M_s is the molecular weight of the species, A_ϕ is the Debye-Huckel parameter, I_x is the ionic strength on a mole fraction basis, and ρ is the closest approach parameter.

$$\frac{G_m^{*E,PDH}}{RT} = -\sum_i x_k \left(\frac{1000}{M_s} \right)^{0.5} \left(\frac{4A_\phi I_x}{\rho} \right) \ln(1 + \rho I_x^{0.5}) \quad \text{Equation 3-11}$$

The ionic strength, I_x , and Debye-Huckel parameter, A_ϕ , are calculated by Equations 3-12 and 3-13, respectively.

$$I_x = 0.5 \sum_i x_i z_i^2 \quad \text{Equation 3-12}$$

$$A_\phi = \frac{1}{3} \left(\frac{2\pi N_0 d}{1000} \right)^{0.5} \left(\frac{e^2}{D_w kT} \right)^{1.5} \quad \text{Equation 3-13}$$

In Equation 3-12 x_i is the component mole fraction and z_i is the charge. In Equation 3-13 N_0 is Avogadro's Number, d is the solvent density, e is the charge of an electron, D_w is the dielectric constant for water, k is the Boltzmann constant, and T is the temperature in K. Of the parameters that go into the calculation of the long-range contribution the only adjustable parameters are ρ , which is fixed in Aspen Plus[®], and d , which should not be adjusted in this regression.

The Born correction accounts for the change in reference state from the local to the long-range contribution. The long-range contribution is referenced to infinite dilution in mixed solvent, whereas the local contribution is referenced to infinite dilution in water. Equation 3-14 references both contributions to infinite dilution in water.

$$\frac{G_m^{*E,Born}}{RT} = \left(\frac{e^2}{2kT} \right) \left(\frac{1}{D_m} - \frac{1}{D_w} \right) \frac{\sum_i x_i z_i^2}{r_i} 10^{-2} \quad \text{Equation 3-14}$$

D_m is the dielectric constant of the mixture and r_i is the Born radius. The only adjustable parameter in Equation 3-14 is D_m . This study assumes that the dielectric constant of PZ is the same as piperidine (Hilliard, 2008). The dielectric constant of MDEA and H₂O are already part of the Aspen Plus[®] databases.

The local contribution offers the greatest opportunity for parameter regression. Equations 3-15 to 3-18 calculate the local contribution.

$$\frac{G_m^{*E,lc}}{RT} = \sum_m X_m \frac{\sum_j X_j G_{jm} \tau_{jm}}{\sum_k X_k G_{km}} + \sum_c X_c \sum_{a'} \left(\frac{X_{a'}}{\sum_{a''} X_{a''}} \right) \frac{\sum_j G_{jc,a'} \tau_{jc,a'}}{\sum_k X_k G_{jc,a'}} + \dots$$

$$\dots + \sum_a X_a \sum_{c'} \left(\frac{X_{c'}}{\sum_{c''} X_{c''}} \right) \frac{\sum_j G_{ja,a'} \tau_{ja,a'}}{\sum_k X_k G_{ja,a'}}$$

Equation 3-15

$$\tau_{mc,ac} = -\ln \left[\frac{\sum_a X_a \exp(-\alpha_{ca,m} \tau_{ca,m})}{\sum_{a'} X_{a'}} \right] - \tau_{ca,m} + \tau_{m,ca}$$

Equation 3-16

$$G_{mc,ac} = \exp(-\alpha_{ca,m} \tau_{mc,ac})$$

Equation 3-17

$$\tau_{m,ac} = A_{m,ac} + \frac{B_{m,ac}}{T} + C_{m,ac} \left(\frac{(T^{ref} - T)}{T} + \ln \left(\frac{T}{T^{ref}} \right) \right)$$

Equation 3-18

The only adjustable parameters are A, B, and C in Equation 3-18, which correspond to the Aspen Plus[®] parameters GMELCC, GMELCD, and GMELCE, respectively. Just as with the parameters in Equation 3-9 for the Henry's constant, the parameters in Equation 3-18 correspond to ΔG_f^0 , ΔH_f^0 , and C_p^0 in Equation 3-2.

The long-range interaction, Born correction, and local contribution for the excess Gibbs energy are simply added together and put into Equation 3-10 to calculate the activity coefficient for ionic species. Henry's components are referenced to an infinite dilution activity coefficient calculated by Equations 3-19 and 3-20.

$$\ln \gamma_x^\infty = \tau_{yx} + \tau_{xy} \exp(-\alpha_{xy} \tau_{xy})$$

Equation 3-19

$$\tau_{xy} = A_{xy} + \frac{B_{xy}}{T} + C_{xy} \ln T + D_{xy} T$$

Equation 3-20

The α_{xy} term roughly corresponds to the reciprocal of the coordination number of the species. The stronger the interaction is between species x and solvent y, the smaller the value of α_{xy} .

3.3.3 Vapor-Liquid Equilibrium Calculation in Aspen Plus[®]

Vapor-liquid equilibrium is defined as the condition where the fugacity of the vapor and fugacity of the liquid are equal. Equation 3-21 describes this condition.

$$y_i \phi_i^v P = x_i \gamma_i \left(\frac{H_i}{\gamma_i^\infty} \right) \exp \left[\frac{V_i^\infty (P - P_{H_2O}^0)}{RT} \right] \quad \text{Equation 3-21}$$

In Equation 3-21 V_i^∞ is the Brelvi-O'Connell partial molar volume for the supercritical component at infinite dilution, and $P_{H_2O}^0$ is the saturation pressure of water at that condition.

3.4 OPERATING RANGES OF MODELS

A major goal of this study is to improve the accuracy of thermodynamic and kinetic models over wider temperature, loading, and amine concentration ranges. Coal-fired power plants represent a significant global source of CO₂, but there is growing interest in mitigating emissions from natural gas, cement, and steel plants. Aspen Plus[®] models must be able to represent equilibrium and rate-based data at conditions relevant to all of these applications.

3.4.1 Temperature

Operational temperature ranges are limited on the cold side by cooling water availability and on the hot side by thermal degradation limits and available steam quality. Most amines in this study must be regenerated at or below 120 °C. The exception to this

rule is concentrated PZ, which can tolerate temperatures up to 150 °C. The cold side limit is generally assumed to be 40 °C, but build sites in the North Sea or Canada have readily available cooling water that can maintain operating conditions down to 20 °C. These colder conditions offer interesting design opportunities for blended amines. For all amines in this study, experimental data is regressed to guarantee accurate predictions from 20 °C to 150 °C. It should be noted that concentrated PZ has debilitating solubility limitations below 40 °C, and, thus, does not have available thermodynamic data below that condition.

3.4.2 Loading

The operational loading range is dictated by the concentration of CO₂ in the flue gas. Previous studies have only considered coal-fired applications, which have a typical CO₂ concentration of 12 %. To maintain a concentration gradient in the absorber, the equilibrium partial pressure of CO₂ is assumed to be held at a 5:12 ratio with the flue gas CO₂ pressure. If it is assumed that the absorber is designed for 90 % capture at atmospheric pressure, the operational loading range corresponds to 0.5 to 5.0 kPa equilibrium partial pressure of CO₂. If the same principle is applied to the flue gas of a natural gas combined cycle (~3% CO₂), the operational range is 0.125 to 1.25 kPa CO₂. Steel and cement plants (20% CO₂) would operate between 0.8 to 8.0 kPa CO₂. This study also considers CO₂ removal rates up to 99% in the coal-fired applications, which lowers the lean loading partial pressure of CO₂ by an order of magnitude to 0.05 kPa. The operational loading range for models in this study is corresponds to 0.1 to 8.0 kPa equilibrium partial pressure of CO₂.

3.4.3 Amine Concentration

Except for instances of solubility limitations, amine concentration is confined by the thermal efficiency of the process. Increasing the concentration of amine increases the capacity of the solvent, but it also increases viscosity and the heat transfer area required in cross exchangers. A zero-order approximation of the optimum is 50 wt % amine, which is the basis for 7 m MDEA/2 m PZ and 5 m MDEA/5 m PZ. The thermodynamic model should accurately predict experimental data for each amine from its most dilute concentration up to 50 wt % amine. For example, in 7 m MDEA/2 m PZ, PZ is relatively dilute (<10 wt %) but it is in a 50 wt % amine solution. The properties of PZ will be somewhere between that of a dilute solution and 50 wt % amine solution. As will be discussed in the next section, the sequential regression method greatly benefits from the inclusion of this much wider range of PZ.

3.5 SEQUENTIAL REGRESSION METHODOLOGY

Ideally, every parameter for every component in a model should be independently regressed and validated using experimental data. While it is impossible to do this for every component in loaded amine systems, key parameters for several components (especially the uncharged molecules) can be accurately regressed by a sequential regression. A sequential regression consists of several regressions performed in order of increasing complexity. Before increasing the order of complexity (from N to N+1), every relevant combination of components at the lower order (N) for which experimental data are available must be regressed. If experimental data are unavailable for a particular system, the parameters relevant to that system must be determined in a higher order

regression. Also, parameters adjusted to fit data at a higher order must not affect the model predictions of lower order regressions.

For example, if the ultimate goal is to model loaded MDEA, one starts by regressing pure component parameters for all apparent species (MDEA, H₂O, and CO₂). The pure component properties of H₂O and CO₂ are built into Aspen Plus[®], leaving only pure MDEA properties undetermined. Because experimental data are unavailable for pure MDEA, the parameters that would have been regressed for pure MDEA must be determined in a higher order regression.

There are three second order systems: MDEA/H₂O, H₂O/CO₂, and MDEA/CO₂. Parameters for H₂O/CO₂ are built into Aspen Plus[®], and there are no experimental data for MDEA/CO₂. Amine volatility and heat capacity data were fit by regressing the following MDEA/H₂O (and MDEA) parameters: MDEA ideal gas heat capacity, the infinite dilution activity coefficient of MDEA in H₂O, and the Henry's constant of MDEA in H₂O.

Having regressed all of the second order parameters, VLE and loaded heat capacity data may be fit by regressing ΔG_f° , ΔH_f° , and C_p° for MDEAH molecule/(cation, anion) activity coefficient parameters. These have been tabulated in Table 3-1 along with the MDEA/H₂O parameters.

Table 3-1: Parameters used for MDEA/H₂O and MDEA/H₂O/CO₂ regressions

Parameter	Species	Number of Terms Regressed
MDEA/H₂O		
γ_{m-m}	MDEA-H ₂ O	2
γ_{m-m}	H ₂ O-MDEA	2
Henry's Constant	MDEA-H ₂ O	3
C_P^{IG}	MDEA	2
MDEA/H₂O/CO₂		
τ_{m-ca}/τ_{ca-m}	MDEA/(MDEAH ⁺ , HCO ₃ ⁻)	6
τ_{m-ca}/τ_{ca-m}	H ₂ O/(MDEAH ⁺ , HCO ₃ ⁻)	6
ΔG_{FM}	MDEAH ⁺	1
ΔH_{FM}	MDEAH ⁺	1
C_P	MDEAH ⁺	1

Notice that in the absence of CO₂ none of the parameters in the MDEA/H₂O/CO₂ regression will influence model predictions. The last set of thermodynamic data that must be fit concerns CO₂ activity coefficients calculated from N₂O solubility data. Because the concentration of free CO₂ in the liquid phase is so small, changes in its activity coefficient will have a negligible effect on macroscopic thermodynamic properties. However, several reaction rates are directly proportional to the activity of CO₂, making it necessary to fit the CO₂ activity coefficient before regressing reaction kinetics. CO₂ activity coefficients are regressed using an Aspen Tech-supplied FORTRAN subroutine.

Having obtained all of the thermodynamic parameters, transport and kinetic data may be fit. Because transport properties (viscosity, density, and diffusivity) influence reaction kinetics, they must be set first. All transport property data collected by experimentalists are reported as functions of temperature, amine concentration, and loading. Transport properties in Aspen Plus[®] are a function of temperature and

speciation. Rather than leave transport properties as a function of speciation and, thus, several calculated thermodynamic properties, FORTRAN subroutines may be implemented that calculate transport properties purely as a function of loading, amine concentration, and temperature. Finally, kinetic data may be regressed using a wetted wall column simulation in Aspen Plus[®].

This example is a relatively simple one. The ultimate goal of this study is to develop a model for MDEA/PZ/H₂O/CO₂, which has one more order of complexity than MDEA/H₂O/CO₂ and significantly more complex speciation and kinetics. Models have been completed for MDEA/H₂O/CO₂, PZ/H₂O/CO₂, and MDEA/PZ/H₂O using the sequential regression approach, and thermodynamic and transport properties for MDEA/PZ/H₂O/CO₂ have been regressed. The sequential regression method can be applied to any amine or blended amine. It is only limited by the available experimental data.

3.6 MODEL REGRESSION

3.6.1 Amine/H₂O

All molecular amine species in this study are modeled as Henry's components. The parameters required to model Henry's component vapor-liquid equilibrium are the Henry's constant (HENRY-1) and the infinite dilution activity coefficient of amine in water (NRTL-1). Amine liquid heat capacity is regressed by fixing ideal gas heat capacities and adjusting parameters in HENRY-1 and NRTL-1 that relate the vapor and liquid heat capacity.

The methodology used in the development of earlier versions of the thermodynamic models was modified to regress all amine-water properties simultaneously. In earlier models the MDEA/H₂O, PZ/H₂O, and MDEA/PZ/H₂O systems were regressed separately to ensure strict adherence to sequential regression methodology. However, this approach limits the set of parameters available to regress MDEA/PZ/H₂O to only MDEA/PZ interaction parameters, which is inadequate to represent all available experimental data. Table 3-2 reports the results of the regression for MDEA/H₂O, PZ/H₂O, and MDEA/PZ/H₂O amine volatility and heat capacity, and Table 3-3 reports the data sources.

Table 3-2: Regression results for MDEA/H₂O, PZ/H₂O, and MDEA/PZ/H₂O

Parameter	Species	Value	Standard Dev.
NRTL 1	MDEA-H ₂ O	-0.291	0.00348
(NRTL 2)/313	MDEA-H ₂ O	-0.295	0.00304
(NRTL 5)(ln313)	MDEA-H ₂ O	-0.292	0.00359
(NRTL 6)(313)	MDEA-H ₂ O	2.191	0.0347
HENRY 1	MDEA-H ₂ O	49.1	1.11
(HENRY 2)/313	MDEA-H ₂ O	-38.0	0.706
(HENRY 4)(313)	MDEA-H ₂ O	-9.58	0.476
NRTL 1	PZ-H ₂ O	-0.817	4.41x10 ⁻³
(NRTL 2)/313	PZ-H ₂ O	-0.823	4.35x10 ⁻³
HENRY 1	PZ-H ₂ O	40.9	1.46
(HENRY 2)/313	PZ-H ₂ O	-33.9	0.958
(HENRY 4)(313)	PZ-H ₂ O	-4.10	0.629

Table 3-3: Data sources for Amine/H₂O regression

Data	[Am]	Temperature (°C)	Source (Year)
MDEA Volatility	0.3-24.5 m	40-100	Kim (2008)
MDEA Volatility	0.5-20 m	40-70	Nguyen (2012)
MDEA C _p	3-20 mol %	5-95	Zhang (2002)
PZ Volatility	2-10 m	40-70	Nguyen (2012)
PZ C _p	2-3.6 m	40-120	Hilliard (2008)
PZ C _p	8 m	70-150	Nguyen (2012)
MDEA/PZ Volatility	7/2; 5/5	40-70	Nguyen (2012)
MDEA/PZ C _p	7/2; 5/5	40-120	Nguyen (2012)

All parameters related to the temperature dependence of NRTL or HENRY are centered at 313 K. If a parameter describing an amine/H₂O parameter is not listed in Table 3-2, it has been left at a default value of zero. The only exception to this is the value for NRTL 3, which is set to 0.3 for PZ/H₂O and 0.2 for MDEA/H₂O. The value of NRTL 3 roughly corresponds to the inverse of the amine coordination number. MDEA possesses three hydrophilic groups, which suggests that it would interact more strongly with H₂O than PZ. None of the MDEA/PZ cross parameters are required to represent the MDEA/PZ/H₂O experimental data. Regressions involving the cross parameters do not exhibit statistically significant dependences on cross parameters. The standard deviations were always several orders of magnitude larger than the parameter values. As the range of MDEA/PZ/H₂O experimental data expands to include higher temperatures the cross parameters may be required to represent heat capacity and amine volatility at regeneration conditions. CPIG parameters are not regressed but rather left fixed.

Figure 3-1 compares experimental data (Nguyen, 2012) and model predictions for amine volatility as a function of temperature for 7 m MDEA/2 m PZ from 40-70 °C. The Gibbs energy and enthalpy of vaporization for a Henry's component may be calculated by Equations 3-22 and 3-23, respectively.

$$\Delta G_f^{\infty,aq} = \Delta G_f^{IG} + RT \ln \left(\frac{H_{i,H_2O}}{P^{ref}} \right) \quad \text{Equation 3-22}$$

$$\Delta H_f^{\infty,aq} = \Delta H_f^{IG} - RT^2 \frac{\partial \ln H_{i,H_2O}}{\partial T} \quad \text{Equation 3-23}$$

In Equations 3-22 and 3-23 H_{i,H_2O} is the Henry's constant of solute I in water, P^{ref} is the reference pressure of 1 bar, the superscript ∞ denotes infinite dilution in water, and the superscript IG denotes the ideal gas reference state. Applying Equation 3-23 to the results in Figure 3-1 gives heats of vaporization for PZ and MDEA of 74.3 kJ/mol and 71.0 kJ/mol, respectively. Applying a trend line to the raw data suggests that the average heats of vaporization from 40-70 °C are 72.1 kJ/mol and 61.8 kJ/mol, respectively.

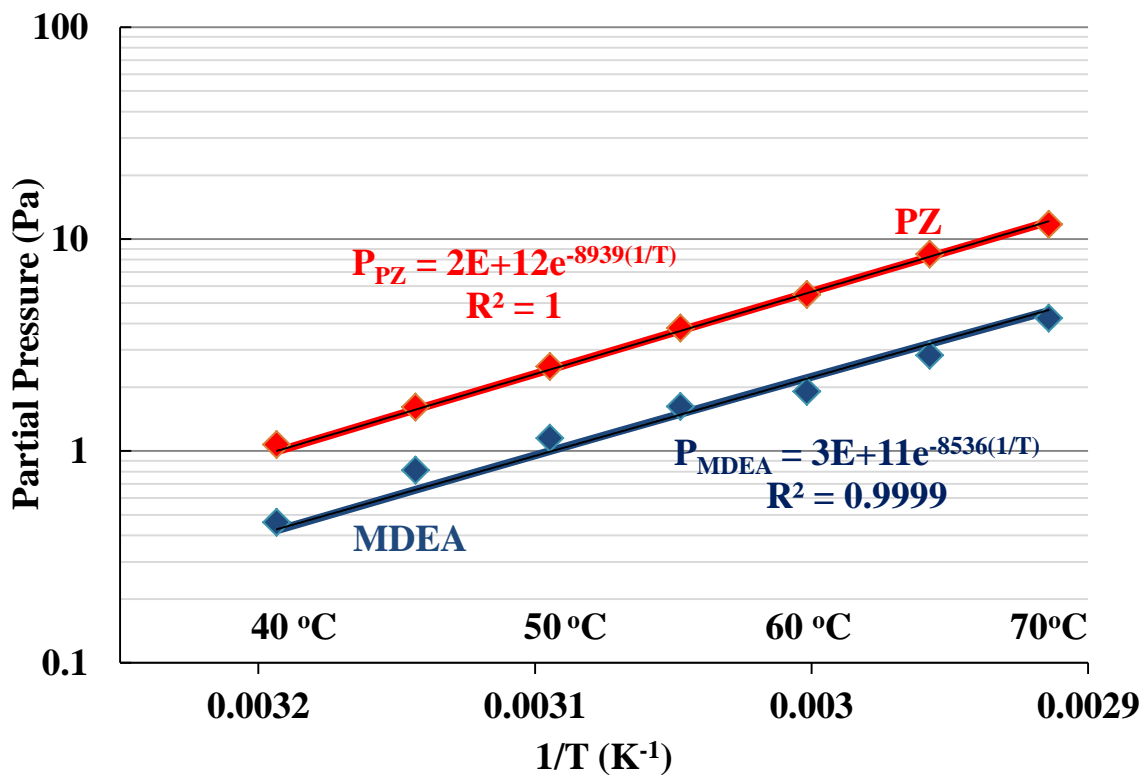


Figure 3-1: Experimental data (points) and model predictions (lines) for unloaded amine volatility as a function of temperature for 7 m MDEA/2 m PZ

Figure 3-2 compares experimental data (Nguyen, 2012) and model predictions for unloaded heat capacity of MDEA/PZ from 40-120 °C.

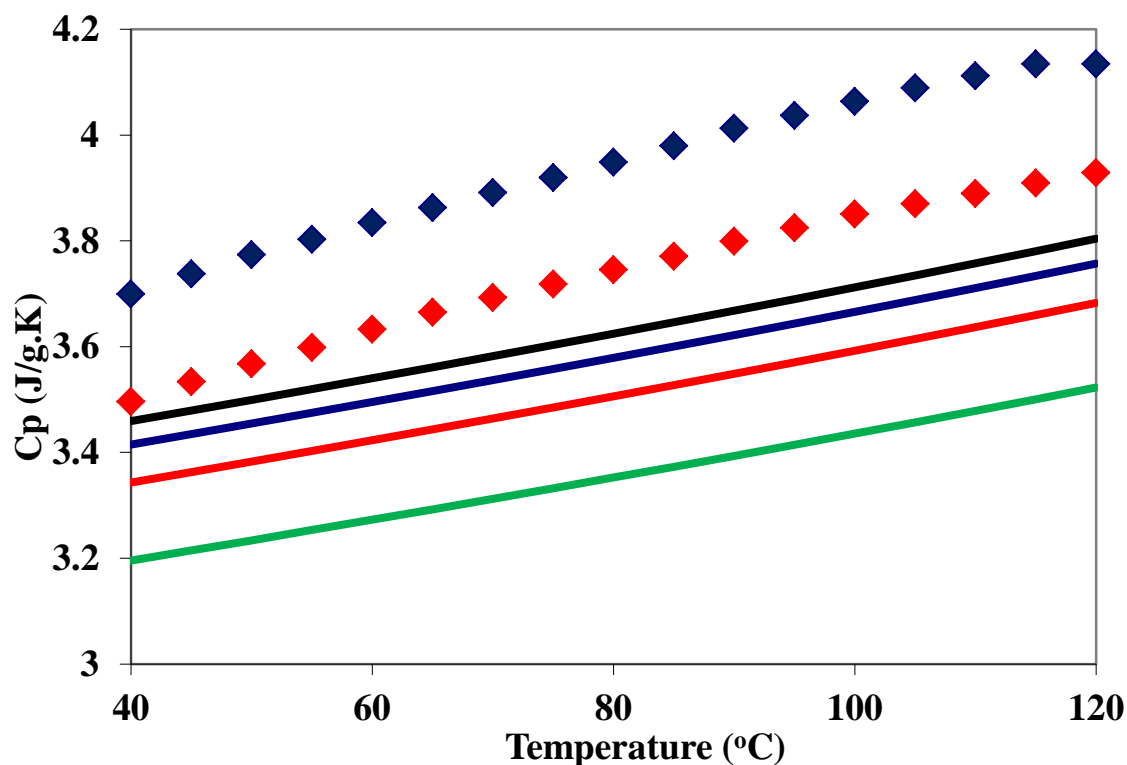


Figure 3-2: Experimental data (points) and model predictions (lines) for unloaded amine heat capacity as a function of temperature for 7 m MDEA/2 m PZ, 5 m MDEA/5 m PZ, 50 wt % PZ, and 50 wt % MDEA

Though it accurately and precisely predicts MDEA/H₂O and PZ/H₂O heat capacity measurements, model predictions for unloaded MDEA/PZ heat capacity systematically under-predict experimental data by at least 5%. Experimental values for blend heat capacity are, as expected, between those of concentrated PZ and MDEA. All of the solvents represented in Figure 3-2 are 50 wt % amine. Figures 3-3 and 3-4 compare experimental data and model predictions for unloaded heat capacity of MDEA (Zhang, 2002) and PZ (Hilliard, 2008; Nguyen, 2012), respectively.

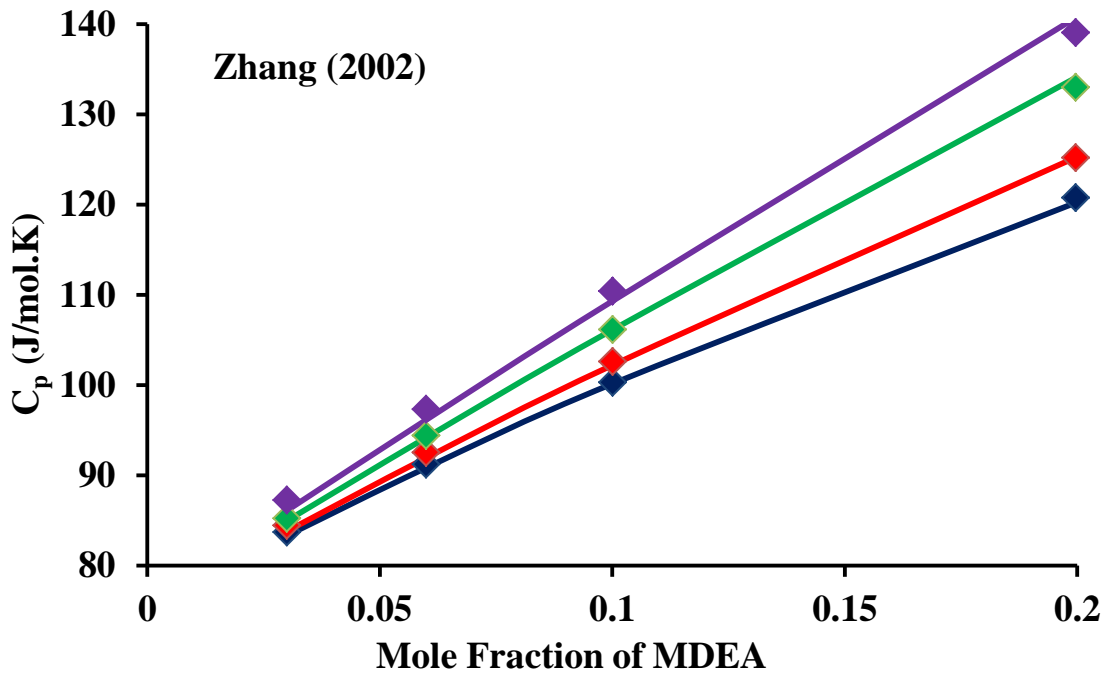


Figure 3-3: Experimental data (points) and model predictions (lines) for unloaded MDEA/H₂O heat capacity as a function of MDEA mole fraction at 25 °C (blue), 40 °C (red), 70 °C (green), and 95 °C (purple)

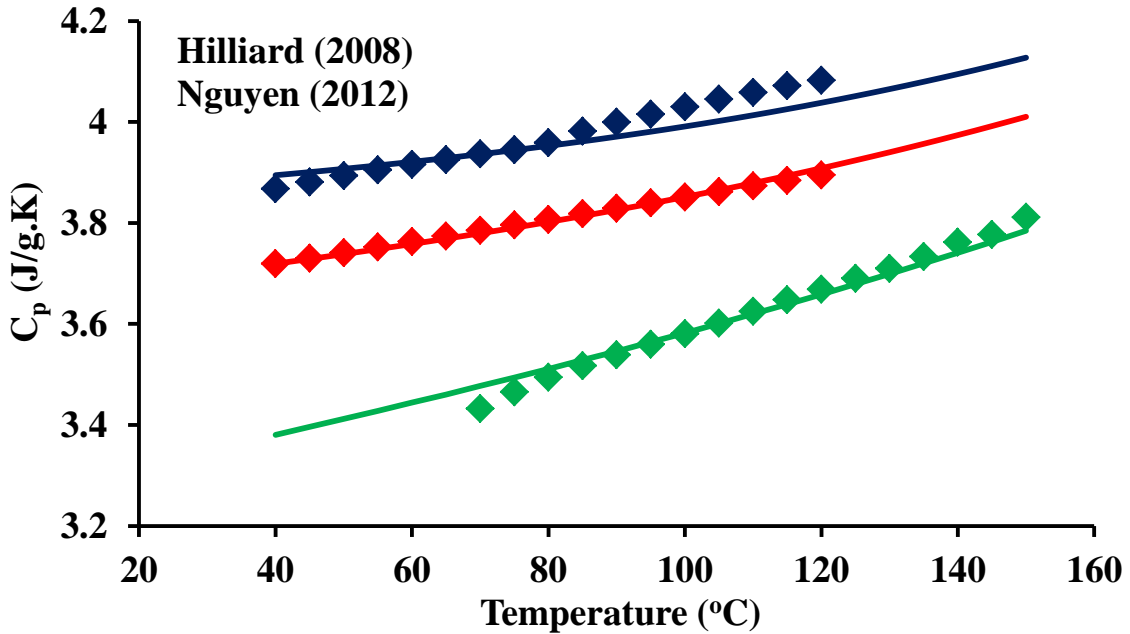


Figure 3-4: Experimental data (points) and model predictions (lines) for unloaded PZ/H₂O heat capacity as a function of temperature for 2 m (blue), 3.6 m (red), and 8 m (green) PZ

The experimental error associated with liquid heat capacity measurements ($\pm 15\%$) is large enough to accommodate the discrepancy between experimental and model values. Rather than include non-default binary interaction parameters for MDEA/PZ to force a fit of the heat capacity data in Figure 3-2, the MDEA/PZ NRTL parameters were set to default values, which assume an ideal interaction between amine molecules (i.e. $\gamma = 1$).

3.6.2 MDEA/H₂O/CO₂ Regression

Loaded MDEA is a difficult system to model because there is a substantial amount of literature data spanning large temperature, loading, and amine concentration ranges but only a few adjustable parameters. The only species present at significant concentrations are MDEA, H₂O, CO₂, MDEAH⁺, HCO₃⁻, and CO₃²⁻. Pure component, binary interaction, and electrolyte interaction parameters for these species must be adjusted to fit data for CO₂ solubility, pKa, heat capacity, amine volatility, CO₂ activity coefficient, and heat of CO₂ absorption. Table 3-4 reports the results of the regression for MDEA/H₂O/CO₂, and Table 3-5 reports the data sources.

Table 3-4: Regression results for MDEA/H₂O/CO₂

Parameter	Species	Value	Standard Dev.	Units
DGAQFM	MDEAH ⁺	-2.565x10 ⁸	N/A	J/kmol
DHAQFM	MDEAH ⁺	-4.95x10 ⁸	N/A	J/kmol
CPAQ0 1	MDEAH ⁺	3.50x10 ⁵	1.17%	J/kmol.K
GMELCC	H ₂ O/(MDEAH ⁺ ,HCO ₃ ⁻)	7.71	0.11	N/A
GMELCC	(MDEAH ⁺ ,HCO ₃ ⁻)/H ₂ O	-4.15	0.047	N/A
GMELCC	H ₂ O/(MDEAH ⁺ ,CO ₃ ²⁻)	7.70	0.097	N/A
GMELCC	(MDEAH ⁺ ,CO ₃ ²⁻)/H ₂ O	-3.94	0.045	N/A
GMELCD/313	H ₂ O/(MDEAH ⁺ ,HCO ₃ ⁻)	1.27	0.012	K
GMELCC	MDEA/(MDEAH ⁺ ,HCO ₃ ⁻)	25.7	0.35	N/A
GMELCC	(MDEAH ⁺ ,HCO ₃ ⁻)/MDEA	-5.57	0.086	N/A
GMELCC	MDEA/(MDEAH ⁺ ,CO ₃ ²⁻)	9.25	0.14	N/A
GMELCC	(MDEAH ⁺ ,CO ₃ ²⁻)/MDEA	-1.99	0.024	N/A
GMELCD/313	MDEA/(MDEAH ⁺ ,HCO ₃ ⁻)	-14.6	0.31	K

Table 3-5: Data sources for MDEA/H₂O/CO₂ regression

Data	[MDEA]	Loading	T (°C)	Source (Year)
Loaded C _p	30-60 wt %	0-0.5	25	Weiland (1997)
CO ₂ Solubility	4.5 m	0.01-0.52	40-100	Jou (1993)
CO ₂ Solubility	25-50 wt %	0.01-0.7	25-120	Jou (1982)
MDEA pKa	N/A	N/A	20-150	Hamborg (2007)
MDEA ΔH _{ABS}	10-40 wt %	0.4-1.0	20-60	Kierzkowska-Pawlak (2007)
γ _{CO2}	50 wt %	0.1-0.3	25-60	Rinker (1997)

All parameters not listed in Table 3-4 that affect predicted properties are left at Aspen Plus[®] default values. For most parameters the default value is zero. However, GMELCC default values are set in accordance with Chen (2004). If the molecule is water, τ_{m-ca}/τ_{ca-m} is set to 8/-4 for all cation/anion pairs. If the molecule is MDEA they are set to 10/-2. Note that even the regressed GMELCC values, with the exception of those concerning MDEA/(MDEAH⁺, HCO₃⁻), are close to defaults. The pKa, ΔH_{ABS}, and γ_{CO2} data were not regressed using the Aspen Plus[®] Data Regression System but rather via manual adjustment of parameters. For example, the pKa of MDEA was fit by manually adjusting ΔG_f^o and ΔH_f^o for MDEAH⁺. Because the ΔG_f^o and ΔH_f^o of MDEA and H⁺ are fixed, these are the only parameters available to adjust the equilibrium constant. According to Equation 3-2, ΔG_f^o is adjusted to fit K_{EQ} at the reference temperature (25 °C), and ΔH_f^o accounts for the temperature dependence.

Figure 3-5 compares the experimental data (Hamborg, 2007) and model predictions for the pKa of MDEA as a function of temperature. The model heat of reaction is 38.3 kJ/mol. Hamborg reports heats of reaction from several studies with an average of 35.0 kJ/mol, though fitting the experimental data with a trend line (red

equation) gives a heat of reaction of 38.3 kJ/mol. Fixing the values of ΔG_f° and ΔH_f° for MDEAH^+ before regressing CO_2 solubility data limits the available handles to binary interaction, electrolyte pair, and ion heat capacity (CPAQ0) parameters. Nevertheless this is adequate for representing the data sets listed in Table 3-5. Figure 3-6 compares experimental data (Jou, 1982) and model predictions for the partial pressure of CO_2 as a function of loading for a 50 wt % MDEA solution from 25-120 °C.

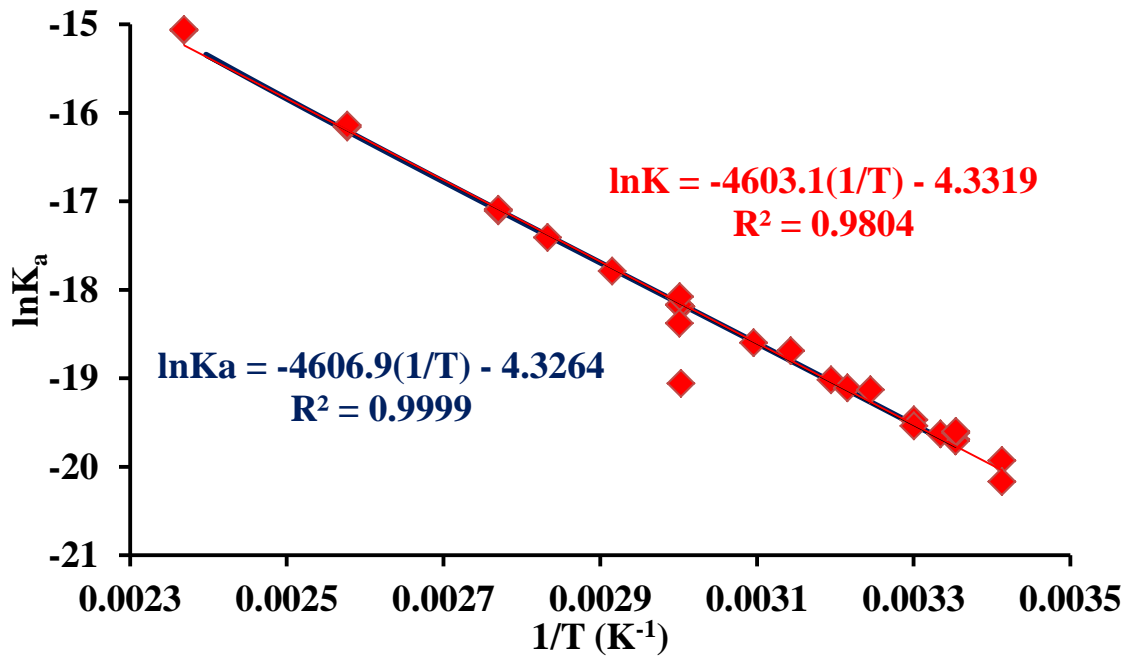


Figure 3-5: Experimental data (points) and model predictions (line) for the dissociation constant of MDEA as a function of temperature

It should be noted that the built-in rate-based Aspen Plus[®] model for CO_2 capture uses Ermatchkov (2006) and Austgen (1989) rather than Jou (1982) as a source of CO_2 solubility data for MDEA solvents. Figure 3-6 shows the Ermatchkov (2006) data as (\square) at 40 °C and 120 °C, and data from Austgen (1989) is represented by (Δ) at 40 °C. These data were not included in the regression for two reasons: (1) they do not represent all of

the relevant temperature and loading ranges for this study, and (2) below a loading of 0.25 mol CO₂/mol alkalinity they significantly disagree with Jou (1982). It is recommended that future versions of the MDEA/H₂O/CO₂ thermodynamic model include these experimental data in the regression.

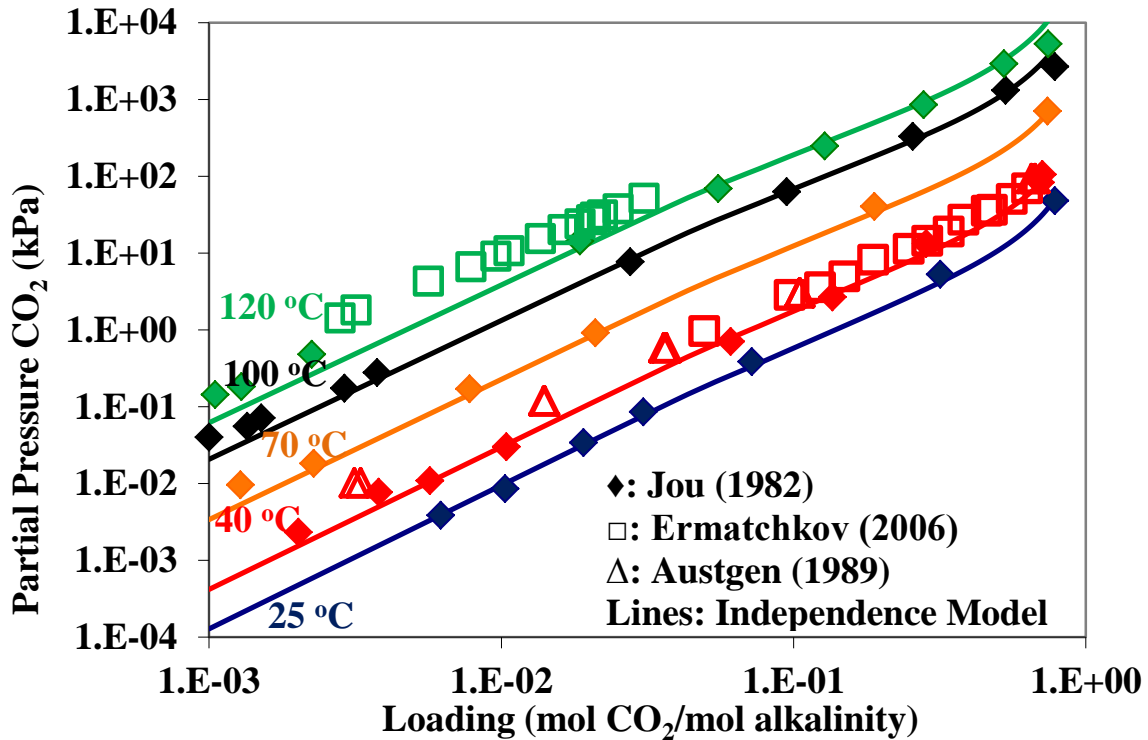


Figure 3-6: Experimental data (points) and model predictions (lines) for partial pressure of CO₂ as a function of loading for 50 wt % MDEA

The activity coefficient of CO₂ was not regressed using the Aspen Plus[®] DRS, but rather through the direct adjustment of τ parameters (Equations 3-16 and 3-18). Table 3-6 reports the results of this regression, and Figure 3-5 compares Aspen Plus[®] predictions to experimental data (Rinker, 1997). Binary interaction parameters for MDEA and CO₂ are more significant at low loadings; electrolyte pair parameters are more significant in loaded solutions. Because the mole fraction of free CO₂ in the liquid phase is on the

order of 10^{-5} , adjusting these parameters will not significantly affect previously regressed bulk properties. However, it is important to regress CO_2 activity coefficients to improve reaction rate predictions.

Table 3-6: Regression results for activity coefficient of CO_2 in MDEA/ $\text{H}_2\text{O}/\text{CO}_2$

Parameter	Species	Value
NRTL 1	MDEA/ CO_2	-5
NRTL 1	CO_2/MDEA	-5
(NRTL 2)/313K	MDEA/ CO_2	6.39
(NRTL 2)/313K	CO_2/MDEA	6.39
NRTL 3	MDEA/ CO_2	0.2
GMELCC	$\text{CO}_2/(\text{MDEAH}^+, \text{HCO}_3^-)$	10
GMELCC	$(\text{MDEA}, \text{HCO}_3^-)/\text{CO}_2$	-12.25
GMELCC	$\text{CO}_2/(\text{MDEAH}^+, \text{CO}_3^{2-})$	15
GMELCC	$(\text{MDEA}, \text{CO}_3^{2-})/\text{CO}_2$	-8
GMELCD/313K	$(\text{MDEA}, \text{HCO}_3^-)/\text{CO}_2$	6.39
GMELCD/313K	$(\text{MDEA}, \text{CO}_3^{2-})/\text{CO}_2$	6.39

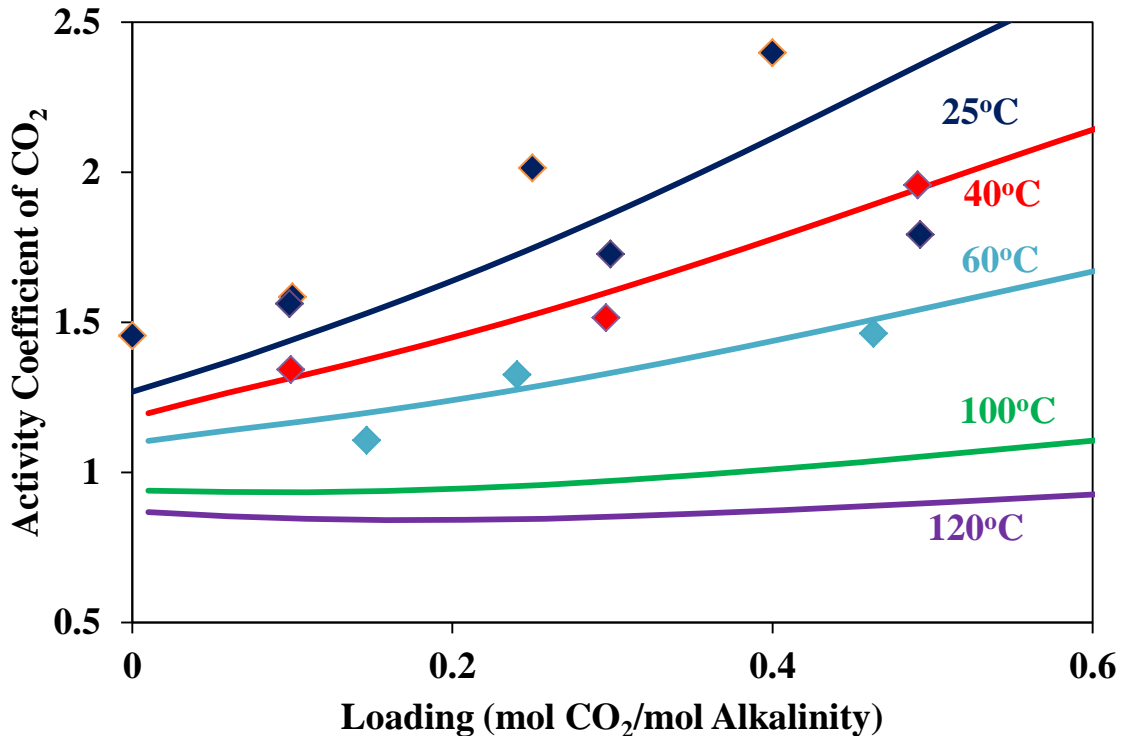


Figure 3-7: Experimental data (points; Rinker, 1997) and Aspen Plus[®] predictions (lines) for the activity coefficient of CO_2 in 50 wt % MDEA

3.6.3 PZ/H₂O/CO₂ Regression

Because of the number of ionic species present in loaded solutions, the PZ/H₂O/CO₂ system has several hundred possible binary interaction and electrolyte pair parameters. Unlike during the MDEA/H₂O/CO₂ regression, emphasis must be placed on eliminating as many unnecessary parameters from the regression as possible. Minimizing the number of non-default parameters improves model behavior at extrapolated conditions. Table 3-7 summarizes the regressed parameters, and Table 3-8 reports the data sources for the regression. Parameter values are omitted to protect IP.

The parameters for ion heat capacities were regressed in Microsoft ExcelTM to put the calculation of solution heat capacity on an apparent species basis. The partial heat capacity of PZ was calculated using unloaded 2 m, 3.6 m, and 8 m PZ data, and the partial heat capacity of CO₂ was calculated using loaded 8 m PZ data. The default values for electrolyte interaction τ parameters were 8/-4 for τ_{m-ca}/τ_{ca-m} when the molecular species is H₂O or H⁺PZCOO⁻ and 10/-2 when the molecule is PZ. Experimental data for the solubility of CO₂ in 0.15 m PZ solutions are included to account for water wash conditions. Figure 3-8 compares experimental data from Dugas (2009) and Xu (2011) and Aspen Plus[®] predictions for CO₂ solubility in 8 m PZ. It should be noted that experimental CO₂ solubility data was first regressed in Microsoft Excel to give an empirical expression (Equation 3-24) developed by Xu (2011), and the predictions of the empirical expression were directly regressed in the Aspen Plus[®] DRS.

$$\ln P_{CO_2} = 35.3 - \frac{91,542}{RT} - 18\alpha^2 + \frac{4,789\alpha}{T} + \frac{9,765\alpha^2}{T} \quad \text{Equation 3-24}$$

Table 3-7: Regression results for PZ/H₂O/CO₂

Parameter	Species	Standard Dev.	Units
DGFORM	H ⁺ PZCOO ⁻	1.75x10 ⁵	J/kmol
DHFORM	H ⁺ PZCOO ⁻	N/A	J/kmol
DGAQFM	H ⁺ PZCOO ⁻	1.75x10 ⁵	J/kmol
DHAQFM	H ⁺ PZCOO ⁻	N/A	J/kmol
CPIG 1	H ⁺ PZCOO ⁻	N/A	J/kmol.K
CPIG 2	H ⁺ PZCOO ⁻	N/A	J/kmol.K
DGAQFM	PZH ⁺	N/A	J/kmol
DHAQFM	PZH ⁺	N/A	J/kmol
CPAQ0 1	PZH ⁺	N/A	J/kmol.K
CPAQ0 2	PZH ⁺	N/A	J/kmol.K
DGAQFM	PZCOO ⁻	4.9x10 ⁵	J/kmol
DHAQFM	PZCOO ⁻	1.01x10 ⁵	J/kmol
CPAQ0 1	PZCOO ⁻	N/A	J/kmol.K
CPAQ0 2	PZCOO ⁻	N/A	J/kmol.K
DGAQFM	PZ(COO) ₂ ²⁻	N/A	J/kmol
DHAQFM	PZ(COO) ₂ ²⁻	N/A	J/kmol
CPAQ0/1	PZ(COO) ₂ ²⁻	N/A	J/kmol.K
CPAQ0/2	PZ(COO) ₂ ²⁻	N/A	J/kmol.K
GMELCC	H ₂ O/(PZH ⁺ , PZCOO ⁻)	0.103	N/A
GMELCC	(PZH ⁺ , PZCOO ⁻)/H ₂ O	0.0653	N/A
GMELCC	H ₂ O/(PZH ⁺ , PZ(COO) ₂ ²⁻)	0.137	N/A
GMELCC	(PZH ⁺ , PZ(COO) ₂ ²⁻)/H ₂ O	0.0556	N/A
GMELCC	PZ/(PZH ⁺ , PZCOO ⁻)	0.262	N/A
GMELCC	(PZH ⁺ , PZCOO ⁻)/PZ	0.0655	N/A
GMELCC	PZ/(PZH ⁺ , PZ(COO) ₂ ²⁻)	0.140	N/A
GMELCC	(PZH ⁺ , PZ(COO) ₂ ²⁻)/PZ	0.0299	N/A
GMELCC	H ⁺ PZCOO ⁻ /(PZH ⁺ , PZCOO ⁻)	0.135	N/A
GMELCC	(PZH ⁺ , PZCOO ⁻)/H ⁺ PZCOO ⁻	0.0333	N/A
GMELCC	H ⁺ PZCOO ⁻ /(PZH ⁺ , PZ(COO) ₂ ²⁻)	0.118	N/A
GMELCC	(PZH ⁺ , PZ(COO) ₂ ²⁻)/H ⁺ PZCOO ⁻	0.0744	N/A
GMELCC	H ⁺ PZCOO ⁻ /(PZH ⁺ , HCO ₃ ⁻)	0.0998	N/A
GMELCC	(PZH ⁺ , HCO ₃ ⁻)/H ⁺ PZCOO ⁻	0.0498	N/A

Table 3-8: Data sources for PZ/H₂O/CO₂ regression

Data	[PZ]	Loading	Temperature (°C)	Source (Year)
Loaded C _p	8 m	0.21-0.4	40-150	Freeman (2010)
CO ₂ Solubility	0.15 m	0.31-0.40	40	Fulks (2011)
CO ₂ Solubility	5-12 m	0.20-0.40	40-100	Dugas (2009)
CO ₂ Solubility	8 m	0.20-0.40	100-160	Xu (2011)
PZ pKa	0.01-0.05 m	N/A	0-50	Hetzer (1968)
γ _{CO2}	8 m	0.25-0.40	25-60	Svendsen (2009)

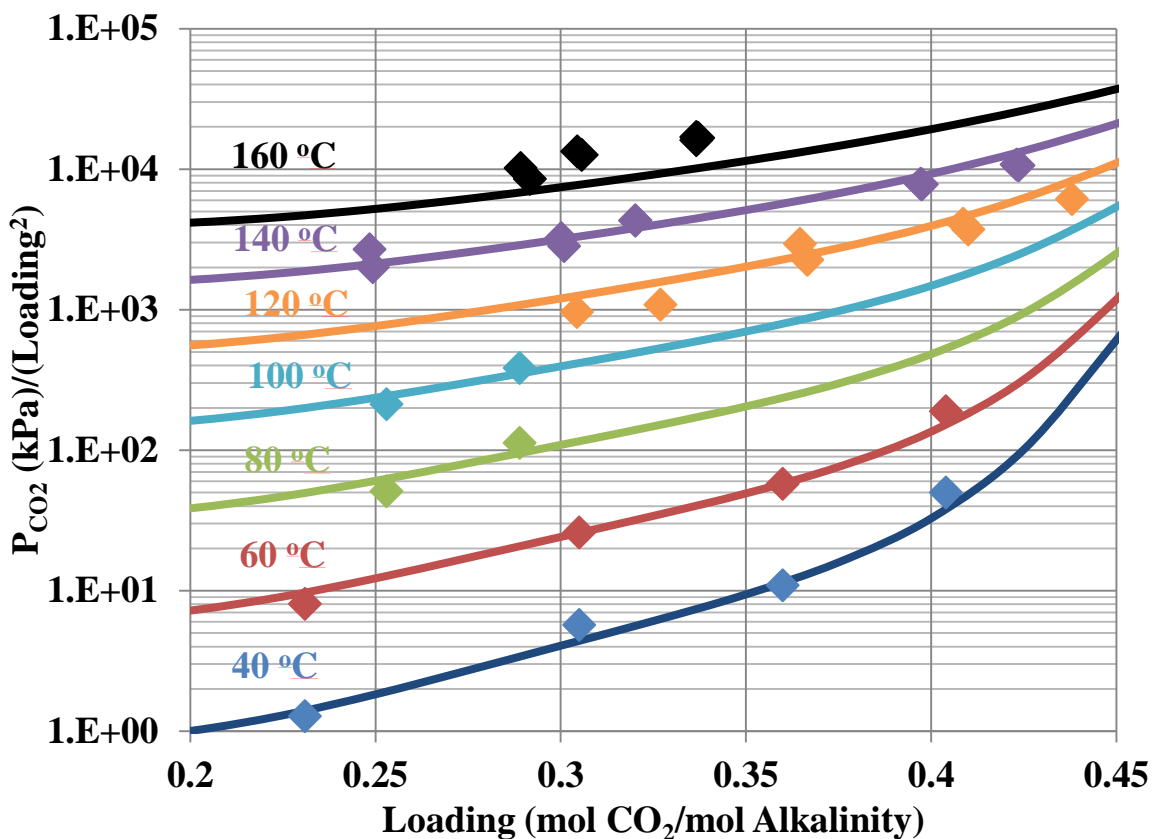


Figure 3-8: Experimental data (points; Dugas, 2009; Xu, 2011) and Aspen Plus[®] predictions (lines) for the partial pressure of CO₂ divided by the loading squared as a function of loading for 8 m PZ

NMR data (Nguyen, 2012) were not directly regressed, but Figure 3-9 compares model predictions to experimental data. Model predictions for speciation at operational temperatures and loadings are important when selecting kinetic reactions for modeling CO₂ absorption rates. Figure 3-9 suggests that PZCOO⁻ is a significant base at operationally significant loadings (0.3-0.4 mol CO₂/mol alkalinity), and it should be modeled as a catalyst for PZCOO⁻ and PZ(COO)₂²⁻ formation. It also suggests that the contribution of the HCO₃⁻ forming reaction to the overall CO₂ absorption rate is minimal.

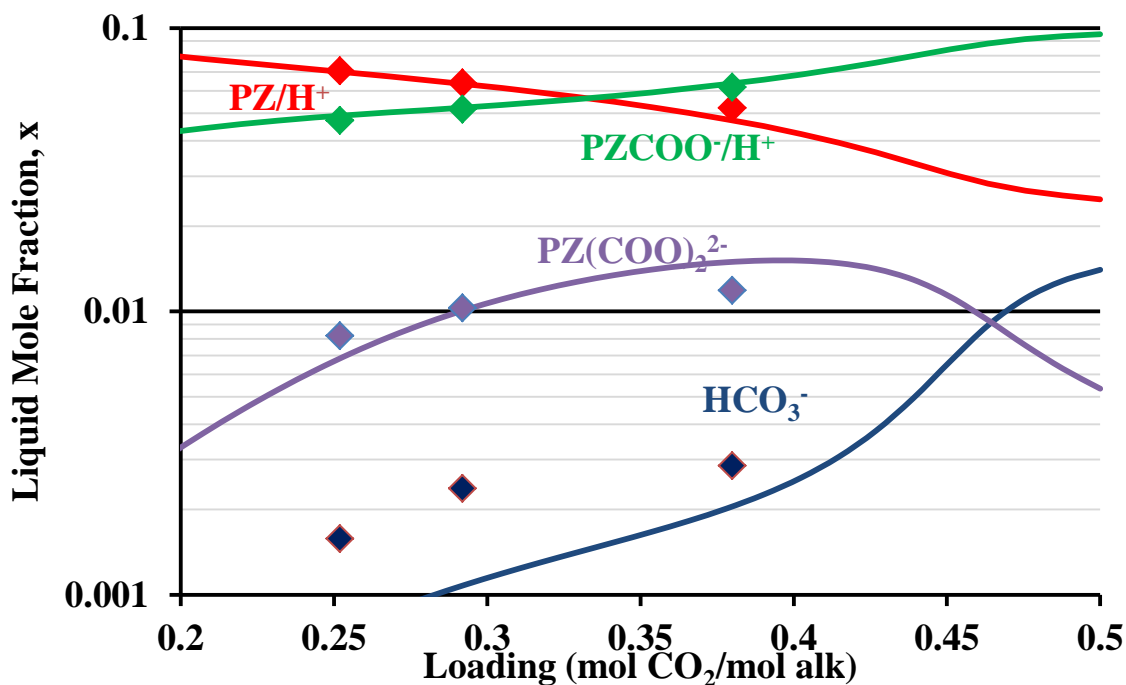


Figure 3-9: Experimental data (points; Nguyen, 2012) and Aspen Plus[®] predictions (lines) for speciation of 8 m PZ at 40 °C

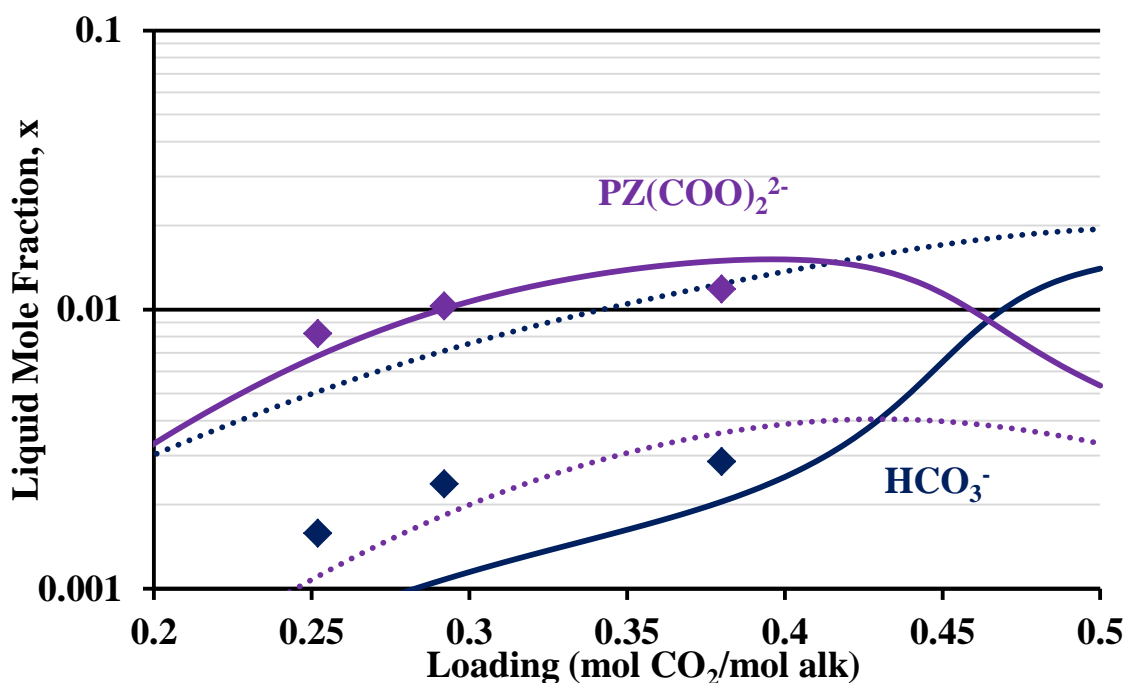


Figure 3-10: Experimental data at 40 °C (points) Aspen Plus[®] predictions for the mole fraction of HCO_3^- (blue) and $\text{PZ}(\text{COO})_2^{2-}$ (purple) as a function of loading at 40 °C (solid lines) and 150 °C (dotted lines)

Figure 3-10 compares the temperature dependence of HCO_3^- and $\text{PZ}(\text{COO})_2^{2-}$ concentration in loaded 8 m PZ. The concentration profiles of the bicarbonate and dicarbamate species invert as temperature increases from absorber conditions (40 °C) to stripper conditions (150 °C), but more importantly the slopes of the speciation curves with respect to loading change dramatically. Table 3-10 reports the change in mole fraction over the change in CO_2 concentration at loadings of 0.2, 0.3, and 0.4 mol CO_2 /mol alkalinity at 40 °C and 150 °C for all species present in 8 m PZ. The slopes are calculated by generating Aspen Plus[®] predictions at loadings that are ± 0.001 mol CO_2 /mol alkalinity from the point in question.

Table 3-9: Slopes of speciation curves for 8 m PZ at 40 °C and 150 °C

Loading (mol CO_2 /mol alk)	Species	Slope at 40 °C dx/dx_{CO_2}	Slope at 150 °C dx/dx_{CO_2}
0.2	PZ	-1.49	-1.36
	PZH ⁺	0.727	0.531
	H ₂ O	-0.020	-0.130
	HCO_3^-	0.020	0.129
	H ⁺ PZCOO ⁻	0.273	0.462
	$\text{PZ}(\text{COO})_2^{2-}$	0.214	0.035
	PZCOO ⁻	0.280	0.333
0.3	PZ	-0.536	-0.747
	PZH ⁺	-0.128	0.082
	H ₂ O	-0.034	-0.224
	HCO_3^-	0.034	0.224
	H ⁺ PZCOO ⁻	1.13	0.889
	$\text{PZ}(\text{COO})_2^{2-}$	0.302	0.082
	PZCOO ⁻	-0.765	-0.306
0.4	PZ	-0.167	-0.317
	PZH ⁺	-0.746	-0.226
	H ₂ O	-0.166	-0.268
	HCO_3^-	0.167	0.268
	H ⁺ PZCOO ⁻	1.74	1.08
	$\text{PZ}(\text{COO})_2^{2-}$	-0.031	0.044
	PZCOO ⁻	-0.801	-0.583

The loading and temperature dependence of the heat of absorption (Figure 3-11) is determined by the differences between the slopes of the speciation curves across the different loading and temperature conditions. In Figure 3-11 the heat of absorption is calculated using Equation 3-25, where f_{CO_2} is the fugacity of CO_2 , R is the gas constant, and ΔH_{ABS} is the heat of absorption.

$$\frac{d \ln f_{CO_2}}{d \frac{1}{T}} = \frac{-\Delta H_{ABS}}{R} \quad \text{Equation 3-25}$$

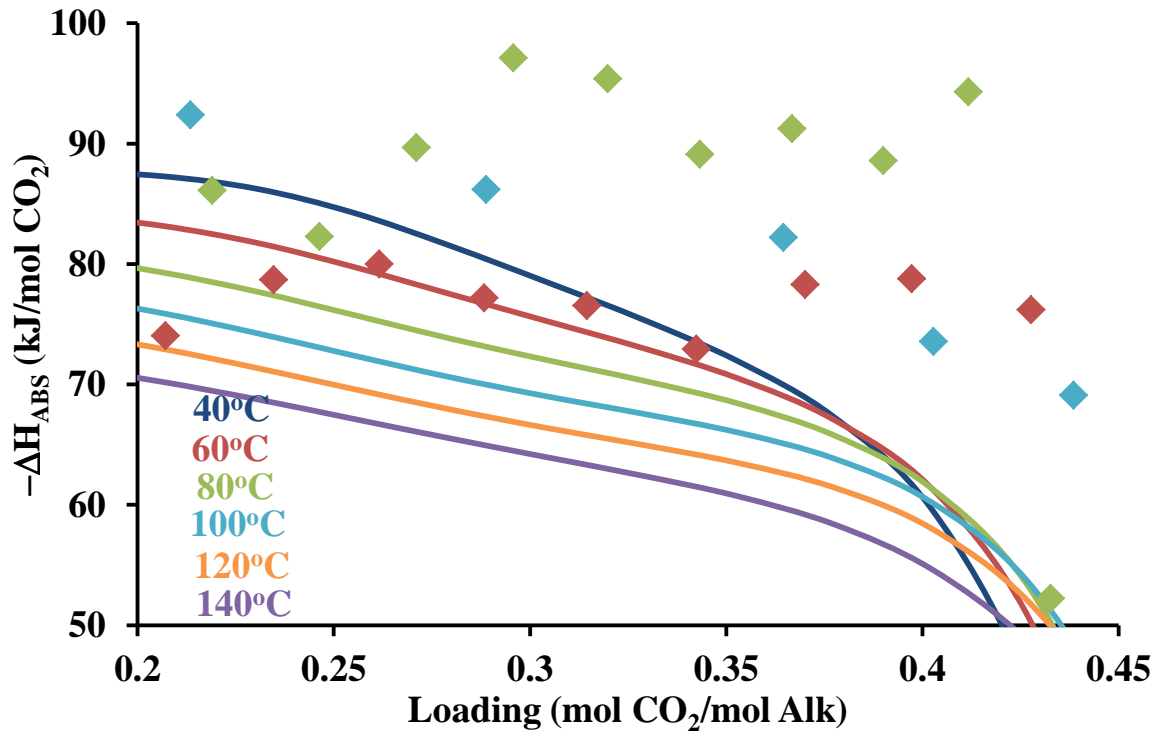


Figure 3-11: Experimental data (points; Freeman, 2011) and Aspen Plus[®] predictions (lines) for the heat of CO_2 absorption for 8 m PZ as a function of loading from 40-140 °C

At a loading of 0.2 mol CO_2 /mol alkalinity the solvent is rapidly consuming unreacted PZ and generating bicarbonate and every carbamate species. As temperature increases from 40 °C to 150 °C the solvent is still rapidly consuming unreacted PZ but the

products favor HCO_3^- and H^+PZCOO^- more and $\text{PZ}(\text{COO})_2^{2-}$ less. At a loading of 0.4 mol CO_2 /mol alkalinity almost all of the free PZ has reacted and the CO_2 must react with PZH^+ and H_2O to form H^+PZCOO^- and, to a lesser extent, HCO_3^- . As the temperature increases to 150 °C these are still the prominent products and reactants, but the rate of formation of HCO_3^- and $\text{PZ}(\text{COO})_2^{2-}$ slightly increase and the rate of formation of H^+PZCOO^- slightly decreases. The loading dependence of the heat of absorption is a result of the shift from forming a relatively uniform mixture of carbamate species at low loadings to forming predominantly HCO_3^- and H^+PZCOO^- at high loadings. This suggests that the reactions that form HCO_3^- and H^+PZCOO^- have a relatively low enthalpy change. This is corroborated by the strong temperature dependence of the heat of absorption at a loading of 0.2 mol CO_2 /mol alkalinity.

Just as with MDEA/ H_2O / CO_2 , the activity coefficient of CO_2 in loaded solutions is regressed independently of all other loaded solution data sets. Table 3-10 reports the results of the regression and Figure 3-12 compares experimental data (Svendsen, 2010) and Aspen Plus[®] predictions from 25-60 °C. Rather than directly regress the limited set of experimental data, Equation 3-26, developed by Plaza (2011), was used to generate predictions for γ_{CO_2} between loadings of 0.1 and 0.5 mol CO_2 /mol alkalinity and temperatures of 25 and 160 °C. In Equation 3-26 [PZ] is the molality of PZ, T is the temperature in K, and $X_{\text{CO}_2}^{\text{T}}$ is the total concentration of CO_2 present in the solvent as free CO_2 , carbamate, and bicarbonate.

Table 3-10: Regression results for activity coefficient of CO₂ in PZ/H₂O/CO₂

Parameter	Species	Value	Standard Dev.	Units
GMELCC	(PZH ⁺ , PZCOO ⁻)/CO ₂	-7.02	1.33	N/A
GMELCD	(PZH ⁺ , PZCOO ⁻)/CO ₂	1670	442	K
GMELCC	(PZH ⁺ , HCO ₃ ⁻)/CO ₂	-0.832	1.85	N/A
GMELCC	(PZH ⁺ , PZ(COO) ₂ ²⁻)/CO ₂	-2.86	0.257	N/A
NRTL/1	H ⁺ PZCOO ⁻ /CO ₂	-22.3	2.86	N/A
NRTL/2	H ⁺ PZCOO ⁻ /CO ₂	8850	1070	K
NRTL/1	PZ/CO ₂	-6.98	1.59	N/A
NRTL/2	PZ/CO ₂	2770	512	K
NRTL/3	H ⁺ PZCOO ⁻ /CO ₂	0.05	FIXED	N/A
NRTL/3	PZ/CO ₂	0.05	FIXED	N/A

$$\ln \gamma_{CO_2} = 0.045 + 0.061[PZ] + 0.034X_{CO_2}^T + 360\left(\frac{1}{T} - \frac{1}{298.15}\right) \quad \text{Equation 3-26}$$

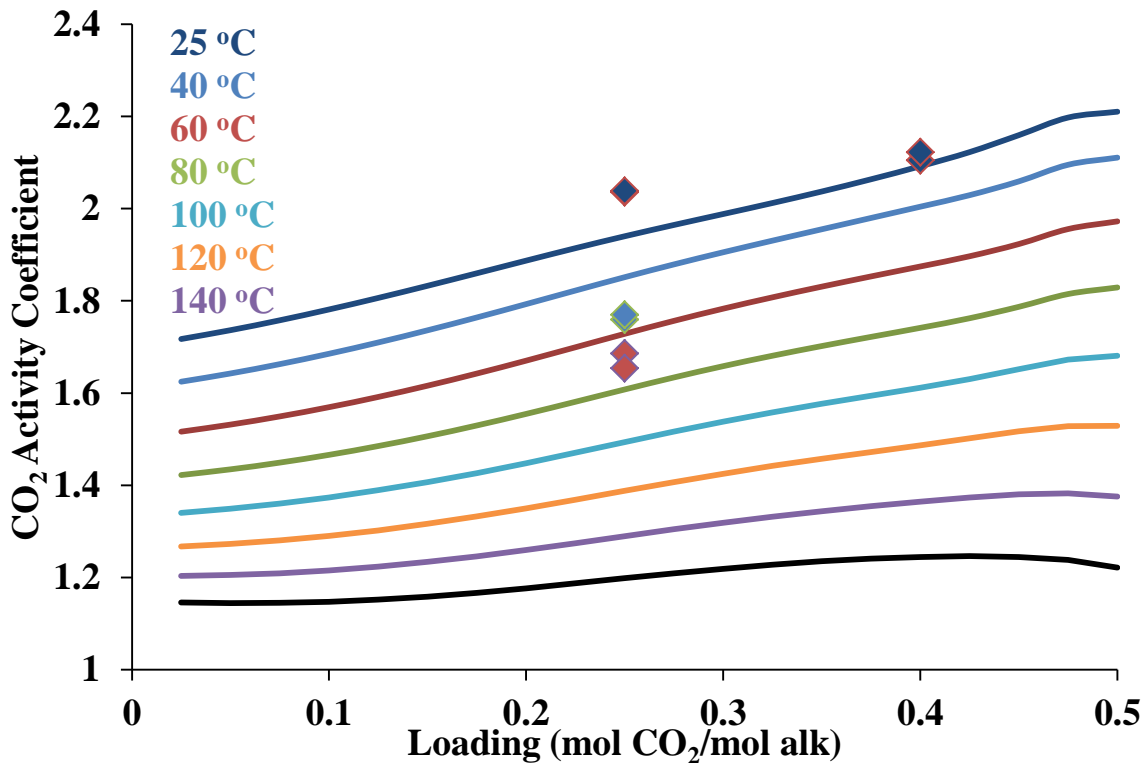


Figure 3-12: Experimental data (points) and Aspen Plus[®] predictions (lines) for activity coefficient of CO₂ from 25-160 °C

3.6.4 MDEA/PZ/H₂O/CO₂ Regression

Table 3-11 summarizes the final set of regressed parameters, and Table 3-12 reports the data sources for the regression. Cross parameters for the activity coefficient of CO₂ were left at default values. As shown in Figure 3-11, model predictions for the activity coefficient of CO₂ are well-behaved over operationally significant temperature, loading, and amine concentration ranges.

Table 3-11: Regression results for MDEA/PZ/H₂O/CO₂

Parameter	Species	Standard Dev.	Units
GMELCC	(MDEAH ⁺ , PZ(COO) ₂ ²⁻)/H ₂ O	0.0488	N/A
GMELCD/313	(MDEAH ⁺ , PZCOO ⁻)/MDEA	2.13	K
GMELCD/313	(PZH ⁺ , HCO ₃ ⁻)/MDEA	3.35	K
GMELCC	(MDEAH ⁺ , HCO ₃ ⁻)/H ⁺ PZCOO ⁻	0.600	N/A
GMELCD/313	(MDEAH ⁺ , PZCOO ⁻)/H ⁺ PZCOO ⁻	1.78	K
GMELCD/313	(MDEAH ⁺ , HCO ₃ ⁻)/H ⁺ PZCOO ⁻	0.626	K
GMELCC	(MDEAH ⁺ , PZCOO ⁻)/PZ	0.0502	N/A

Table 3-12: Data sources for MDEA/PZ/H₂O/CO₂ regression

Data	[Am]	Loading	Temperature (°C)	Source (Year)
Loaded C _p	7m MDEA/2m PZ	0.04-0.27	40-120	Nguyen (2012)
Loaded C _p	5m MDEA/5m PZ	0.10-0.25	40-120	Nguyen (2012)
Loaded Am. Vol.	7m MDEA/2m PZ	0.143-0.24	40-60	Nguyen (2012)
Loaded Am. Vol.	5m MDEA/5m PZ	0.221-0.307	40-60	Nguyen (2012)
CO ₂ Solubility	7m MDEA/2m PZ	0.093-0.286	40-100	Chen (2011)
CO ₂ Solubility	7m MDEA/2m PZ	0.13-0.225	100-160	Xu (2011)
CO ₂ Solubility	5m MDEA/5m PZ	0.18-0.37	40-100	Chen (2011)
CO ₂ Solubility	5m MDEA/5m PZ	0.219-0.271	100-160	Xu (2011)
CO ₂ Solubility	5m MDEA/5m PZ	0.20-0.33	10-40	Li (2011)

In the absence of experimental data, model predictions should be well-behaved and convergent over all operationally significant temperature, loading, and amine concentration ranges. In Figures 3-7 and 3-11 the activity coefficient of CO₂ decreases with temperature, is roughly a linear function of loading, and is always between 0.5 and

2.0 for 40-160 °C. These three trends are also apparent in Figure 3-12. If the MDEA/PZ system were the only amine regressed into the thermodynamic framework, the predictions in Figure 3-12 would constitute an extrapolation. Because the activity coefficient of CO₂ in 50 wt % MDEA and concentrated PZ is regressed into the framework, the predictions in Figure 3-13 are an interpolation on the axis of amine concentrations. If done properly, a sequential regression will improve the stability of model predictions and reduce the number of regressed cross parameters for blended amines.

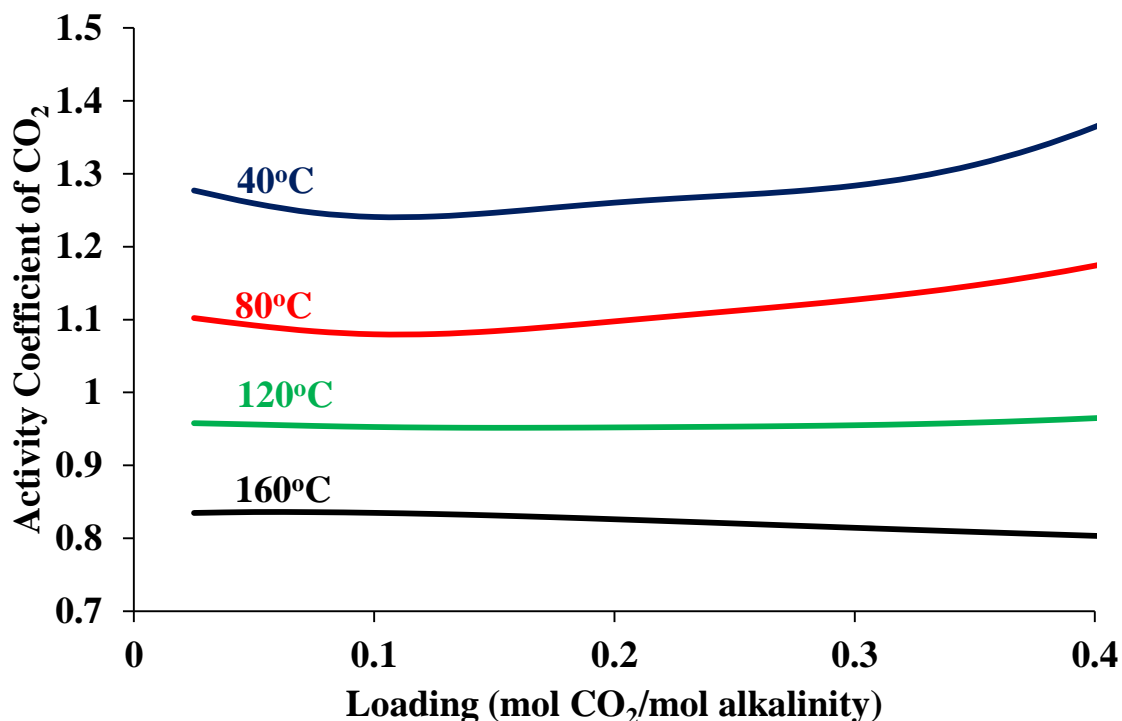


Figure 3-13: Activity coefficient of CO₂ as a function of loading for 7 m MDEA/2 m PZ from 40-160 °C

Because PZ reacts much more readily than MDEA, solvent properties will be PZ-like at low loadings and transition to MDEA-like as PZ saturates. Stoichiometrically, the

PZ would be saturated at a loading of 0.18 mol CO₂/ mol alkalinity. Near this point in Figure 3-14 the heat of absorption goes from decreasing with temperature (PZ-like) to increasing (MDEA-like). This effect cannot be expressed by the simple empirical prediction (dotted line) because it does not account for the temperature dependence of the heat of absorption. The model predicts that the heat of absorption of MDEA/PZ is between that of concentrated PZ (-75 kJ/mol CO₂) and MDEA (-55 kJ/mol CO₂). Figures 3-11 and 3-15 report the heat of absorption of concentrated PZ and 50 wt % MDEA, respectively, as a function of loading. Equation 3-25 is used to calculate all of the Aspen Plus[®] predicted values of the heat of absorption.

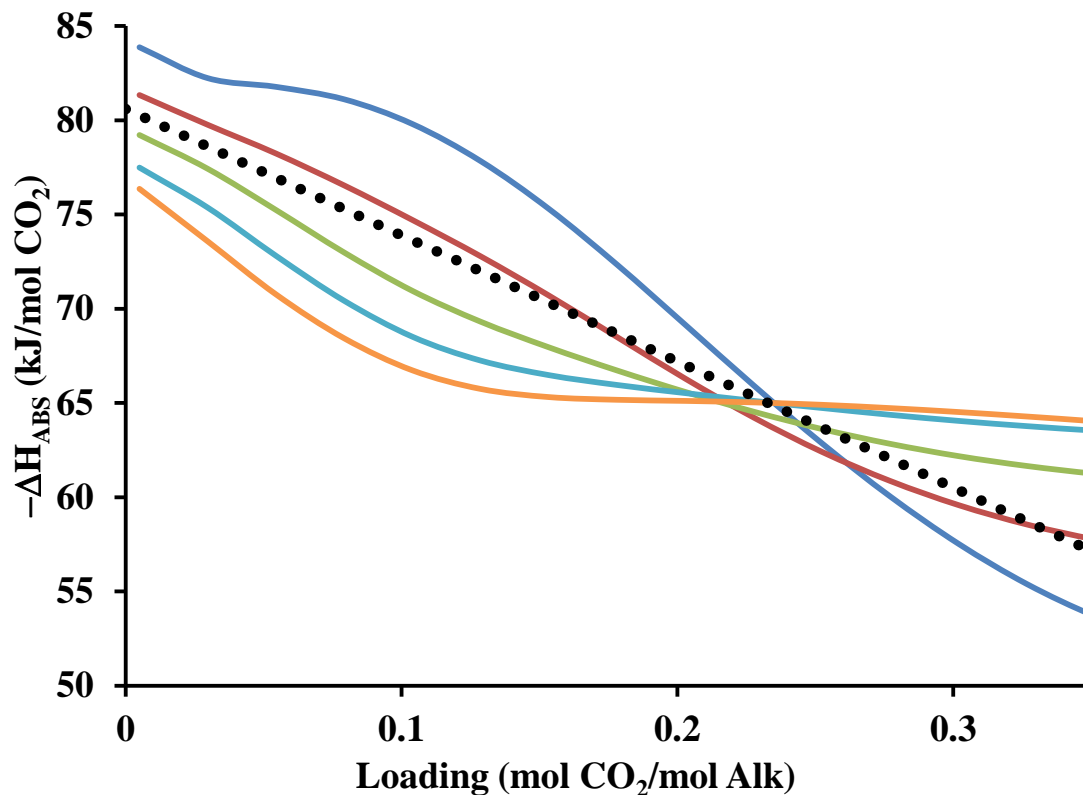


Figure 3-14: Heat of CO₂ absorption for 7 m MDEA/2 m PZ as a function of loading from 40-120 °C. Solid lines are predicted by Aspen Plus[®], dotted line is result of empirical expression (Xu, 2011).

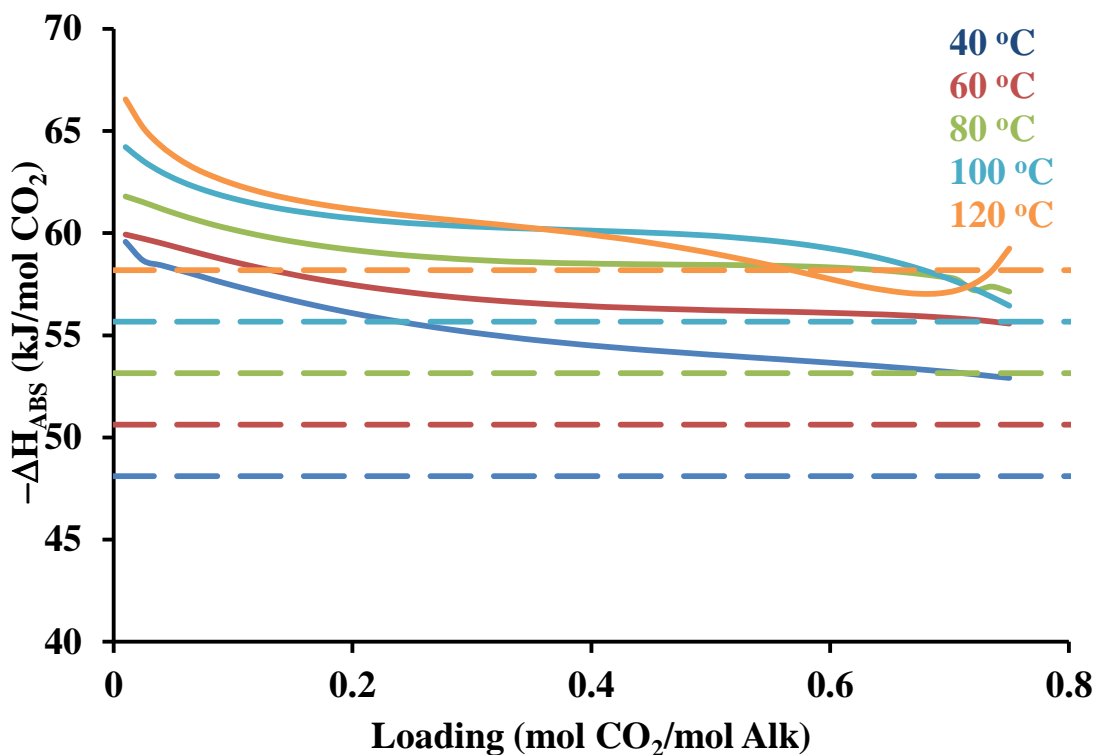


Figure 3-15: Experimental data (dashed lines; Kierzkowska-Pawlak, 2007) and Aspen Plus[®] predictions (lines) for the differential heat of CO₂ absorption for 50 wt % MDEA as a function of loading from 40-120 °C.

The dashed lines in Figure 3-15 are predictions from a correlation developed by Kierzkowsha-Pawlak (2007) that takes into account the findings of several studies. The Aspen Plus[®] predictions suggest that the heat of absorption for 50 wt % MDEA is a much weaker function of temperature. Both models predict that the heat of absorption increases with temperature, but the magnitude of the increase from 40 °C to 120 °C for the Aspen Plus[®] model is about half that of the model based on experimental data.

Figure 3-16 compares experimental data (Chen, 2011; Xu, 2011; Li, 2011) and model predictions for the partial pressure of CO₂ as a function of loading for 5 m MDEA/5 M PZ from 10-160 °C.

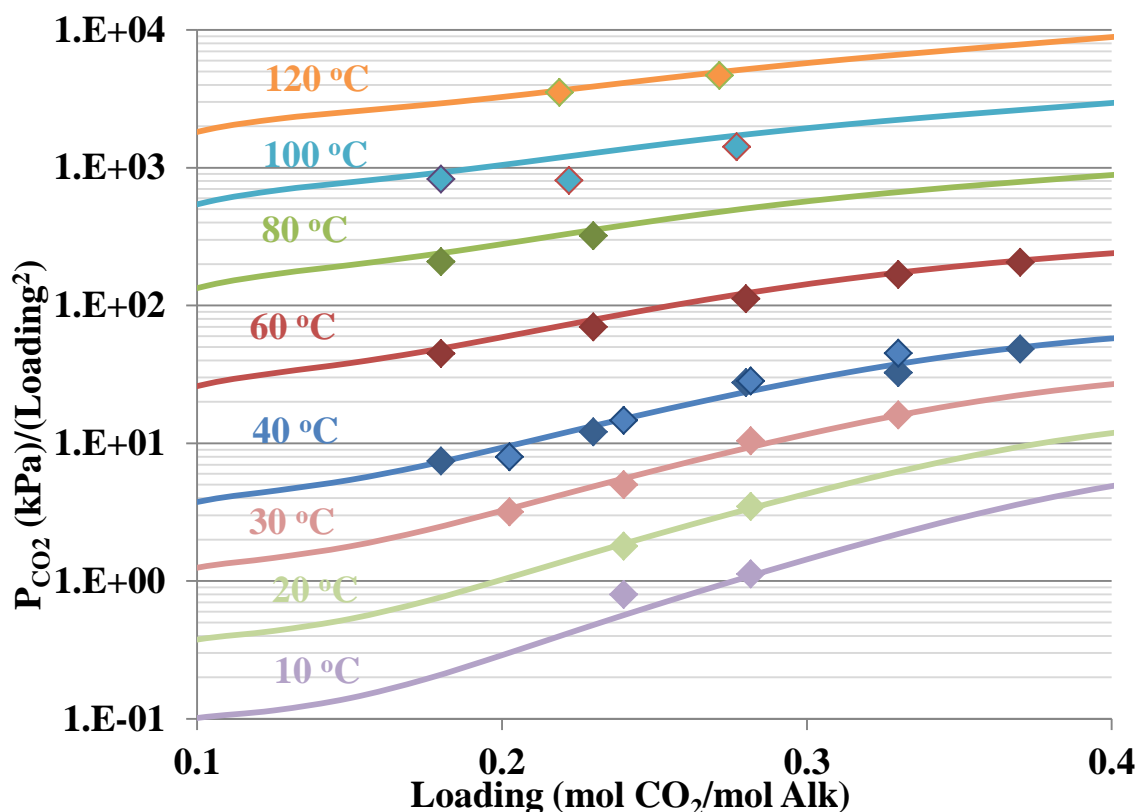


Figure 3-16: Experimental data (points; Chen, 2011; Xu, 2011; Li, 2011) and Aspen Plus[®] model predictions (lines) for partial pressure of CO₂ divided by the loading squared as a function of loading for 5 m MDEA/5 m PZ from 10-120 °C

Low temperature CO₂ solubility data were not available during the development of earlier thermodynamic models. These data are particularly important for the prediction of process performance for novel configurations with blended amines, which can be operated at lower temperatures without the solid solubility limitations observed with concentrated PZ. Previous versions of the model relied on extrapolations to predict CO₂ solubility at these conditions. Regressing data at these conditions not only improves confidence in the accuracy of the predictions but also the likelihood that the model will converge.

Figure 3-17 compares model predictions (lines) to experimental data (points) for the speciation of the 7 m MDEA/2 m PZ blend at 20 °C.

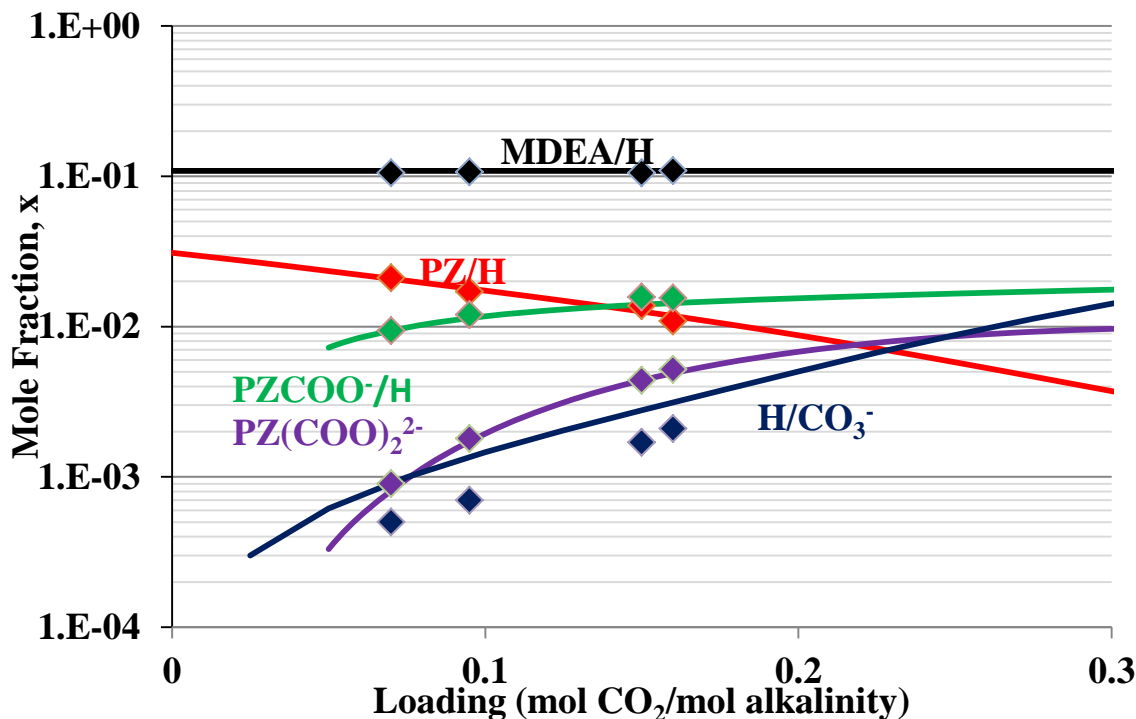


Figure 3-17: Experimental data (points; Nguyen, 2012) and Aspen Plus[®] predictions (lines) for speciation of 7 m MDEA/ 2m PZ at 40 °C as a function of loading

The slopes of the curves in Figure 3-16 can be used to determine the important reactions for kinetics. Table 3-13 reports the change in mole fraction over the change in CO₂ concentration at loadings of 0.12, 0.23, and 0.35 mol CO₂/mol alkalinity at 40 °C and 120 °C for all CO₂-containing species as well as MDEA and PZ in 7 m MDEA/2 m PZ. The slopes are calculated by generating Aspen Plus[®] predictions at loadings that are ±0.001 mol CO₂/mol alkalinity from the point in question. Just as with 8 m PZ (Table 3-9) there is a strong shift toward H⁺PZCOO⁻ and HCO₃⁻ production as temperature increases at a loading of 0.12 mol CO₂/mol alkalinity. This shift accounts for the

temperature dependence of the heat of absorption at this loading (Figure 3-14). At a loading of 0.35 mol CO₂/mol alkalinity the dominant reaction is the formation of HCO₃⁻ catalyzed by MDEA, which will increase the heat of absorption as temperature increases (Figure 3-15).

Table 3-13: Slopes of speciation curves for 7 m MDEA/2 m PZ at 40 °C and 120 °C for CO₂-containing species, MDEA, and PZ

Loading (mol CO ₂ /mol alk)	Species	Slope at 40 °C dx/dx _{CO2}	Slope at 120 °C dx/dx _{CO2}
0.12	MDEA	-0.606	-0.448
	PZ	-0.587	-0.592
	CO ₃ ²⁻	0.018	0.015
	HCO ₃ ⁻	0.127	0.410
	H ⁺ PZCOO ⁻	0.391	0.467
	PZ(COO) ₂ ²⁻	0.288	0.044
	PZCOO ⁻	-0.113	0.001
0.23	MDEA	-0.943	-0.728
	PZ	-0.118	-0.203
	CO ₃ ²⁻	0.009	0.008
	HCO ₃ ⁻	0.446	0.675
	H ⁺ PZCOO ⁻	0.286	0.276
	PZ(COO) ₂ ²⁻	0.206	0.041
	PZCOO ⁻	-0.153	-0.079
0.35	MDEA	-0.940	-0.825
	PZ	-0.014	-0.041
	CO ₃ ²⁻	0.032	0.003
	HCO ₃ ⁻	0.855	0.827
	H ⁺ PZCOO ⁻	0.194	0.145
	PZ(COO) ₂ ²⁻	-0.007	0.007
	PZCOO ⁻	-0.070	-0.059

Just as with 8 m PZ, PZCOO⁻ is a significant catalyst at operational loadings (0.12-0.27 mol CO₂/mol alkalinity). HCO₃⁻ is a significant species at all temperatures and loadings, but its importance increases with both loading and temperature. Blending PZ with MDEA increases the significance of the HCO₃⁻ forming reaction at operational

conditions. This will slow the CO₂ absorption rate at the rich end of the absorber and increase the capacity of the solvent.

Table 3-14 compares the model-predicted CO₂ capacities for 8 m PZ, 7 m MDEA/2 m PZ, and 5 m MDEA/5 m PZ at 40 °C for coal-fired applications. This definition of capacity assumes lean and rich loadings that correspond to 500 and 5,000 Pa equilibrium partial pressure of CO₂, respectively. Solvent capacities predicted by the empirical expression and Aspen Plus[®] model differ by less than 3 % for all cases.

Table 3-14: Empirical expression and model predicted capacities of 8 m PZ, 7 m MDEA/2 m PZ, and 5 m MDEA/5 m PZ between 500 and 5,000 Pa equilibrium partial pressure of CO₂ at 40 °C.

Amine	Experimental Capacity (mol CO ₂ /kg H ₂ O+Am)	Model Capacity (mol CO ₂ /kg H ₂ O+Am)
8 m PZ	0.79	0.799
7 m MDEA/2 m PZ	0.80	0.813
5 m MDEA/5 m PZ	0.98	0.970

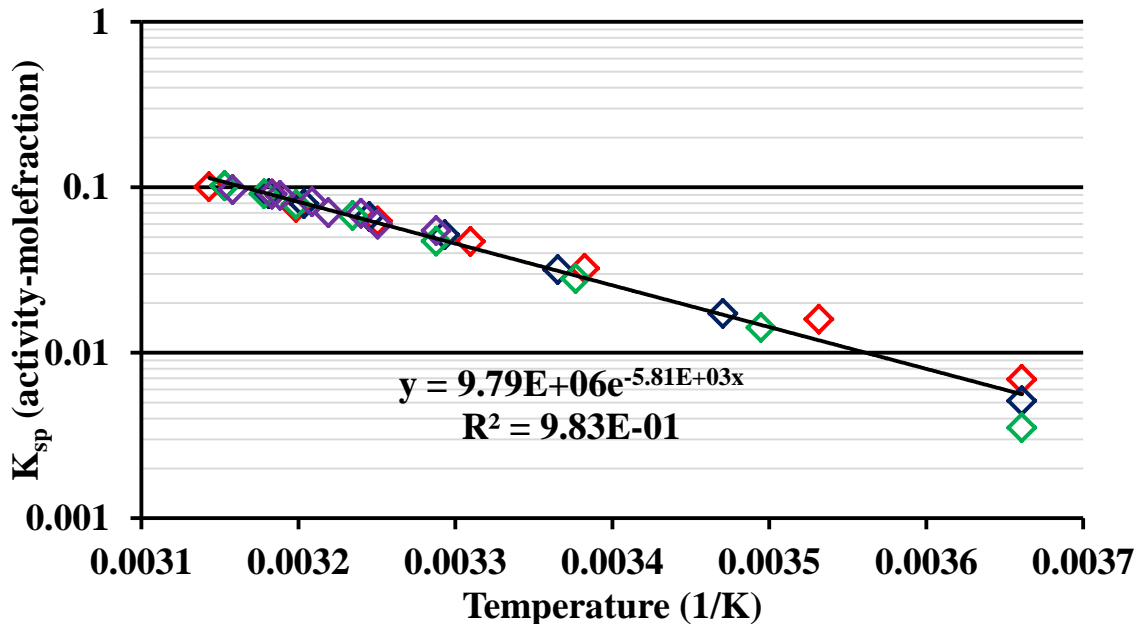


Figure 3-18: Solubility constant, K_{sp} , as a function of inverse temperature for loaded and unloaded 3-7 m (purple), 8 m (red), 9 m (blue), and 10 m (green) PZ

Figure 3-18 shows the solubility constant, K_{sp} , for $PZ \cdot 6H_2O (s)$ as a function of inverse temperature. The points are generated from experimental data (Freeman, 2011) for the melting point of $PZ \cdot 6H_2O (s)$ at various amine concentrations and loading using Aspen Plus[®] predictions for the mole fractions and activity coefficients of PZ and H_2O at the reported experimental conditions. The coefficient on the exponent (-5,810) corresponds to the heat of fusion divided by the gas constant, R . The line of best fit in Figure 3-18 gives a heat of fusion of 48 kJ/mol $PZ \cdot 6H_2O (s)$, which is eight times that of H_2O . This suggests that the PZ molecule in the $PZ \cdot 6H_2O (s)$ crystal is behaving like two molecules of H_2O , which is consistent with the two electronegative nitrogens in PZ.

Figures 3-19 and 3-20 show the activity coefficient as a function of loading for all species in 7 m MDEA/2 m PZ at 40 °C.

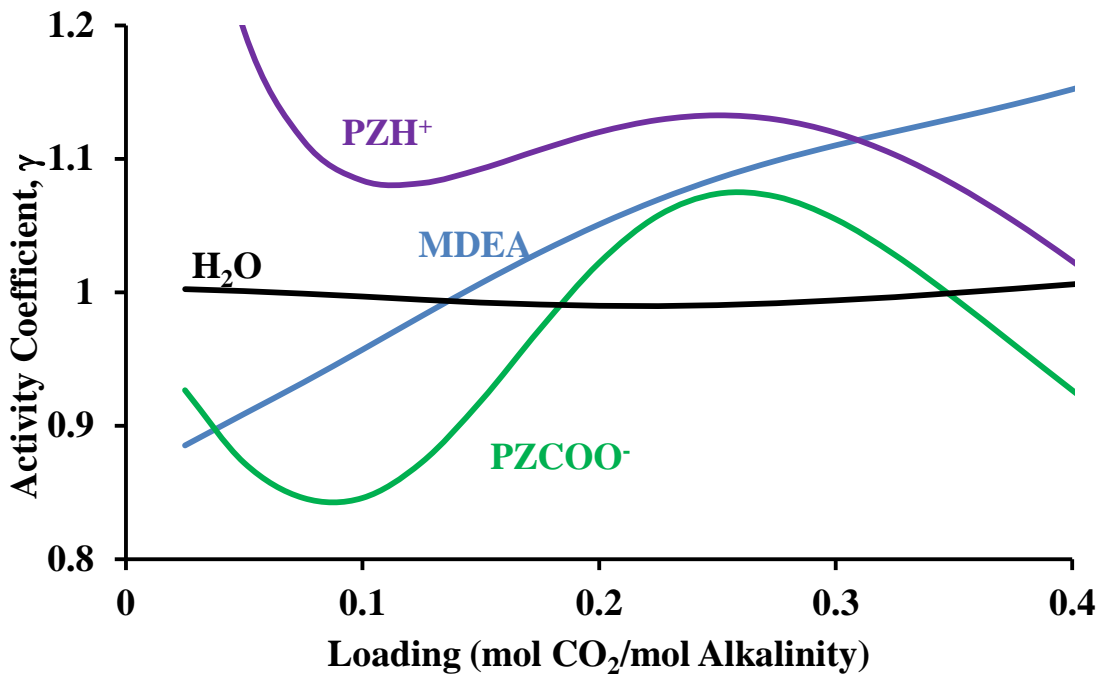


Figure 3-19: Aspen Plus[®] predictions for the activity coefficient of H_2O , $PZCOO^-$, PZH^+ , and MDEA in 7 m MDEA/2 m PZ at 40 °C

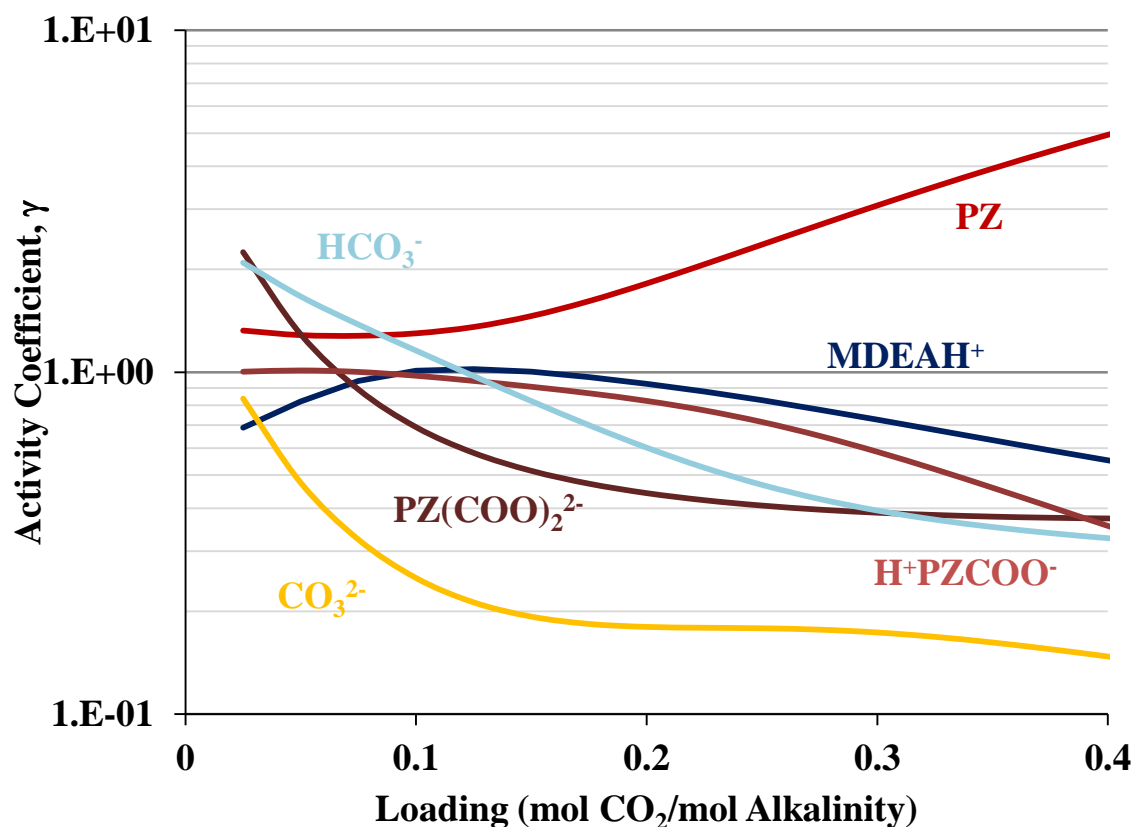


Figure 3-20: Aspen Plus[®] predictions for the activity coefficient of MDEAH⁺, PZ, CO₃²⁻, HCO₃⁻, H⁺PZCOO⁻, and PZ(COO)₂²⁻ in 7 m MDEA/2 m PZ at 40 °C as a function of loading

Most of the activity coefficients hold close to one throughout the loading range. The activity coefficient of water is never greater than 1.02 nor less than 0.99. The greatest deviation from ideality at low loadings is observed for PZ(COO)₂²⁻, CO₃²⁻, and HCO₃⁻, none of which is predicted to be present at a significant concentration at low loadings. It is expected that the activity coefficients of ions with a -2 charge will decrease significantly as the ionic strength of solution increases. The activity coefficient of PZ deviates significantly from ideality above a loading of 0.18 mol CO₂/mol alkalinity, at which point it is assumed that the concentration of free PZ is insignificant.

3.6.5 Generic Amines

Figure 3-21 compares Aspen Plus[®] predictions for heats of absorption at 40 °C and 120 °C and viscosity normalized capacity at 40 °C for MDEA/PZ with 50 wt % amine and variable PZ wt %. The viscosity normalized capacity is defined by Equation 3-27, where α_{lean} and α_{rich} are lean and rich loadings corresponding to 500 Pa and 5,000 Pa equilibrium partial pressures of CO₂ at 40 °C, respectively, and $\mu_{\alpha,mid}$ is the viscosity of the amine at 40 °C and a loading corresponding to 1,500 Pa equilibrium partial pressure of CO₂. The 10 cP corresponds to the viscosity of 8 m PZ at 40 °C and a loading corresponding to 1,500 Pa equilibrium partial pressure of CO₂. Omitting the viscosity-dependent term will calculate the standard solvent capacity.

$$Capacity_{\mu} = \frac{(\alpha_{rich} - \alpha_{lean}) \times n_{alk}}{kg(Am + H_2O)} \times \frac{1}{\left(\frac{\mu_{\alpha,mid}}{10cP}\right)^{0.25}} \quad \text{Equation 3-27}$$

The heats of absorption are calculated using Equation 3-25. The two vertical black lines are plotted at the PZ wt % corresponding to 7 m MDEA/2 m PZ and 5 m MDEA/5 m PZ, each of which is approximately 50 wt % amine. The heats of absorption are calculated at a loading corresponding to an equilibrium partial pressure of CO₂ of 1,500 Pa at 40 °C. Figure 3-21 suggests that the heat of CO₂ absorption at 120 °C is not a strong function of PZ wt %, which is consistent with the results of Tables 3-9 and 3-13. The formation of HCO₃⁻ dominates solution chemistry at higher temperatures, regardless of PZ wt %. The heat of CO₂ absorption at 40 °C is a strong function of PZ wt %, with a maximum value near 5 m MDEA/5 m PZ.

Had the capacity not been normalized to solvent viscosity (red dotted line) it would appear that increasing the PZ wt % is always beneficial. A higher solvent capacity will decrease the solvent circulation rate, which benefits process economics in both capital and operating expenses. However, increasing the wt % of PZ significantly increases the viscosity, which is detrimental to mass, heat, and momentum transfer. Accounting for the effect of viscosity in Equation 3-27 (solid red line) suggests a maximum capacity between 7 m MDEA/2 m PZ and 5 m MDEA/5 m PZ.

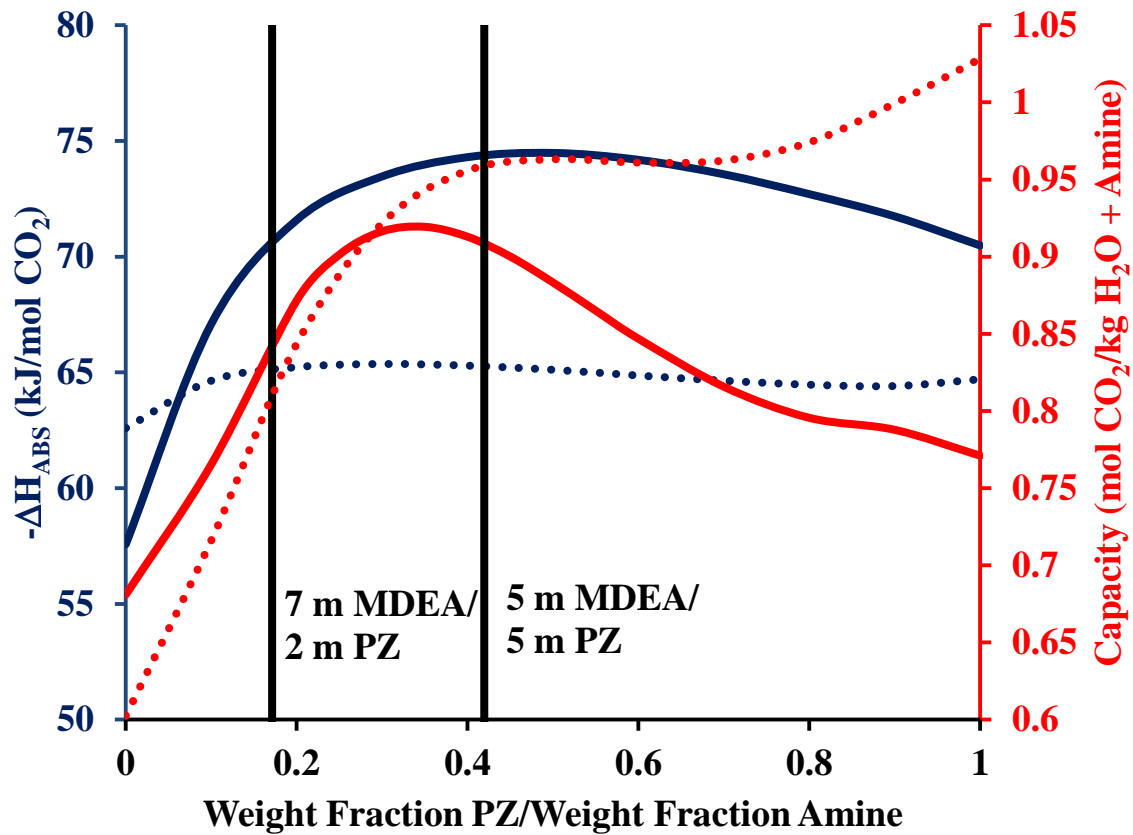


Figure 3-21: Heat of CO_2 absorption (blue) at 40 °C (solid line) and 120 °C (dotted line) and capacity (red) with (solid line) and without (dotted line) a viscosity correction at 40 °C for 50 wt % amine MDEA/PZ mixtures as a function of wt % PZ divided by wt % amine.

At stripper conditions a high heat of CO₂ absorption will increase the stripper pressure and reduce the compressor work. Model predictions in Figure 3-21 suggest that for a given weight fraction of amine on a CO₂-free basis the relative amounts of MDEA and PZ will not significantly influence stripper performance. However, at absorber conditions, where a high heat of CO₂ absorption will increase the magnitude of the temperature bulge, the heat of CO₂ absorption exhibits a strong dependence on PZ concentration. This suggests that packing requirement and intercooling duty will also exhibit a dependence on PZ concentration.

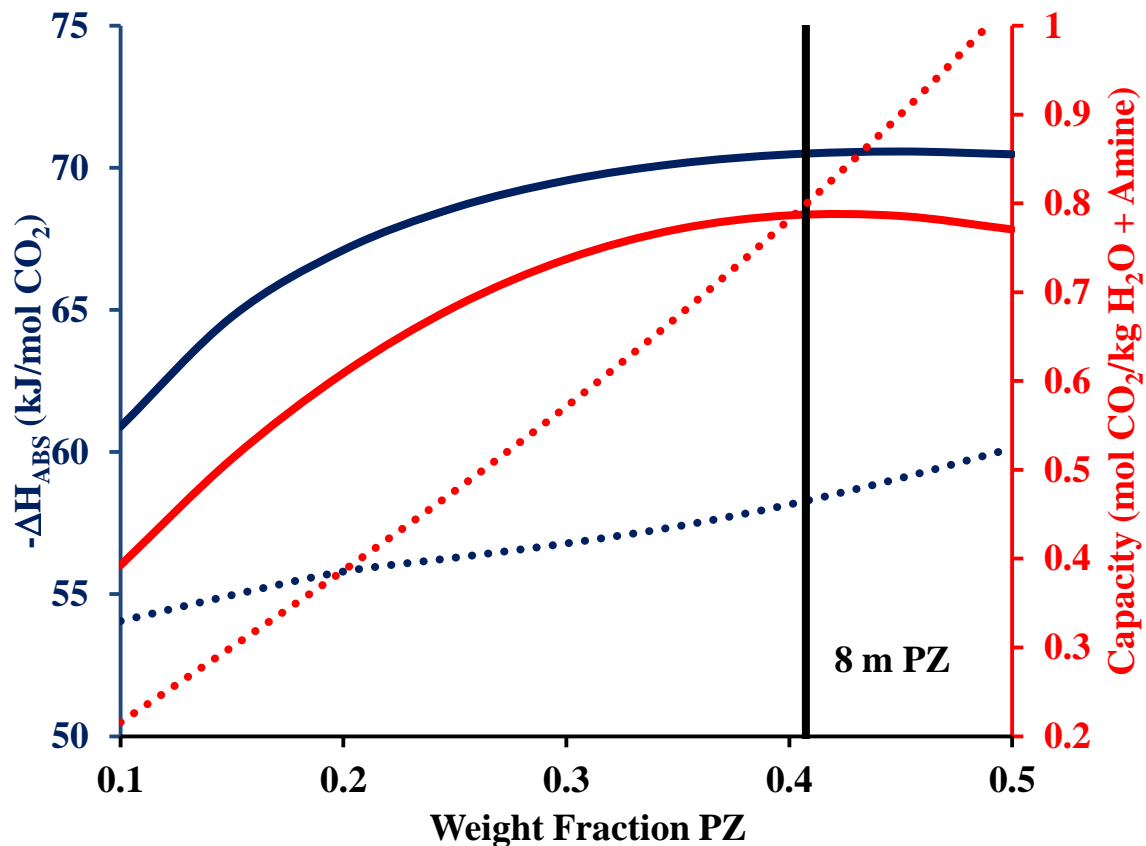


Figure 3-22: Heat of CO₂ absorption (blue) at 40 °C (solid line) and 120 °C (dotted line) and capacity (red) with (solid line) and without (dotted line) a viscosity correction at 40 °C for PZ as a function of wt % PZ.

Figure 3-22 compares Aspen Plus[®] predictions for heats of absorption at 40 °C and 150 °C and viscosity normalized capacity at 40 °C for PZ as a function of PZ wt %. The vertical black line corresponds to 8 m PZ. The heat of CO₂ absorption is a weak function of PZ concentration, which is consistent with the results of Figure 3-21, Table 3-9, and Table 3-13. Just as in Figure 3-21 the viscosity normalized capacity has a maximum value, and the normal capacity monotonically increases with PZ wt %. The optimum concentration of PZ is near 8 m, but the optimum is not sensitive to PZ wt %. The PZ concentration can be reduced to 30 wt % (5 m) without significantly reducing the viscosity normalized capacity. Lowering the PZ concentration would reduce volatile amine losses, improve heat transfer coefficients in cross exchangers, and avoid solvent precipitation. Normalizing the capacity to viscosity accounts for a few of these advantages, but a rigorous economic comparison is required to determine the true optimum PZ concentration.

3.7 CONCLUSIONS

- Model predictions for the heat of CO₂ absorption at 40 °C and an equilibrium CO₂ partial pressure of 1,500 Pa for 8 m PZ, 7 m MDEA/2 m PZ, and 5 m MDEA/5 m PZ are 70.5, 70.7, and 74.5 kJ/mol CO₂, respectively.
- Model predictions for the CO₂ capacity at 40 °C between equilibrium CO₂ partial pressures of 500 Pa and 5,000 Pa for 8 m PZ, 7 m MDEA/2 m PZ, and 5 m MDEA/5 m PZ are 0.799, 0.813, and 0.970 mol CO₂/kg H₂O + Amine, respectively.
- The temperature dependence of the heat of absorption for 8 m PZ is the result of shifting towards generation of HCO₃⁻ and H⁺PZCOO⁻ at high temperatures. MDEA

shows very little variation in the temperature dependence of the heat of absorption across operationally significant loadings. MDEA/PZ reflects both of these trends, with the effects balancing each other at a loading of 0.23 mol CO₂/mol alkalinity for 7 m MDEA/2 m PZ.

- Model predictions for speciation at operational temperature and loading ranges suggest that PZCOO⁻ is a significant base in both concentrated PZ and MDEA/PZ kinetics. HCO₃⁻ formation is significant in MDEA/PZ at all operational loadings and temperatures, but its importance increases with loading and temperature.
- The model-predicted heat of fusion for PZ·6H₂O is 48 kJ/mol. This result suggests that PZ acts as two H₂O molecules in the hydrated crystal.
- An improvement over empirical models for CO₂ solubility, Aspen Plus[®] predictions for the heat of absorption reflect the temperature dependence of CO₂ absorption for amines and amine blends.
- Experimental data for MDEA, PZ, and MDEA/PZ can be regressed into a single thermodynamic model in Aspen Plus[®] over operationally significant temperature, loading, and amine concentration ranges.
- Though it was not directly regressed, model predictions for the activity coefficient of CO₂ in MDEA/PZ blends are well-behaved.
- The lack of precision in experimental measurements of liquid heat capacities has given rise to inexplicable trends in unloaded amine/H₂O heat capacities, which cannot be represented in Aspen Plus[®] without the inclusion of physically infeasible binary interaction parameters for MDEA/PZ.

Chapter 4: Kinetic Modeling

4.1 INTRODUCTION

Chapter 3 focused on the prediction of solvent properties at equilibrium conditions. Typical process configurations include large swings of temperature, pressure, and CO₂ loading, and solvents are always transitioning from one equilibrium state to another. The rate at which the system approaches equilibrium is affected by CO₂ loading, temperature, vapor and liquid diffusivities, vapor and liquid concentration profiles, and heats of reaction. This study seeks to continue the refinement of rate-based models developed at The University of Texas at Austin to include more complex sets of kinetic reactions and a more useful treatment of ion diffusivities.

Recently collected wetted wall column (WWC) data for the solubility and absorption rate of CO₂ in 7 m MDEA/2 m PZ, 5 m MDEA/5 m PZ, and concentrated PZ are directly regressed by adjusting reaction rate constants and binary diffusivities in Aspen Plus[®]. The sensitivity of each point to the reaction rate constant and binary diffusivity is determined and used in Microsoft Excel[™] to minimize the difference between experimental and predicted CO₂ absorption rates. As long as the thermodynamics in the MDEA/PZ are not adjusted, the rate model can easily be expanded to include other solvents containing either MDEA or PZ.

4.2 LITERATURE REVIEW

Bishnoi (2000) developed a rate-based model for 0.6 M PZ/4 M MDEA that used enhancement factors to predict CO₂ flux measurements reported by Xu (1992) and

Kaganoi (1997). The thermodynamics of the model were based on measurements reported by both Bishnoi and Austgen (1989). Early PZ kinetic models focused on dilute systems free of the solubility limitations of concentrated PZ. Cullinane (2005) developed a rate-based model for K⁺/PZ with 0.45-3.6 m PZ. The first attempt to regress wetted wall column data for PZ into Aspen Plus[®] was made by Dugas (2009). Lack of an adequate thermodynamic model forced this approach to be abandoned and replaced by a spreadsheet Microsoft Excel[™] model that accurately predicts CO₂ absorption rate data for both MEA and PZ. AspenTech[™] (2011) and BASF (Asprion, 2006) developed their own rate-based MDEA/PZ models. The proprietary model developed by BASF uses enhancement factors and a discretized two-film model to represent CO₂ absorption rate data for gas treating applications. AspenTech[™] consolidates thermodynamic and rate data from Austgen (1989), Hilliard (2008), and Bishnoi and Rochelle (2002) to construct an activity-based model for MDEA/PZ.

The model presented in Chapter 3 is the third version of MDEA/PZ thermodynamics developed in this work. There is only one previous version of MDEA/PZ kinetics, which was referred to as the Fawkes Model. The model described here expands the set of experimental data regressed in the Fawkes Model to include a wider range of PZ concentration and low temperature MDEA/PZ CO₂ absorption rates.

4.3 METHODOLOGY

4.3.1 Hydraulic Properties

The correlations used to calculate density and viscosity are modified versions of those proposed by Weiland (1998). They are referenced to pure water to improve the

accuracy of model predictions at low amine concentrations. Density units and viscosity units are calculated using Equations 4-1 and 4-2, respectively. In Equations 4-1 and 4-2, x_i is component mole fraction, w_i is component weight fraction, α is loading units, and T is temperature in K. One modification of the Weiland equation for density is the omission of a term for binary interaction between water and amine. To improve model predictions of MDEA/PZ properties, both equations had to be modified to include terms for both MDEA and PZ. This results in 8 adjustable parameters for density and 10 for viscosity.

$$\rho = (x_{H_2O}) (\rho_{H_2O}) + (x_{MDEA}) (AT + B) + (x_{PZ}) (CT + D) + (x_{CO_2}) (ET + F) + \dots$$

$$\dots + (x_{CO_2}) (x_{MDEA} + x_{PZ}) (GT + H) \quad \text{Equation 4-1}$$

$$\frac{\mu}{\mu_{H_2O}} = \exp \left[\frac{[(Aw_{MDEA} + Bw_{PZ} + C)T + (Dw_{MDEA} + Ew_{PZ} + F)] [\alpha(Gw_{MDEA} + Hw_{PZ} + IT + J) + 1] w_{Am}}{T^2} \right] \quad \text{Equation 4-2}$$

Densities for loaded solutions of 7 m MDEA/2 m PZ and 5 m MDEA/5 m PZ were collected for this study using a Mettler Toledo DE40 densitometer (Mettler-Toledo, Inc., Columbus, OH). Viscosities for loaded solutions of 7 m MDEA/2 m PZ and 5 m MDEA/5 m PZ were collected for this study using a Physica MCR 301 cone and plane rheometer (Anton Paar GmbH, Graz, Austria). Detailed descriptions of the apparatus, analysis procedures, and experimental errors can be found in Freeman (2011). Loaded solutions were prepared by Xi Chen using procedures described in detail in Chen (2011). CO₂ loadings were verified both gravimetrically and spectroscopically by Dr. Chen. Duplicates were not measured for density, as the densitometer requires a large volume of liquid for each reading. Ten viscosity measurements between shear rates of 100 and 1,000 s⁻¹ were averaged for each amine, CO₂ loading, and temperature combination, and

the standard deviation of each measurement never exceeded 2% of the mean value. Complete results of the experiments are tabulated in Appendix C.

Tables 4-1 and 4-2 report the regression results and data sources, respectively, for the density of MDEA, PZ, and MDEA/PZ. The parameters accounting for temperature dependence (A, C, E, and G) have been centered at 40 °C so that their contribution to the overall density can be compared to that of the other parameters. The parameters have also been weighted to reflect their relative contributions to the density of 7 m MDEA/2 m PZ at a loading of 0.15 mol CO₂/mol alkalinity. The apparent mole fractions of MDEA, PZ, and CO₂ in that solution are 0.106, 0.030, and 0.025, respectively.

Table 4-1: Regression results for MDEA, PZ, and MDEA/PZ density

Parameter	MDEA	PZ	MDEA/PZ
A(313)(x _{MDEA})	-0.075	N/A	-0.087
B(x _{MDEA})	0.22	N/A	0.21
C(313)(x _{PZ})	N/A	-0.022	-0.024
D(x _{PZ})	N/A	0.060	0.073
E(313)(x _{CO2})	0	0.018	0.23
F(x _{CO2})	0.096	0.050	0.035
G(313)(x _{CO2})(x _{MDEA} +x _{PZ})	0	-0.011	-0.21
H(x _{CO2})(x _{MDEA} +x _{PZ})	-0.041	0.0010	0.0049

Table 4-2: Data sources for MDEA, PZ, and MDEA/PZ density

Amine	Loading	T (°C)	Source
7 m MDEA/2 m PZ	0.094-0.25	20-60	This work
5 m MDEA/5 m PZ	0.18-0.37	20-60	This work
5-9 m PZ	0.2-0.4	20-60	Freeman (2011)
MDEA/H ₂ O	0	10-90	Bernal-Garcia (2003)
30-60 wt % MDEA	0-0.50	25	Weiland (1998)

It should be noted that parameters E and G were not needed to regress MDEA density data because loaded MDEA data is regressed at one temperature (25 °C). The temperature behavior of unloaded MDEA is well characterized, but the partial molar

density of CO₂ in MDEA is assumed to be independent of temperature. The parameters accounting for amine concentration (A-D) differ by less than 20% across the different amines. However, the loading dependent terms vary significantly. This may be due to differences in CO₂ concentrations at operationally significant conditions. Concentrated PZ will have apparent CO₂ mole fractions between 0.05 and 0.10, which is twice the expected concentration of CO₂ in MDEA and MDEA/PZ (0.01-0.05 mol CO₂/mol). Equation 4-1 could be regressed to predict MDEA/H₂O, PZ/H₂O, and MDEA/PZ/H₂O density using one set of parameters, but loaded conditions require the use of separate expressions.

Tables 4-3 and 4-4 report the regression results and data sources, respectively, for the viscosity of MDEA, PZ, and MDEA/PZ. Just as was done with density, the regression results have been normalized to 40 °C and a solution of 7 m MDEA/2 m PZ at a loading of 0.15 mol CO₂/mol alkalinity. The apparent weight fractions of MDEA, PZ, and CO₂ are 0.402, 0.082, and 0.035, respectively.

Table 4-3: Regression results for MDEA, PZ, and MDEA/PZ viscosity

Parameter	MDEA	PZ	MDEA/PZ
A(w _{MDEA})(313)	5.13x10 ⁴	N/A	5.46x10 ⁴
B(w _{PZ})(313)	N/A	1.08x10 ⁴	4290
C(313)	3.57x10 ⁵	4.23x10 ⁵	3.94x10 ⁵
D(w _{MDEA})	0.539	N/A	0.555
E(w _{PZ})	N/A	0.111	0.0444
F	3.69	4.22	3.93
G(w _{MDEA})(α)	0.134	N/A	0.377
H(w _{PZ})(α)	N/A	0.116	0.171
I(313)(α)	-0.0859	-0.212	-0.479
J(α)	0.0267	-0.0237	0.0618

Table 4-4: Data sources for MDEA, PZ, and MDEA/PZ viscosity

Amine	Loading	T (°C)	Source
7 m MDEA/2 m PZ	0.094-0.25	20-60	This work
5 m MDEA/5 m PZ	0.18-0.37	40-60	This work
5-9 m PZ	0.2-0.4	25-60	Freeman (2011)
MDEA/H ₂ O	0	25-80	Teng (1994)
30-60 wt % MDEA	0-0.50	25	Weiland (1998)

Figures 4-1 and 4-2 compare experimental data and Aspen Plus[®] predictions for the density and viscosity of 5 m MDEA/5 m PZ as a function of loading from 40-60 °C. Model predictions are also shown at 120 °C to demonstrate the correlation stability at stripper conditions.

The biggest deficiency in the regression is the lack of high temperature data, which is especially important for predicting heat transfer coefficients and pressure drops in cross exchangers. Using FORTRAN subroutines guarantees good behavior of model predictions at these conditions, but accuracy can only be corroborated by experimental data.

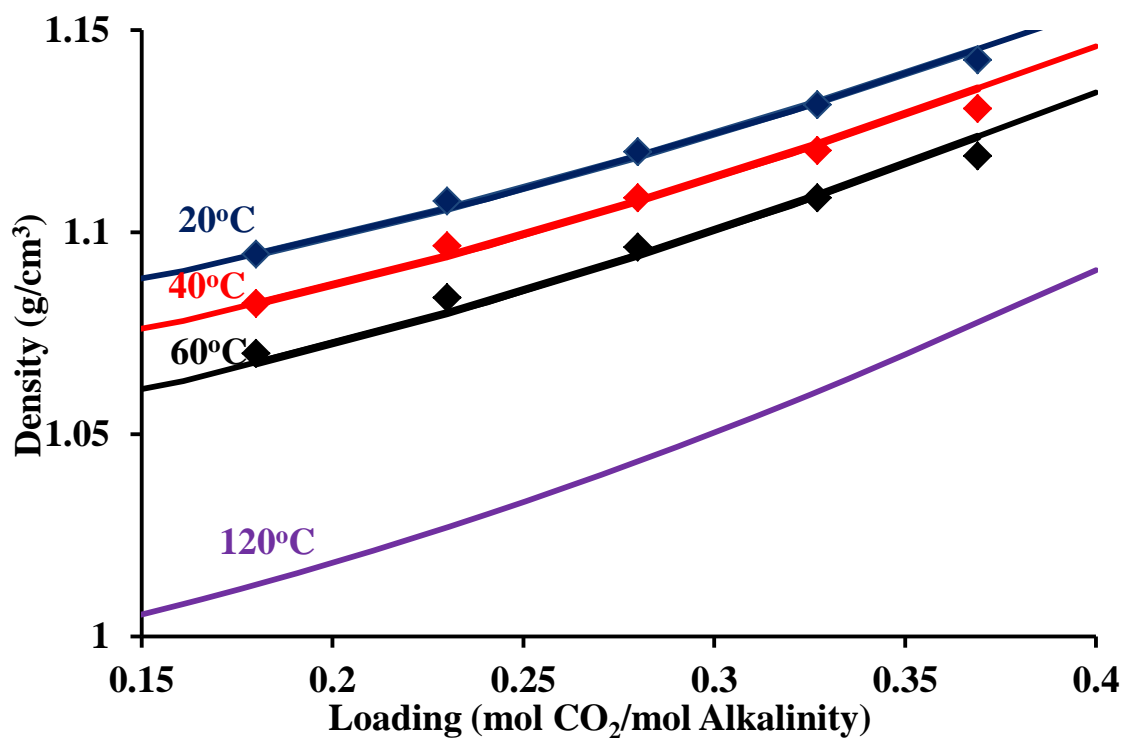


Figure 4-1: Density of 5 m MDEA/5 m PZ experimental data (points; This Work) and Aspen Plus[®] predictions (lines)

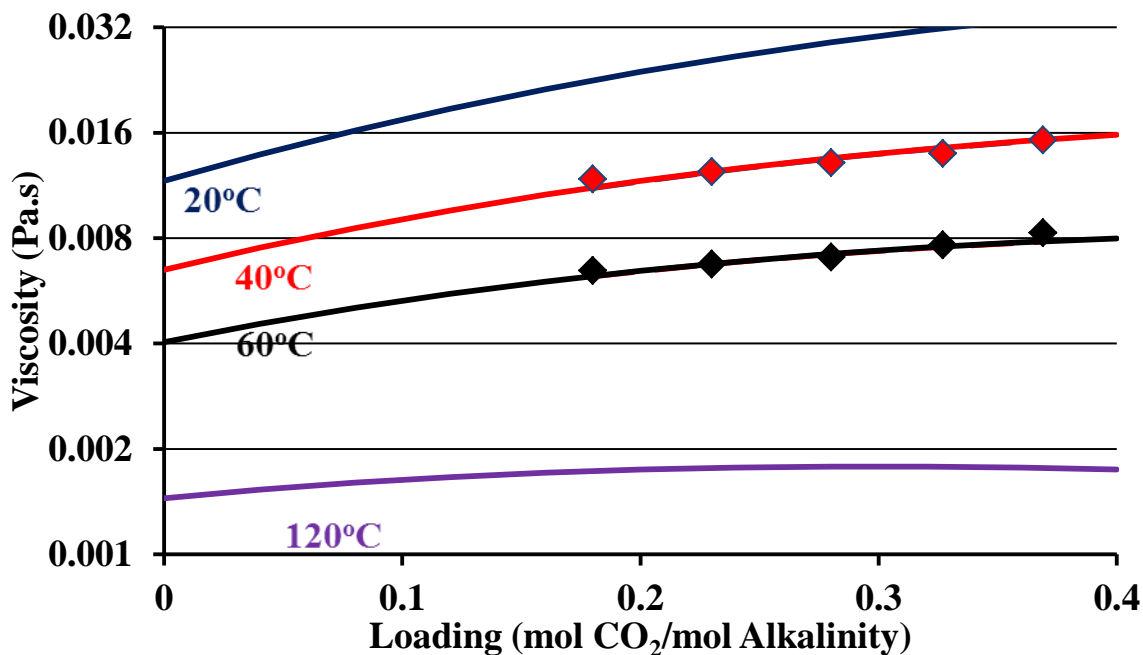


Figure 4-2: Viscosity of 5 m MDEA/5 m PZ experimental data (points, This Work) and Aspen Plus[®] predictions (lines)

The binary diffusivity of CO₂ is calculated by Equations 4-3, 4-4, and 4-5.

$$D_{CO_2,H_2O} = 2.35 \times 10^{-6} \exp\left(\frac{-2,119}{T}\right) \quad \text{Equation 4-3}$$

$$\mu_{H_2O} = 2.4055 \times 10^{-5} \exp\left[\left(4.42 \times 10^{-4}\right)P + \frac{4.753 - 9.565 \times 10^{-4} P}{R(T - 139.7 - 0.0124P)}\right] \quad \text{Equation 4-4}$$

$$D_{CO_2,Am} = D_{CO_2,H_2O} \left(\frac{\mu_{H_2O}}{\mu_{Am}}\right)^{0.8} \quad \text{Equation 4-5}$$

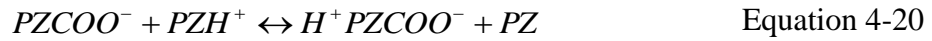
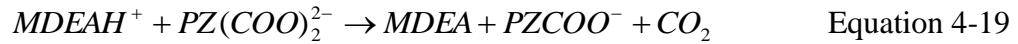
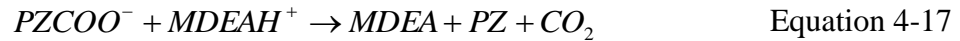
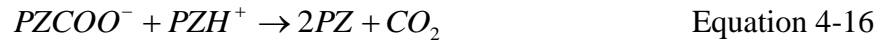
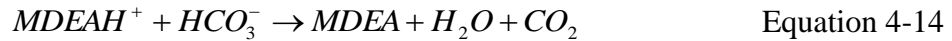
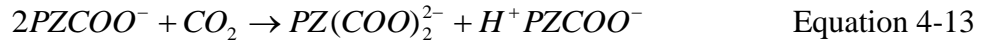
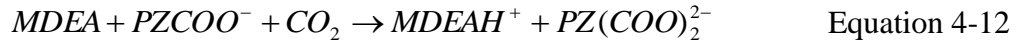
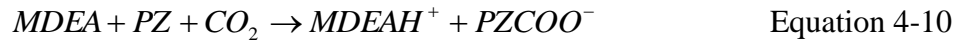
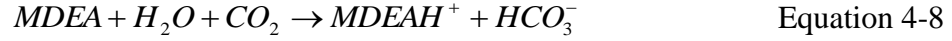
In Equations 4-3 through 4-5 T is temperature in K, P is pressure in bar, R is the gas constant, μ is viscosity in centipoise, and D is binary diffusivity in meters squared per second. The binary diffusivity of reactants and products is regressed along with reaction rate constants to fit experimental CO₂ absorption rate data. The binary diffusivity of reactants and products is calculated by Equation 4-6, which has the adjustable parameters D_0 , α , and β . Equation 4-6 is based on Equation 4-7 derived by Wilke-Chang (1955), and it is implemented in Aspen Plus[®] using FORTRAN subroutines. In Equation 4-7 ξ_{sol} is the solvent specific parameter, MW_{sol} is the molecular weight of the solvent, V_{Am} is the molar volume of the amine, T is temperature, m_{sol} is viscosity, and ∞ indicates that it is the infinite dilution binary diffusivity of the component.

$$D = D_0 \left(\frac{T}{313.15}\right)^\beta \left(\frac{\mu}{0.0155}\right)^{-\alpha} \quad \text{Equation 4-6}$$

$$D_{Am}^\infty = \frac{1.17 \times 10^{-13} (\xi_{sol} MW_{sol})^{0.5} T}{V_{Am}^{0.6} \mu_{sol}} \quad \text{Equation 4-7}$$

4.3.2 Reactions and Reaction Rate Constants

Equations 4-8 through 4-22 are used to predict CO₂ absorption rate for MDEA, PZ, and MDEA/PZ.



Equations 4-8 through 4-19 are kinetic reactions and Equations 4-20 through 4-22 are equilibrium reactions that account for proton transfers between species. Of the

kinetic reactions, 4-8 through 4-13 are forward reactions and 4-14 through 4-19 are reverse reactions. The six forward reactions can be broken into two groups: those catalyzed by MDEA and those catalyzed by PZ or PZCOO⁻. Each base catalyzes the formation of PZCOO⁻, PZ(COO)₂²⁻, and HCO₃⁻.

Rate constants for Equations 4-8 through 4-19 are calculated using the Arrhenius expression in Equation 4-23, where k is the reaction rate constant at temperature, T , T_{ref} is the reference temperature, E_A is the activation energy, and k_0 is the reaction rate constant at T_{ref} .

$$k = k_0 \exp \left[\frac{-E_A}{R} \left(\frac{1}{T} - \frac{1}{T_{ref}} \right) \right] \quad \text{Equation 4-23}$$

Rate constants for reverse reactions are calculated by Equation 4-24, which relates forward and reverse rate constants to the equilibrium constant at that temperature.

$$\frac{k_f}{k_r} = K_{eq} = \prod_i a_i^{v_i} = \exp \left(\frac{-\Delta G^0}{RT} \right) \quad \text{Equation 4-24}$$

In Equation 4-24, ΔG^0 is the Gibbs energy, k_f is the forward rate constant, k_r is the reverse rate constant, a_i is the activity of component i , and v_i is the stoichiometric coefficient of component i . Defining kinetic rate constants by Equation 4-23 assumes that equilibrium constant is of the form $A+B/T$, similar to the first two terms of Equation 3-1. The equilibrium conditions regressed into the thermodynamics exhibit a complex temperature dependence that is a function of ΔG^0_f , ΔH^0_f , and C_p^0 for all species in solution. Because the kinetic and equilibrium expressions assume different temperature

dependences, the reverse rate constants calculated by Equation 4-23 are only applicable over a narrow temperature range (± 20 °C).

With the exception of Equation 4-11, every kinetic reaction is first order in each reactant. The rates for Equations 4-11, r_f , and 4-16, r_r , are calculated by Equations 4-25 and 4-26, respectively, where k is the reaction rate constant and a_i is the activity of species, i .

$$r_f = \frac{k_f a_{PZ} a_{CO_2}}{a_{PZCOO^-}} \quad \text{Equation 4-25}$$

$$r_r = \frac{k_r a_{PZH^+} a_{PZCOO^-}^2}{a_{PZ}} \quad \text{Equation 4-26}$$

Kinetic rate constants are regressed into Aspen Plus[®] using a wetted wall column (WWC) simulation similar to the one used by Plaza (2011). Figure 4-3 depicts the process flow diagram for the WWC in Aspen Plus[®].

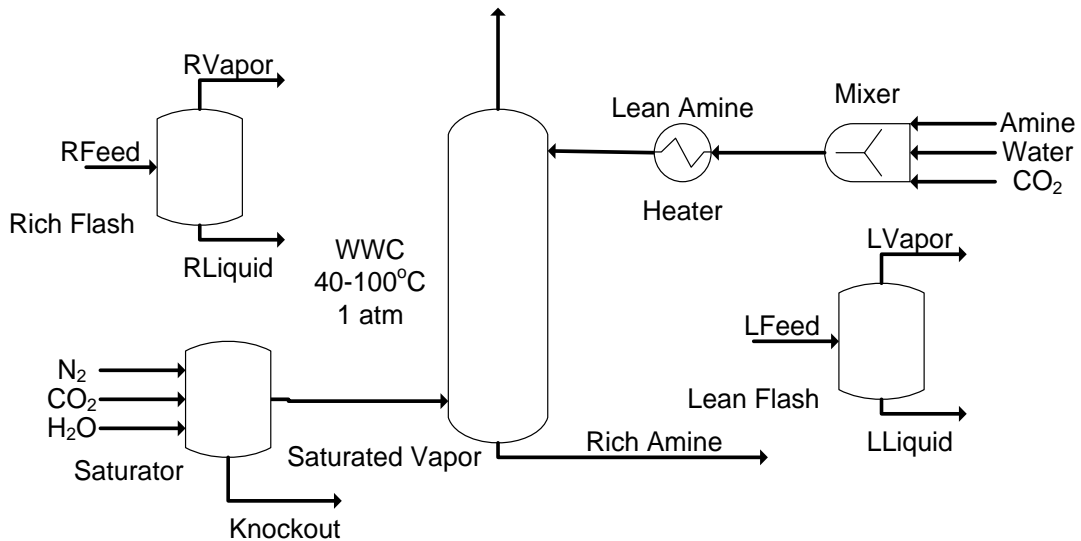


Figure 4-3: Process flow diagram for the wetted wall column Aspen Plus[®] simulation

The solution being tested is fed as separate amine, water, and CO₂ streams into a mixer. A lean amine heater is used to remove the heat of mixing. The vapor fed to the bottom of the column consists of N₂ and CO₂ saturated with H₂O at the temperature of the column. Excess water is knocked out and removed from the saturator. To calculate the liquid side mass transfer coefficient with a gas side concentration gradient, k_g' , the rich and lean streams are transferred to “Rich Flash” and “Lean Flash”, respectively, to determine the equilibrium partial pressure of CO₂ for each stream.

There are six kinetic reactions and one adjustable parameter in the WWC simulation. The other five rates are either fixed using experimental data or regressed independently. Equation 4-8 is well studied in literature, and its rate was fixed throughout the regression (Ko, 2000). The forward rate for Equation 4-9 is set using methodology outlined in Plaza (2011). The activation energy is approximated using data for MDEA (49.0 kJ/mol) reported by Pacheco (1998), and k_o is set such that the forward rate constant at 25 °C satisfies Equation 4-27 presented in Rochelle et al. (2001) for the formation of HCO₃⁻ catalyzed by various amines. The second order rate constant calculated from Equation 4-27 must be converted to an activity basis using Equation 4-28, where k_f^a is the reaction rate constant on an activity basis, k_f^c is the reaction rate constant in kmol/m³.s, ρ_s is the molar density of the solvent at 25 °C, and g_{PZCOO} and g_{CO_2} are the activity coefficients of PZCOO⁻ and CO₂ at 25 °C and a loading of 0.30.

$$k_f^c = 3.278 \exp(-1.11 pK_b) \quad \text{Equation 4-27}$$

$$k_f^a = \frac{k_f^c \rho_s^2}{(\gamma_{PZCOO^-})(\gamma_{CO_2})} \quad \text{Equation 4-28}$$

Equations 4-11 and 4-13 are adjusted simultaneously to fit CO₂ absorption rate for concentration PZ solutions. They cannot be adjusted independently in the WWC simulation, so the ratio of the forward reaction rates is set equal to the ratio of the rates predicted in Figure 4-2. The same ratio is used for the MDEA catalyzed cases (Equations 4-10 and 4-12) when regressing the CO₂ absorption rate for MDEA/PZ.

4.3.3 Sensitivity Analysis

In order to determine the optimum values for rate constants, activation energies, and binary diffusivity parameters, the sensitivity of each experimental point to each parameter was determined. Rate constants and binary diffusivities were individually increased by 10%, and the effect on the predicted flux was documented. Equation 4-29 was used to calculate the sensitivity, α , of each experimental data point to each parameter, P. The subscript “+10%” refers to the parameter and flux values after the parameter is increased by 10%.

$$\alpha = \frac{\ln(\text{Flux}_{+10\%} / \text{Flux})}{\ln(P_{+10\%} / P)} \quad \text{Equation 4-29}$$

Once the sensitivity of each experimental flux to each parameter was determined, the parameters were adjusted in Microsoft Excel™ to minimize the difference between predicted and experimental CO₂ absorption rates using Equation 4-30. In Equation 4-30 x denotes the parameter number, α_x is the sensitivity of the flux to parameter P_x, and the

subscripts “initial” and “final” denote the flux and parameter values before and after the regression is performed, respectively.

$$\frac{Flux_{final}}{Flux_{initial}} = \prod_{x=1}^n \left(\frac{P_{x,final}}{P_{x,initial}} \right)^{\alpha_x} \quad \text{Equation 4-30}$$

4.3.4 Mass Transfer Correlations

A detailed description of the mass transfer coefficients and the concentration gradients they describe may be found in Chapter 2. Experimental data collected in the WWC reports the overall mass transfer coefficient, K_G , as the sum of a gas film mass transfer coefficient, k_g , and a liquid side mass transfer coefficient in the gas side units, k_g' . Equation 4-31 describes the relationship between the three mass transfer coefficients.

$$\frac{1}{K_G} = \frac{1}{k_g} + \frac{1}{k_g'} \quad \text{Equation 4-31}$$

Fitting experimental CO_2 absorption data in requires adjusting K_G . Because there is no chemical reaction in the vapor phase, k_g can be directly calculated by Aspen Plus[®] and used in the simulation. Simultaneous mass transfer and chemical reaction in the liquid boundary layer complicates the prediction of k_g' . Under pseudo first order conditions, where the diffusion of free amine to and from the reactive boundary layer is assumed to be non-limiting, k_g' is approximated by Equation 4-32.

$$k_g' \approx \frac{\sqrt{k_2 D_{\text{CO}_2} a_{\text{Am}} \gamma_{\text{CO}_2}}}{H_{\text{CO}_2}} \quad \text{Equation 4-32}$$

Because the diffusion coefficient of CO₂, D_{CO₂}, and the Henry's Constant of CO₂, H_{CO₂}, are both fixed, only the activity-based overall second order reaction rate constant, k₂, is adjustable. This assumption is valid under lean conditions, but as the solution saturates with CO₂ the diffusion of reactants becomes a limiting factor, and Equation 4-32 no longer describes the liquid side mass transfer coefficient. At high loading and temperature the diffusion of reactants and products must also be adjusted to predict CO₂ absorption rates.

A FORTRAN subroutine was created by Dugas (2009) that directly calculates k_g and k_l⁰ for the wetted wall column. Equations 4-33 through 4-36 are used to calculate k_g, and Equations 4-37 through 4-42 are used to calculate k_l.

$$k_g = \frac{1.075 D_{CO_2}}{dRT} \left(\frac{ud^2}{D_{CO_2} h} \right)^{0.85} \quad \text{Equation 4-33}$$

$$D_{CO_2} = 0.00186T^{3/2} \frac{\left(\frac{1}{MW_{CO_2}} + \frac{1}{MW_{N_2}} \right)^{0.5}}{\Omega P (3.87)^2} \quad \text{Equation 4-34}$$

$$\Omega = 0.030476 \left(\frac{k_B T}{\varepsilon} \right)^2 - 0.268762 \left(\frac{k_B T}{\varepsilon} \right) + 1.480762 \quad \text{Equation 4-35}$$

$$\frac{k_B T}{\varepsilon} = \frac{T}{(195.2 \times 71.4)^{0.5}} \quad \text{Equation 4-36}$$

$$k_l^0 = \frac{Q_{sol}}{A} (1 - \Theta) \quad \text{Equation 4-37}$$

$$\Theta = 1 - 3\sqrt{\frac{\eta}{\pi}} \quad \text{Equation 4-38}$$

$$\eta = \frac{D_{CO_2} \tau}{\delta^2} \quad \text{Equation 4-39}$$

$$\tau = \frac{h}{u_s} \quad \text{Equation 4-40}$$

$$\delta = \sqrt[3]{\frac{3\mu Q_{sol}}{\rho g W}} \quad \text{Equation 4-41}$$

$$u_s = \frac{\rho g \delta^2}{2\mu} \quad \text{Equation 4-42}$$

In Equations 4-33 through 4-42, u is fluid velocity, d is the WWC diameter, T is the temperature in K, h is the height of the WWC, Q_{sol} is the solvent volumetric flow rate, A is the contact area, P is the pressure, Θ is the dimensionless driving force, W is the circumference of the cylindrical contactor, k_B is the Boltzmann constant, μ is the fluid viscosity, ρ is the fluid density, g is the acceleration due to gravity, δ is the film thickness, u_s is the surface velocity, τ is the surface contact time, and η is the dimensionless penetration distance.

4.3.5 Loading Adjustment

Experimental predictions of k_g' at a given temperature and loading are based on CO_2 absorption rates at six different log mean driving forces (LMDF). Figure 4-4 shows the CO_2 flux as a function of LMDF for 7 m MDEA/2 m PZ at a loading of 0.21 mol CO_2 /mol alkalinity and 40 °C.

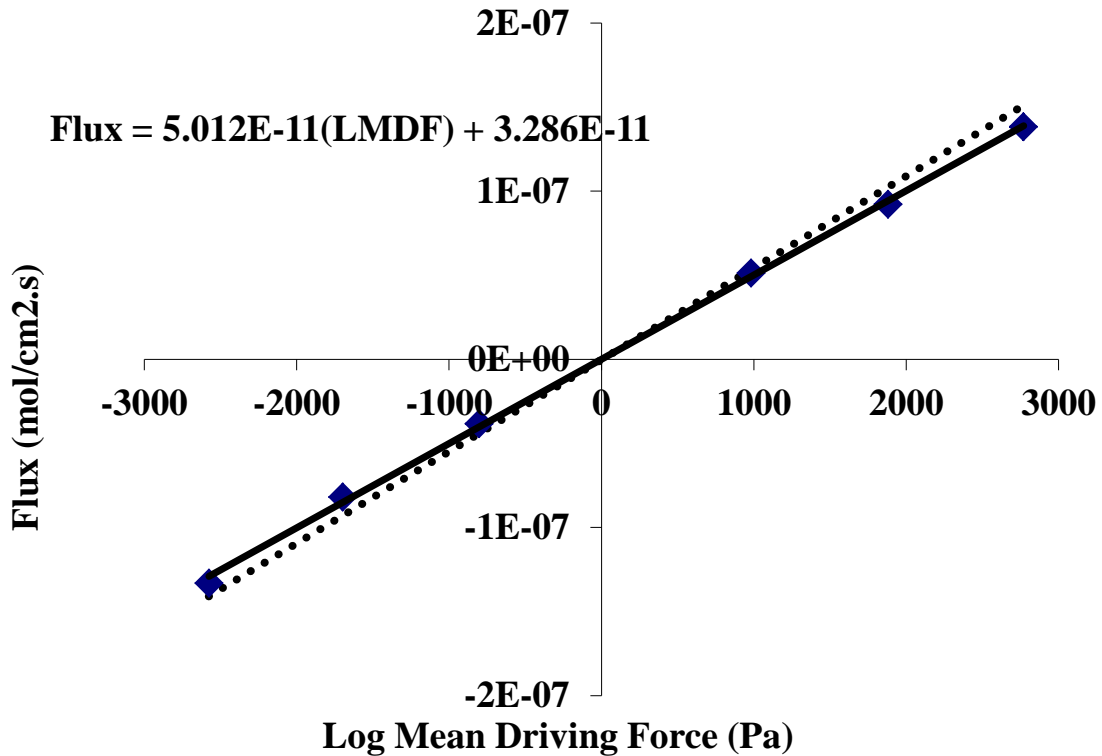


Figure 4-4: Experimental values (points and solid line) and Aspen Plus[®] predictions (dotted line) for 7 m MDEA/2 m PZ at a loading of 0.21 mol CO₂/mol alkalinity at 40 °C (Chen, 2011)

The slope of the line in Figure 4-4 corresponds to the overall mass transfer coefficient, K_G . The liquid side mass transfer coefficient, k_g' is calculated by subtracting the gas side mass transfer coefficient from K_G per Equation 4-10. This calculation could be performed for each of the six experimental points, but the regression gives an average K_G and, thus, an average experimental k_g' . The Aspen Plus[®] WWC simulation adjusts reaction rates to set the model-predicted flux equal to the experimental flux for the two extreme LMDFs. Only one rate constant and activation energy can be assigned to each kinetic reaction, and the final model will not perfectly predict the CO₂ absorption rate at all conditions. One condition, however, that must be met for each set of

absorption/desorption measurements is that the CO₂ flux is zero when the LMDF is zero. This condition will be met when the relative errors in the flux (i.e., Flux_{pred}/Flux_{exp}) for the absorption and desorption points are equal. If the reaction rate is fixed, one way to meet this condition is to adjust the experimental loading until the relative errors are equal, as depicted in Figure 4-2.

4.4 RESULTS

4.4.1 Reaction Constants and Binary Diffusivity

Table 4-5 reports rate constants and activation energies for all kinetic reactions. The values of the rate constants are not reported here to protect the proprietary nature of the Independence model.

Table 4-5: Regression results for MDEA, PZ, and MDEA/PZ viscosity

Rate Constant (k_{Am-b})	E_A (kJ/mol)
k _{f,H2O-MDEA}	44.9
k _{f,H2O-PZ}	49.0
k _{f,PZ-MDEA}	20.5
k _{f,PZ-PZCOO}	14.2
k _{f,PZCOO-MDEA}	20.5
k _{f,PZCOO-PZCOO}	14.2
k _{r,H2O-MDEA}	85.9
k _{r,H2O-PZ}	73.7
k _{r,PZ-MDEA}	85.6
k _{r,PZ-PZCOO}	85.1
k _{r,PZCOO-MDEA}	108
k _{r,PZCOO-PZCOO}	89.3

As mentioned in Section 4.3.2, the rates and activation energies for all reverse reactions (k_{r,Am-b}) are calculated using forward reaction rates and equilibrium constants at 40 °C and 60 °C. The k₀ and E_A for k_{f,H2O-MDEA} and k_{f,H2O-PZ} were obtained from Ko (2000) and Cullinane (2005), respectively. Throughout the regression the forward rate

constants for $\text{PZ}(\text{COO})_2^{2-}$ forming reactions ($k_{f,\text{PZCOO-b}}$) were set to be 1.35 times greater than that of the corresponding PZCOO^- forming reaction, per Cullinane (2005). The only two manually adjusted rate constants were for $k_{f,\text{PZ-MDEA}}$ and $k_{f,\text{PZ,PZCOO}}$. Because the relative values of $k_{f,\text{PZ-b}}$ and $k_{f,\text{PZCOO-b}}$ were held constant for all temperatures, the corresponding activation energies for the forward reactions are equal. The activation energies for reverse reactions differ for these cases because the equilibrium constants exhibit different temperature dependences.

At low loading conditions in PZ the reaction between PZ and CO_2 may be catalyzed by PZ or PZCOO^- . The rate constant for $k_{f,\text{PZ,PZCOO}}$ was selected because NMR data suggest that it is a more significant reaction across operationally significant conditions. Because there are two competing reaction mechanisms, the MDEA-catalyzed reactions could not be simply scaled to the PZ or PZCOO^- -catalyzed reactions during the regression. At 25 °C the ratio of $k_{f,\text{PZ,PZCOO}}$ to $k_{f,\text{PZ-MDEA}}$ is 6.46. The pK_a values at 25 °C for MDEA, PZ, and PZCOO^- are 8.55, 9.73, and 8.94, respectively. Estimating the rate constant of the MDEA-catalyzed reaction using PZ and PZCOO^- gives factors of 15.1 and 2.45, respectively. This suggests that, even though the reaction in Aspen Plus[®] is catalyzed by PZCOO^- , the effect of the PZ-catalyzed reaction is imbedded in the result.

As loading and temperature increase, the absorption of CO_2 is less limited by reaction rate and more limited by the diffusion of reactants and products to and from the boundary layer. Figure 4-5 compares the sensitivity of k_g' to diffusion and reaction control for 8 m PZ as a function of the partial pressure of CO_2 . In this case, diffusion control considers the diffusivity of reactants and products (dashed line with \blacklozenge) as well as

CO₂ (solid line with □), and reaction control considers the PZCOO⁻ and PZ(COO)₂²⁻-forming reactions. The pre-exponential factor, k₀, from Equation 4-23 and the reference binary diffusivities from Equations 4-3 and 4-6 were adjusted to determine sensitivity.

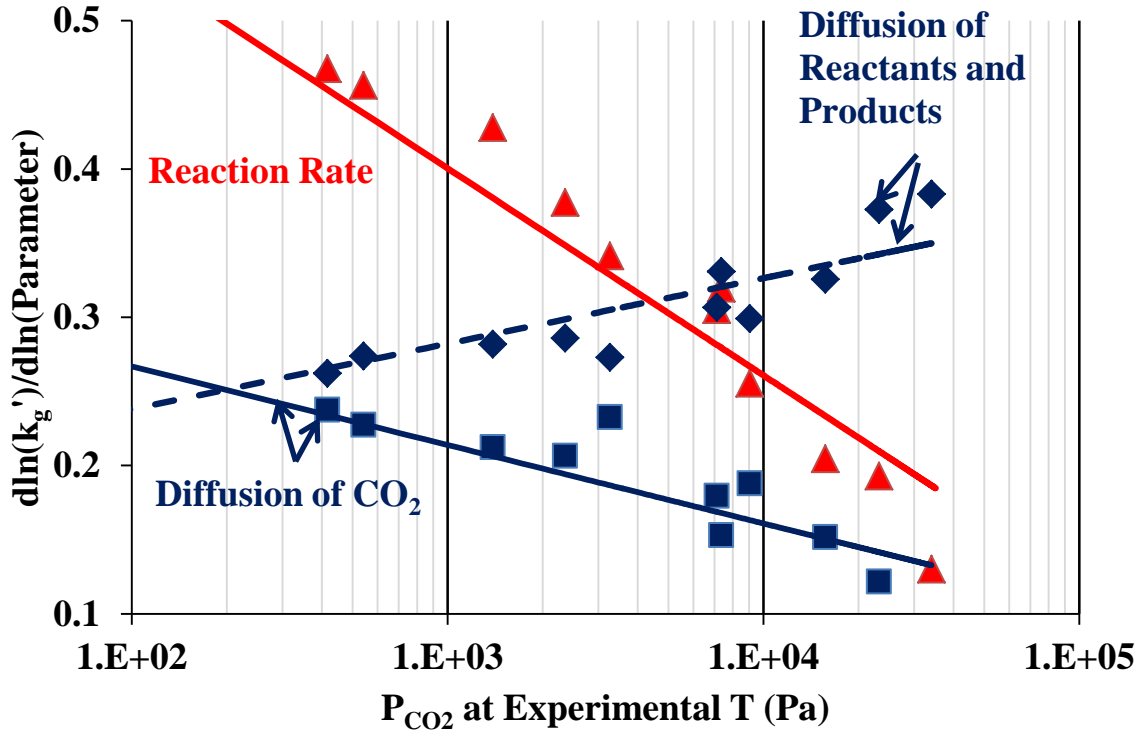


Figure 4-5: Sensitivity of k_g' to diffusion (blue) and reaction (red) control for 8 m PZ from 40-100 °C

The pseudo first order assumption, which is used to derive Equation 4-32, neglects diffusion of reactants and products, and it suggests that k_g' varies with D_{CO_2} to the 0.5 power. Figure 4-5 suggests that the combined dependence of k_g' on D_{CO_2} and the diffusion of reactants and products is 0.49 ± 0.01 . Plaza (2011) explains that this inconsistency is due to the treatment of mass transfer coefficients in Aspen Plus[®], which overemphasizes the dependence of CO₂ absorption on the diffusion of reactants and products at low loading and temperature conditions.

Figure 4-6 compares calculated k_g' to experimental results from Dugas (2009) and Chen (2011) for 8 m PZ, 5 m PZ, 7 m MDEA/2 m PZ, and 5 m MDEA/5 m PZ.

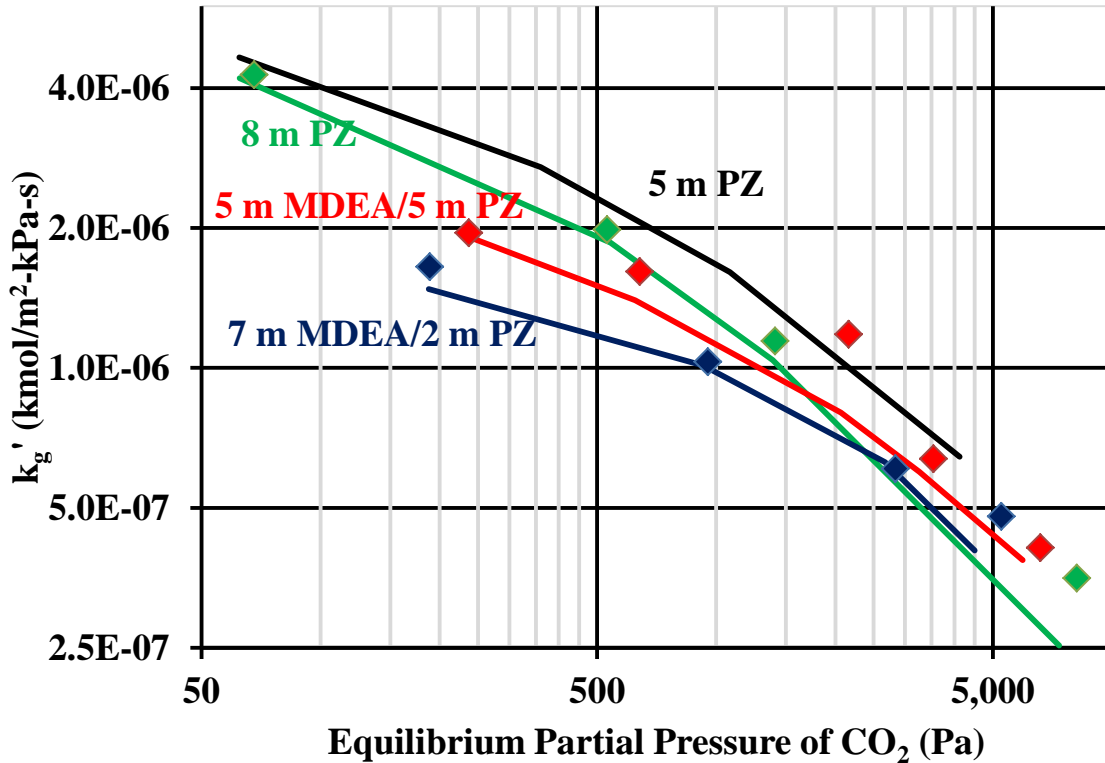


Figure 4-6: Experimental data (points) and Aspen Plus[®] predictions (lines) for k_g'

At low loadings where the absorption of CO₂ is predominantly limited by reaction rates, PZ exhibits a higher CO₂ absorption rate than MDEA/PZ. As loading increases and the solution shifts to diffusion control, the relatively low viscosity of 5 m PZ causes it to outperform all other solvents on the basis of k_g' . Calculating the sensitivity of CO₂ absorption rate to reaction kinetics and diffusion of reactants and products enables the prediction of performance trends linked to each absorption mechanism.

The diffusivity of CO₂ was calculated using Equations 4-2 through 4-5. The diffusivity of reactants and products as calculated by Equation 4-6 was regressed

simultaneously with reaction rate constants, and the resulting values for D_0 , α , and β are substituted below in Equation 4-43.

$$D = 2.26 \times 10^{-10} \left(\frac{T}{313.15} \right)^{-2.58} \left(\frac{\mu}{0.0155} \right)^{-1.45} \quad \text{Equation 4-43}$$

The temperature dependence of Equation 4-43 comes from both T and μ . Wilke and Chang (1955) predicted that the infinite dilution diffusion coefficient of amines and organic molecules depends on T to the first power and μ to the negative first power (Equation 4-7). If the exponent on T is fixed at the Wilke and Chang prediction and the exponent on μ is adjusted to give the same temperature dependence as Equation 4-43, the resulting exponent is -1.06. Therefore, the dependence of diffusivity on temperature predicted by Equation 4-43 is similar to that of Equation 4-7, but the exponent on viscosity is -1.45 rather than -1.0. This may be a result of the extrapolation from infinite dilution in water to a concentrated amine solution.

Figures 4-7 and 4-8 compare the experimental and model-predicted CO_2 fluxes as a function of the equilibrium partial pressure of CO_2 for PZ and MDEA/PZ, respectively, as regressed in Microsoft Excel. To guarantee agreement between the Microsoft Excel and Aspen Plus[®] predictions, the WWC simulation was rerun using the regression results and the predicted fluxes were compared. When comparing the Excel and Aspen Plus[®] values for the ratio of the experimental to model-predicted CO_2 flux the average difference in flux predictions across all conditions is 0.01%. This difference is too miniscule to be observed graphically, and, thus, a plot comparing the predictions is omitted.

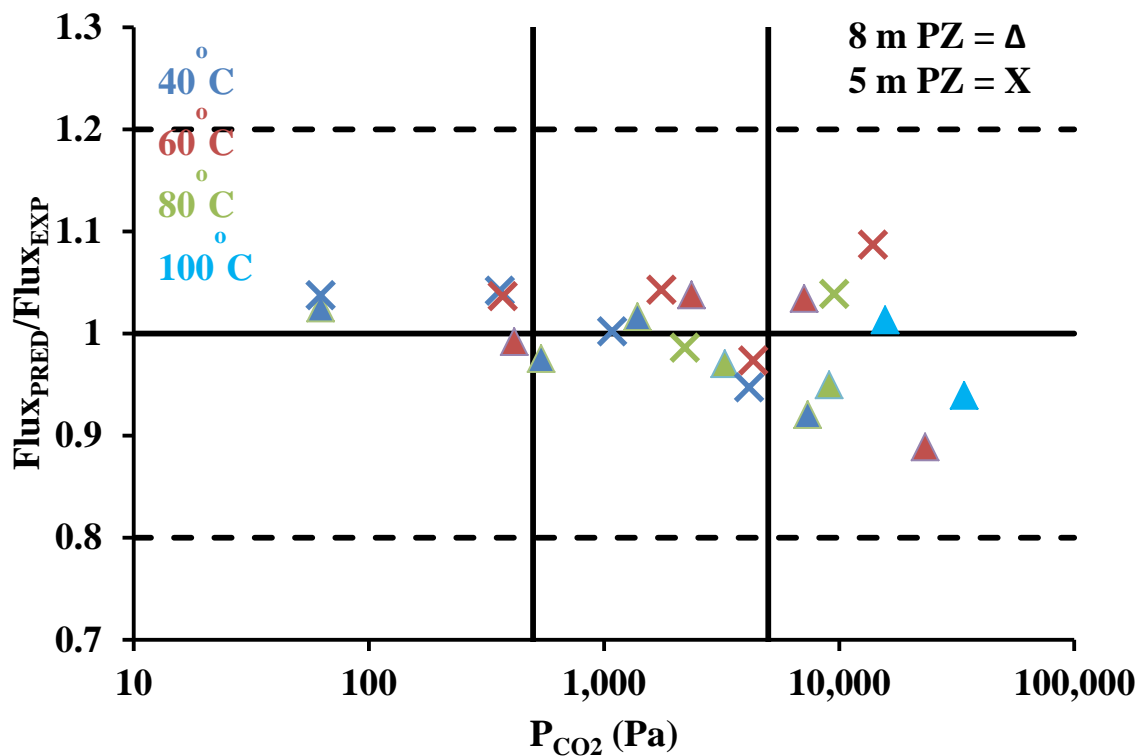


Figure 4-7: Flux_{PRED}/Flux_{EXP} for 8 m PZ and 5 m PZ from 40-100 °C

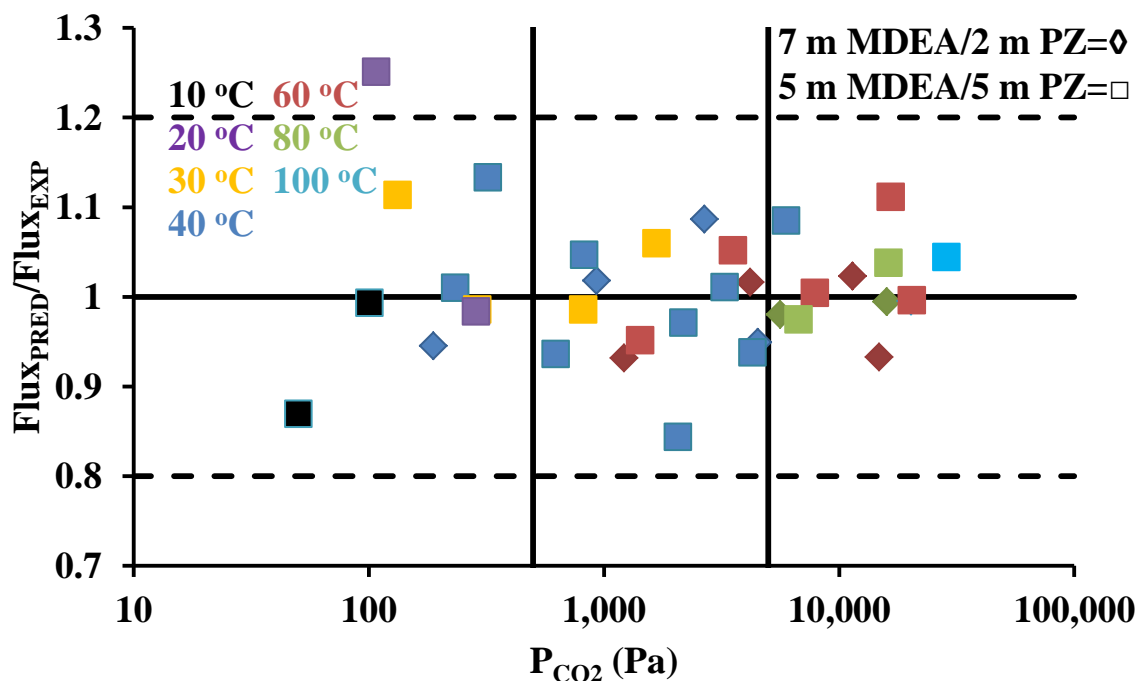


Figure 4-8: Flux_{PRED}/Flux_{EXP} for 7 m MDEA/2 m PZ and 5 m MDEA/5 m PZ from 10-100 °C

The two vertical lines in Figure 4-7 correspond to the nominal lean and rich partial pressures of CO₂. The dashed lines at 0.8 and 1.2 account for the reported ±20% confidence in experimental predictions of CO₂ absorption rate in the WWC.

Figure 4-9 compares experimental and model predicted CO₂ fluxes as a function of bulk vapor CO₂ partial pressure. The closed points are Independence model predictions, and the closed points are predictions from Bishnoi (2000) and Samanta (2011). The experimental data are from Bishnoi (2000), Samanta (2011), Derks (2006), and Kaganoi (1997). Table 4-6 summarizes the experimental data.

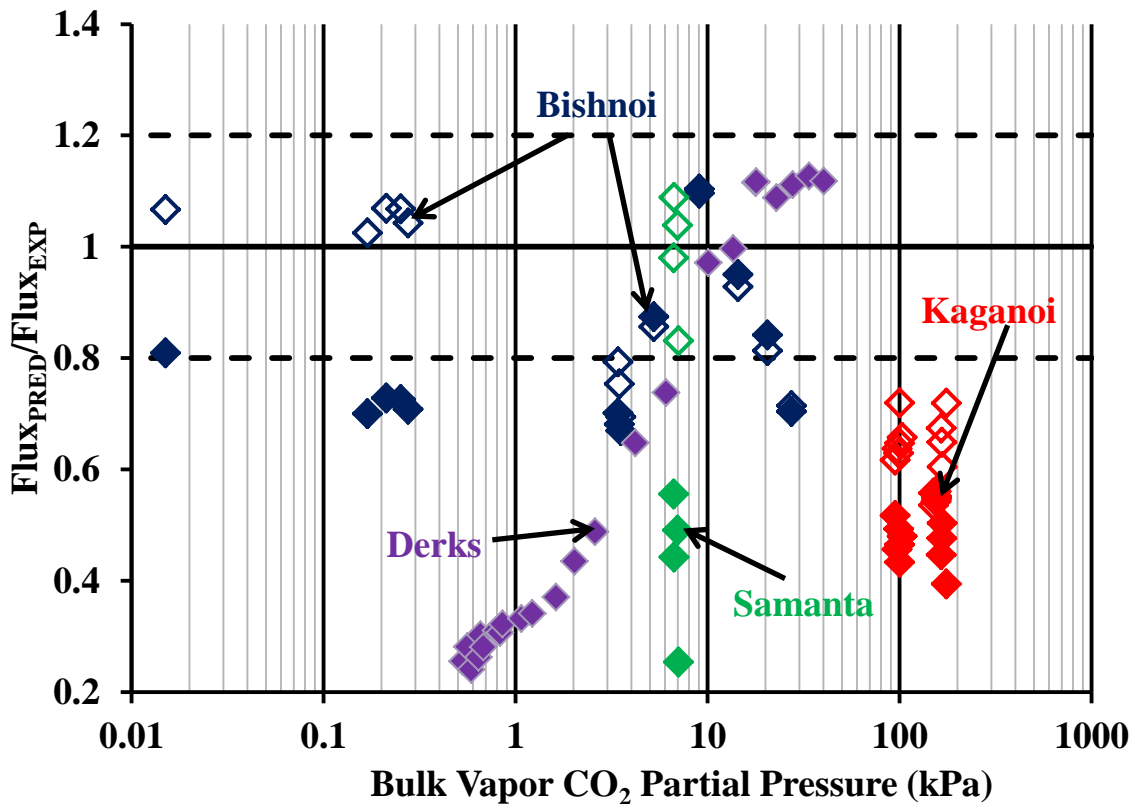


Figure 4-9: Flux_{PRED}/Flux_{EXP} for MDEA, PZ, and MDEA/PZ at 40 °C. Solid points are Independence model predictions and open points are Bishnoi (2000) and Samanta (2011) predictions.

Table 4-6: Experimental data for CO₂ absorption rate in MDEA, PZ, and MDEA/PZ CO₂ at 40 °C

Amine	CO ₂ Loading (mol CO ₂ /mol alk)	Bulk Vapor P _{CO2} (kPa)	Source
4 M MDEA/0.6 M PZ	0.0034-0.0050	0.015-0.276	Bishnoi (2000)
4 M MDEA/0.6 M PZ	0.084-0.275	3.42-27.3	Bishnoi (2000)
4 M MDEA/0.6 M PZ	0.216-0.553	97-175	Kaganoi (1997)
30 wt % MDEA – 22 wt % MDEA/8 wt % PZ	0	7	Samanta (2011)
1.0 M PZ	0	0.531-40.3	Derks (2006)

The Independence model under predicts CO₂ absorption rates at low CO₂ loadings with the exception of Derks (2006) at high CO₂ driving forces. At these conditions H₂O is an important catalyst for carbamate formation, and the first order reaction is omitted from Independence model kinetics. Bishnoi model predictions for loaded 4 M MDEA/0.6 M PZ at moderate CO₂ driving forces compare favorably to Independence model predictions. Both the Bishnoi and Independence model under predict Kaganoi (1997) CO₂ absorption rates at high CO₂ loadings and driving forces.

4.4.2 Stability Analysis

A stability analysis was performed on the 7 regressed parameters as well as the pre-exponential factor in Equation 4-3 and the exponent in Equation 4-5 (i.e., parameters concerning the binary diffusivity of CO₂). Table 4-7 reports the relative change in parameter values required to cause a 1% increase in the sum of squares error. The results in Table 4-7 support the sensitivities in Figure 4-5. The kinetic model is more sensitive to terms concerning the binary diffusivity of reactants and products than those concerning the binary diffusivity of CO₂. The final model is least sensitive to reaction activation energies and the temperature exponent for the binary diffusivity. All parameters exhibit

comparable stabilities on either side of the final regressed value. Significant imbalance in stabilities would suggest that the tested solution is not at an optimum. The most significant differences are observed for the activation energies. It should be noted that the tight sensitivity and stability observed for the parameters concerning the binary diffusivity of CO₂ do not necessarily attribute accuracy to the parameters. The diffusion coefficient of CO₂ is never the dominant determinant of CO₂ absorption rate (Figure 4-5), and every other significant parameter determining the absorption rate of CO₂ is being adjusted.

Table 4-7: Stability analysis for regressed kinetic parameters and parameters defining the binary diffusivity of CO₂

Parameter	Equation Ref.	% Increase	% Decrease
$k_{f,PZ-PZCOO}$	4-23	3.8	3.7
$E_{A, PZ-PZCOO}$	4-23	11.2	13.7
$k_{f,PZ-MDEA}$	4-23	5.6	5.3
$E_{A, PZ-MDEA}$	4-23	12.8	14.7
D_o	4-6	2.7	2.7
α	4-6	1.5	1.5
β	4-6	12.0	12.2
$D_{CO_2-H_2O}$ Pre-Exponential	4-3	5.5	5.1
D_{CO_2-Am} Exponent	4-5	2.5	2.9

4.4.3 Generic Amines

The kinetics model predicts values of k_g' for generic mixtures of MDEA and PZ. Figure 4-10 compares Aspen Plus[®] predictions for k_g' , viscosity-normalized capacity, and the heat of CO₂ absorption at 40 °C for MDEA/PZ with 50 wt % total amine and variable PZ. The viscosity-normalized capacity is defined by Equation 3-27. The lean and rich loadings correspond to CO₂ equilibrium partial pressures of 500 and 5,000 Pa, respectively. The two vertical black lines are plotted at the PZ wt % corresponding to

7 m MDEA/2 m PZ and 5 m MDEA/5 m PZ, each of which is approximately 50 wt % amine. The k_g' is calculated at a loading corresponding to a CO_2 partial pressure of 1,500 Pa. The bulk partial pressure of CO_2 is 3,000 Pa, and the $(L/G)_{\text{mol}}$ is maintained near wetted wall column conditions (~ 35). Between the lean and rich ends of the wetted wall column simulation the equilibrium partial pressure did not change by more than 1% at any reported condition.

Both k_g' and capacity have a maximum between 7 m MDEA/2 m PZ and 5 m MDEA/5 m PZ. The maximum in viscosity-normalized capacity, discussed in Section 3.6.5, is due to competing effects of PZ concentration on standard solvent capacity and viscosity. As MDEA is replaced by PZ both the standard solvent capacity and viscosity increase monotonically. Because viscosity increases at a significantly greater rate than standard capacity, the viscosity-normalized capacity eventually decreases with increasing PZ concentration. The predicted k_g' curve in Figure 4-10 is also the result of competing effects of PZ concentration. The reaction at 40 °C between PZ and CO_2 is significantly faster than the reaction between MDEA and CO_2 , which accounts for the dramatic increase in k_g' at low PZ concentrations in Figure 4-10. At a CO_2 equilibrium partial pressure of 1,500 Pa the overall rate of CO_2 absorption is strongly influenced by the diffusion of reactants and products between the reaction film and the bulk liquid. Increasing viscosity will decrease diffusion coefficients and slow the absorption of CO_2 .

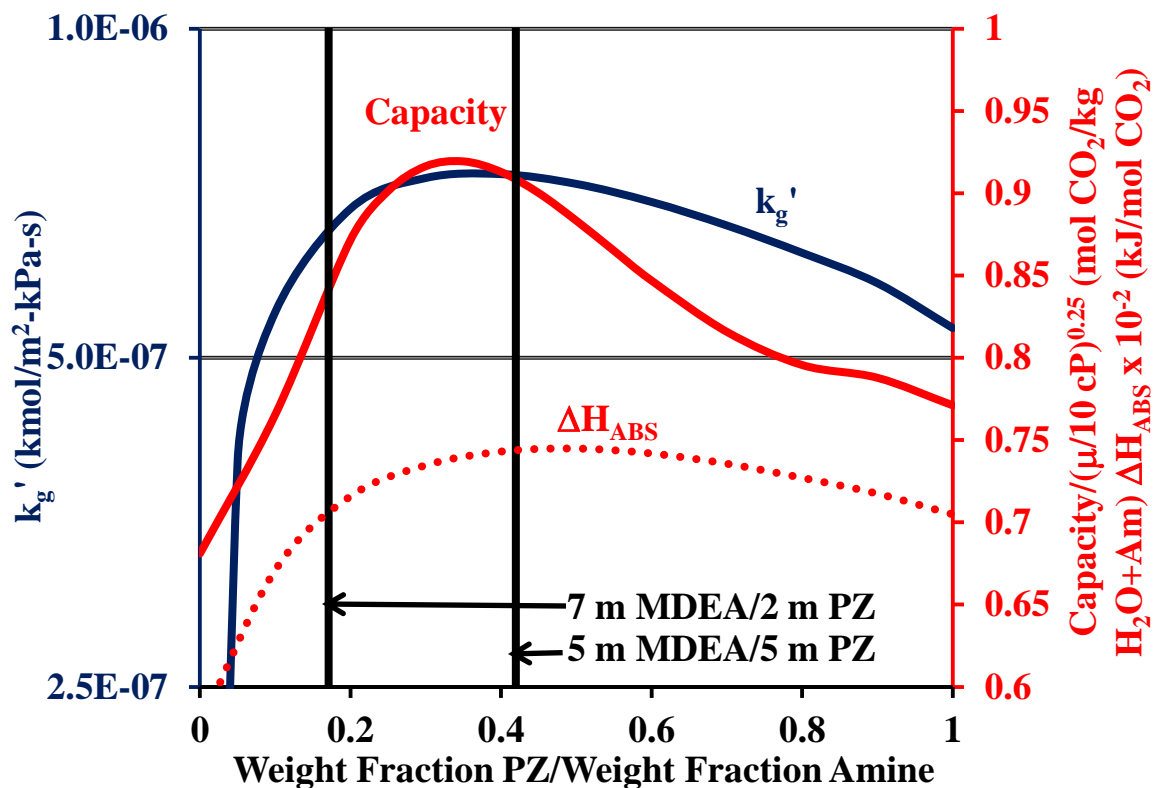


Figure 4-10: Aspen Plus® predictions for k_g' (blue), viscosity normalized capacity (red solid line) and heat of CO_2 absorption (red dotted line) at 40°C for MDEA/PZ with 50 wt % amine

Table 4-8: Comparison between PZ and MDEA/PZ on the basis of heat of absorption, CO_2 absorption rate, and capacity

Amine	$\Delta H_{\text{ABS}}@40^\circ\text{C}$ (kJ/mol CO_2)	$k_g'@1,500\text{ Pa}$ $\times 10^7$ ($\text{kmol}/\text{m}^2\text{-kPa}\cdot\text{s}$)	Viscosity-Normalized Capacity (mol $\text{CO}_2/\text{kg H}_2\text{O+Am}$)
7 m MDEA/2 m PZ	70.7	6.49	0.813
5 m MDEA/5 m PZ	74.5	7.21	0.904
12 m PZ	70.4	5.12	0.767
8 m PZ	70.5	7.51	0.787
5 m PZ	69.6	9.10	0.738
5.9 m MDEA/3.5 m PZ	73.5	7.29	0.916
4.7 m MDEA/2.8 m PZ	72.3	8.10	0.937
3.54 m MDEA/2.1 m PZ	70.8	8.68	0.708
7.7 m MDEA/1.1 m PZ	66.7	5.34	0.754

Table 4-8 compares several concentrations of PZ and MDEA/PZ on the basis of heat of absorption, CO₂ absorption rate, and viscosity-normalized capacity. 5.9 m MDEA/3.5 m PZ corresponds to the optimum MDEA/PZ blend predicted in Figure 4-10. 4.7 m MDEA/2.8 m PZ is the optimum MDEA to PZ ratio but in a 40 wt % amine solution (compare to 8 m PZ). 3.54 m MDEA/2.1 m PZ is the optimum MDEA to PZ ratio but in a 30 wt % amine solution (compare to 5 m PZ). 7.7 m MDEA/1.1 m PZ is the blend studied by Bishnoi (2000).

Decreasing the weight fraction of amine from 50 wt % to 30 wt % improves CO₂ absorption rate, decreases heat of absorption, and goes through a maximum viscosity-normalized capacity for both PZ and MDEA/PZ in the optimum ratio. Figure 4-11 compares the heat of absorption, k_g' , and viscosity-normalized capacity as a function of weight fraction of amine for MDEA/PZ in the optimum ratio. The capacity is calculated between loadings corresponding to equilibrium CO₂ partial pressures of 500 and 5,000 Pa, and the heat of absorption and k_g' are calculated at a loading corresponding to an equilibrium CO₂ partial pressure of 1,500 Pa. The maximum viscosity-normalized capacity is at an amine weight fraction of 35 wt %, and the maximum k_g' is at an amine weight fraction of 25 wt %.

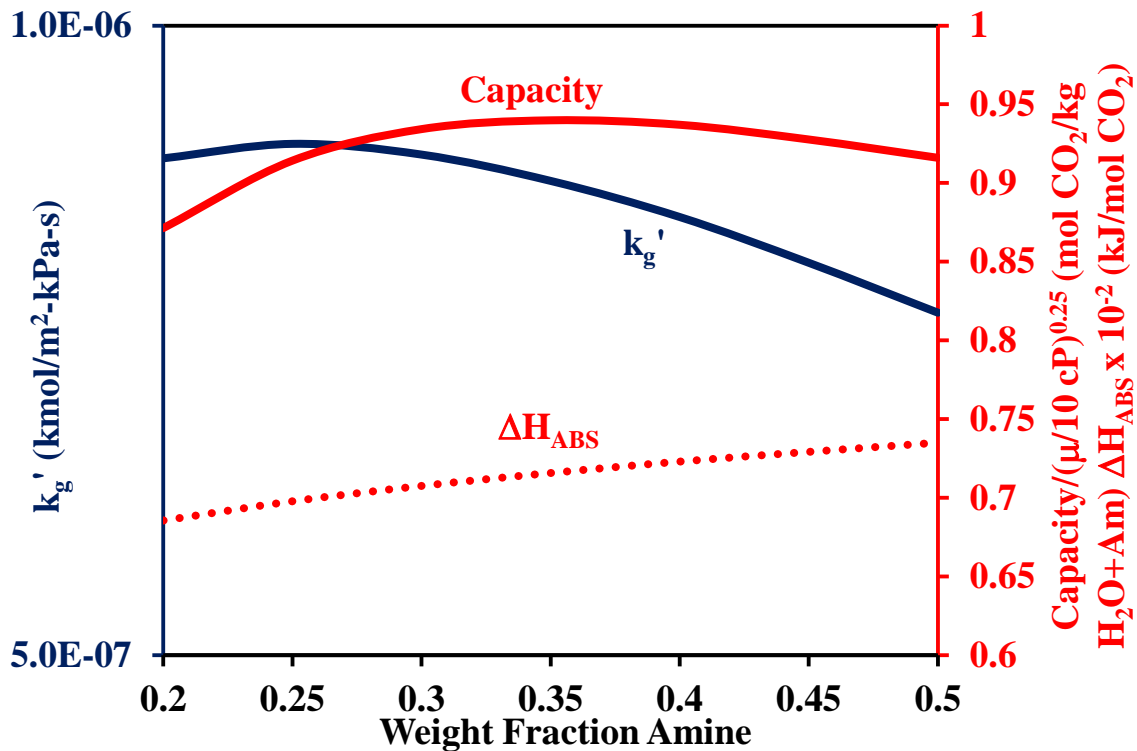


Figure 4-11: Aspen Plus[®] predictions for k_g' (blue), viscosity-normalized capacity (red solid line) and heat of CO₂ absorption (red dotted line) at 40 °C for MDEA/PZ in the ratio of 35 wt % to 15 wt %.

4.4.4 Rate-Based Stripper Modeling

Rate-based absorber modeling is discussed in Chapter 5. Previous stripper model studies (Van Wagener, 2011; Oyenekan, 2007) assumed desorption of CO₂ not to be limited by the rate of reaction in the liquid boundary layer. The temperature of the stripper, which is typically between 120 °C and 150 °C, is high enough to drive all reactions to equilibrium. To test this assumption, a rate-based stripper with a 5 °C cold side approach on the main cross exchanger, a rich loading of 0.40 mol CO₂/mol alkalinity, and a lean loading of 0.31 mol CO₂/mol alkalinity was simulated using 8 m PZ. The lean loading of 0.31 mol CO₂/mol alkalinity was chosen because it results in a minimum equivalent work (W_{eq}) at 150 °C with a 0.40 mol CO₂/mol alkalinity rich

solution. All columns were designed with 0.9 m of Mellapak 250X and a column diameter of 2 m. Mass transfer coefficients were calculated by Aspen Plus[®] using the methods of Bravo et al. (1985) at the conditions of the stage directly above the reboiler. The gas side mass transfer coefficient, k_g , is taken directly from Aspen Plus[®]. The liquid side resistance due to chemical reaction, k_g'' , is calculated using Aspen Plus[®] predictions and Equation 4-14. The liquid side resistance due to diffusion of reactants and products (k_L/m) is calculated indirectly by subtracting k_g and k_g'' from the overall mass transfer coefficient, K_g . Figure 4-12 compares the contributions of each resistance to the overall mass transfer coefficient as a function of reboiler temperature from 90-150 °C.

It should be noted that the forward and reverse reaction rate constants used to simulate a rate-based absorber had to be modified for stripper conditions. Equation 4-8 oversimplifies the temperature dependence of the equilibrium constant. Figure 4-13 compares the equilibrium constants for the carbamate- (Equation 3-3), dicarbamate- (Equation 3-4), and bicarbonate- (Equation 3-5) forming reactions calculated using Equation 3-2 and Equation 4-9. The reverse reaction rate constants used in the calculation are referenced to 40 °C, and their activation energies reference conditions at 60 °C. The two K_{EQ} values only agree between these temperatures. Extrapolating to stripper conditions gives inaccurate predictions of equilibrium constants, which compromises the accuracy of all thermodynamic predictions. To ensure thermodynamic consistency in the rate-based stripper simulations, the reverse reaction rate constants are recalculated between the reboiler temperature, T_{reb} , and 20 K less than T_{reb} .

The gas side resistance increases and the liquid side resistance due to reaction decreases as temperature increases, crossing around a temperature of 100 °C. The contribution of the liquid side resistance due to diffusion of reactants and products fluctuates from 30-40%. Figure 4-12 suggests that the contribution of k_g'' to K_g is less than 14% over operationally significant desorption temperatures, and the overall desorption of CO₂ is mostly gas side controlled. The diffusion of reactants and products is significant and should not be neglected during simulations. The most accurate and well-behaved method for simulating a rate-based stripper is to set the chemistry to equilibrium reactions but use RateSepTM to predict mass transfer coefficients.

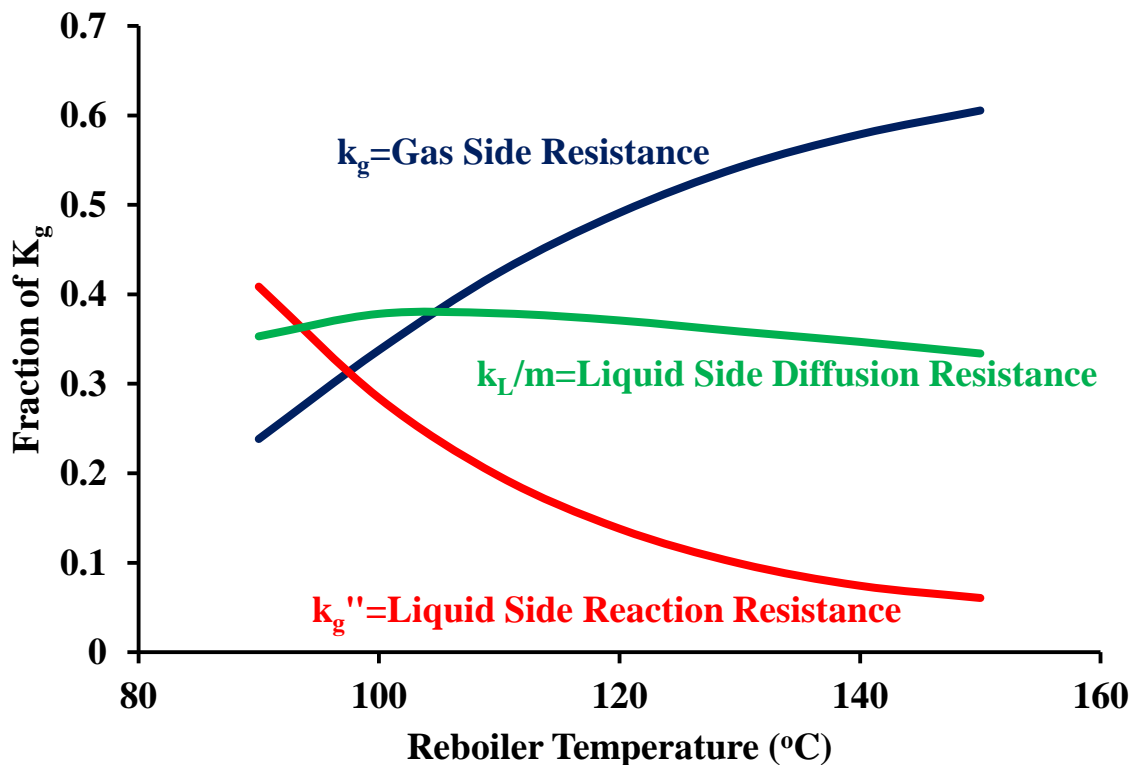


Figure 4-12: Fractional contribution of k_g , k_g'' , and k_L/m to the overall mass transfer resistance in a simple stripper with 8 m PZ

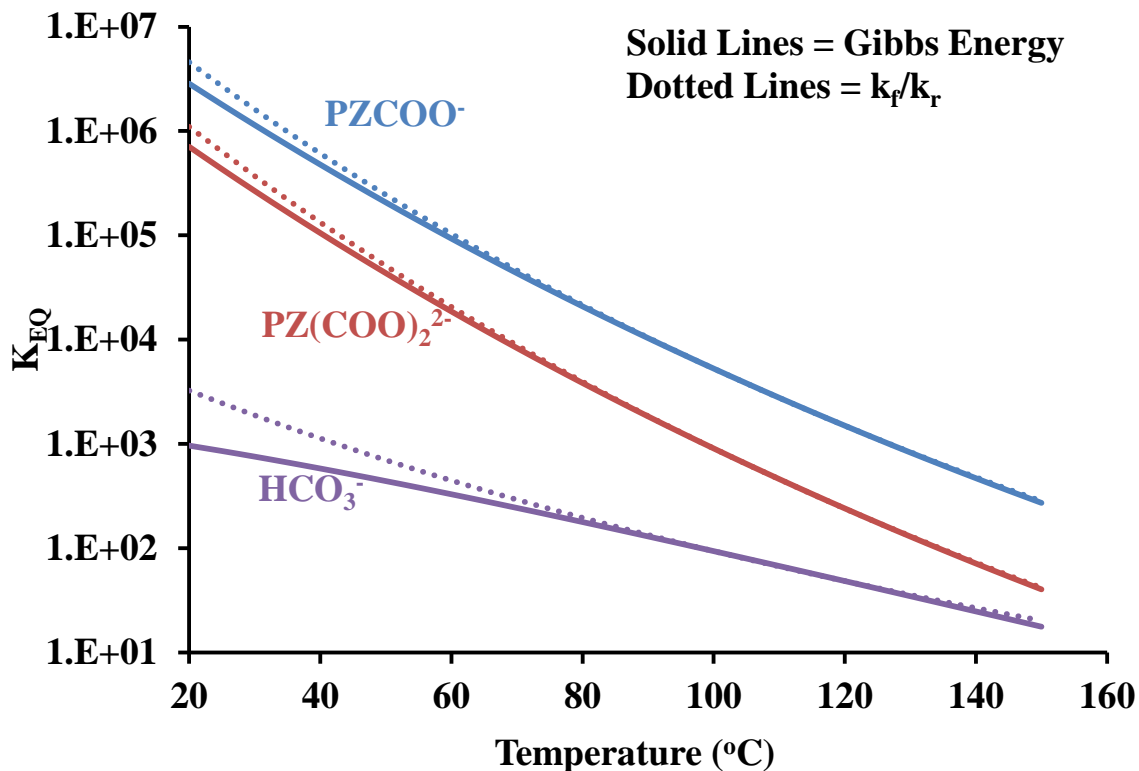


Figure 4-13: K_{EQ} calculated from Gibbs energy (solid lines) and k_f/k_r predictions (dotted lines) for $PZCOO^-$, $PZ(COO)_2^{2-}$, and HCO_3^- forming reactions

4.5 CONCLUSIONS

- At the nominal lean condition (i.e., 500 Pa equilibrium partial pressure of CO_2) the four solvents evaluated in order from fastest to slowest CO_2 absorption rate are 5 m PZ, 8 m PZ, 5 m MDEA/5 m PZ, and 7 m MDEA/2 m PZ. At the nominal rich condition (i.e. 5,000 Pa equilibrium partial pressure of CO_2) 5 m PZ still has the fastest CO_2 absorption rate, but the other three solvents have converged to a similar CO_2 absorption rate that is 30% less than that of 5 m PZ.
- The optimum viscosity-normalized capacity and k_g' are achieved with 15 wt % PZ/ 35 wt % MDEA (5.4 mol % PZ/ 9.1 mol % MDEA).

- The regressed temperature dependence of the binary diffusivity of reactants and products ($T^{1.06}$) is comparable to Wilke-Chang predictions (T^1). The regressed viscosity dependence ($\mu^{-1.45}$) is greater than that predicted by Wilke-Chang (μ^{-1}).
- For all solvents at low loadings and temperatures the absorption rate of CO_2 is limited by reaction kinetics; at high loadings and temperatures the diffusion of reactants and products is limiting.
- The CO_2 absorption rates of 8 m PZ, 5 m PZ, 7 m MDEA/2 m PZ, and 5 m MDEA/5 m PZ can be accurately predicted in Aspen Plus[®] over operationally significant temperature and loading ranges using a single set of reaction rate constants and binary diffusivities.
- At operationally significant loadings and temperatures, PZCOO^- is a significant catalyst for the formation of PZCOO^- in both concentrated PZ and MDEA/PZ.
- Reaction rates have a negligible effect on CO_2 desorption rate at stripper conditions, but the diffusion of reactants and products accounts for 30-40% of the overall mass transfer coefficient. Rate-based strippers should be modeled with equilibrium reactions and use RateSep[™] to predict mass transfer coefficients.
- Reverse reaction rate constants must be adjusted at high temperatures to guarantee that thermodynamics and kinetics generate consistent equilibrium constant predictions.

Chapter 5: Process Modeling

5.1 INTRODUCTION

This work integrates designs of the absorber by Plaza (2011) and the stripper by Van Wagener (2011) to innovate the entire absorption/stripping process. Much of process optimization concerns the tradeoff between capital expenses (CAPEX) and operating expenses (OPEX). Absorber optimization has traditionally concerned the tradeoff between packing area (CAPEX) and capacity (OPEX), and stripper optimization has concerned the tradeoff between process complexity (CAPEX) and equivalent work (OPEX). Ultimately the cost of the entire process must be quantified, and this requires combining the costs of the absorption and stripping systems.

This study also continues innovating novel process configurations for 8 m piperazine (PZ), and it introduces configurations targeting 7 m methyldiethanolamine (MDEA)/2 m PZ and 5 m MDEA/5 m PZ. The advanced flash stripper is presented as an alternative to the simple stripper. It bypasses cold and warm rich solvent to recover steam exiting with the product gas. Multiple intercooling configurations, variable absorption temperature, and variable CO₂ removal are considered for absorber configurations. Each modeled combination of absorber configuration, absorber temperature, CO₂ removal, and amine is evaluated with both the simple stripper and the advanced flash stripper.

5.2 LITERATURE REVIEW

Recent studies on absorber modeling have focused on the development and validation of rate-based simulations of pilot plant campaigns (Dugas, 2008; Liu, 2006;

Plaza, 2008). At absorber conditions it cannot be assumed that reactions reach equilibrium. The rate at which the system approaches equilibrium is affected by several parameters including CO₂ loading, temperature, vapor and liquid diffusivities, vapor and liquid concentration profiles, and heats of reaction. Once completed, the rate-based Aspen Plus[®] model will be used to determine the performance of several absorber configurations. Intercooling has already been shown to improve solvent capacity for MEA, AMP, and PZ-promoted potassium carbonate (Plaza, 2009; Sipocz, 2011; Tobiesen, 2007). Because less amine is needed to capture the same amount of CO₂, less amine must be pumped, heated, and cooled, thus reducing the equivalent work. Another process condition that will be evaluated is absorber temperature. All year in colder climates (e.g. Canada, Scandinavia, etc.) and seasonally in temperate climates colder heat sinks are available for power plants. Lowering the absorber temperature has the potential to improve process efficiency by increasing both the capacity and the partial pressure of CO₂ being fed into the compressor.

Previous work on advanced stripper configurations (Leites et al., 2003; Oyenekan, 2007; Van Wagener, 2011) has focused on one tradeoff: improving process reversibility (operating cost) in exchange for process complexity (capital cost). By operating several columns and vessels at several temperatures and pressures, the desorption of CO₂ can be accomplished with much smaller driving forces, thus improving process reversibility. Van Wagener (2011) simulated several process configurations for MEA and PZ including multi-stage flash, interheated stripper, and cold-rich bypass. Relative to the simple stripper, each of these configurations applies heat and/or strips CO₂ in more steps using

smaller heat and material driving forces. The relative advantages of these configurations varied from one amine to another. This study will both expand the set of amines tested in these advanced configurations and develop novel multi-temperature/multi-pressure configurations that improve process reversibility.

5.3 METHODOLOGY

5.3.1 Aspen Plus[®] Thermodynamic and Kinetic Framework

A detailed description of the development and capabilities of the Independence model is provided in Chapters 3 and 4. Improvements in model predictions over wider temperature and loading ranges allow for the development and optimization of novel absorber configurations. Lower absorber temperatures (i.e. $< 40\text{ }^{\circ}\text{C}$), higher rates of CO_2 capture (i.e. $> 90\%$), and a variable CO_2 feed concentration can all be studied using a single rate-based model. Figure 5-1 depicts the base case process cycle for 90% CO_2 capture from the flue gas of a coal fired power plant (12% CO_2 feed) using 5 m MDEA/ 5 m PZ. Lean amine is fed to an absorber at $40\text{ }^{\circ}\text{C}$ at a CO_2 loading corresponding to an equilibrium CO_2 partial pressure of 0.5 Pa (1). The amine captures 90% of the CO_2 from a feed stream containing an initial CO_2 partial pressure of 12 kPa. Assuming a vapor to liquid CO_2 partial pressure gradient of 12 to 5 and an isothermal absorber, the rich amine exits the absorber with an equilibrium CO_2 partial pressure of 5.0 kPa at $40\text{ }^{\circ}\text{C}$ (2). The rich solution is heated to the desorption temperature (2 \rightarrow 3), and CO_2 is desorbed to generate the lean solution (3 \rightarrow 4). The solvent is cooled back to $40\text{ }^{\circ}\text{C}$ (4 \rightarrow 1), and the cycle repeats.

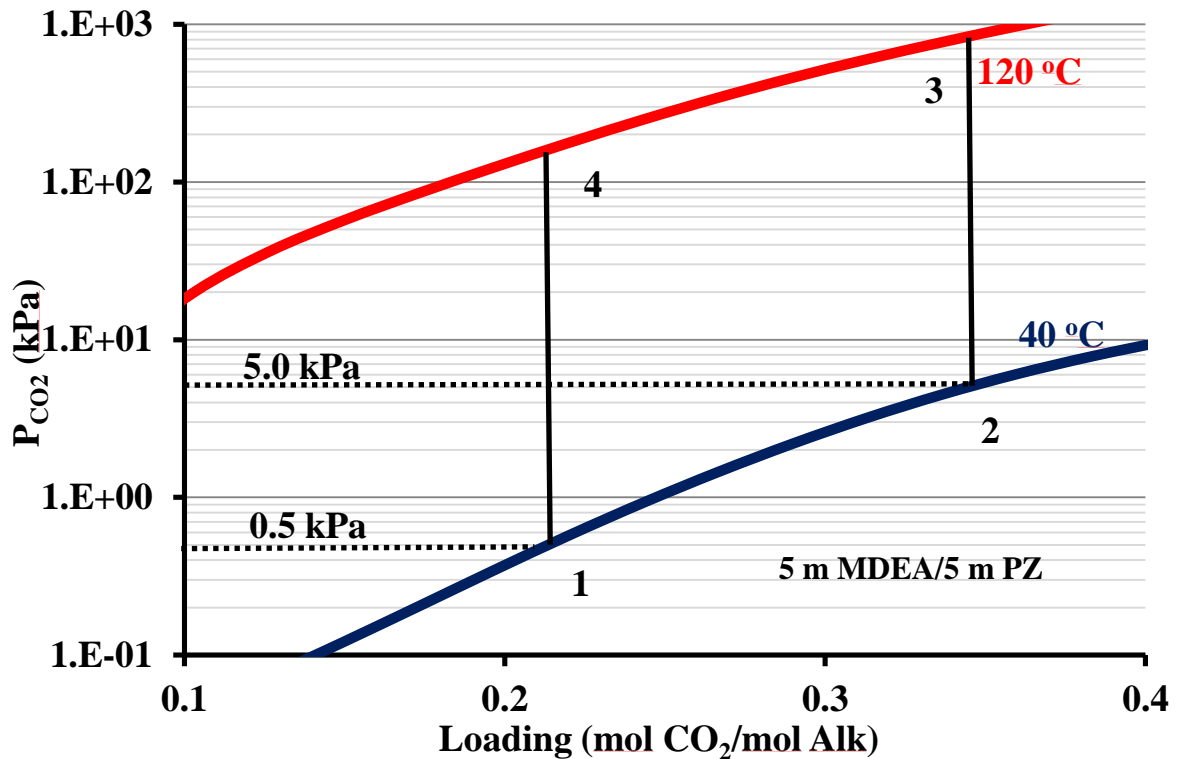


Figure 5-1: Base case process cycle for 90% CO₂ capture from coal-fired power plant using 5 m MDEA/5 m PZ

The high temperature limit is determined by thermal degradation, which is discussed in detail for several relevant amines and amine blends by Freeman (2010). The low temperature limit is constrained by cooling water availability. Plant sites farther from the equator (ex: Scandinavia, Canada, etc.) could cool the absorber to 20 °C, which has the potential to increase solvent capacity and regeneration pressure. Both of these improvements may be attributed to the effect depicted in Figure 5-2. Assuming that the operational loading range always corresponds to equilibrium partial pressures of 0.5 and 5.0 kPa at the lean and rich ends, respectively, decreasing the absorber temperature from 40 °C to 20 °C both increases the capacity of 5 m MDEA/5 m PZ from 0.98 mol CO₂/ kg

H₂O + amine to 1.30 mol CO₂/kg H₂O + amine and increases the partial pressure of CO₂ at 120 °C from 130 kPa to 500 kPa at the lean loading.

Both of these benefits may be attributed to the upward shift in the operational loading range. The effect on partial pressure of CO₂ is trivial; the effect on capacity is a little more complex. PZ is a much stronger base than MDEA. When the first molecule of CO₂ is absorbed by unloaded MDEA/PZ, PZ is much more likely than MDEA to catalyze the reaction. Therefore, low loading amine properties (e.g. capacity, CO₂ absorption rate, heat of absorption) are dictated by PZ. Shifting to a higher operational loading range implies shifting from a PZ-dominated system towards a MDEA-dominated system. Because MDEA exhibits a greater capacity than PZ, lowering the temperature of activated MDEA solvents has the potential to increase capacity.

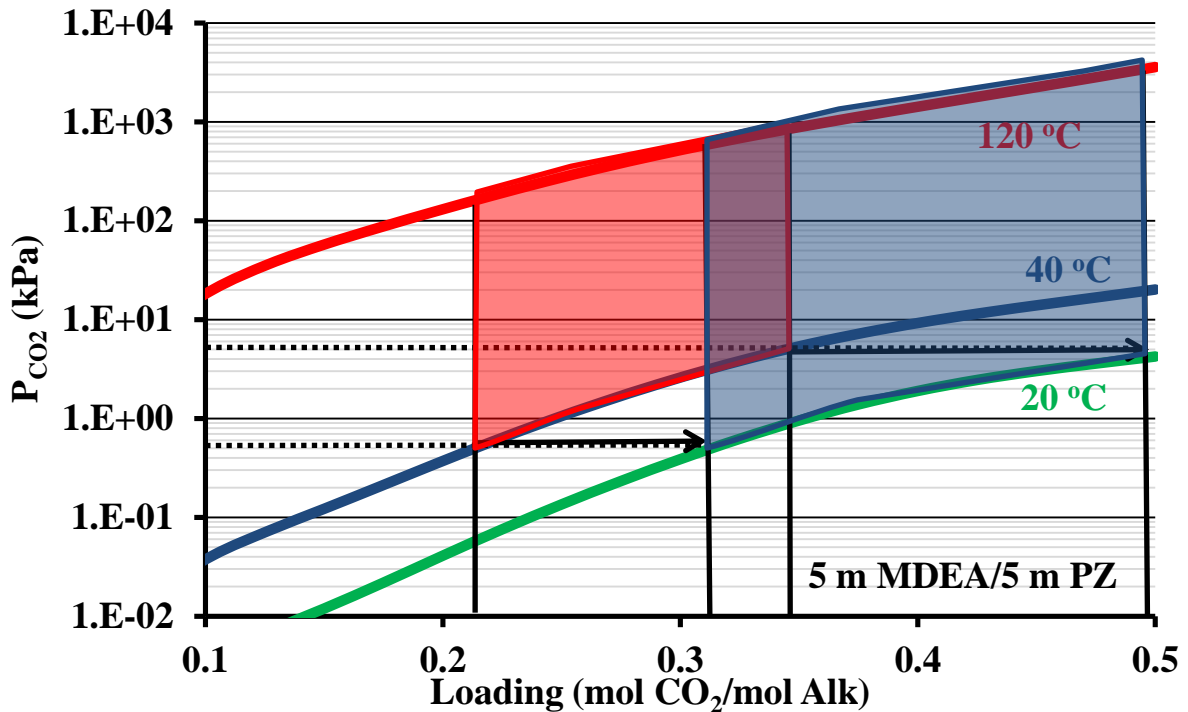


Figure 5-2: Process cycles for 90% CO₂ capture from coal-fired power plant using 5 m MDEA/5 m PZ assuming 40 °C (red) and 20 °C (blue) absorber

As Figure 5-2 suggests, a wider range of conditions must be regressed to model the effect of absorber temperature on process performance. This range continues to grow if higher fraction of capture is tested, which will decrease the equilibrium CO₂ partial pressure on the lean end. Figure 5-3 compares the operating ranges for 90% and 99% CO₂ capture from a coal-fired power plant using 5 m MDEA/5 m and assuming an equilibrium CO₂ partial pressure gradient of 12 to 5.

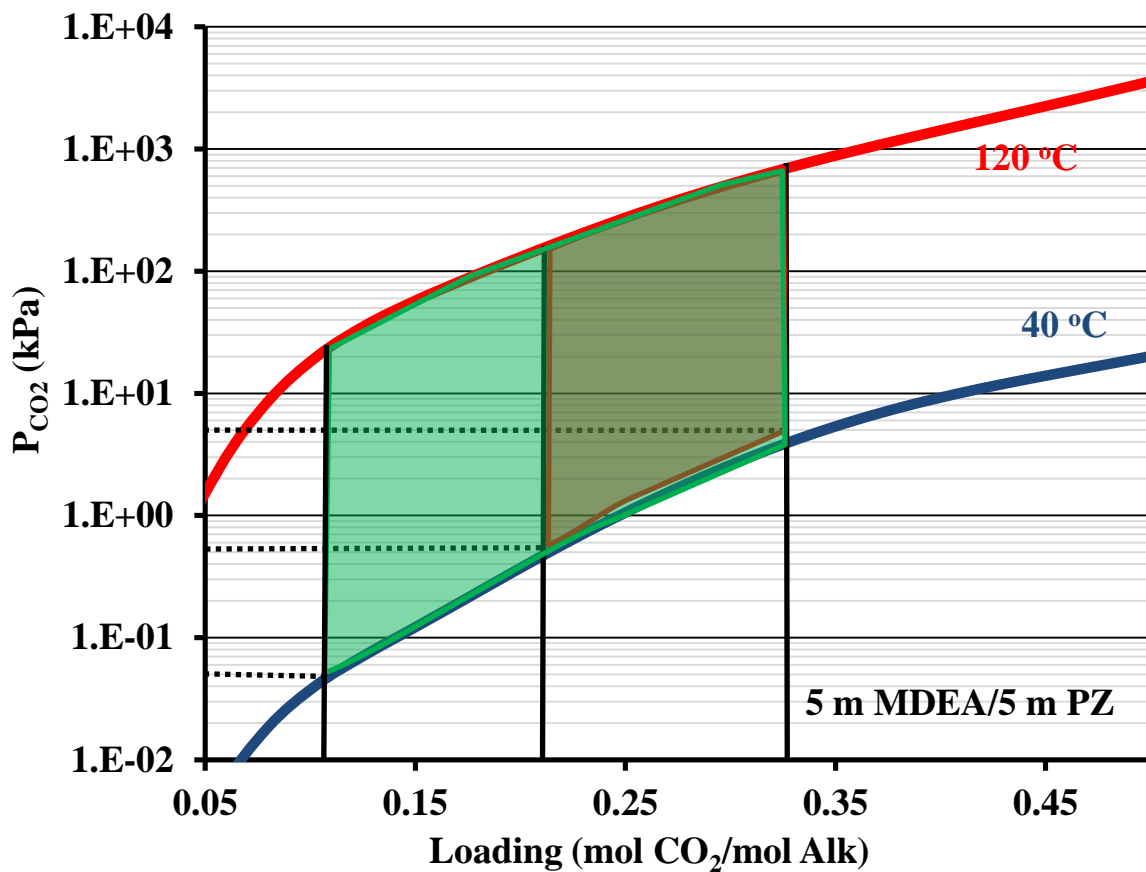


Figure 5-3: Process cycles for 90% (red) and 99% (green) CO₂ capture from coal-fired power plant using 5 m MDEA/5 m PZ assuming 40 °C absorber

PZ operating conditions will not always fall along the boundaries of Figures 5-1, 5-2, and 5-3, but under these temperature and pressure constraints all operating

conditions will fall within them. With the exception of the thermal degradation limit, each condition can be adjusted to optimize unit operation. The thermodynamic and kinetic framework was developed with this in mind. Rather than constraining the operating ranges to the cycle in Figure 5-1, the model was designed to include wider ranges of temperature, loading, and amine concentration. Table 5-1 summarizes the CO₂ absorption rate data regressed in the Independence model.

Table 5-1: Operating conditions regressed into Independence model kinetics

Amine	Temperature (°C)	Loading (P_{CO2} @ 40°C in kPa)
8 m PZ	40-100	0.06-7.4
5 m PZ	40-80	0.06-4.1
7 m MDEA/2 m PZ	40-100	0.19-4.3
5 m MDEA/5 m PZ	10-100	0.23-6.0

Above 100 °C it is assumed that all reactions go to equilibrium. For all amines the equilibrium conditions up to 160 °C are also regressed, but the temperatures listed in Table 5-1 are the most relevant to absorber conditions. It should be noted that even though CO₂ absorption data for 7 m MDEA/2 m PZ was not available below 40 °C these conditions are tested extensively in this work. Model predictions for a low temperature absorber using 7 m MDEA/2 m PZ constitute extrapolations of the low temperature 5 m MDEA/5 m PZ data. Low temperature 8 m PZ and 5 m PZ data was not collected due to solubility limitations.

5.3.2 Absorber Configurations

All configurations in this study are designed with structured packing and cylindrical shells. Because of degradation concerns, versatility, and technical and economic data availability, the packing for most sections is assumed to be Mellapak

250X made with 316 SS. The column diameter was adjusted to set a maximum flooding approach of 70%. For each case the feed liquid, feed vapor, and intercooling temperatures, when applicable, are assumed to be equal. Sensitivity to these conditions is not evaluated in this study, but they are addressed by other experimentalists (Tsai, 2010; Wang, 2014). The direct operating costs associated with the absorber are assumed to be negligible relative to the direct capital costs. Therefore, optimization of all configurations focuses on the minimization of packing area. Mass transfer coefficients and the effective packing area are calculated using correlations described by Hanley and Chen (2012).

5.3.2.1 Adiabatic Absorber

The simplest configuration counter-currently contacts solvent and CO₂ laden flue gas at atmospheric pressure. The exothermic heat of absorption increases the temperature of the liquid and vapor as the extent of reaction increases. Increasing the temperature of the solvent will decrease the CO₂ driving force and, thus, the CO₂ absorption rate. As the solvent approaches the bottom of the column the cold feed vapor and vaporization of water in the solvent cool the liquid, creating a temperature bulge in the center of the column. The heat generated by the absorption of CO₂ exits the column as sensible heat and steam in the vapor, and sensible heat in the liquid. The position of the temperature bulge is determined by the relative flow rates (L/G) and heat capacities of the liquid and vapor. As L/G increases the position of the temperature bulge migrates towards the bottom of the column and decreases in magnitude because more of the heat is being carried by the liquid, which has a relatively high heat capacity. Both of these trends are

illustrated in Figure 5-3, which reports the bulk liquid temperature profiles for adiabatic absorbers using 8 m PZ to capture 90% of the CO₂ from the flue gas of a coal-fired power plant. Because the absorber height was varied to maintain 90% CO₂ capture, the temperature is shown as a function of normalized position within the column.

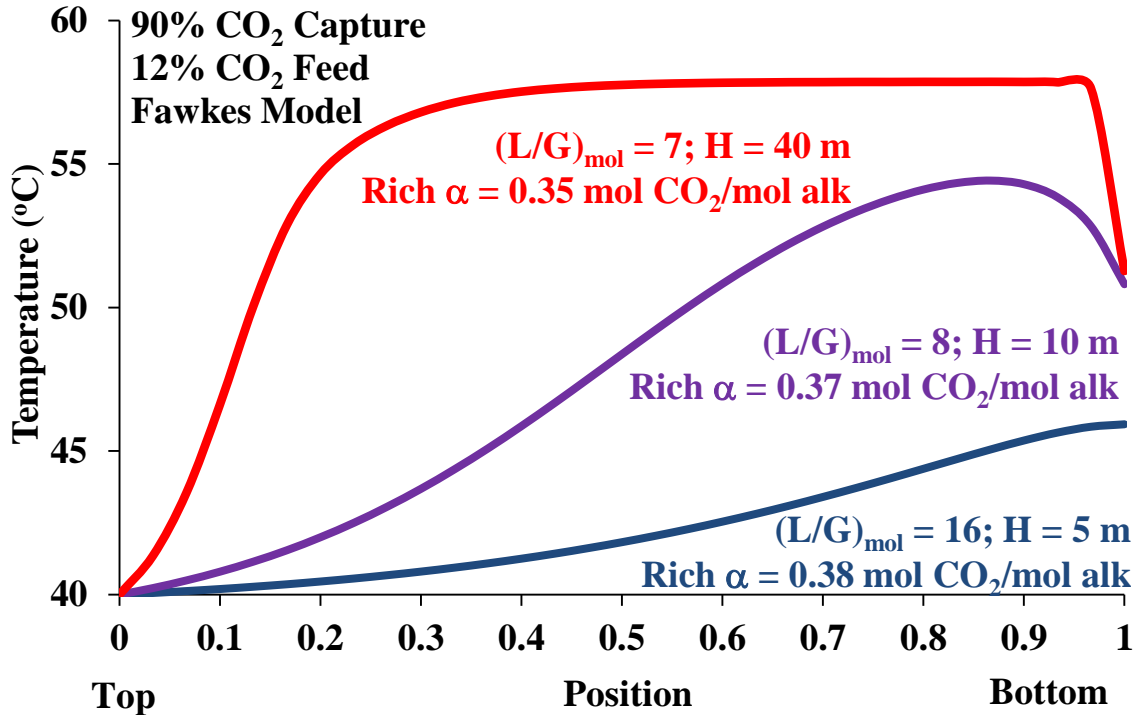


Figure 5-4: Bulk liquid temperature profile for adiabatic absorber using 8 m PZ with lean loading of 0.32 mol CO₂/mol alkalinity for (L/G)_{mol} = 16 (blue), (L/G)_{mol} = 8 (purple), and (L/G)_{mol} = 7 (red)

The temperature profile for the (L/G)_{mol} = 7 case is nearly constant across most of the profile because it has reached a mass transfer pinch. The rise in bulk liquid equilibrium CO₂ partial pressure eliminates CO₂ driving force and significantly reduces the average CO₂ flux.

5.3.2.2 In-and-Out Intercooling

Intercooling improves CO₂ driving forces in the column by removing heat that contributes to the mass transfer pinch at the temperature bulge. The simplest intercooling configuration is in-and-out intercooling, which removes the liquid from the middle of the column, cools it to the feed temperature, and feeds the liquid back into the column just below the point where the liquid was removed. If the lean loading and L/G are fixed, the only degree of freedom available for optimization is the location of the intercooling. Typically the optimum intercooling location coincides with the temperature bulge.

5.3.2.3 Pump-Around Intercooling

Pump-around intercooling removes semi-rich solvent from one point in the column, cools it to the feed temperature, and feeds the cooled solvent back at both a higher point in the column and just below the point that it was removed (Figure 5-4). Enough liquid is fed to the lower stage to avoid accumulation of solvent. This effectively splits the column into three sections: (1) a top section where lean solvent enters and scrubbed gas leaves, (2) a middle section containing 2–5 times more solvent than the top section, and (3) a bottom section containing the same amount of liquid as the top section from which the rich solution exits and the flue gas enters. A coarser packing must be used in the middle section to avoid excessive pressure drop from the higher liquid load. For this study Mellapak 125X was chosen for the middle section. Another degree of freedom with this configuration is the pump-around rate, defined as the $(L/G)_{\text{mol}}$ associated with the additional liquid in the middle section. Sachde (2012) examined the

technical and economic effects of varying the pump-around rate for coal-fired and natural gas applications, but this study fixes the pump-around rate to $(L/G)_{\text{mol}} = 5$.

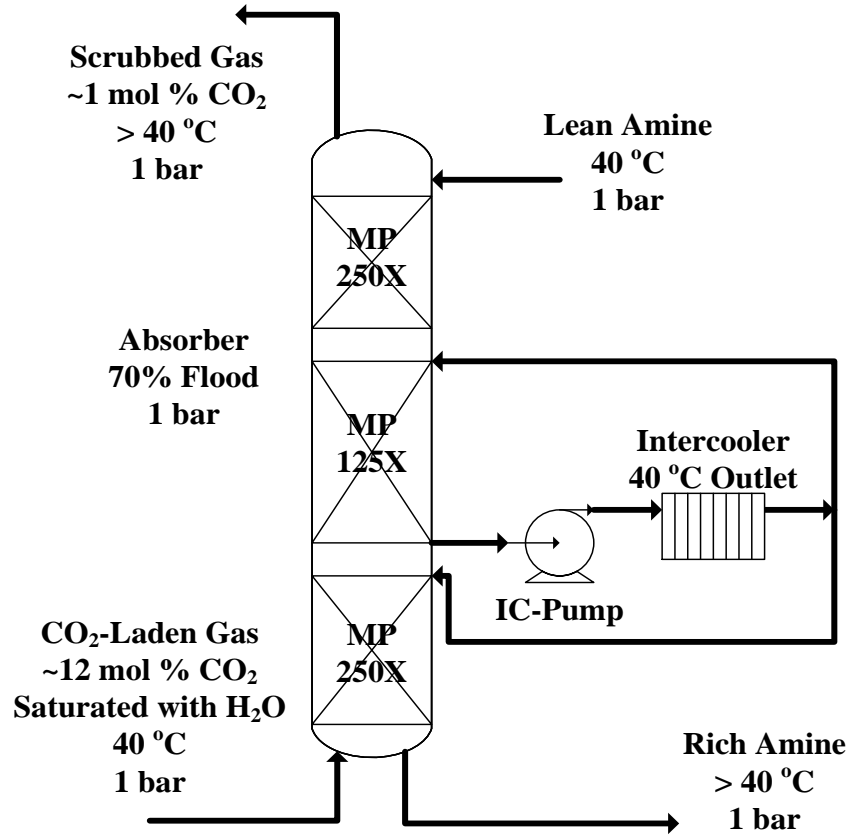


Figure 5-5: Process flow diagram for absorber with pump-around intercooling
5.3.3 Stripper Configurations

All stripper configurations in this study are a combination of flash tanks, packed columns, cross-exchangers, and reboilers/steam heaters. All pressurized flash tanks are cylindrical and made from 316 SS. For economic analyses they are sized on the basis of 50% capacity and a 5 min residence time to allow for nitrosamine degradation (Fine, 2013). Packed columns are designed with similar specifications to absorber columns: 316 SS shell, Mellapak 250X packing, and diameter adjusted to set a maximum flooding approach of 70%. All cross exchangers are plate-and-frame with 316 SS plates. If both

fluids in the cross exchanger are solvent, the exchanger is designed with a 5 K log mean temperature difference (LMTD). If one fluid is solvent and the other is vapor, the exchanger is designed with a 15 K LMTD. Optimization of the LMTD is not considered in this study. Reboilers and steam heaters all assume saturated steam with a 5 K LMTD.

Energy performance is always expressed as equivalent work, which corresponds to the electrical equivalent of the energy required to capture and compress CO₂ to 150 bar at 40 °C for geologic sequestration. Equation 5-1 calculates the equivalent work, W_{EQ} (kJ/mol CO₂) as a function of reboiler duty, Q_i, reboiler temperature, T_{reb}, pump work, W_{pump}, and compressor work, W_{comp}. The sink temperature, T_{sink}, is assumed to be 40 °C. Equations 5-2 and 5-3 calculate W_{comp} as a function of inlet pressure, P_{in}. Equation 5-1 assumes a steam turbine efficiency of 75%.

$$W_{eq} = \sum_{i=1}^{n_{reboilers}} 0.75Q_i \left(\frac{T_i + 5K - T_{sink}}{T_i + 5K} \right) + W_{pumps} + W_{comps} \quad \text{Equation 5-1}$$

$$W_{comps} (kJ/mol CO_2) = 4.572 \log \left(\frac{148}{P_{in} (atm)} \right) - 4.096 \quad P_{in} \leq 4.5 atm \quad \text{Equation 5-2}$$

$$W_{comps} (kJ/mol CO_2) = 4.023 \log \left(\frac{148}{P_{in} (atm)} \right) - 2.181 \quad P_{in} > 4.5 atm \quad \text{Equation 5-3}$$

Equations 5-2 and 5-3 were introduced in Van Wagener (2011) as smooth functions for calculating the equivalent work of CO₂ compression (72% polytropic efficiency, 40 °C intercooling at P_j+/P_{j-1} < 2, 150 bar final pressure). The rigorous calculation of compressor work is a stepwise function determined by available compressor trains and efficiencies, but its optimization is beyond the scope of this study.

5.3.3.1 Simple Stripper

Figure 5-5 shows the process flow diagram for the simple stripper.

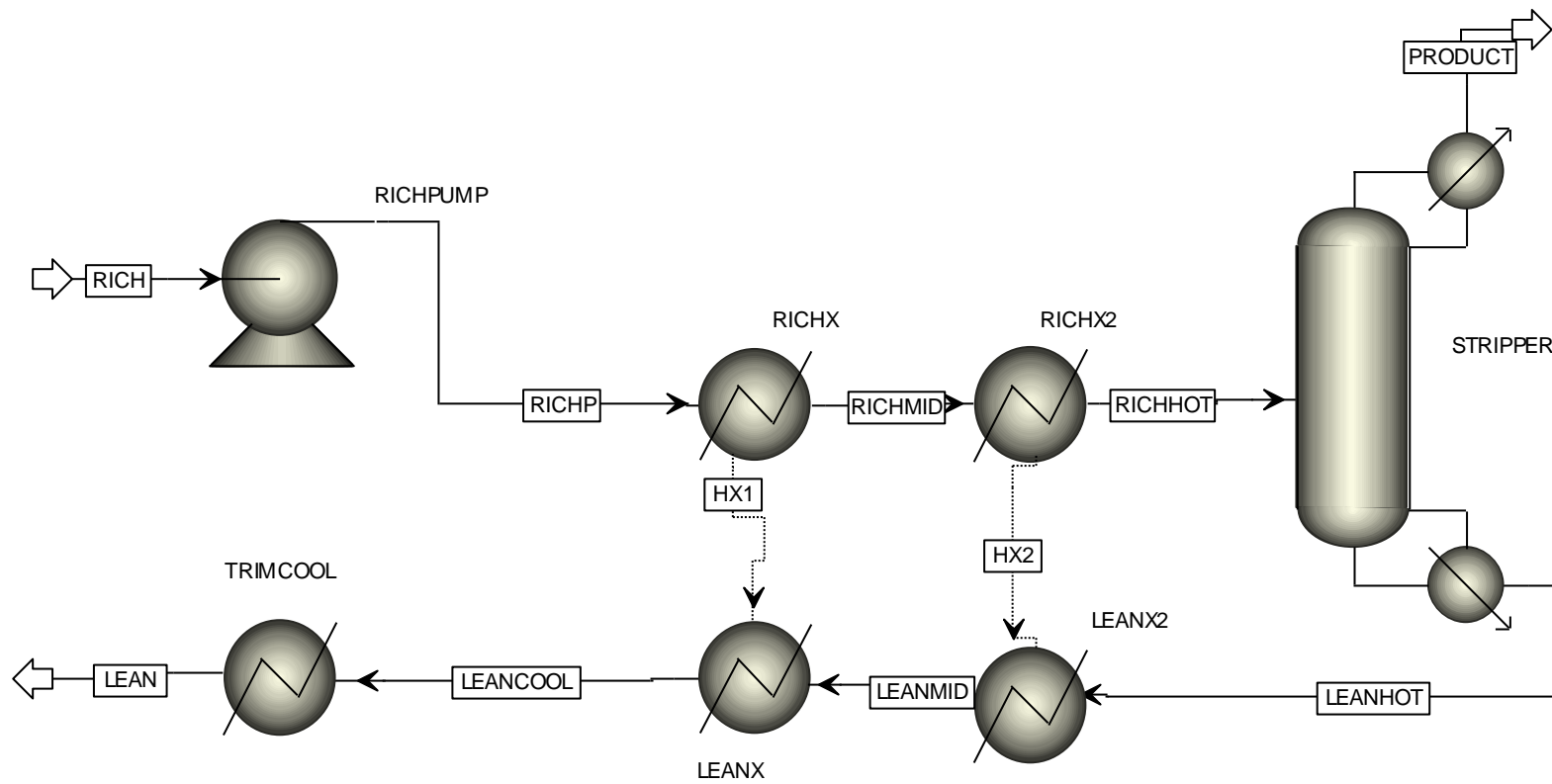


Figure 5-6: Process flow diagram for simple stripper

Rich amine from the absorber is pumped up to stripper pressure, counter-currently heated by hot lean amine in the main cross-exchanger, and fed to the top of the stripper column. Liquid falls through a 5 m packed section before collecting in a sump and heated in a reboiler to the regeneration temperature, which is 150 °C for PZ and 120 °C for MDEA/PZ. The hot vapor, which is primarily CO₂ and H₂O, travels up the stripper column and counter-currently contacts the semi-rich amine in the packing. The hot lean amine exits the reboiler and goes to the main cross exchanger where it heats the rich amine. A water-cooled trim cooler is used to get the lean amine down to absorber temperature before the cycle repeats.

The main cross exchanger is modeled as two sets of Heater blocks. The set connected by heat stream HX1 is specified to generate an outlet vapor fraction of 10⁻⁵ for the rich amine. HX2 is varied to give an overall LMTD of 5 K, as defined by Equation 5-4. Q is the heat duty of an exchanger, and the subscripts HX1 and HX2 refer to the two heat exchangers in series.

$$LMTD_{TOT} = \frac{Q_{HX1} + Q_{HX2}}{\frac{Q_{HX1}}{LMTD_{HX1}} + \frac{Q_{HX2}}{LMTD_{HX2}}} \quad \text{Equation 5-4}$$

Using an LMTD to size a cross exchanger assumes linear temperature profiles. Flashing in the cross exchanger generates two sets of linear temperature profiles. Figure 5-6 reports the temperature profiles in cross exchangers modeled as one (dotted lines) and two (solid lines) sets of Heater blocks. The position in the exchanger refers to the portion of the total heat duty that has been exchanged. After 85% of the heat has been exchanged

the temperature difference between the rich and lean streams begins to increase as more of the heat goes toward the latent heat associated with stripping the CO₂. Modeling the cross exchanger as a single set of Heater blocks distributes this divergence across the entire exchanger, thus requiring a tighter temperature difference at the cold end of the exchanger. This increases the amount of heat exchanged by 3% (1,185 MW_{th} vs. 1,150 MW_{th}) and decreases the W_{eq} by 1.8 kJ/mol CO₂.

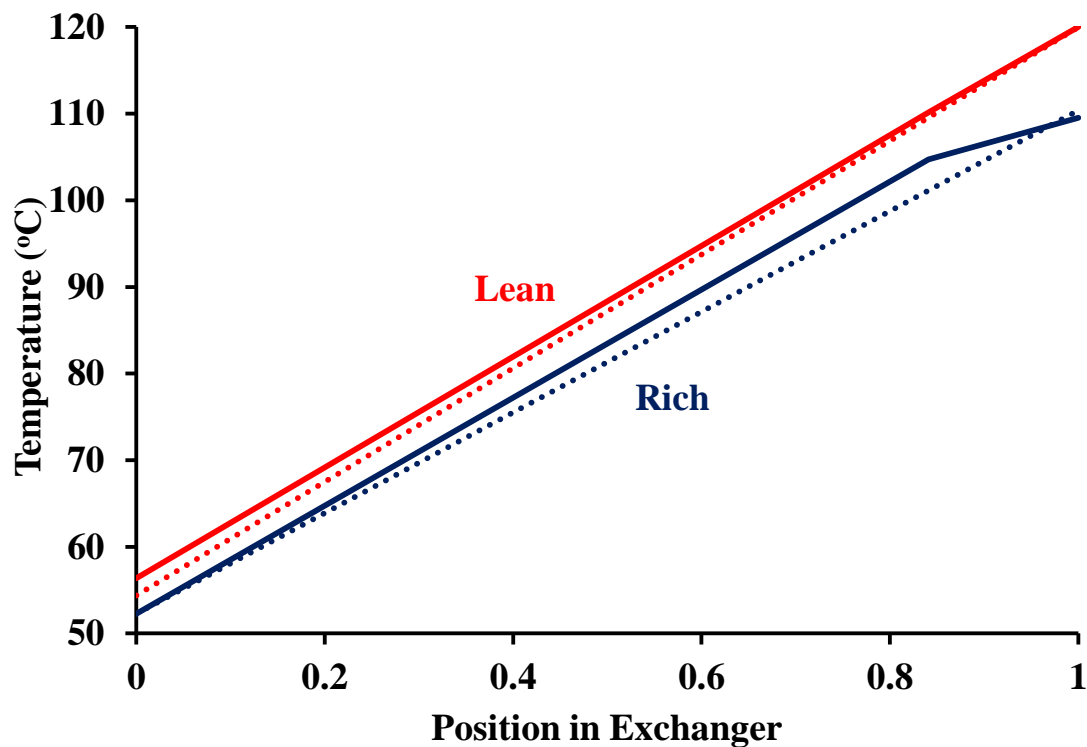


Figure 5-7: Temperature profiles for the main cross exchanger modeled as one (dotted lines) and two (solid lines) sets of Heater blocks for 7 m MDEA/2 m PZ with a lean loading of 0.13 mol CO₂/mol alkalinity and LMTD = 5 K.

5.3.3.2 Advanced Flash Stripper

Figure 5-6 shows the process flow diagram for the advanced flash stripper.

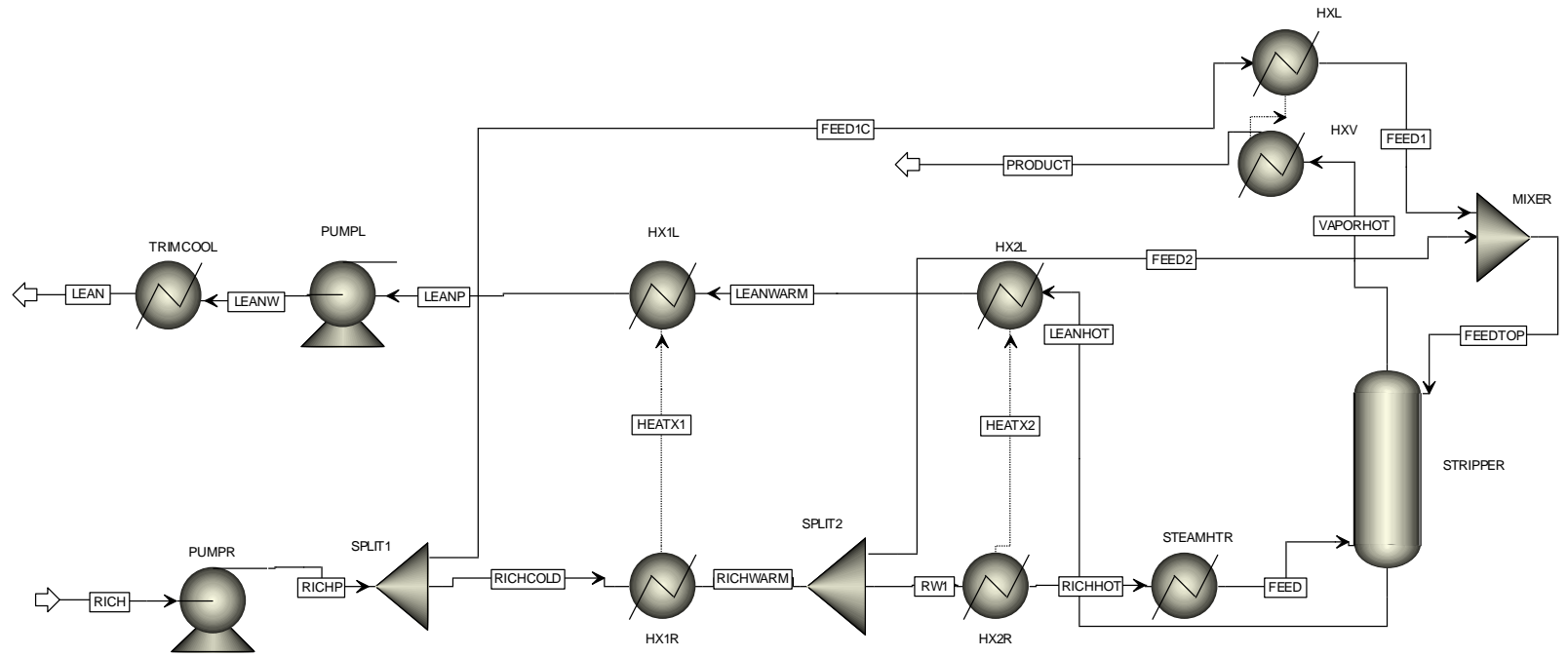


Figure 5-8: Process flow diagram for advanced flash stripper

The reboiler duty (1) reverses the reaction between CO₂ and amine, (2) supplies the sensible heat associated with the hot-side temperature approach on the main cross-exchanger, and (3) supplies the latent heat associated with the water vapor in the product stream. The advanced flash stripper directly addresses (2) and (3). The advanced flash stripper contains both a cold rich bypass (CRB) and warm rich bypass (WRB). A fraction of the cold rich solvent exiting the bottom of the absorber is heated by the product gas in a cross exchanger with a 15 K LMTD before being fed into the top of the stripper. The remaining rich solvent is heated to its bubble point by a warm solution from the bottom of the stripper in a cross exchanger. Another portion of the warm rich solvent is bypassed, mixed with the CRB stream, and fed directly into the top of the stripper. The remaining rich solution is heated first by the hot lean liquid in a cross exchanger and finally by a steam heater to the regeneration temperature and flashed into the bottom of the column. The two liquid-liquid cross exchangers are designed to have a combined 5 K LMTD, as defined by Equation 5-4. There are three variables that affect process performance, and subsequently, overall costs: (1) the amounts of solvent removed in the CRB and WRB, (2) the total height of packing in the stripper, and (3) the solvent lean loading. Rich solvents generated by the various absorber configurations (Section 5.3.2) are tested over a range of lean loading while adjusting the CRB and WRB to minimize W_{EQ} at a given lean loading. W_{EQ} exhibits a negligible sensitivity to packing height, which was fixed at 5 m of Mellapak 250X. This study uses the advanced flash stripper for process design, and the simple stripper is modeled for comparison.

5.3.4 L/L_{\min} Analysis

Assuming a constant CO_2 removal and lean loading, the liquid flow rate is a function of the packing area. As the packing area increases the liquid flow rate decreases until it reaches a minimum. As the packing area decreases the column approaches an isothermal condition with an infinite liquid flow rate. Between these extremes exists a case that balances the capital cost of packing area and the operating cost of circulating solvent. Ultimately a techno-economic analysis is needed to determine this point, but experience suggests that the optimum liquid flow rate is between 1.05 and 1.3 times the minimum liquid flow rate. Fixing the liquid flow rate as a percentage of the minimum liquid flow rate is equivalent to fixing the approach to mass transfer pinch.

Because the minimum liquid flow rate is a function of the lean loading, the L/G in this study is a function of lean loading. Figure 5-5 shows the minimum $(L/G)_{\text{mol}}$ as a function of lean loading for 7 m MDEA/2 m PZ for 90% CO_2 removal from coal-fired power plant flue gas. All amines and absorber configurations are constrained on the rich end by the inlet partial pressure of CO_2 . At the minimum liquid flow rate solvent pinches on the rich end for most lean loadings. Therefore, as the lean loading increases the solvent capacity decreases and the minimum amount of solvent required to capture a given amount of CO_2 increases.

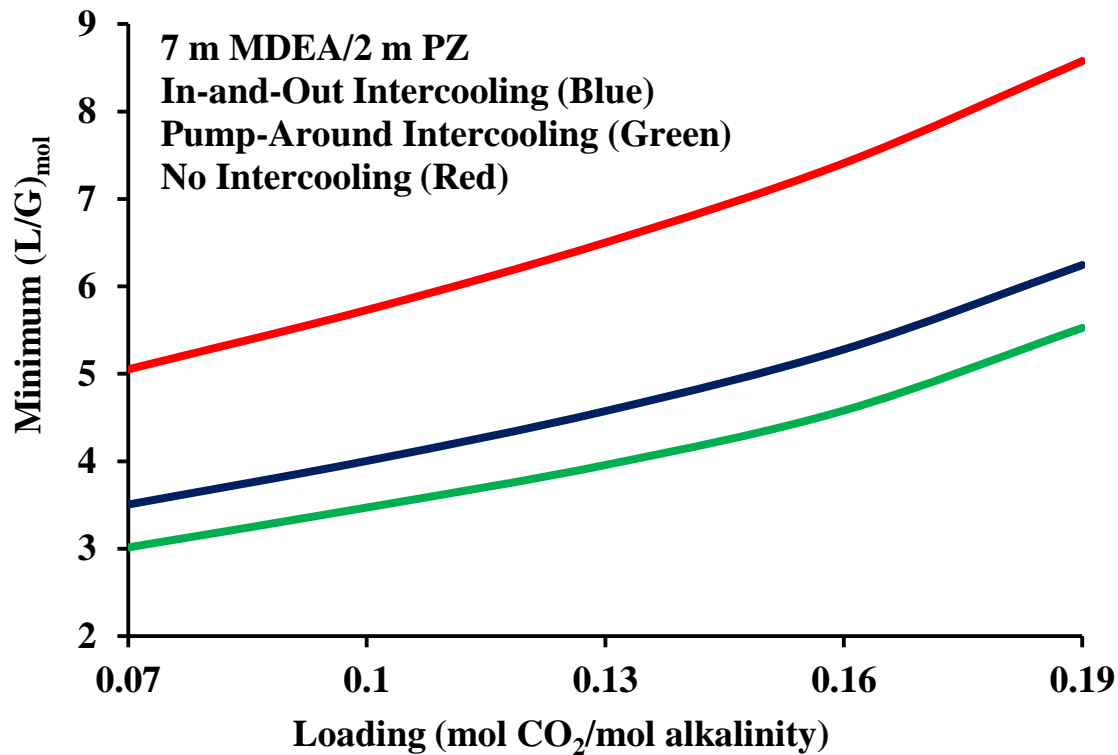


Figure 5-9: Minimum (L/G)_{mol} for an absorber with in-and-out intercooling (blue) and pump-around intercooling (green) and without intercooling (red) at 40 °C for 7 m MDEA/2 m PZ at 90% CO₂ capture from coal-fired power plant flue gas.

The minimum L/G is also a function of the absorber configuration. Figure 5-7 suggests that the minimum L/G with the pump-around intercooling configuration is about 13% less than the minimum L/G for in-and-out intercooling. Removing heat via intercooling will reduce the temperature of the rich liquid exiting the column and, thus, increase the rich loading at mass transfer pinch. This effectively increases the capacity of the solvent and decreases the minimum L/G. It also complicates the determination of the minimum L/G for intercooled configurations. If the relative heights of the sections in an intercooled absorber are kept equal and the overall height of the column is increased, the

amount of heat removed by intercooling increases and the temperature of the rich solution decreases. The rigorous approach would be to optimize the location of the intercooling (i.e. maximize the solvent capacity) for a given total column height, and increase the total column height until the L/G has reached a minimum. Given the number of amines, absorber configurations, and process conditions tested in this study, a less rigorous definition is used for the minimum L/G. The minimum L/G for 90% removal cases corresponds to the liquid flow rate needed to capture the specified amount of CO₂ from an absorber that has a total height of 100 m. An absorber height of 200 m is used for 99% removal cases.

5.4 RESULTS

5.4.1 L/L_{min}

Fixing the liquid flow rate relative to the minimum liquid flow rate is analogous to fixing the solvent capacity relative to the maximum solvent capacity for a given absorber configuration. Figure 5-8 shows solvent capacity in mol CO₂/kg H₂O + amine as a function of lean loading for 8 m PZ at 40 °C in an adiabatic absorber and liquid flow rates corresponding 1.0, 1.1, 1.2, and 1.3 times the minimum liquid flow rate. When L/L_{min} = 1.0 the column contains a mass transfer pinch, which significantly reduces the average CO₂ flux in the column. As the liquid flow rate increases the effects of the mass transfer pinch are diluted. Figure 5-9 shows the mass transfer area normalized to CO₂ capture rate and equivalent work as a function of lean loading using 8 m PZ in an adiabatic absorber and liquid flow rates corresponding to 1.1, 1.2, and 1.3 times the minimum liquid flow rate.

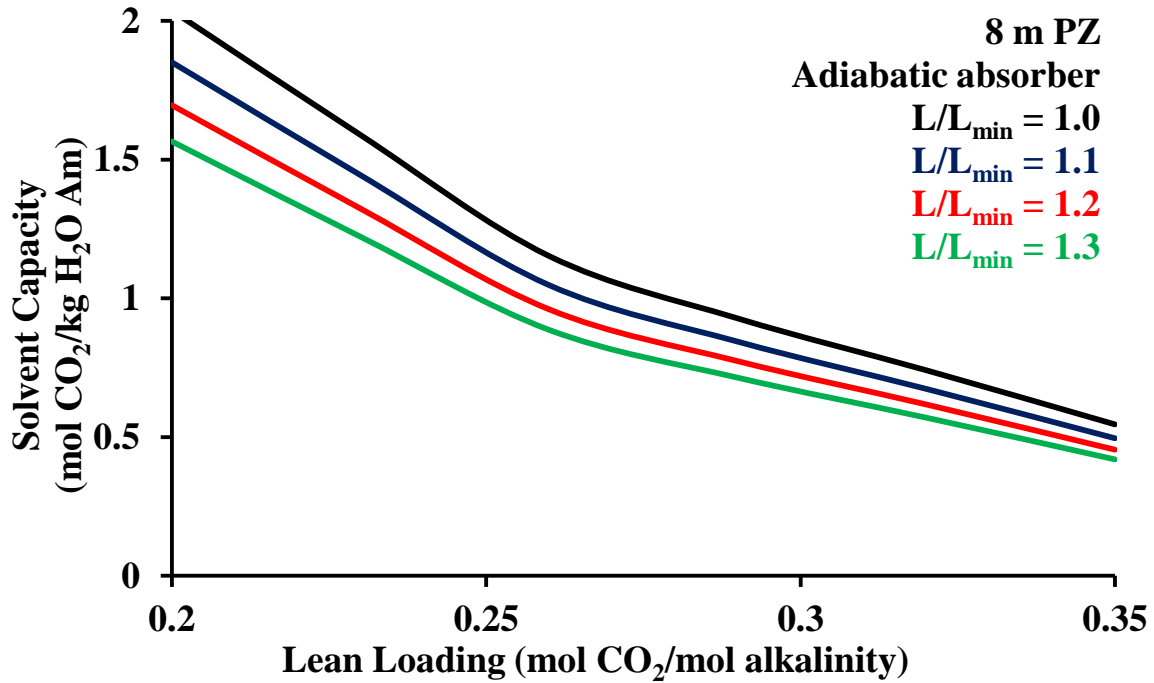


Figure 5-10: Capacity for 8 m PZ in an adiabatic absorber and liquid flow rates corresponding to 1.0, 1.1, 1.2, and 1.3 times the minimum.

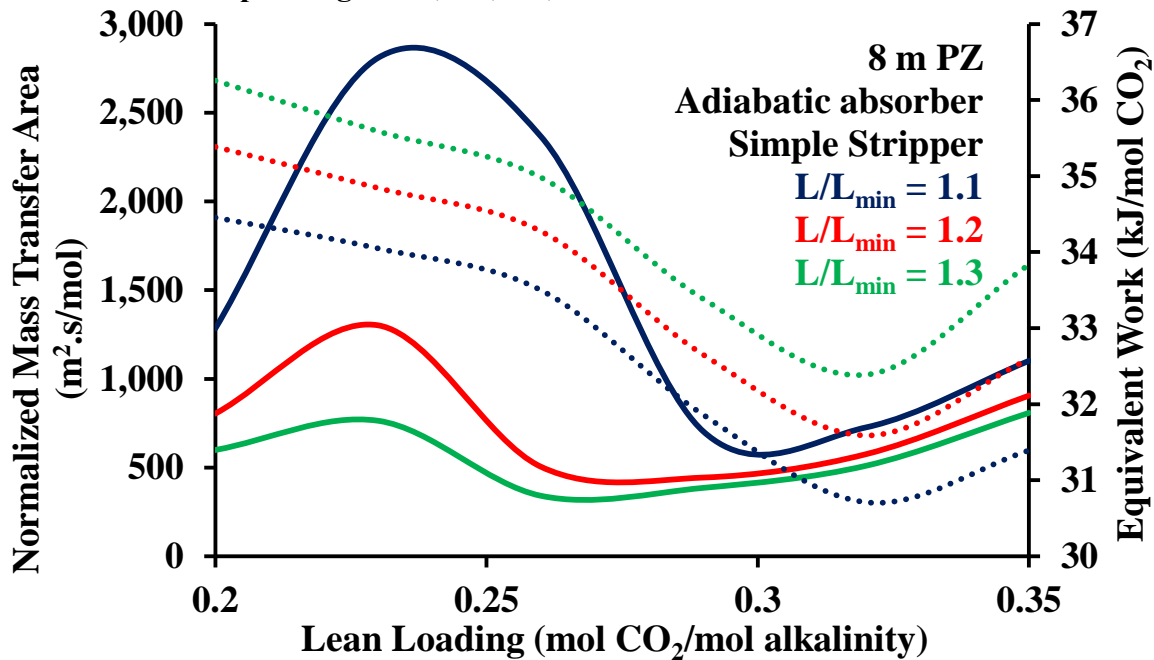


Figure 5-11: Mass transfer area (solid lines) and equivalent work (dotted lines) for 8 m PZ in an adiabatic absorber with a simple stripper and liquid flow rates corresponding to 1.1, 1.2, and 1.3 times the minimum, 90% removal, 40 °C, 12% CO₂.

Increasing either the temperature or the loading will decrease the average driving force in the column and increase the packing requirement. At high lean loadings the packing area increases due to the loading effect. At low lean loading the packing area peaks because of the temperature effect. In Figure 5-9 the most dramatic dependence of packing area on lean loading is observed for the $L/L_{\min} = 1.1$ case. Figure 5-10 compares the absorber temperature profiles for several lean loadings assuming $L/L_{\min} = 1.1$.

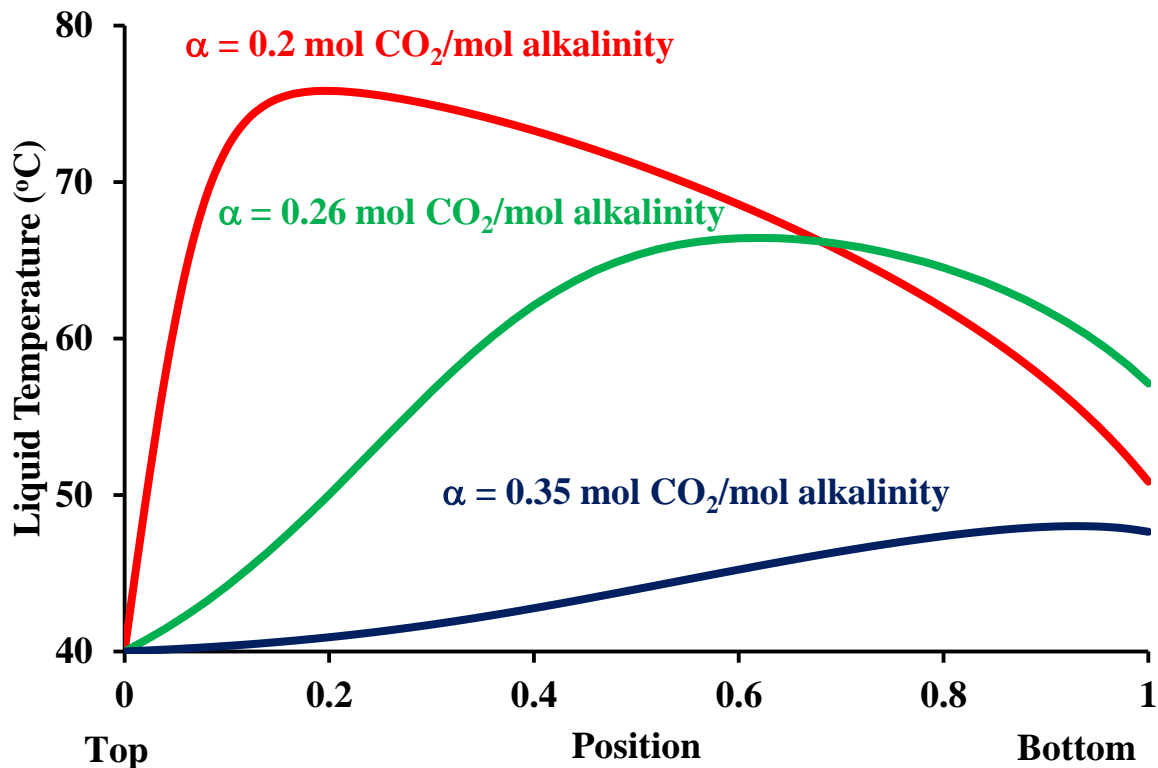


Figure 5-12: Temperature profiles for 8 m PZ in adiabatic absorbers at a liquid flow rate corresponding to 1.1 times the minimum liquid flow rate and lean loadings of 0.2 (red), 0.26 (green), and 0.35 (blue) mol CO₂/ mol alkalinity, 90% removal, 40 °C inlet gas and liquid.

As the lean loading increases the liquid flow rate increases and the temperature bulge migrates from the top to the bottom of the column. At a lean loading of 0.2 mol

CO₂/mol alkalinity the temperature bulge is close to the top of the column, but the relatively low loadings maintain healthy CO₂ driving forces. At a lean loading of 0.35 mol CO₂/mol alkalinity the CO₂ driving force is primarily determined by the liquid loading. The relatively large liquid flow rate has significantly reduced the magnitude of the temperature bulge and, thus, the effect of temperature on the average CO₂ driving force. The packing area peak in Figure 5-9 is due to the combined temperature and loading effects. Plaza (2011) refers to this condition as the critical L/G. Intercooled configurations show the greatest benefit at this condition, since it constitutes the greatest opportunity to improve CO₂ driving forces by removing heat from the column.

Liquid flow rate exhibits a more regular effect on equivalent work. All equivalent work curves in Figure 5-9 exhibit the same trend with an optimum lean loading at 0.32 mol CO₂/mol alkalinity. Below the optimum the compression work and steam losses hurt the equivalent work. Above the optimum the pump work goes up significantly as the solvent circulation rate increases. Below the optimum lean loading the average increase in equivalent work as the liquid flow rate increases from 1.1 to 1.2 times the minimum liquid flow rate is 0.82 ± 0.07 kJ/mol CO₂, compared to 0.76 ± 0.07 kJ/mol CO₂ as the liquid flow rate increases from 1.2 to 1.3 times the minimum liquid flow rate. These differences increase by more than 40% above the optimum lean loading, but the irregular behavior exhibited in normalized packing area does not appear in equivalent work predictions.

A rigorous optimization of the liquid flow rate is beyond the scope of this study. Increasing the liquid flow rate decreases the capital cost of the absorber (Figure 5-9) and

increases the operating cost associated with capacity (Figure 5-8) and, thus, equivalent work (Figure 5-9). Over the range of lean loadings the most significant improvement in packing area is observed as the liquid flow rate increases from 1.1 to 1.2 times the minimum liquid flow rate. Increasing the liquid flow rate dampens the temperature effects at the lower lean loadings. This benefit decreases as the liquid flow rate increases from 1.2 to 1.3 times the minimum liquid flow rate, but the energy hit and the cost of solvent capacity increase at the same rate. As a first order approximation of the optimum condition, this study will assume a liquid flow rate that is 1.2 times the minimum liquid flow rate for all absorber designs.

5.4.2 Intercooling Configurations

Intercooling has the potential to reduce mass transfer area and increase solvent capacity for absorbers experiencing mass transfer limitations due to the temperature bulge. Figure 5-9 shows the packing area (blue) and solvent capacity (red) as a function of lean loading for 8 m PZ at 40 °C and a liquid flow rate that is 1.2 times the minimum and 90% removal for an adiabatic absorber (dashed lines), in-and-out intercooling (dotted lines), and pump-around intercooling (solid lines).

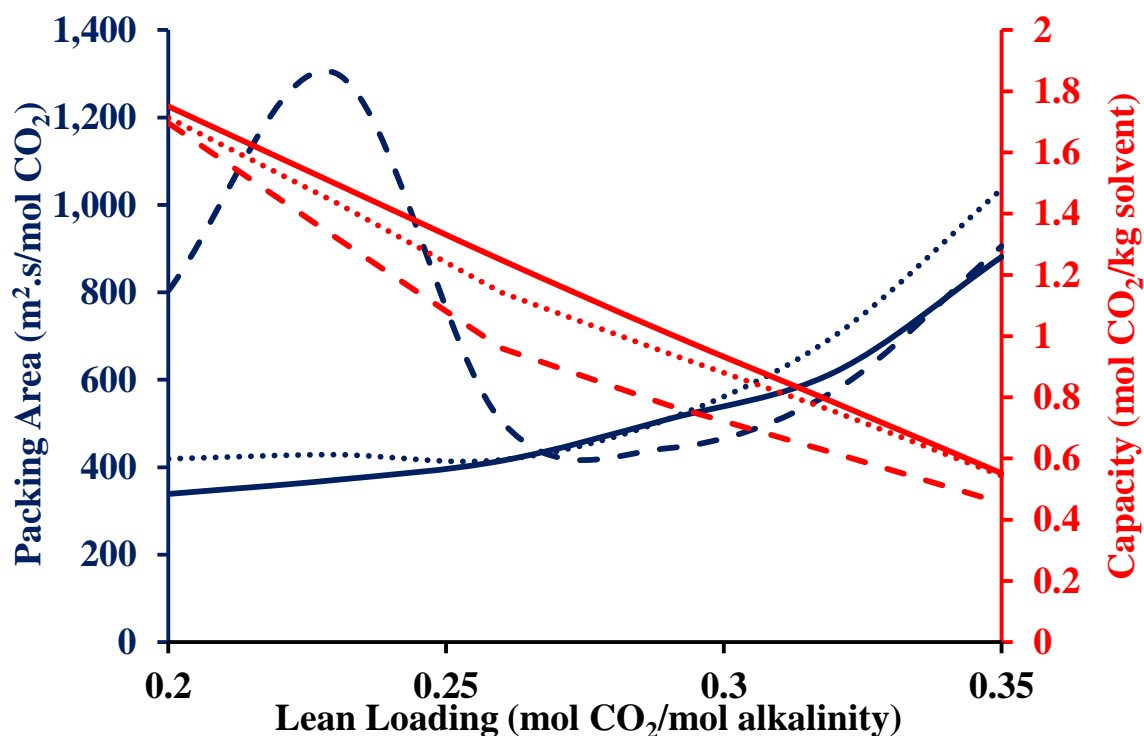


Figure 5-13: Normalized packing area (blue) and capacity (red) as a function of lean loading for 8 m PZ at 40 °C with an adiabatic absorber (dashed lines), in-and-out intercooling (dotted lines), and pump-around intercooling (solid lines) with a liquid flow rate that is 1.2 times the minimum and 90% removal.

Intercooling improves capacity by reducing the temperature of the rich liquid leaving the absorber. The temperature of the rich liquid leaving an adiabatic absorber with a liquid flow rate equal to 1.2 times the minimum varies from 48-57 °C with the maximum coming at a lean loading of 0.26 mol CO₂/mol alkalinity. Over the range of lean loadings in Figure 5-9, the average rich liquid temperatures with standard deviations for the in-and-out and pump-around intercooling configurations are 46±2.5 °C and 42.1±0.5 °C, respectively. Table 5-2 compares the three configurations at lean loadings of 0.23, 0.26, and 0.32 mol CO₂/mol alkalinity for 8 m PZ at 40 °C and a liquid flow rate that is 1.2 times the minimum.

Table 5-2: Configuration comparison at lean loadings of 0.23, 0.26, and 0.32 mol CO₂/mol alkalinity for 8 m PZ at 40 °C and 90% removal from an inlet stream with 12% CO₂ and a CO₂ flow rate of 130 kg/s and a liquid flow rate that is 1.2 times the minimum

Lean Loading	Property	Adiabatic	IO IC	PA IC
0.23	Rich Loading	0.370	0.382	0.388
	Packing Area (m ²)	9.86x10 ⁵	3.17x10 ⁵	2.52x10 ⁵
	L/G (mol/mol)	3.78	3.48	3.33
	Diameter (m)	17.9	16.8	15.8
	Section H (m)	15.3	2.5,3.09	1.8,4.8,1.1
	Rich T (°C)	54.7	49.5	42.7
	Vapor T (°C)	58.6	47.2	45.3
	IC Duty (kJ/mol CO ₂)	N/A	43.3	65.0
0.26	Rich Loading	0.362	0.380	0.392
	Packing Area (m ²)	3.99x10 ⁵	3.21x10 ⁵	2.88x10 ⁵
	L/G (mol/mol)	5.20	4.38	4.00
	Diameter (m)	18.1	17.2	16.0
	Section H (m)	6.06	2.65,2.74	2.1,5.3,1.1
	Rich T (°C)	57.1	48.5	42.4
	Vapor T (°C)	45.5	43.8	43.5
	IC Duty (kJ/mol CO ₂)	N/A	43.1	64.2
0.32	Rich Loading	0.385	0.399	0.403
	Packing Area (m ²)	4.82x10 ⁵	5.58x10 ⁵	4.51x10 ⁵
	L/G (mol/mol)	8.09	6.64	6.38
	Diameter (m)	18.7	18.1	16.5
	Section H (m)	6.86	5.4,3.07	3.1,7.6,1.7
	Rich T (°C)	50.9	44.0	42.0
	Vapor T (°C)	41.1	41.1	41.0
	IC Duty (kJ/mol CO ₂)	N/A	44.1	58.7

Intercooling also reduces the packing requirement with the most significant improvement between lean loadings of 0.23 and 0.26 mol CO₂/mol alkalinity, where the mass transfer pinch is in the middle of the column. Removing heat from the middle of the column at these conditions directly improves the average CO₂ driving force, thus reducing the packing requirement. As the lean loading increases and the temperature bulge migrates to the bottom of the column the mass transfer pinch also migrates to the bottom of the column. Intercooling can still improve solvent performance by reducing

the temperature of the rich liquid and increasing the capacity, but the opportunity to improve CO₂ driving forces and reduce packing requirement diminishes. Both benefits of intercooling can be easily observed in Figure 5-9.

The intercooled configurations exhibit comparable improvements in capacity and packing requirement over the adiabatic configuration for coal-fired applications. Sachde (2012) showed that pump-around intercooling with a large pump-around rate is more effective for applications that must cool the CO₂ laden stream as well as remove the CO₂ heat of absorption. Because this study focuses on coal-fired applications, in-and-out intercooling will be the focus of process design and optimization.

5.4.3 Stripper Configurations

Figure 5-10 shows the equivalent work and rich loading as a function of lean loading for 8 m PZ with a liquid flow rate equal to 1.2 times the minimum for a simple stripper with rich solutions generated by an adiabatic absorber (solid lines), absorber with in-and-out intercooling (dashed lines), and absorber with pump-around intercooling (dotted lines). The equivalent work (Equations 5-1, 5-2, and 5-3) is the sum of three terms: (1) electrical equivalent of the reboiler/steam heater duty, (2) pump work, and (3) compressor work. The latter two terms are determined by the lean loading and regeneration temperature. At a given lean loading and regeneration temperature they are independent of rich loading (i.e. absorber configuration) and stripper configuration. All process modifications address the electrical equivalent of the reboiler/steam heater duty, which can be thought of as three components: (1) the heat of CO₂ desorption, (2) the

sensible heat associated with the difference between rich feed and lean product, and (3) the latent heat of the steam in the product stream.

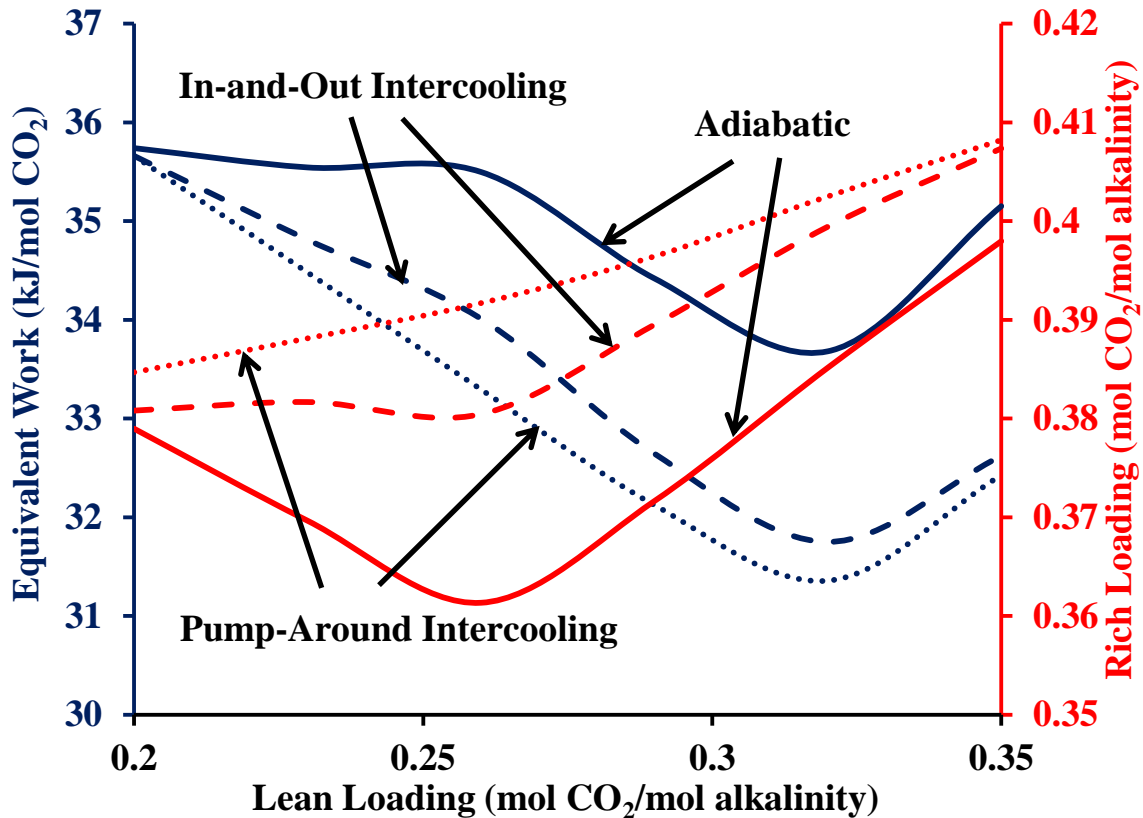


Figure 5-14: W_{EQ} (blue) and rich loading (red) 8 m PZ with a liquid flow rate equal to 1.2 times the minimum for a simple stripper with rich solutions from an adiabatic absorber (solid lines), in-and-out intercooling (dashed lines), and pump-around intercooling (dotted lines).

The heat of CO₂ desorption is practically constant for a given amine, rich/lean loading, and regeneration temperature. Technically the CO₂ is being desorbed over a temperature range and the component of the reboiler duty associated with it represents an average heat of desorption over that temperature range. Figure 5-11 illustrates this point.

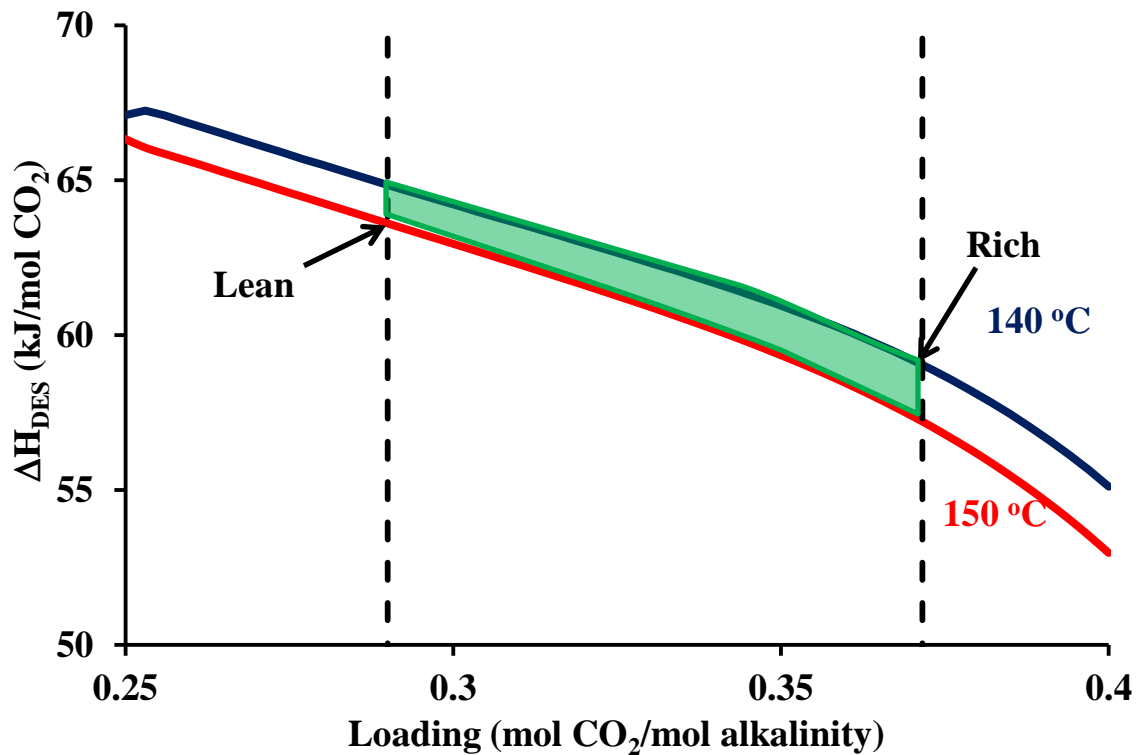


Figure 5-15: Heat of desorption for 8 m PZ at 140 °C (blue) and 150 °C (red). Temperatures correspond to feed and product temperatures for simple stripper. Vertical lines at 0.29 and 0.37 mol CO₂/mol alkalinity correspond to rich and lean loadings, respectively, for adiabatic absorber with a liquid rate equal to 1.2 times the minimum.

Regardless of packing height, column diameter, or any other simple stripper design parameter, the liquid will go from the rich point to the lean point traveling through the highlighted region. The average heat of CO₂ desorption is calculated by taking the area under the operating line and dividing by the loading range. Because the change in heat of CO₂ desorption from 140 °C to 150 °C is less than 4% over the operational loading range, the average heat of CO₂ desorption is not going to vary appreciably.

The inefficiencies most easily addressed by process modifications are the lost steam in the product gas and the sensible heat difference between the rich feed and lean

product liquids. Figure 5-12 compares the three components of the reboiler duty in kJ/mol CO₂ as a function of lean loading for 8 m PZ with simple stripper using rich solvents generated by an adiabatic absorber, absorber with in-and-out intercooling, and an absorber with pump-around intercooling, all using a liquid flow rate equal to 1.2 times the minimum.

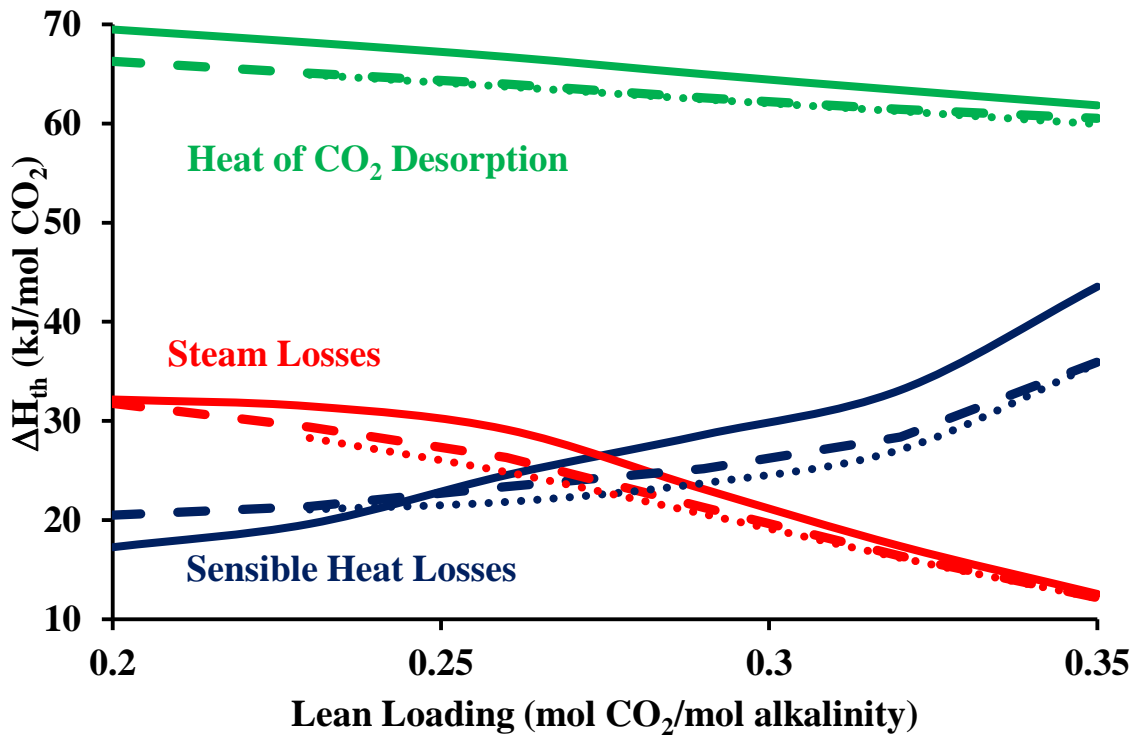


Figure 5-16: Heat of CO₂ Desorption (green), steam losses (red), and sensible heat losses (blue) for a simple stripper with 8 m PZ and an adiabatic absorber (solid lines), absorber with in-and-out intercooling (dashed lines), and absorber with pump-around intercooling (dotted lines) and a liquid flow rate equal to 1.2 times the minimum absorbed at 40 °C.

When comparing energy losses, the steam losses are more significant at low lean loadings, and the sensible heat losses are more significant at high lean loadings. Process design and optimization focuses on the tradeoff between process complexity and energy performance. Increasing process complexity should improve process reversibility

(reduce operating cost), but this also requires a greater capital investment. Figures 5-10 and 5-12 suggest that absorber complexity significantly improves process reversibility at high lean loadings but not at low lean loadings. In Figure 5-10 at a lean loading of 0.2 mol CO₂/mol alkalinity all three absorber configurations have an equivalent work of 35.5 kJ/mol CO₂. However, above a lean loading of 0.3 mol CO₂/mol alkalinity the intercooled configurations improve equivalent work by 5-10%. This result suggests that intercooling is more effective at addressing sensible heat losses than steam losses. The primary benefit of intercooling as it pertains to stripper design is improved solvent capacity. Increasing capacity reduces solvent circulation rate and, thus, the sensible heat required to cycle solvent between absorber and stripper temperatures.

The advanced flash stripper (Section 5.3.3.2) focuses on improving steam losses. Figure 5-13 shows the equivalent work as a function of lean loading for 8 m PZ with a simple stripper (blue) and advanced flash stripper (red) using rich solutions generated by adiabatic absorbers (solid lines), absorbers with in-and-out intercooling (dashed lines), and absorbers with pump-around intercooling (dotted lines). Just as with the simple stripper, the advanced flash stripper gives the same equivalent work for all absorber configurations at a lean loading of 0.2 mol CO₂/mol alkalinity. However, the advanced flash stripper reduces the equivalent work by 15%. As lean loading increases the relative advantage of the advanced flash stripper decreases until the curves cross near a lean loading of 0.32 mol CO₂/mol alkalinity. The ultimate tradeoff in process design is improving process reversibility by increasing process complexity. Bypassing cold and warm solvent directly addresses steam losses; intercooling indirectly addresses sensible

heat losses by improving capacity. Figures 5-12 and 5-13 suggest that absorber complexity decreases irreversibilities associated with sensible heat losses, and stripper complexity decreases irreversibilities associated with steam losses.

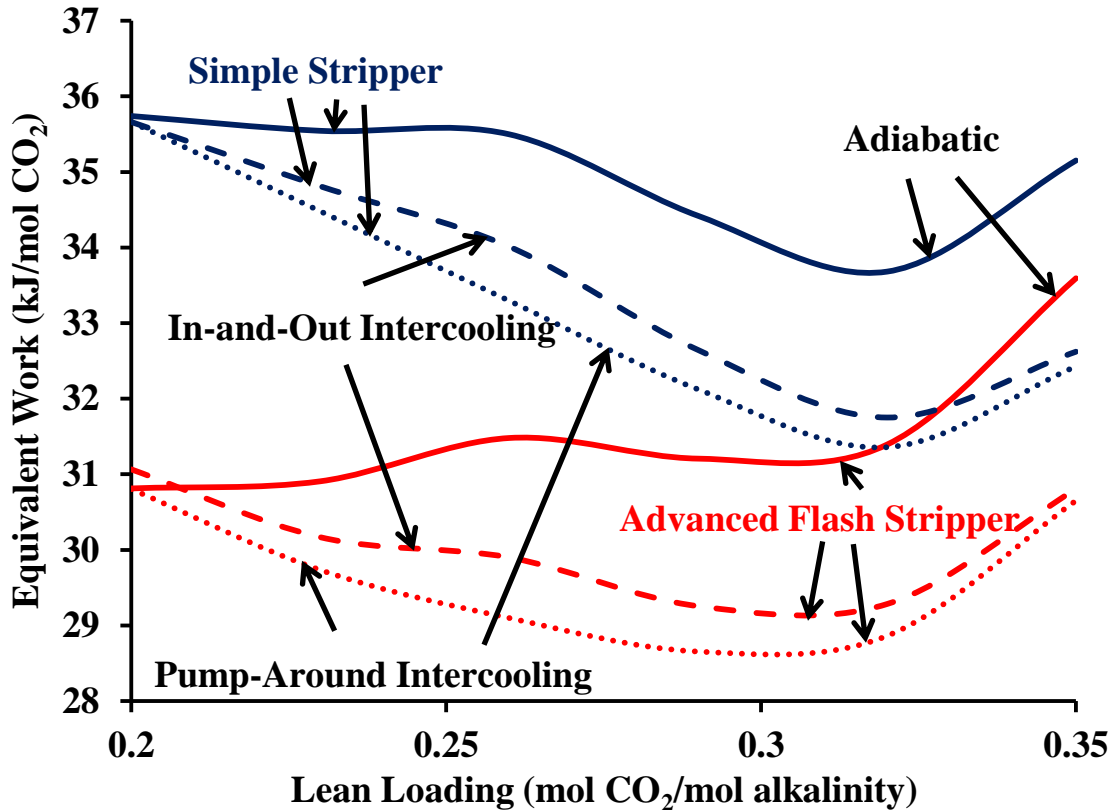


Figure 5-17: Equivalent work for 8 m PZ with a simple stripper (blue) and advanced flash stripper (red) using rich solutions generated by an adiabatic absorber (solid lines), in-and-out intercooling (dashed lines), and pump-around intercooling (dotted lines).

5.4.4 Absorber Temperature

Figure 5-14 shows the normalized packing area (blue) and solvent capacity (red) as a function of lean loading for 7 m MDEA/2 m PZ at 40 °C (solid lines), 30 °C (dashed lines), and 20 °C (dotted lines) and a liquid flow rate that is 1.2 times the minimum and 90% removal for an adiabatic absorber. Reducing the temperature of the absorber

categorically increases the capacity of the solvent at a given lean loading, but it does not require a larger absorber at low lean loadings. The trend in solvent capacity is reflective of the effect of temperature on the rich loading limit of the solvent (Figure 5-2). Holding the lean loading constant while decreasing the solvent temperature will increase the operational loading range and, thus, the solvent capacity.

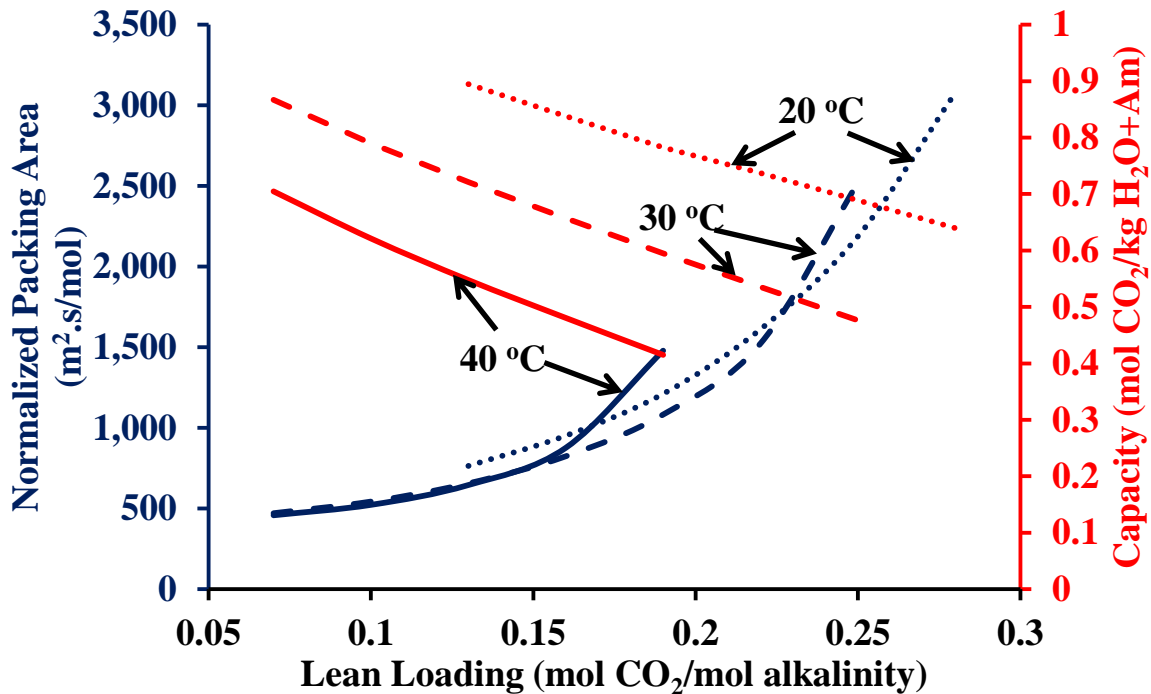


Figure 5-18: Normalized packing area (blue) and solvent capacity (red) for 7 m MDEA/2 m PZ at 40 °C (solid lines), 30 °C (dashed lines), and 20 °C (dotted lines) and a liquid flow rate equal to 1.2 times the minimum and 90% removal for an adiabatic absorber.

The effect of temperature on normalized packing area is due to competing effects on k_g' and CO_2 driving forces. The normalized area is the reciprocal of the average CO_2 flux, which is calculated by Equation 5-1. LMPD is the log mean pressure difference as calculated by Equation 5-2, and k_g' is the liquid side CO_2 mass transfer coefficient expressed in units of partial pressure.

$$Flux = k'_g LMPD \quad \text{Equation 5-1}$$

$$LMPD = \frac{(P_{in} - P_{out}^*) - (P_{out} - P_{in}^*)}{\ln \frac{(P_{in} - P_{out}^*)}{(P_{out} - P_{in}^*)}} \quad \text{Equation 5-2}$$

In Equation 5-2 P_{in} is the inlet bulk gas CO_2 partial pressure, P_{out}^* is the rich solvent equilibrium partial pressure of CO_2 , P_{out} is the outlet bulk gas CO_2 partial pressure, and P_{in}^* is the lean solvent equilibrium CO_2 partial pressure. At cold absorber conditions it is assumed that the pseudo first order assumption applies, which allows for the direct calculation of k'_g by Equation 5-3, in which k_2 is the second order reaction rate constant, D_{CO_2} is the diffusivity of CO_2 , $[Am]$ is the concentration of free amine, and H_{CO_2} is the Henry's constant of CO_2 . Because k_2 , D_{CO_2} , and H_{CO_2} exhibit similar dependences on temperature, k'_g is independent of temperature at a given loading (i.e. $[Am]$).

$$k'_g = \frac{\sqrt{k_2 D_{CO_2} [Am]}}{H_{CO_2}} \quad \text{Equation 5-3}$$

Figure 5-14 suggests that up to a lean loading of 0.15 mol CO_2 /mol alkalinity k'_g and LMPD are indirectly proportional with temperature. Reducing the temperature will increase LMPD by decreasing bulk liquid equilibrium partial pressures of CO_2 at a given loading and increasing the bulk CO_2 partial pressures. Therefore, k'_g must be decreasing with temperature, which seems to contradict the pseudo first order assumption. However, the values of k'_g calculated using the results in Figure 5-14 represent average values over the operational loading range. Because decreasing absorber temperature will increase the rich loading (i.e. decrease $[Am]$) the average k'_g will also decrease. Table 5-3 compares

adiabatic absorbers at temperatures of 40 °C, 30 °C, and 20 °C and lean loadings of 0.13, 0.19, and 0.25 mol CO₂/mol alkalinity for 7 m MDEA/2 m PZ with a liquid flow rate that is 1.2 times the minimum. The results for “ΔT Rich Liquid” and “ΔT Product Vapor” correspond to the difference between feed and product temperatures for the liquid and vapor streams, respectively.

Table 5-3: Adiabatic absorbers at temperatures of 40 °C, 30 °C, and 20 °C and lean loadings of 0.13, 0.19, and 0.25 mol CO₂/mol alkalinity for 7 m MDEA/2 m PZ with a liquid flow rate that is 1.2 times the minimum

Lean Loading	Property	40 °C	30 °C	20 °C
0.13	Capacity (mol CO ₂ /kg H ₂ O+Am)	0.548	0.721	0.895
	Normalized Area (m ² .s/mol)	646	656	764
	Rich Loading (mol CO ₂ /kg H ₂ O+Am)	0.23	0.26	0.29
	ΔT Rich Liquid (°C)	14.1	16.9	22.0
	ΔT Product Vapor (°C)	1.1	4.7	5.7
	Average k _g ' x 10 ⁷ (mol/m ² .Pa.s)	4.16	3.44	2.69
	LMPD (kPa)	3.72	4.43	4.87
0.19	Capacity (mol CO ₂ /kg H ₂ O+Am)	0.415	0.595	0.783
	Normalized Area (m ² .s/mol)	1,480	1,080	1,210
	Rich Loading (mol CO ₂ /kg H ₂ O+Am)	0.27	0.30	0.33
	ΔT Rich Liquid (°C)	9.2	12.6	16.2
	ΔT Product Vapor (°C)	0.2	0.8	1.1
	Average k _g ' x 10 ⁷ (mol/m ² .Pa.s)	3.30	2.53	1.88
	LMPD (kPa)	2.05	3.66	4.39
0.25	Capacity (mol CO ₂ /kg H ₂ O+Am)	N/A	0.476	0.689
	Normalized Area (m ² .s/mol)	N/A	2,520	2,190
	Rich Loading (mol CO ₂ /kg H ₂ O+Am)	N/A	0.34	0.38
	ΔT Rich Liquid (°C)	N/A	9.8	13.5
	ΔT Product Vapor (°C)	N/A	0.2	0.6
	Average k _g ' x 10 ⁷ (mol/m ² .Pa.s)	N/A	1.95	1.29
	LMPD (kPa)	N/A	2.04	3.54

At a lean loading of 0.13 mol CO₂/mol alkalinity the LMPD and k_g' are inversely proportional across all temperatures. As the lean loading increases to 0.19 mol CO₂/mol alkalinity this trend persists for the absorbers at 30 °C and 20 °C, but the LMPD for the absorber at 40 °C has dropped significantly. At the lean loading limit (i.e. the point at

which the activity of CO₂ in the bulk liquid is equal to the activity of CO₂ in the outlet gas), the LMPD goes to zero and the normalized packing area goes to infinity. Plotting Figure 5-14 with the lean equilibrium partial pressure of CO₂ on the x-axis shows this effect (Figure 5-15).

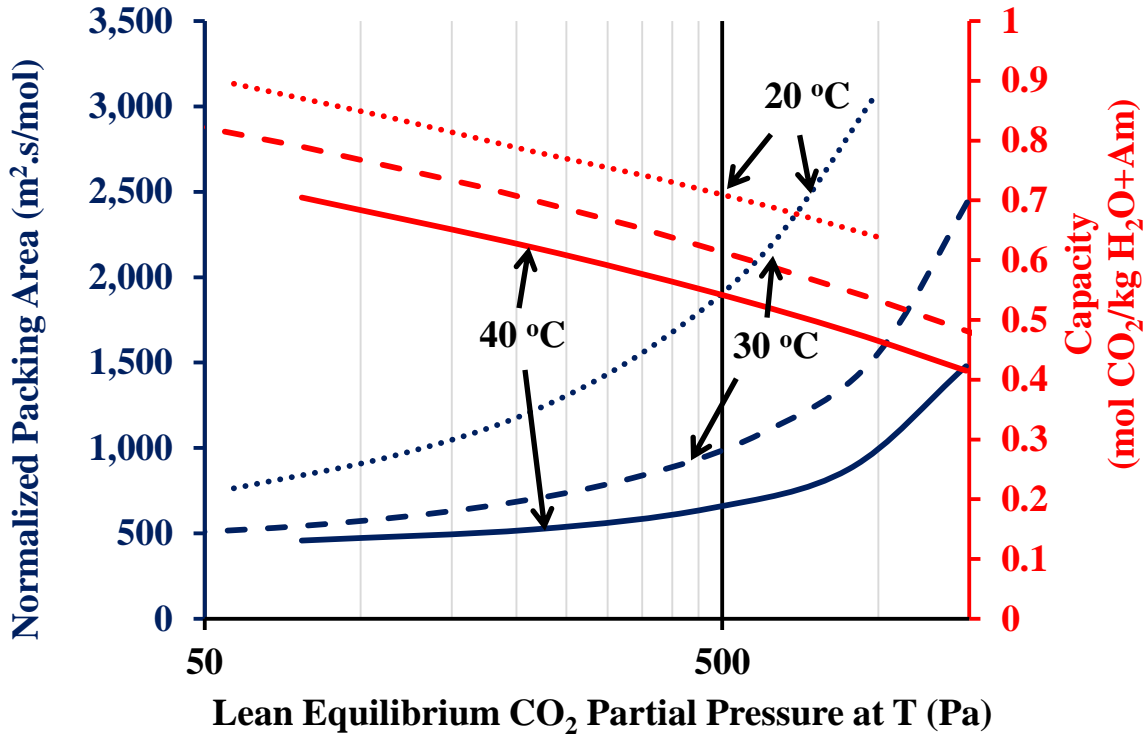


Figure 5-19: Normalized packing area (blue) and solvent capacity (red) for 7 m MDEA/2 m PZ at 40 °C (solid lines), 30 °C (dashed lines), and 20 °C (dotted lines) and a liquid flow rate equal to 1.2 times the minimum and 90% removal for an adiabatic absorber.

The curves in Figure 5-15 terminate near a lean equilibrium CO₂ partial pressure of 1.8 kPa. Above that limit there is no driving force on the lean end of the column. This limit is set by the arbitrary removal rate of 90%. If the system were designed for 99% removal, the lean end pinch would occur at about 0.18 kPa of CO₂.

Figure 5-16 shows equivalent work for the simple stripper and advanced flash stripper as a function of lean equilibrium CO₂ partial pressure with absorbers operating at 40 °C, 30 °C, and 20 °C.

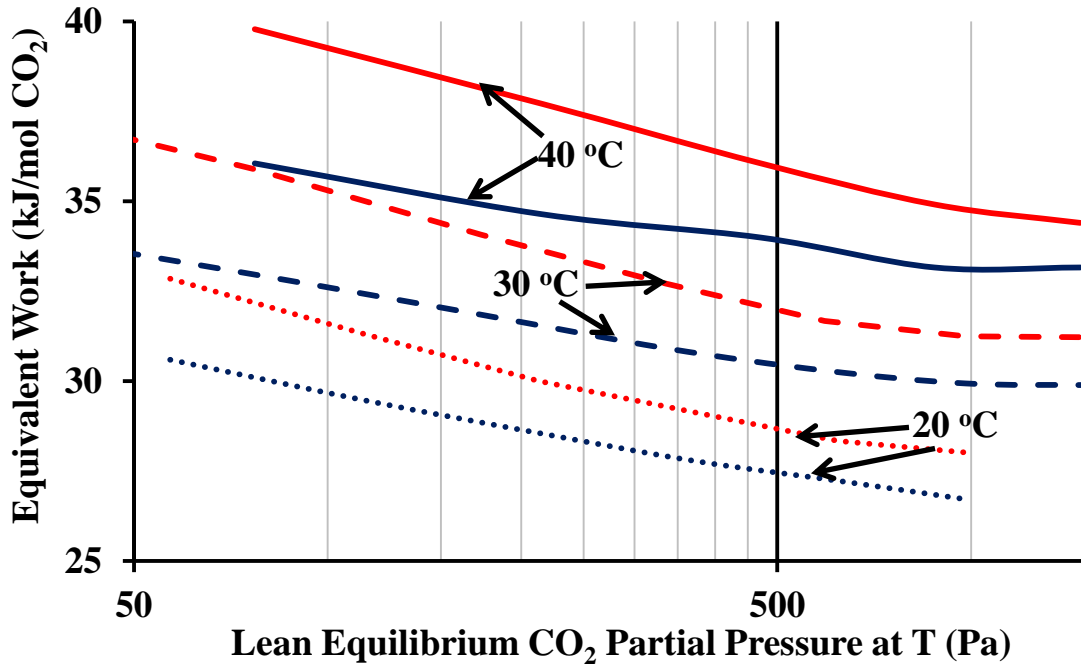


Figure 5-20: Equivalent work for 7 m MDEA/2 m PZ with a simple stripper (red) and advanced flash stripper (blue) and an adiabatic absorber at 40 °C, 30 °C, and 20 °C and a liquid flow rate equal to 1.2 times the minimum and 90% removal.

The advanced flash stripper always has a lower equivalent work than the simple stripper, but the relative advantage at a given lean CO₂ partial pressure diminishes as the temperature of the absorber decreases. The relative advantage of the advanced flash stripper correlates with the lean loading, which determines the regeneration pressure and the amount of steam in the product gas. The average improvement in equivalent work going from the simple stripper to the advanced flash stripper at 0.16 mol CO₂/mol alkalinity is 1.8±0.04 kJ/mol CO₂, but this improvement drops to 1.4±0.1 kJ/mol CO₂ at a

loading of 0.19 mol CO₂/mol alkalinity. As lean loading continues to increase the advantage will continue to drop until the CRB and WRB are optimized out of the design.

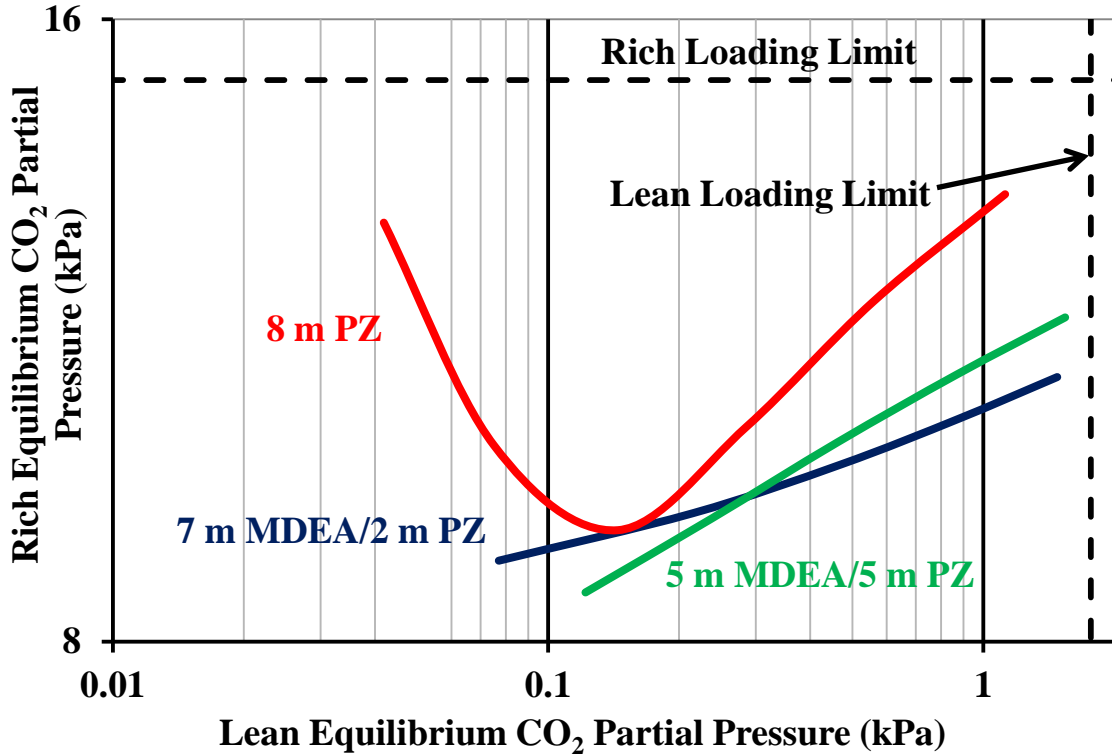


Figure 5-21: Operational loadings for adiabatic absorbers at 40 °C and the minimum liquid flow rates.

Another interesting result in Figure 5-16 is that the equivalent work curves do not have well-defined optimum lean loadings like those for 8 m PZ in Figure 5-9. The increase in equivalent work at high loadings is due to the rich loading limit. The equilibrium partial pressure of CO₂ in the rich solvent cannot exceed the partial pressure of CO₂ in the feed gas. As lean loading increases the rich loading does not, which quickly reduces the capacity and increases the solvent circulation rate. Figure 5-17 compares how close the three amines in this study approach the lean and rich loading limits. The MDEA/PZ solvents are not as constrained by the rich loading limit as 8 m PZ

because of the slopes of the CO₂ solubility curves at absorber conditions. Figure 5-18 compares the equilibrium partial pressure of CO₂ at 40 °C for 8 m PZ, 7 m MDEA/2 m PZ, and 5 m MDEA/ 5 m PZ as a function of the CO₂ concentration in the units of capacity (mol CO₂/kg H₂O + amine) and normalized to the CO₂ concentration corresponding to the nominal lean equilibrium partial pressure of CO₂ of 500 Pa.

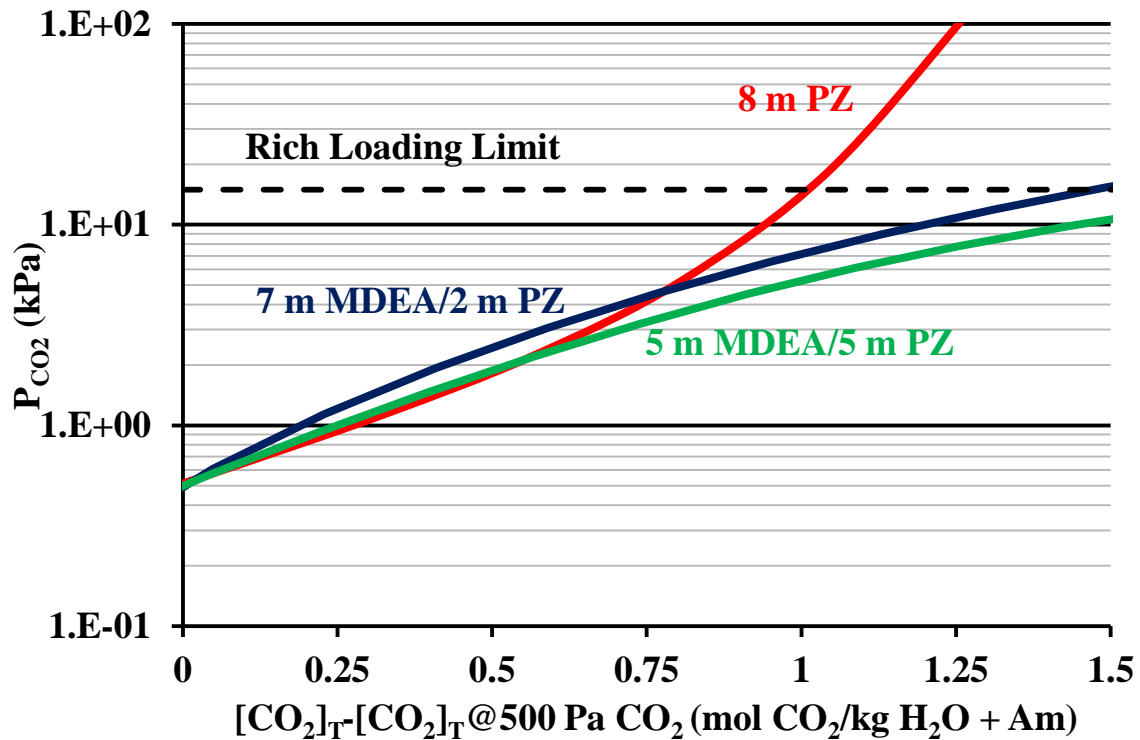


Figure 5-22: CO₂ solubility at 40 °C for 8 m PZ, 7 m MDEA/2 m PZ, and 5 m MDEA/5 m PZ.

As the concentration of CO₂ increases the PZ in each solvent is becoming saturated. As 8 m PZ saturates CO₂ mass transfer coefficients drop rapidly, and a much higher partial pressure driving force is required. MDEA/PZ is far from being saturated at the conditions in Figure 5-18, and the CO₂ mass transfer coefficients are dropping less

dramatically. This leads to a 50% increase the theoretical maximum capacity of 7 m MDEA/2 m PZ over 8 m PZ (Figure 5-18).

5.4.5 CO₂ Removal

Figure 5-19 compares Aspen Plus[®] predictions for the minimum (L/G)_{mol} as a function of lean loading for 7 m MDEA/2 m PZ at 40 °C in adiabatic and intercooled absorbers with 90% and 99% CO₂ capture.

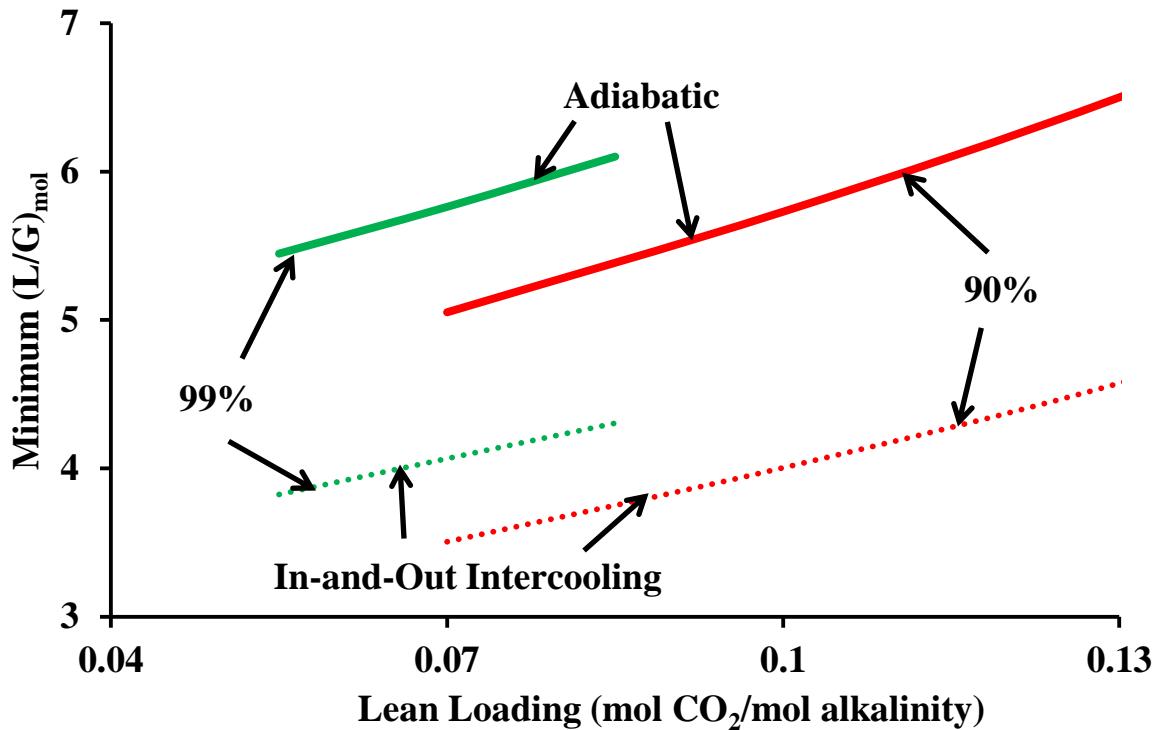


Figure 5-23: Minimum (L/G)_{mol} for 7 m MDEA/2 m PZ at 40 °C in adiabatic (solid lines) and intercooled (dotted lines) absorbers with 90% (red) and 99% (green) capture from the flue gas of a coal-fired power plant

For all values of lean loading and CO₂ removal intercooling reduces the minimum (L/G)_{mol} by 29.7±0.6%. For both configurations at a lean loading of 0.07 mol CO₂/mol alkalinity increasing the CO₂ removal rate from 90% to 99% increased the minimum (L/G)_{mol} by 15%. A zero order approximation would anticipate the minimum (L/G)_{mol}

increasing by 10%. However, this assumes a constant capacity, and the capacity decreases by 4-6% as the CO₂ removal increases from 90% to 99%. This will adversely affect both energy performance and capital investment, but the process is capturing 10% more CO₂. If the combined increase in energy cost and capital investment (in dollars per ton of CO₂) are less than 10%, increasing the removal rate to 99% is beneficial. Figure 5-20 compares the normalized mass transfer area of an adiabatic absorber and equivalent work of a simple stripper for 7 m MDEA/2 m PZ with 90% and 99% removal.

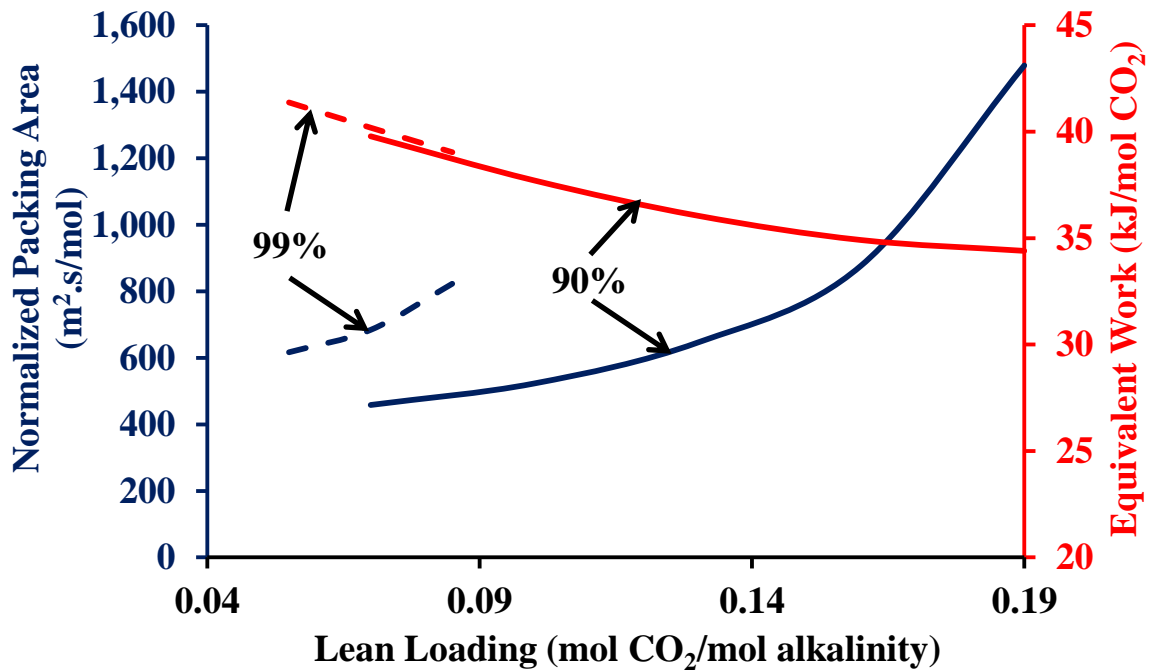


Figure 5-24: Normalized mass transfer area and equivalent work for 7 m MDEA/2 m PZ with an adiabatic absorber at 40 °C and simple stripper.

At a lean loading of 0.07 mol CO₂/mol alkalinity increasing the removal rate from 90% to 99% increases the normalized mass transfer area by 64% and the equivalent work by 1%. A zero order analysis would assume that increasing the CO₂ capture rate from 90% to 99% would double the packing requirement and have no effect on the equivalent

work. The slight increase in equivalent work is a direct result of the unexpected decrease in solvent capacity. The packing area did not double because of the favorable rates on the lean end of the column. Figure 5-21 compares the liquid temperature profiles and CO₂ fluxes normalized to CO₂ partial pressure for adiabatic absorbers with 90% and 99% removal rates. The CO₂ driving force is weak at the top of the column, but the average reaction rate in the top section of the column is larger than the average reaction rate for the 90% removal case.

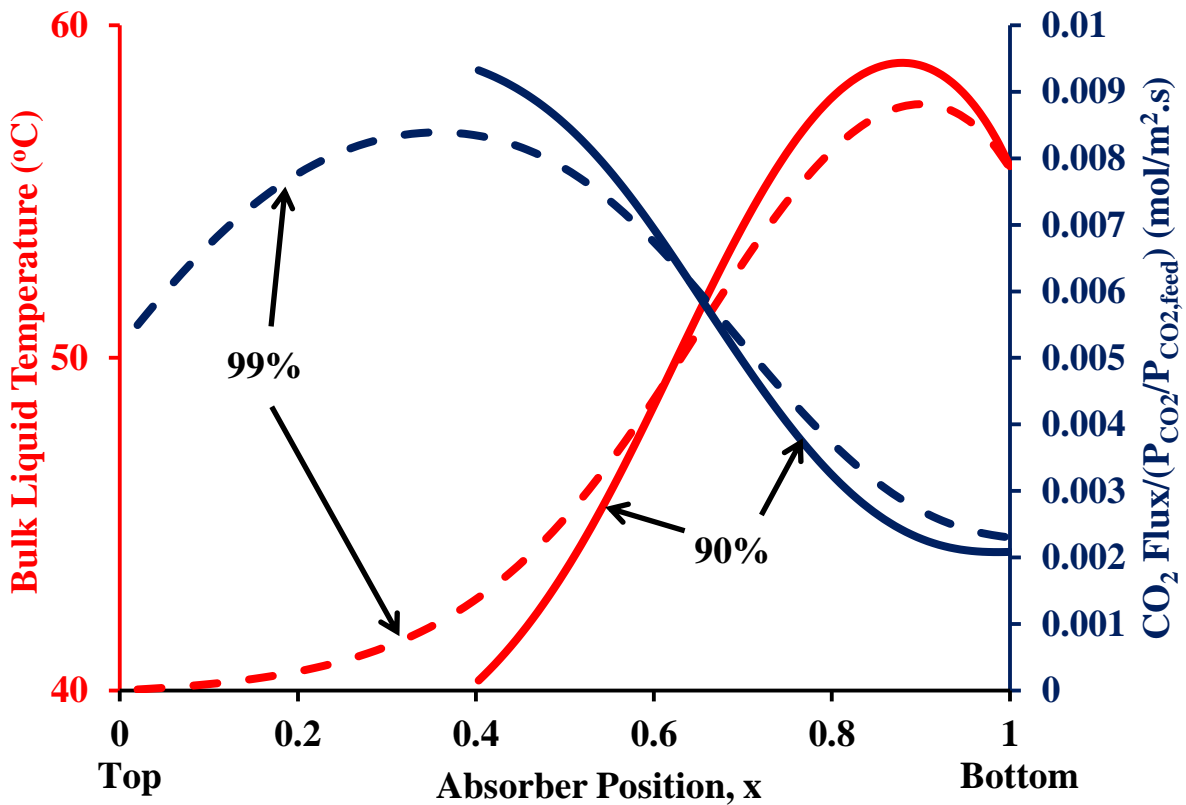


Figure 5-25: Bulk liquid temperature and CO₂ flux normalized to CO₂ partial pressure for 7 m MDEA/2 m PZ with a lean loading of 0.07 mol CO₂/mol alkalinity in adiabatic absorbers with 90% (solid lines) and 99% (dashed lines) CO₂ removal rates. Absorber position refers to the 99% removal case.

Figure 5-22 compares the bulk liquid temperature and CO₂ flux normalized to CO₂ partial pressure for 7 m MDEA/2 m PZ with a lean loading of 0.07 mol CO₂/mol alkalinity for the in-and-out intercooled configurations.

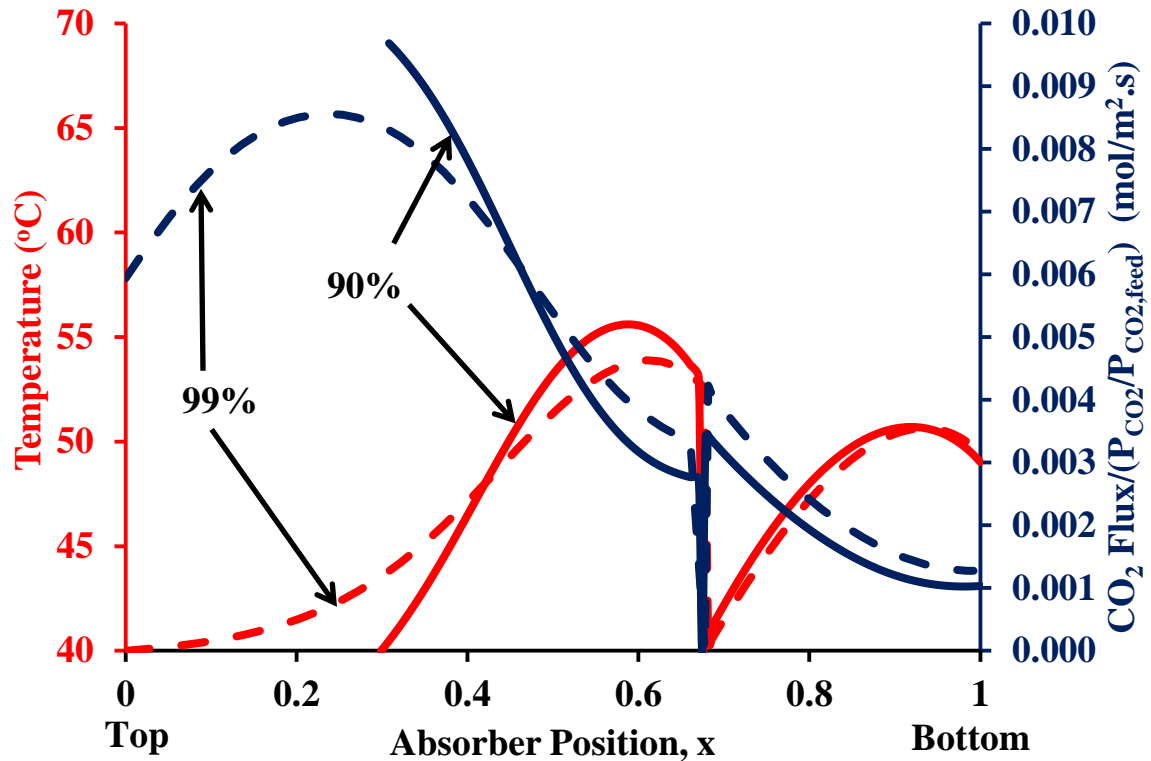


Figure 5-26: Bulk liquid temperature and CO₂ flux normalized to CO₂ partial pressure for 7 m MDEA/2 m PZ with a lean loading of 0.07 mol CO₂/mol alkalinity in in-and-out intercooled absorbers with 90% (solid lines) and 99% (dashed lines) CO₂ removal rates. Absorber position refers to the 99% removal case.

The configuration with in-and-out intercooling exhibits similar trends to the adiabatic absorber, and all four cases are compared in Table 5-4. It is interesting to note that the same amount of packing had to be added to each configuration to increase the removal rate from 90% to 99%. Intercooling addresses the temperature-related mass transfer pinch at the rich end of the column, and the CO₂ removal rate mostly concerns

the lean end of the column. The effect of CO₂ removal rate on equivalent work is insignificant and entirely a result of the slight reduction in capacity.

Table 5-4: Comparison of adiabatic and intercooled absorbers with 90% and 99% CO₂ capture for 7 m MDEA/2 m PZ with a lean loading of 0.07 mol CO₂/mol alkalinity at 40 °C and 1.2 times the minimum liquid flow rate

Property	Intercooled		Adiabatic	
	90%	99%	90%	99%
Minimum (L/G) _{mol}	3.51	4.07	5.05	5.76
Capacity (mol CO ₂ /kg H ₂ O+Am)	1.02	0.96	0.56	0.54
Intercooling Duty (kJ/mol CO ₂)	46.8	47.3	N/A	N/A
ΔH _{ABS} in Rich Liquid (kJ/mol CO ₂)	33.4	36.8	82.8	85.5
Temperature of Rich Liquid (°C)	49.1	49.5	55.8	55.8
Mass Transfer Area (m ² .s/mol CO ₂)	627	819	458	684
AFS W _{EQ} (kJ/mol CO ₂)	33.4	33.7	36.1	36.4
Simple Stripper W _{EQ} (kJ/mol CO ₂)	36.1	36.4	39.8	40.2

The effect of increasing the CO₂ removal with 8 m PZ is complicated by the temperature-related pinch at low lean loading and rich end pinch at high lean loading. Figure 5-23 compares the normalized mass transfer area and capacity of 8 m PZ in an adiabatic absorber with a liquid flow rate equal to 1.2 times the minimum. At low lean loading the column is limited by a temperature bulge at the lean end of the column. At high lean loadings the column is limited by the heat that must exit through the rich end. The bend in the capacity curve for the 90% case at a lean loading of 0.25 mol CO₂/mol alkalinity is the point at which the absorber transitions from the lean end pinch to the rich end pinch. This is covered in Section 5.4.1. Increasing the removal rate decreases the CO₂ driving force at the top of the column, which will shift this bend to a lower lean loading. Between these transition points the lower removal, in this case 90%, significantly outperforms the higher removal in terms of capacity and, thus, energy

performance. However, the 90% removal case is pinching at the top of the column and requires a much greater packing area.

Near a lean loading of 0.2 mol CO₂/mol alkalinity the normalized mass transfer areas cross, at which point a single absorber design could accommodate 90% and 99% removal. This is impractical from a process design standpoint, as the lower capacity at higher removal rates would require significantly larger heat exchangers, pumps, etc. Nevertheless these cases will be compared in Chapter 6 after establishing a cost estimation method.

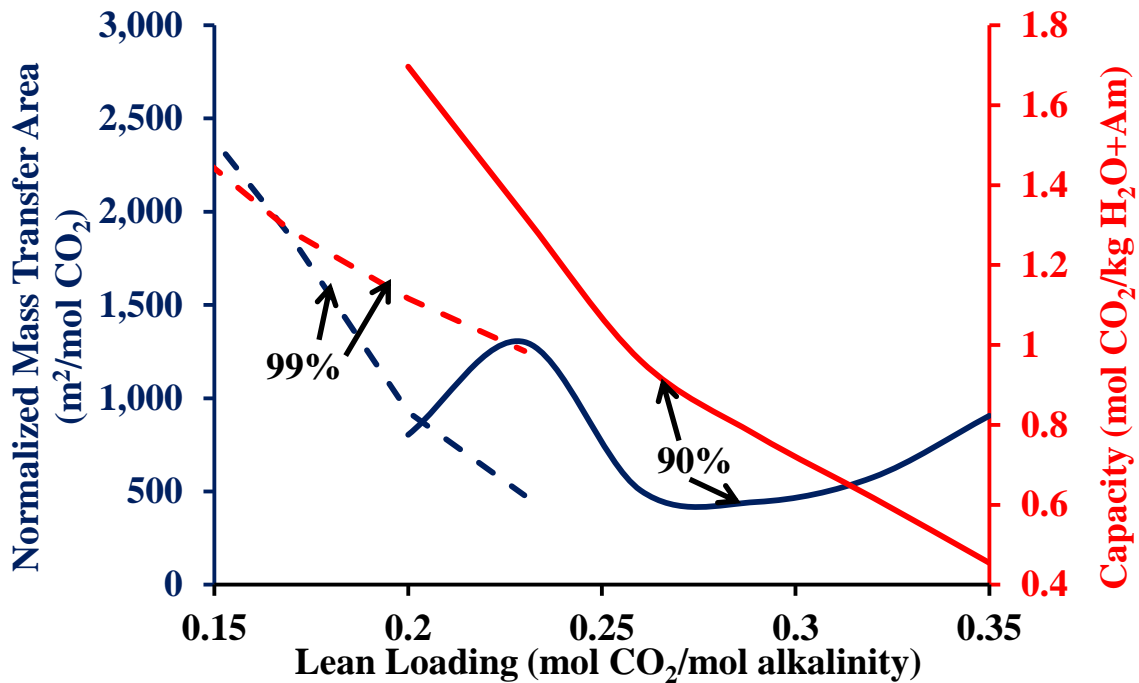


Figure 5-27: Normalized mass transfer area and equivalent work for 8 m PZ with an adiabatic absorber at 40 °C and a liquid flow rate equal to 1.2 times the minimum with 90% and 99% removal.

5.5 CONCLUSIONS

- Increasing CO₂ removal in an adiabatic absorber from 90% to 99% for 7 m MDEA/2 m PZ at a lean loading of 0.07 mol CO₂/mol alkalinity increases packing area by 64% and equivalent work by 1%. Higher CO₂ absorption rates at the lean conditions avoid doubling the packing requirement, and a slight reduction in capacity induces the slight increase in equivalent work.
- Cooling an adiabatic absorber with 7 m MDEA/2 m PZ and a liquid flow rate that is 1.2 times the minimum increases capacity by 16-17% and packing area by 2-5X between lean loadings of 0.07 and 0.19 mol CO₂/mol alkalinity.
- For 8 m PZ at coal conditions intercooling always improves capacity but is only beneficial to packing requirement between lean loadings of 0.2 and 0.26 mol CO₂/mol alkalinity. Not enough heat is carried by the gas to justify pump-around intercooling over in-and-out intercooling at these conditions.
- At coal conditions 8 m PZ is constrained by the rich loading limit, and 7 m MDEA/2 m PZ and 5 m MDEA/5 m PZ are constrained by the lean loading limit.
- Absorber complexity directly addresses sensible heat losses, and stripper complexity directly addresses steam losses.
- The advanced flash stripper reduces equivalent work by 4-14% relative to the simple stripper. The most significant improvement is observed at low lean loadings.

Chapter 6: Process Economics

6.1 INTRODUCTION

To determine the optimum process configuration and conditions, the total cost of CO₂ capture must be quantified. This requires placing the capital expense (CAPEX) and operating expense (OPEX) on a common basis. Previous work in process design and optimization approximates CAPEX as absorber packing area and OPEX as equivalent work when determining an optimum configuration. While this is an acceptable zeroth-order approximation, it is inadequate for a rigorous process optimization. This work establishes methods and baselines that can be applied to novel process configurations to approximate the total cost of CO₂ capture for a wide variety of amines, process configurations, and process conditions. The method is based on the same principals used to derive the pricing methods from private and governmental groups. These methods are considered by many to be confusing and frustrating because they are continuously evolving. Solvents, process configurations, and operating conditions are also evolving continuously, and they must be compared on a common basis. Establishing a set of methods will facilitate the economic evaluation process for future studies.

6.2 METHODS

6.2.1 Scaling

The same methods employed in the 2012 DOE NETL Report (Sexton, 2012) for derating power generation and CO₂ capture facilities were employed in this study. The CO₂ source is a 550 MW_e supercritical pulverized coal power plant described in the 2010

DOE Cost and Performance Baseline Case 11 (DOE-NETL, 2010). Case 12 modifies the plant in Case 11 to be fit with the Econamine scrubbing system while maintaining 550 MW_e net production. All systems in this report have the same constraint, and all prices are in 2007 dollars.

6.2.2 Derating

In addition to the 550 MW_e output of the power plant, the total steam turbine power includes the equivalent work of the steam heater or reboiler, compression, capture auxiliaries, and a balance of plant auxiliaries. The following is a summary of how each was calculated.

- Equivalent work of the steam heater or reboiler – A heat duty predicted in Aspen Plus[®] for the reboiler/steam heaters in the scrubber of a 593 MW_e power plant is converted first to an equivalent amount of steam by assuming 902 BTU/lb of steam. It is then converted to an equivalent electrical output using computer simulated results for the steam turbine of a supercritical pulverized coal power plant. That number is expressed as a percentage of the total electrical output of the plant, allowing for direct scaling.
- Compression – The compression work values in the 2012 DOE NETL report were calculated using vendor quotes. The compression work in this study is calculated by scaling Aspen Plus[®] predictions for compressor inlet pressures to those in the 2012 DOE NETL Report. The compression work is first calculated using Equations 6-1 and 6-2 developed by Van Wagener (2011) in Aspen Plus[®] with 72% polytropic efficiency, intercooling of wet gas to 40 °C at a maximum compression ratio of 2.0

per intercooling stage, and no allowance for pressure drop through the intercoolers.

P_{in} is the inlet pressure to the compression train in atmospheres.

$$W_{comps}(kJ/mol CO_2) = 4.572 \log\left(\frac{148}{P_{in}(atm)}\right) - 4.096 \quad P_{in} \leq 4.5 atm \quad \text{Equation 6-1}$$

$$W_{comps}(kJ/mol CO_2) = 4.023 \log\left(\frac{148}{P_{in}(atm)}\right) - 2.181 \quad P_{in} > 4.5 atm \quad \text{Equation 6-2}$$

Using data from steam and equipment tables in the 2012 DOE NETL Report the compression work was calculated for the PZ-SS and PZ-HT cases and compared to the compression work estimated by vendors. It was determined that the vendor estimates for compression work were categorically 20% less than those calculated using Equations 6-1 and 6-2. To ensure consistency, compression work for the new configuration is calculated by Equations 6-1 and 6-2 and reduced by 20%. This value is expressed as a percentage of the gross plant power and scaled directly when converting from CO₂ captured to CO₂ avoided.

- Capture auxiliaries – This includes the pump work and blower work required to overcome pressure drop and reach regeneration temperature. These works were all calculated using proprietary software. For this study the percentage of total electrical production devoted to capture auxiliaries is set equal to that of the other 8 m PZ cases, which is approximately 2.6%.
- Balance of plant auxiliaries – The percentage of total power plant electrical production devoted to plant auxiliaries was calculated in the 2010 DOE Cost and Performance Baseline Case 12 to be 5.3%.

Because each of these additional electrical requirements can be calculated directly from the total steam turbine power, the total steam turbine power can be calculated directly from the desired net electrical output.

6.2.3 Scaling Purchased Equipment Cost to 2010 DOE Cost and Performance

Baseline

Because of the lack of information in the 2010 DOE Cost and Performance Baseline concerning the calculation of PEC, factors were derived in the 2012 DOE NETL report to establish a common basis for the cost estimation methods. The two goals of this activity were (1) to develop exponents that would allow for the calculation of PEC for the capture and compression plants as a function of total power plant electrical capacity and (2) to determine the relative difference between 2010 DOE Cost and Performance Baseline and 2012 DOE NETL PEC estimates. The first goal was accomplished by calculating the PEC for a base case of 593 MW_e total power, assigning each component of the PEC an exponent on the basis of expected scalability, and weighting those exponents by the base case PEC to give a single exponent that represents the entire process. Separate exponents were calculated for capture and compression systems. The second goal was accomplished by replicating Case 12 using in house costing methodology and comparing it to the DOE reported values. This study replicates this method and calculates its own scaling exponents for capture and compression.

6.3 CALCULATING PEC

A major goal of this study is to improve the methods for estimating PEC using Aspen Plus[®] predictions. Emphasis has been placed on accurately calculating the PEC of

the major cost centers, which were determined to be the absorber, cross exchangers, reboiler or steam heaters, and the compressor. These process units can account for 80 % of the plant PEC.

6.3.1 Absorber

The PEC of the absorber was calculated by developing expressions for each column component that could then use Aspen Plus[®] predictions to estimate a total column price. Pricing information from Sulzer reported in Tsai (2010) for 304 SS baffle distributors and supports (Pilling, 2009), and packing (Pilling, 2008) is used to estimate to cost of column internals. Equation 6-3 calculates the total cost of distributors and their supports as a function of column diameter, D , and Equation 6-4 calculates the cost of packing per cubic meter as a function of specific area, a_p .

$$\text{Distributor Purchased Cost (\$)} = 7929(D)^{1.6031} \quad \text{Equation 6-3}$$

$$\text{Packing Cost (\$/m}^3\text{)} = 12.14 * a_p + 337.15 \quad \text{Equation 6-4}$$

It should be noted that Equations 6-3 and 6-4 include factors to convert predictions from 304 SS to 316 SS. Shell price was estimated using Equation 6-5 from Peters, Timmerhaus, and West (5th Ed.) for a 2 cm shell made of 316 SS as a function of shell mass, M , in kg.

$$\text{Shell Cost (\$)} = 10^{0.657 \times \log(M) + 2.65} \quad \text{Equation 6-5}$$

In addition to the CO₂ absorption section a 3 m water wash is assumed to be part of the column. The absorber intercooler is a plate-and-frame heat exchanger with 316 stainless steel plates. The area of the exchanger is calculated using the same method

outlined in Section 6.3.2. The SO₂ polisher is assumed to be part of the power plant, per the 2010 DOE Cost and Performance Baseline.

6.3.2 Cross Exchangers

Pricing and performance information for plate and frame heat exchangers was obtained from equipment vendors. Heat duties and log mean temperature differences predicted by Aspen Plus[®] can be used to calculate the required heat transfer area for a given overall heat transfer coefficient. The areas in this study are calculated using overall heat transfer coefficients provided by equipment manufacturers. There are, however, several methods for calculating overall heat transfer coefficients using Aspen Plus[®] predicted fluid properties in conjunction with the heat duties and temperature differences. This first requires the calculation of heat transfer coefficients for the liquids and the exchanger material, in this case 316 SS. Equation 6-6 from Hewitt et al. (1994) can be used to calculate the heat transfer coefficient for a liquid in the turbulent regime.

$$\alpha = \frac{0.4\lambda}{D_l} (\text{Pr})^{0.4} (\text{Re})^{0.64} \quad \text{Equation 6-6}$$

In Equation 6-6 α is the heat transfer coefficient, λ is the thermal conductivity of the liquid, D_l is two times the plate spacing, Pr is the Prandlt Number, and Re is the Reynolds Number. Re and Pr are dimensionless numbers calculated using Equations 6-7 and 6-8, respectively.

$$\text{Re} = \frac{\rho V D_l}{\mu} \quad \text{Equation 6-7}$$

$$\text{Pr} = \frac{C_p \mu}{\lambda} \quad \text{Equation 6-8}$$

In Equations 6.7 and 6.8, ρ is the fluid density, V is the bulk fluid velocity, μ is the fluid viscosity, and C_p is the fluid heat capacity. Aspen Plus[®] predictions can be used to calculate each of these terms for the hot and cold ends of the cross exchanger, which can be used to calculate the overall heat transfer coefficient, U , for an end of the cross exchanger by Equation 6-9.

$$\frac{1}{U} = \frac{1}{\alpha_h} + \frac{1}{\alpha_c} + \frac{1}{\lambda_p} \quad \text{Equation 6-9}$$

In Equation 6-9 α_h is the heat transfer coefficient of the hot liquid, α_c is the heat transfer coefficient of the cold liquid, and λ_p is the thermal conductivity of the plate at the mean temperature. The hot end and cold end heat transfer coefficients, U_h and U_c , their respective temperature differences, ΔT_h and ΔT_c , and the heat duty, Q , predict a heat transfer area, A , by Equation 6-10.

$$A = \frac{Q}{\frac{(U_h \Delta T_c - U_c \Delta T_h)}{\ln\left(\frac{U_h \Delta T_c}{U_c \Delta T_h}\right)}} \quad \text{Equation 6-10}$$

6.3.3 Reboiler or Steam Heater

This study uses the method described in the 2012 DOE NETL report. An Aspen Plus[®] predicted heat duty, a heat transfer coefficient consistent with a 2007 report submitted to SBIR (Fisher, 2007), and a 5 K LMTD are used to calculate the required heat transfer area for the convective steam heater that supplies the heat for regeneration.

The heat transfer area is then used to determine the price of the process unit by scaling to the price of a high pressure convective steam heater predicted by PDQ\$. A similar method was used to calculate the price of a reboiler with a comparable heat duty and temperature approach, and it was determined that the convective steam heater is less expensive.

6.3.4 Compressor

Compressor prices are scaled on the basis power consumption in MW to vendor quotes confirmed by proprietary software. Aspen Plus[®] calculates the energy required to compress each mole of CO₂ from the regeneration pressure to 15 MPa using Equations 6-1 and 6-2. This value is multiplied by the CO₂ removal rate to give the power consumption of the compressor train. The resulting price is assumed to include a skid package including electric motors, interstage coolers, and interstage separators. Pumps and dehydration units are priced separately by scaling to vendor quotes used in the 2007 SBIR Advanced Amine report.

6.3.5 All Other Process Units

Inlet gas blowers, centrifugal pumps, water-cooled heat exchangers, filters, tanks, and the reclaimers are all sized and priced using vendor quotes from the 2012 DOE NETL Report. Most of these process units are priced on the basis of vapor and/or liquid flow rates. The stripper is priced as two separate units: (1) a pressurized flash vessel and (2) a packed column that promotes interaction between the vapor from the flash vessel and rich solvent from the CRB and WRB. The flash vessel is priced using vendor quotes from the 2012 DOE NETL Report, and the packed section is priced using the same methodology

used to price the absorber. Combined, these process units account for less than 20 % of the final PEC.

6.4 ADVANCED FLASH STRIPPER WITH INTERCOOLED ABSORBER

This study proposes a base-case absorber design that tests both pump-around and in-and-out intercooling with 8 m PZ. Pump-around intercooling removes semi-rich solvent from one point in the column, cools it to 40 °C, and feeds the cooled solvent back at both a higher point in the column and just below the point that it was removed (Figure 6.1). Enough liquid is fed to the lower stage to avoid accumulation of solvent. This effectively splits the column into three sections: (1) a top section which lean solvent enters and scrubbed gas leaves, (2) a middle section containing 2–5 times more solvent than the top section, and (3) a bottom section containing the same amount of liquid as the top section from which the rich solution exits and the flue gas enters. A coarser packing must be used in the middle section to avoid excessive pressure drop from the higher liquid load. In-and-out intercooling removes all of the semi-rich liquid from the bottom of the top section, cools it to 40 °C, and feeds it to the top of the bottom section, effectively eliminating the middle section in the pump-around case. There are tradeoffs associated with lean loading, feed liquid flowrate, packing area, and pump-around rate (i.e., the amount of liquid fed back to the top of the second section). The absorber diameter is adjusted to achieve 70% flood in the bottom section.

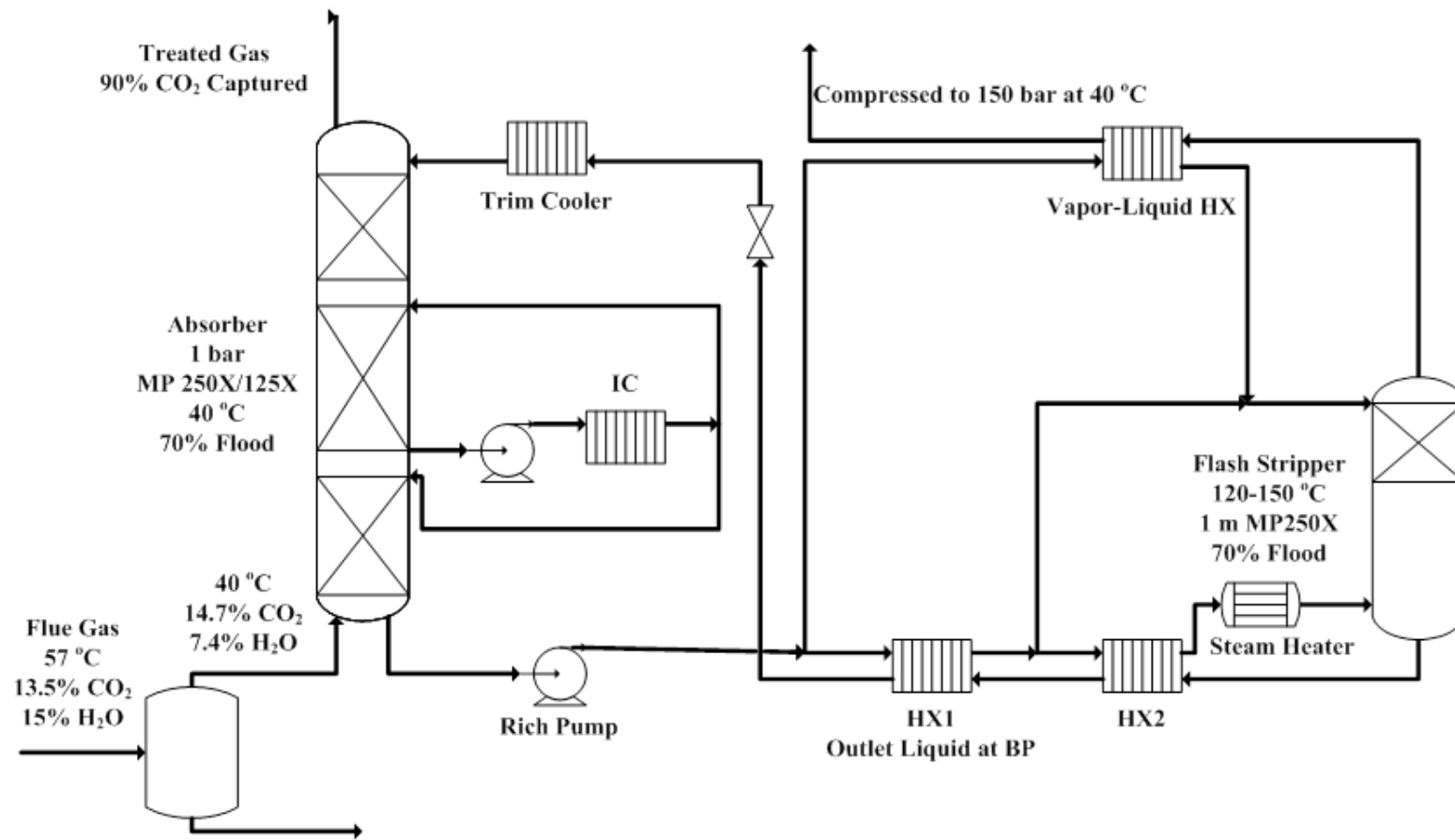


Figure 6-1: Process flow diagram for proposed advanced flash stripper with intercooled absorber

The base-case stripper contains both a cold rich bypass (CRB) and warm rich bypass (WRB) (Figure 6-1). A fraction of the cold rich solvent exiting the bottom of the absorber is heated by the product gas in a cross exchanger with a 20 °C LMTD before being fed into the top of the stripper. The remaining rich solvent is heated to its bubble point by a warm solution from the bottom of the stripper in a cross exchanger. Another portion of the warm rich solvent is bypassed, mixed with the CRB stream, and fed directly into the top of the stripper. The remaining rich solution is heated first by the hot lean liquid in a cross exchanger and finally by a steam heater to 150 °C and flashed into the bottom of the column. The two liquid-liquid cross exchangers are designed to have a combined 5 °C LMTD, as defined by Equation 6-11. Q is the heat duty of an exchanger, and the subscripts 1 and 2 refer to the two heat exchangers in series.

$$LMTD_{TOT} = \frac{Q_1 + Q_2}{\frac{Q_1}{LMTD_1} + \frac{Q_2}{LMTD_2}} \quad \text{Equation 6-11}$$

There are three tradeoffs: (1) the amounts of solvent removed in the CRB and WRB; (2) the total height of packing in the stripper; and (3) the lean loading. Increasing bypass decreases steam losses in the product stream but decreases the amount of heat recovered in the cross exchangers. Increasing stripper height increases the amount of CO₂ removed in the packing but increases the cost of the column.

6.4.1 Intercooled Absorber Optimization

The tradeoffs listed in Section 6.4 are all optimization opportunities. The lean loading optimization is based on energy performance and, therefore, is more closely

associated with the advanced flash stripper. The liquid flow rate and packing area are optimized simultaneously. Assuming 90 % removal, the liquid flow rate is a function of the packing area. As the packing area increases the liquid flow rate decreases until it reaches a minimum. As the packing area decreases the column approaches an isothermal condition with an infinite liquid flow rate. Between these extremes exists a case that balances the capital cost of packing area and the operating cost of circulating solvent. Ultimately a techno-economic analysis is needed to determine this point, but experience suggests that the optimum liquid flow rate is between 1.05 and 1.3 times the minimum liquid flow rate. As a first-order approximation this study always uses a flow rate equal to 1.2 times the minimum. With the liquid flow rate set, the packing area is minimized by adjusting the location of the intercooling. For an absorber with in-and-out intercooling this is relatively straightforward. An absorber with pump-around intercooling has three sections, and the middle section has less packing area per unit volume. This optimization is performed using the Aspen Plus[®] optimization tool. An optimum pump-around rate for coal-fired applications was approximated by Sachde to be five times the inlet vapor flow rate.

6.4.2 Advanced Flash Stripper Design and Optimization

The advanced flash stripper is designed to reduce the equivalent work by reducing both steam losses and sensible heat requirement. Equation 6-12 calculates the equivalent work, W_{EQ} (kJ/mol CO₂) as a function of reboiler duty, Q_i , reboiler temperature, T_{reb} , pump work, W_{pump} , and compressor work, W_{comp} . The sink temperature, T_{sink} , is assumed

to be 40⁰C. Equations 6-13 and 6-14 calculate W_{comp} as a function of inlet pressure, P_{in} . Equation 6-12 assumes a steam turbine efficiency of 75%.

$$W_{eq} = \sum_{i=1}^{n_{reboilers}} 0.75Q_i \left(\frac{T_i + 5K - T_{sink}}{T_i + 5K} \right) + W_{pumps} + W_{comps} \quad \text{Equation 6-12}$$

$$W_{comps} (kJ/mol CO_2) = 4.572 \log \left(\frac{148}{P_{in} (atm)} \right) - 4.096 \quad P_{in} \leq 4.5 atm \quad \text{Equation 6-13}$$

$$W_{comps} (kJ/mol CO_2) = 4.023 \log \left(\frac{148}{P_{in} (atm)} \right) - 2.181 \quad P_{in} > 4.5 atm \quad \text{Equation 6-14}$$

Contacting cold rich liquid with the hot product gas will reduce both the vapor pressure of water in the product and the hot side approach on the main cross exchanger. The amount of cold and warm liquid that is bypassed determines the extent to which these values are reduced. There is, of course, a limit to how much liquid can be bypassed usefully. Higher lean loading cases will not have enough steam to strip the CO₂ from the colder liquid entering the top of the column. If too much liquid is bypassed the desired lean loading will not be achievable. Lower lean loading cases will have higher concentrations of steam, but there must be enough liquid exiting the main cross exchanger to avoid a temperature pinch on the hot side of the exchanger. The equivalent work is minimized by adjusting the relative flow rates in the CRB and WRB without violating these physical constraints.

6.5 CALCULATING COST OF CO₂ AVOIDED

In order to compare the effects of process conditions on annualized CAPEX and energy cost, both expenses must be expressed in dollars per metric ton of CO₂ captured. The PEC can be generally converted to these units using Equation 6-15.

$$\$/MT\ CO_2 = \frac{\alpha \times \beta \times PEC}{Total\ MT\ captured\ per\ year} \quad \text{Equation 6-15}$$

In Equation 6-15 α converts the PEC to a total capital requirement (TCR) and β annualizes the cost. Literature values for α range from as low as 2 to as high as 10, depending on the process unit in question. The 2010 DOE Cost and Performance Baseline results in a value of 2.9. The annualizing factor, β , takes into account return on investment (10%), taxes (35% of return on investment), depreciation (3–10%, depending on plant lifetime), and maintenance (2–3%). Typical values of β range from 0.1 to 0.3.

6.6 RESULTS AND DISCUSSION

6.6.1 Minimum W_{EQ} Design Configuration

The minimum W_{EQ} design is summarized in the accompanying stream tables, Tables 6-1, 6-2, and 6-3, and equipment tables, Tables 6-4 and 6-5. Tables 6-6 and 6-7 are equipment tables for the simple stripper with intercooled absorber. The lean loading is 0.29 moles of CO_2 per mole of alkalinity. At this lean loading the L/G_{min} on a mole basis is 3.8. The operational L/G is 1.2 times the L/G_{min} , or 4.5 mol/mol. The solvent capacity is 1.0 mol CO_2 /kg solvent. This is approximately 20% greater than the solvent capacity typically reported for 8 m PZ when it is assumed that the nominal lean and rich loadings at 40 °C correspond to CO_2 equilibrium partial pressures of 0.5 and 5 kPa, respectively. The operational lean and rich CO_2 equilibrium partial pressures at 40 °C are 0.29 and 4.44 kPa, respectively. The cold rich bypass (CRB) draws off 4.5 mol % of the total liquid leaving the absorber. The warm rich bypass (WRB) draws off 11 mol % of the remaining liquid or 10.5 mol % of the liquid leaving the absorber. In all evaluated

cases the optimum design resulted in a larger WRB than CRB. This is primarily due to the physical limits of the liquid-vapor heat exchanger (X4). Because liquids exhibit much greater heat capacities, the amount of liquid that can be bypassed without pinching on the hot end of the cross exchanger is relatively small. The amount of vapor generated is nearly constant across all cases, so the maximum amount of liquid in the CRB is also nearly constant.

The total packing area of the absorber column is 373,000 m². The column diameter is 16.3 m, and the heights of the top, middle, and bottom sections are 4.25 m, 4.60 m, and 0.64 m, respectively. The location of the middle section suggests that the temperature bulge is near the bottom of the column. Generally speaking, as the L/G increases more heat is being carried by the liquid, causing the temperature bulge to migrate towards the bottom of the column. This trend is observed as the L/G is varied from 1.1 to 1.3 times the L/G_{min}. Across all cases the pump-around rate is fixed at an L/G of 5. The total intercooler duty is 175 MW, and the pressure drop on the amine side of the intercooler is 5 psi.

The total equivalent work, as calculated by Equation 6-12, is 28.7 kJ/molCO₂. The contributions to equivalent work from the reboiler, rich amine pump, and compressors are 18.0, 1.0, and 9.7 kJ per mole of CO₂, respectively. The regeneration pressure is 7.825 bar, and the CO₂ to H₂O ratio in the product gas is 3.6:1. It should be noted that the energy optimum for this configuration is relatively flat. Previous studies in which the rich loading is fixed and rich solvent bypasses are not considered have predicted dramatic increases in equivalent work on either side of the energy optimum.

The advanced flash stripper with intercooled absorber reduces these energy penalties in two ways: (1) at lower lean loading where the $\text{CO}_2/\text{H}_2\text{O}$ is relatively low the CRB and WRB significantly reduce steam losses, and (2) by not fixing the rich loading the solvent capacity at higher lean loading is greater than what would have been predicted in previous studies.

The two main cross exchangers, X2 and X3, have a combined log mean temperature difference (LMTD) of 5 K. The LMTDs of X2 and X3 are 4.6 K and 6.8 K, respectively. As the lean loading increases the LMTD of X2 decreases and the LMTD of X3 increases. This is a consequence of the CRB and WRB. Because it has lost CO_2 and some H_2O , the mass flow rate on the lean side of the exchanger is less than the mass flow rate on the rich side in the absence of bypasses. This mass imbalance will cause the temperature approach on the hot side to be larger than on the cold side. Bypassing rich solvent will reduce this imbalance, the hot side temperature approach, and the steam that must be supplied to the steam heater to account for the sensible heat. Because the opportunity for steam recovery by bypassing rich solvent decreases as lean loading increases, the LMTD of X3 increases.

The heat duties of X2 and X3 are 830 MW and 280 MW, respectively. This ratio increases as the lean loading increases. Because X2 heats the rich solvent to its bubble point, the heat duty of X2 is determined primarily by the regeneration pressure. As the lean loading increases from 0.2 to 0.35 moles of CO_2 per mole of alkalinity, the rich loading only increases from 0.38 to 0.41 moles of CO_2 per mole of alkalinity. Therefore, the bubble point temperature of the rich solvent is determined primarily by the pressure.

Because the regeneration pressure increases as the lean loading increases the bubble point temperature increases. This increases the duty of X2 relative to that of X3.

Table 6-1: Stream table for optimized advanced flash stripper with intercooled absorber

Stream Number	1	2	3	4	5	6	7	8	9
V-L Mole Fraction									
H₂O	0.1517	0.9999	0.07358	0.06999	0.8720	0.8714	0.8714	0.8714	0.8714
CO₂	0.1350	6.38E-05	0.1474	0.01733	1.03E-05	1.30E-05	1.30E-05	1.30E-05	1.30E-05
HCO₃⁻	0	0	0	0	0.002419	0.0029	0.0029	0.0029	0.0029
PZ	0	0	0	1.03E-05	0.001512	0.002002	0.002002	0.002002	0.002002
PZ(COO)₂²⁻	0	0	0	0	0.01494	0.01389	0.01389	0.01389	0.01389
PZCOO⁻	0	0	0	0	0.009562	0.01139	0.01139	0.01139	0.01139
PZH⁺	0	0	0	0	0.04185	0.04208	0.04208	0.04208	0.04208
H⁺PZCOO⁻	0	0	0	6.32E-11	0.05766	0.05633	0.05633	0.05633	0.05633
N₂	0.689	7.45E-06	0.7525	0.8816	3.91E-06	3.83E-06	3.83E-06	3.83E-06	3.83E-06
O₂	0.0243	4.97E-07	0.02654	0.03109	2.56E-07	2.50E-07	2.50E-07	2.50E-07	2.50E-07
Total	1	1	1	1	1	1	1	1	1
Vapor Fraction	1	0	1	1	0	0	0	0	0
Mole Flow (kmol/s)	22	1.855	20.15	17.19	100.0	209.9	209.9	209.9	110.0
Mass Flow (kg/s)	632.6	33.43	599.1	476.5	3095	6487	6487	6487	3400.
Temperature (K)	330.15	313.15	313.15	315.519	314.367	321.3055	321.3055	313.15	313.15
Pressure (Pa)	101325	101433	101433	101433	101433	101433	125526.2	125526.2	125526.2

Table 6-2: Stream table for optimized advanced flash stripper with intercooled absorber

Stream Number	10	11	12	13	14	15	16	17	18
V-L Mole Fraction									
H₂O	0.8714	0.8716	0.8716	0.8716	0.8618	0.8618	0.8618	0.8517	0.8441
CO₂	1.30E-05	1.03E-05	1.03E-05	1.03E-05	0.000645	0.000645	0.000645	0.01530	0.02691
HCO₃⁻	0.0029	0.002526	0.002526	0.002526	0.01175	0.01175	0.01175	0.009046	0.006515
PZ	0.002002	0.001524	0.001524	0.001524	0.0048	0.0048	0.0048	0.01190	0.02045
PZ(COO)₂²⁻	0.01389	0.01493	0.01493	0.01493	0.005648	0.005648	0.005648	0.003209	0.001724
PZCOO⁻	0.01139	0.009635	0.009635	0.009635	0.01625	0.01625	0.01625	0.02587	0.03011
PZH⁺	0.04208	0.04201	0.04201	0.04201	0.0393	0.0393	0.0393	0.04134	0.04007
H⁺PZCOO⁻	0.05633	0.05778	0.05778	0.05778	0.05979	0.05979	0.05979	0.04164	0.03013
N₂	3.83E-06	0	0	0	0	0	0	0	0
O₂	2.50E-07	0	0	0	0	0	0	0	0
Total	1	1	1	1	1	1	1	1	1
Vapor Fraction	0	0	0	0	1.00E-05	1.00E-05	1.00E-05	0.02419	0.05572
Mole Flow (kmol/s)	99.87	99.89	95.40	4.495	95.46	84.96	10.50	86.22	87.25
Mass Flow (kg/s)	3087	3095	2956	139.3	2956	2630	325.1	2630	2630
Temperature (K)	313.15	314.5197	314.5197	314.5197	394.0239	394.0239	394.0239	411.9464	423.15
Pressure (Pa)	125526.2	782498.5	782498.5	782498.5	782498.5	782498.5	782498.5	782498.5	782498.5

Table 6-3: Stream table for optimized advanced flash stripper with intercooled absorber

Stream Number	19	20	21	22	23	24	25	26	27
V-L Mole Fraction									
H₂O	0.8630	0.8622	0.2170	0.2169	0.8658	0.8670	0.8718	0.8718	0.8721
CO₂	0.00041	0.00056	0.7828	0.7828	0.000427	0.00013	1.07E-06	1.07E-06	6.35E-07
HCO₃⁻	0.01075	0.01147	0	1.51E-04	0.006967	0.006087	0.00135	0.001348	0.001055
PZ	0.004339	0.004658	0.000173	1.75E-07	0.02010	0.01871	0.01144	0.01144	0.01089
PZ(COO)₂²⁻	0.006435	0.005872	0	1.71E-09	0.001805	0.002595	0.008991	0.008999	0.009903
PZCOO⁻	0.01570	0.01609	0	3.52E-08	0.03099	0.03221	0.03295	0.03295	0.03259
PZH⁺	0.03932	0.03931	0	0.000151	0.04157	0.04348	0.05228	0.05230	0.05346
H⁺PZCOO⁻	0.06003	0.05988	1.92E-11	2.24E-05	0.03141	0.02981	0.02114	0.02113	0.01997
N₂	0	0	0	0	0	0	0	0	0
O₂	0	0	0	0	0	0	0	0	0
Total	1	1	1	1	1	1	1	1	1
Vapor Fraction	0	0	1	0.8121	0	0	0	0	0
Mole Flow (kmol/s)	4.497	15.00	3.435	3.434	99.19	99.16	99.14	99.14	99.14
Mass Flow (kg/s)	139.3	464.4	131.8	131.8	2963	2963	2963	2963	2963
Temperature (K)	384.3507	391.1395	392.2734	339.699	422.8568	397.8834	319.8781	319.8407	313.15
Pressure (Pa)	782498.5	782498.5	782500	782500	782500	782500	782500	101515	101325

Table 6-4: Equipment table for advanced flash stripper with intercooled absorber

Description	No. Trains	Type	Sizing Basis	PZ-AFS Process	Cost Source
Inlet Gas Blower	1	Centrifugal blower; SS or alloy process-wetter components	1.5 psi increase	4.9 MMlb/hr; 7.9 MW _e	Verbal quote from vendor for blower; PDQ\$ for motor
Absorber	1	Packed Tower (316SS Mellapak 250X/125X); Section heights = 4.25, 4.60, and 0.64 m; 316SS Shell and Distributors	Maximum flood of 70 %; section heights determined by Aspen Plus® optimization tool	16.3 m diameter; 9.5 m height	Vendor quotes for individual components
Absorber Intercooler	1	Plate and Frame; 316SS; 5 psi pressure drop	Cools solvent to 40°C and does not heat water more than 7°C	175 MW _{Th} ; 28.6°C LMTD	Vendor Quote
Absorber Intercooler Pump	1	Centrifugal ; 316SS	Flow rate from simulations	89,958 gpm; 85 ft; 30 pumps; 180 kW _e	PDQ\$
Rich Amine Pump	1	Centrifugal ; 316SS	Flow rate from simulations	42,733 gpm; 198 ft; 15 pumps; 2.5 MW _e	PDQ\$
Rich Amine Carbon Filter	1	316SS with Teflon Gasket	Treats 15 % of rich liquid flow	6,410 gpm	PDQ\$
Particulate Filter	1	316SS with Teflon Gasket	Treats 15 % of rich liquid flow	6,410 gpm	PDQ\$
Amine Cross Exchangers	1	Plate and Frame; 316SS	5°C total LMTD for amine/amine exchangers	1,110 MW _{Th} cumulative duty	Vendor Quote
Lean Solvent Cooler	1	Plate and Frame; 316SS	Cools solvent to 40°C and does not heat water more than 7°C	69 MW _{Th} ; 27.9°C LMTD	Vendor Quote

Table 6-5: Equipment table for advanced flash stripper with intercooled absorber

Description	No. Trains	Type	Sizing Basis	PZ-AFS Process	Cost Source
Stripper	1	HP Flash Vessel and 5 m packed column (316SS Mellapack 250X)	Maximum flood of 70 %; section height set at 5 m; 5 min residence time in HP flash vessel	5.8 m diameter	Vendor quotes for tower and PDQ\$ for HP flash vessel
Convective Steam Heater	1	Shell and tube; 316SS tubes and carbon steel shell	Figure 9-16; GPSA 10th	240 MW _{Th} ; 5°C LMTD; 45,888 m ² ;	PDQ\$
Compressors	1	Centrifugal; multistage; 316SS	86.63% polytropic efficiency	4 stages; 15.8 MW _e	Vendor Quote
Amine/Vapor Exchanger	1	Plate and Frame; 316SS	15°C LMTD for amine/vapor exchanger	34 MW _{Th}	Vendor Quote
Overhead Condenser	3	Shell and tube; 316SS tubes and carbon steel shell; water cooled	Process cooling to 40 °C	7.4 MW _{Th}	Vendor Quote
Overhead Accumulator	3	Horizontal vessel; 316SS	5 min. residence time	5ft. Diameter; 15 ft. length	PDQ\$
Makeup Amine Tank	1	Fixed roof tank	Estimated	200,000 gal	PDQ\$
Makeup Amine Pump	1	Centrifugal	Estimated	4 gpm at 103 ft; 0.12 kW _e	PDQ\$
Water Tank	1	Fixed roof tank	Estimated	75,000 gal	PDQ\$
Water Pump	1	Centrifugal	Estimated	71 gpm at 115 ft; 3 kW _e	PDQ\$
Reclaimer	1	Similar reclamation system to Case 12	% of solution sent and heated (0.5-3%)	1,260 gpm	Scaled vendor quote
Dehydration Unit	1	TEG unit	To pipeline specifications; 7 lb/MMSCF	190 MMSCFD	Scaled vendor quote

Table 6-6: Equipment table for short stripper with intercooled absorber

Description	No. Trains	Type	Sizing Basis	PZ-SS Process	Cost Source
Inlet Gas Blower	1	Centrifugal blower; SS or alloy process-wetter components	1.5 psi increase	4.9 MMlb/hr; 7.9 MW _e	Verbal quote from vendor for blower; PDQ\$ for motor
Absorber	1	Packed Tower (316SS Mellapak 250X/125X); Section heights = 4.25, 4.60, and 0.64 m; 316SS Shell and Distributors	Maximum flood of 70 %; section heights determined by Aspen Plus® optimization tool	16.3 m diameter; 9.5 m height	Vendor quotes for individual components
Absorber Intercooler	1	Plate and Frame; 316SS; 5 psi pressure drop	Cools solvent to 40°C and does not heat water more than 7°C	175 MW _{Th} ; 28.6°C LMTD	Vendor Quote
Absorber Intercooler Pump	1	Centrifugal ; 316SS	Flow rate from simulations	89,958 gpm; 85 ft; 30 pumps; 180 kW _e	PDQ\$
Rich Amine Pump	1	Centrifugal ; 316SS	Flow rate from simulations	42,733 gpm; 198 ft; 15 pumps; 2.5 MW _e	PDQ\$
Rich Amine Carbon Filter	1	316SS with Teflon Gasket	Treats 15 % of rich liquid flow	6,410 gpm	PDQ\$
Particulate Filter	1	316SS with Teflon Gasket	Treats 15 % of rich liquid flow	6,410 gpm	PDQ\$
Amine Cross Exchangers	1	Plate and Frame; 316SS	5°C LMTD for amine/amine exchangers	1,151 MW _{Th} cumulative duty	Vendor Quote
Lean Solvent Cooler	1	Plate and Frame; 316SS	Cools solvent to 40°C and does not heat water more than 7°C	24.6 MW _{Th} ; 25.5°C LMTD	Vendor Quote

Table 6-7: Equipment table for short stripper with intercooled absorber

Description	No. Trains	Type	Sizing Basis	PZ-AFS Process	Cost Source
Stripper	1	0.91 m packed column (316SS Mellapack 250X) with 5 m shell (316SS)	Maximum flood of 70 %; packing height set at 0.91 m	8.3 m diameter	Vendor quotes for tower and PDQ\$ for HP flash vessel
Reboiler	3	Shell and tube; 316SS tubes and carbon steel shell	Typical steam/amine flux 4,500-6,500 Btu/hr.ft ² (Figure 9-16; GPSA 10 th)	240 MW _{Th} ; 5°C LMTD; 45,888 m ² ;	PDQ\$
Compressors	1	Centrifugal; multistage; 316SS	86.63% polytropic efficiency	4 stages; 15.8 MW _e	Vendor Quote
Overhead Condenser	3	Shell and tube; 316SS tubes and carbon steel shell; water cooled	Process cooling to 40 °C	80.6 MW _{Th}	Vendor Quote
Overhead Accumulator	3	Horizontal vessel; 316SS	5 min. residence time	5ft. Diameter; 15 ft. length	PDQ\$
Makeup Amine Tank	1	Fixed roof tank	Estimated	200,000 gal	PDQ\$
Makeup Amine Pump	1	Centrifugal	Estimated	4 gpm at 103 ft; 0.12 kW _e	PDQ\$
Water Tank	1	Fixed roof tank	Estimated	75,000 gal	PDQ\$
Water Pump	1	Centrifugal	Estimated	71 gpm at 115 ft; 3 kW _e	PDQ\$
Reclaimer	1	Similar reclamation system to Case 12	% of solution sent and heated (0.5-3%)	1,260 gpm	Scaled vendor quote
Dehydration Unit	1	TEG unit	To pipeline specifications; 7 lb/MMSCF	190 MMSCFD	Scaled vendor quote

6.6.2 Scaling

6.6.2.1 Derating Summary

Table 6-8 summarizes the results of the derating analysis for the advanced flash stripper (PZ-AFS) and compares them to the results for the 2010 DOE Cost and Performance Baseline Case 12, a short stripper with PZ (PZ-SS), and a two stage flash with PZ (PZ-2SF).

Table 6-8: Derating summary for the four cases considered in this study and the 2012 DOE NETL Report

	Units	Case 12	PZ-SS	PZ-2SF	PZ-AFS
Thermal Input	MW _t	1934.5	1727	1737	1710
Equivalent Electrical Capacity of Boiler	MW _e	783	698.9	702.8	691.9
Total Steam Turbine Power	MW _e	662.8	629.6	628.9	630.0
Reboiler/Steam Heater Equivalent Power Lost	MW _e	120.1	69.2	73.9	61.9
Compression	MW _e	44.9	24.3	22.5	25.2
Capture Auxiliaries	MW _e	26.3	18.1	18.9	18.0
Balance of Plant Auxiliaries	MW _e	41.7	37.2	37.4	36.9
Net Power	MW _e	549.9	550.0	550.0	550.0
Boiler Efficiency	%	40.5	40.5	40.5	40.5
Coal Feed Rate	kg/s	71.3	63.6	64.0	63.3
Coal Feed Rate	MT/hr	257	229	231	227

The thermal input values assume a heating value of 27.135 MJ_t per kg of coal. The advanced flash stripper is more efficient than either of the previously reported PZ cases. This results in a reduction of parasitic losses and, thus, a smaller coal-fired power plant. This improvement is driven by the 10.5% reduction in reboiler/steam heater equivalent power loss. A closer hot-side temperature approach and lower concentration of steam leaving the process reduces the heat that must be supplied by the reboiler or

steam heater to regenerate the solvent. A larger percentage of the heat supplied is desorbing CO₂ from the solvent.

6.6.2.2 Scaling Purchase Equipment Cost (PEC) to 2010 DOE Cost and Performance

Baseline

Table 6-9 summarizes the cost of each process unit for all four cases in this study. A scaling exponent was calculated per the method outlined in the 2012 DOE NETL Report. If it is assumed that increasing the size of the plant will increase the size of the process unit, a multiplier of 0.6 is used. If increasing the size of the plant will necessitate the purchase of additional units, a multiplier of 1.0 is used. The weighted prices of each process unit are added together and divided by the total cost of the process at 593 MW_e. The result is used as a scaling exponent for calculating the purchased equipment cost of the capture and compression units at given power plant electrical capacity, CAP, using Equations 6-16 and 6-17, respectively.

$$PEC_{Capture} = 66,881,000 \left(\frac{CAP}{593MW} \right)^{0.77} \quad \text{Equation 6-16}$$

$$PEC_{Compression} = 12,198,000 \left(\frac{CAP}{593MW} \right)^{0.62} \quad \text{Equation 6-17}$$

The PEC of the PZ-AFS configuration is slightly more than that of the PZ-2SF for a 593 MW_e gross electrical generation. The greatest difference between the configurations is PEC for the cross exchangers and the convective steam heaters. The PZ-AFS attempts to reduce steam requirement by (1) recovering steam in the product stream by bypassing rich cold rich solvent and (2) reducing the hot-side temperature approach and, thus, the portion of the steam heater duty associated with the sensible heat

of the solvent. When going from the PZ-SS to the PZ-AFS the reduction in the CAPEX of the steam heaters (\$6,460,000) is offset by the increase in the CAPEX of the cross exchangers (\$4,316,000) and absorber column (\$2,266,000). The reduction in steam heater PEC and increase in cross exchanger PEC are due to a redistribution of heat duties. The increase in absorber PEC is a result of the pump-around intercooling configuration. The absorber in the PZ-AFS requires approximately 35 % less packing area to capture 90 % of the CO₂ from the 593 MW_e case. However, the pump-around intercooling configuration requires an additional set of distributors and supports, as well as a larger heat exchanger and pump for the additional liquid load in the middle section of the column. Pump-around intercooling improves the solvent capacity and, thus, should also reduce the steam heater duty. This analysis suggests that there is no net effect on CAPEX associated with the configuration, but the reduction in OPEX improves the cost of CO₂ avoidance.

It should also be noted that there is a slight increase in the cost of the compressor for the PZ-AFS case. The PEC of the compressor train is scaled to inlet vapor flow rate and pressure. The average inlet pressure of the PZ-2SF configuration is greater than that of the PZ-SS or PZ-AFS configurations. The pressure of the PZ-AFS (7.8 bar) is slightly greater than that of the PZ-SS (7.4 bar), which accounts for the slight reduction in compressor train PEC.

Table 6-9: Prices of unit operations for PZ-SS, MEA-SS, and PZ-AFS assuming 593 MWe

Description	PZ-SS	Description	MEA-SS	Description	PZ-AFS
<i>Inlet Gas Blower</i>	2,841,000	<i>Inlet Gas Blower</i>	2,841,000	<i>Inlet Gas Blower</i>	2,841,000
<i>Absorber</i>	14,165,000	<i>Absorber</i>	18,846,000	<i>Absorber</i>	14,165,000
<i>Absorber Intercooler</i>	1,699,000	<i>Absorber Intercooler</i>	N/A	<i>Absorber Intercooler</i>	1,699,000
<i>Absorber Intercooler Pump</i>	1,364,000	<i>Reflux Pump</i>	53,000	<i>Absorber Intercooler Pump</i>	1,364,000
<i>Rich Amine Pump</i>	820,000	<i>Rich Amine Pump</i>	472,000	<i>Rich Amine Pump</i>	820,000
<i>Rich Amine Carbon Filter</i>	125,000	<i>Rich Amine Carbon Filter</i>	147,000	<i>Rich Amine Carbon Filter</i>	125,000
<i>Particulate Filter</i>	136,000	<i>Particulate Filter</i>	205,000	<i>Particulate Filter</i>	136,000
<i>Rich/Lean Amine Exchanger</i>	17,507,000	<i>Rich/Lean Amine Exchanger</i>	6,435,000	<i>Amine Cross Exchangers</i>	18,794,000
<i>Lean Solvent Cooler</i>	392,000	<i>Lean Solvent Cooler</i>	3,677,000	<i>Lean Solvent Cooler</i>	914,000
<i>Stripper</i>	1,136,000	<i>Stripper</i>	3,084,000	<i>Stripper Column</i>	2,110,000
				<i>HP Flash Vessel</i>	1,121,000
<i>Reboiler</i>	20,627,000	<i>Reboiler</i>	15,769,000	<i>Steam Heater</i>	8,302,000
<i>Overhead Condenser</i>	1,702,000	<i>Overhead Condenser</i>	3,348,000	<i>Overhead Condenser</i>	341,000
				<i>Vapor-Liquid Exchanger</i>	261,000
<i>Overhead Accumulator</i>	49,000	<i>Condenser Accumulator</i>	84,000	<i>Overhead Accumulator</i>	33,000
<i>Compressors</i>	10,601,000	<i>Compressors</i>	17,411,000	<i>Compressors</i>	10,153,000
<i>Multistage Centrifugal Pump</i>	540,000	<i>Multistage Centrifugal Pump</i>	853,000	<i>Multistage Centrifugal Pump</i>	540,000
<i>Makeup Amine Tank</i>	345,000	<i>Makeup Amine Tank</i>	227,000	<i>Makeup Amine Tank</i>	345,000
<i>Makeup Amine Pump</i>	9,000	<i>Makeup Amine Pump</i>	3,000	<i>Makeup Amine Pump</i>	9,000
<i>Water Tank</i>	103,000	<i>Water Tank</i>	112,000	<i>Water Tank</i>	103,000
<i>Water Pump</i>	13,000	<i>Water Pump</i>	9,000	<i>Water Pump</i>	13,000
<i>Lean PZ Pump</i>	0	<i>Lean PZ Pump</i>	547,000	<i>Lean PZ Pump</i>	0
<i>Reclaimer</i>	4,089,000	<i>Reclaimer</i>	4,508,000	<i>Reclaimer</i>	4,020,000
<i>Dehydration Unit</i>	1,966,000	<i>Dehydration Unit</i>	1,966,000	<i>Dehydration Unit</i>	1,966,000
Total	80,229,000	Total	81,853,000	Total	70,487,000
Capture	67,122,000	Capture	60,367,000	Capture	57,828,000
Compression	13,107,000	Compression	20,230,000	Compression	12,659,000

6.6.3 CAPEX Summary

Table 6-10 compares the PEC for 2010 Cost and Performance Baseline Case 12 and the three PZ cases in 2007 dollars. The power plant capacity reflects a derating to 550 MW_e net production and 90% CO₂ avoided.

Table 6-10: PEC for capture and compression equipment for all four cases scaled to 550 MW_e net power production

	Units	Case 12	PZ-SS	PZ-2SF	PZ-AFS
Power Plant Capacity	MW _e	783	698.9	702.8	691.9
PEC of Capture	\$MM	207.8	168.0	153.3	151.4
PEC of Compression	\$MM	27.6	16.1	15.6	16.1
Total	\$MM	235.4	184.1	168.9	167.5

The PZ processes are categorically less expensive than the MEA-Econamine process in Case 12. The prices in Table 6-10 are reflective of relative differences in both CAPEX and OPEX. Because the plants have been derated to 550 MW_e net power production, the thermal efficiency of the CO₂ capture plant determines the gross power plant capacity. The contribution of CAPEX and OPEX to the total plant PEC requires a closer analysis. For example the PZ-SS and PZ-2SF cases only differ by 0.6% in required power plant capacity, but the PZ-2SF PEC is 8.3% less than that of the PZ-SS. The decrease in PEC between the cases is almost entirely due to the decrease in CAPEX from using two flash vessels and steam heaters rather than a stripper and reboiler. Table 6-10 suggests that the PEC of the advanced flash stripper is nearly identical to that of the two stage flash. The decrease in CAPEX is due to the improved energy performance.

Another difference between the cases worth noting is the actual percentage of CO₂ that is being captured relative to a 550 MW_e plant without CO₂ capture and compression equipment. The CO₂ scrubbing processes are designed to capture 90% of

the total CO₂ in the plant flue gas. If the capacity of the plant is being increased to guarantee 550 MW_e net power production, the CO₂ scrubber has to be scaled to accommodate the added capacity. Because 90% of the total CO₂ in the plant flue gas is being capture, 10% is being emitted. Increasing the capacity of the plant will increase the magnitude of that 10% and, thus, decrease the percent CO₂ avoided. Table 6-11 summarizes the CO₂ avoided across the four cases in this study.

Table 6-11: CO₂ avoided for all four cases on the basis of 550 MW_e net power produced

	Units	Case 12	PZ-SS	PZ-2SF	PZ-AFS
Power Plant Capacity (Gross)	MW _e	783	698.9	702.8	691.9
Power Plant Capacity (Net)	MW _e	550	550	550	550
Percent Captured	%	90	90	90	90
Percent Avoided	%	85.8	87.3	87.2	87.4

To avoid 90% of the CO₂ emissions the process must be either perfectly efficient or designed for a greater percentage CO₂ captured. Future studies will consider the latter as a possible route to achieving 90% avoided.

6.6.4 Absorber Configuration

The processes presented in the next few sections were described in detail in Section 5.4.4. All prices represent the cost of CO₂ capture from the coal fired power plant with 550 MW_e net output. Figure 6-2 compares the total cost of CO₂ capture for the adiabatic absorber, absorber with in-and-out intercooling, and absorber with pump-around intercooling with 8 m PZ and the advanced flash stripper. It should be noted that the prices in Figure 6-3 do not include the cost of transportation, storage, and monitoring (TS&M), which can range from \$10-15/MT CO₂.

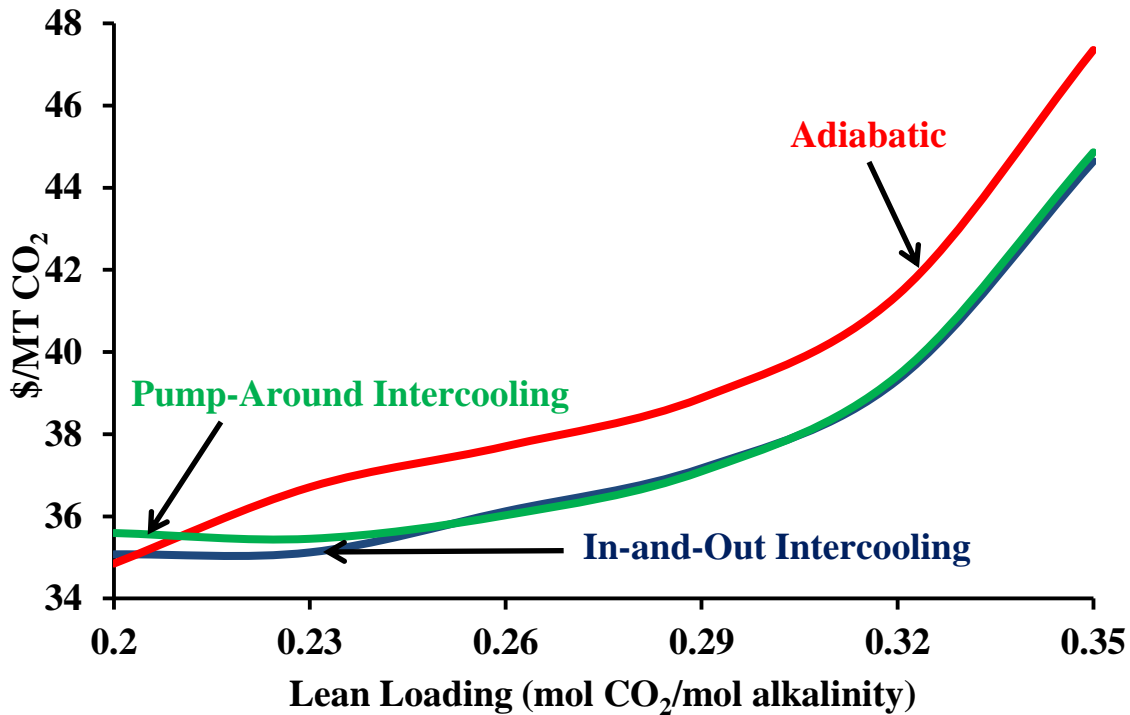


Figure 6-2: Total cost of CO₂ capture for adiabatic, in-and-out intercooled, and pump-around intercooled configurations with 8 m PZ, 90% removal, and the advanced flash stripper. $\alpha\beta=1$ and COE=\$0.10/kWh.

At a lean loading of 0.32 mol CO₂/mol alkalinity in-and-out intercooling and pump-around intercooling reduce the total cost of CO₂ capture by \$2.00/MT. Both intercooled configurations show comparable improvement in the total cost of CO₂ capture above a lean loading of 0.24 mol CO₂/mol alkalinity. As lean loading decreases the benefit of intercooling to equivalent work disappears (Figure 5-13). The added distributors, pumps, and heat exchangers required for intercooling increase annualized CAPEX without decreasing energy cost, which explains the advantage of the adiabatic absorber and the disadvantage of pump-around intercooling at a lean loading of 0.20 mol CO₂/mol alkalinity. From this point forward in-and-out intercooling will be the

configuration of choice. Table 6-12 compares the costs associated with the three configurations at lean loadings of 0.20, 0.29, and 0.35 mol CO₂/mol alkalinity.

Table 6-12: Cost of CO₂ captured for each absorber configuration with 8 m PZ and lean loadings of 0.20, 0.29, and 0.35 mol CO₂/mol alkalinity, 40 °C vapor and liquid feed, L/L_{min}=1.2, and 90% removal

Lean LDG	Property	Units	Adiabatic	IO IC	PA IC
0.20	Total Cost	\$/MT CO ₂	34.9	35.1	35.5
	Annualized CAPEX	\$/MT CO ₂	15.4	15.5	16.1
	Energy Cost	\$/MT CO ₂	19.5	19.6	19.3
	Absorber Price	\$/MT CO ₂	3.6	3.5	4.2
	Packing Cost	\$/MT CO ₂	1.0	0.52	0.62
	Exchanger Cost	\$/MT CO ₂	2.7	2.8	2.9
	Capacity	mol CO ₂ /kg sol	1.70	1.71	1.75
0.29	Total Cost	\$/MT CO ₂	38.9	37.2	37.1
	Annualized CAPEX	\$/MT CO ₂	19.2	18.7	19.0
	Energy Cost	\$/MT CO ₂	19.7	18.5	18.1
	Absorber Price	\$/MT CO ₂	3.3	4.1	4.8
	Packing Cost	\$/MT CO ₂	0.61	0.69	0.76
	Exchanger Cost	\$/MT CO ₂	6.0	5.4	5.2
	Capacity	mol CO ₂ /kg sol	0.77	0.94	1.00
0.35	Total Cost	\$/MT CO ₂	47.4	44.6	44.9
	Annualized CAPEX	\$/MT CO ₂	26.1	25.1	25.5
	Energy Cost	\$/MT CO ₂	21.2	19.5	19.3
	Absorber Price	\$/MT CO ₂	4.4	5.6	6.2
	Packing Cost	\$/MT CO ₂	1.33	1.48	1.66
	Exchanger Cost	\$/MT CO ₂	10.8	9.5	9.5
	Capacity	mol CO ₂ /kg sol	0.45	0.54	0.55

6.6.5 Effect of Absorber Temperature

Figure 6-3 shows the estimated cost of CO₂ capture for 7 m MDEA/2 m PZ with in-and-out intercooling and the advanced flash stripper with the absorber operating at 40 °C, 30 °C, and 20 °C. The vertical line at 1.8 kPa corresponds to the lean loading limit. At low lean CO₂ equilibrium partial pressures the cost of CO₂ capture is nearly constant at a given absorber temperature. Decreasing absorber temperature from 40 °C to 20 °C decreases the cost of CO₂ capture by 9.3%, which is driven by the 15% reduction

in energy cost. As the lean loading approaches the maximum lean loading limit the cost of CO₂ capture increases as capacity decreases and packing requirement increases for all temperatures.

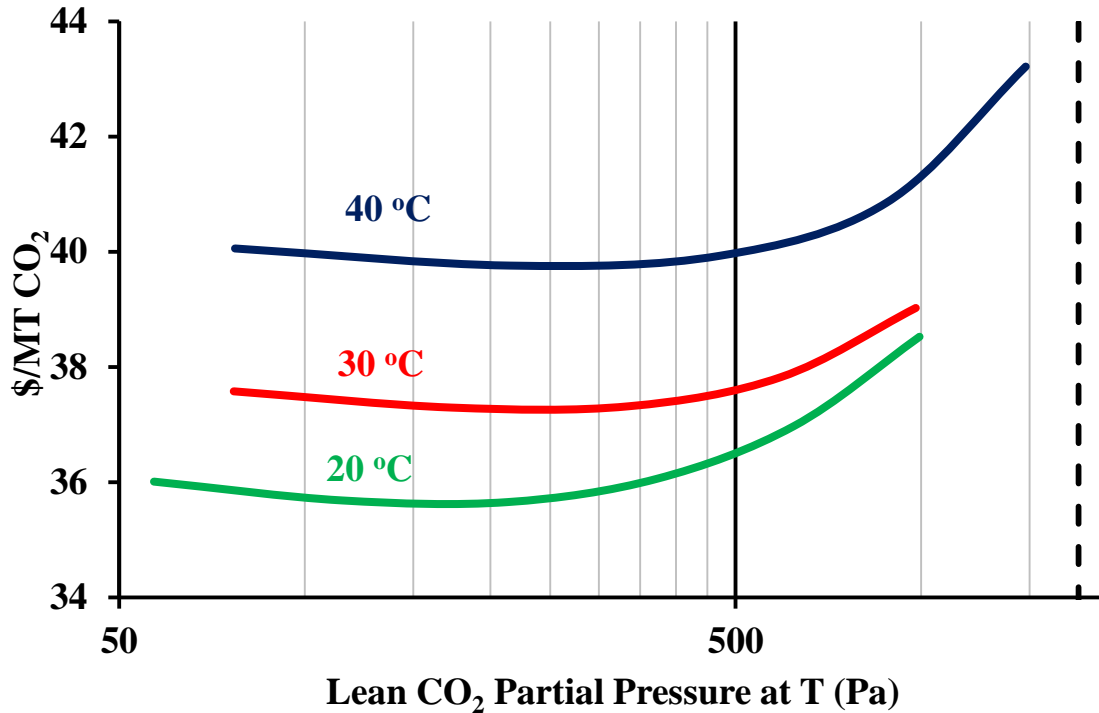


Figure 6-3: Total cost of CO₂ capture for 7 m MDEA/2 m PZ with in-and-out intercooling, the advanced flash stripper, and a variable absorber temperature. $\alpha\beta=1$ and COE=\$0.10/kWh.

Table 6-13 compares the costs associated with the three absorber temperatures at lean loadings of 0.13, 0.19, and 0.22 mol CO₂/mol alkalinity. At a given lean loading the absorber price does not change appreciably, but the capacity increases by 60-85% as the absorber is cooled from 40 °C to 20 °C. This may be attributed to the attractive CO₂ driving forces at lower absorber temperatures. The improvement in capacity at lower temperatures decreases both the annualized CAPEX and energy cost.

Table 6-13: Cost of CO₂ captured for each absorber temperature with 7 m MDEA/2 m PZ and lean loadings of 0.13, 0.19, and 0.22 mol CO₂/mol alkalinity, 90% removal, L/L_{min}=1.2, and in-and-out intercooling

Lean LDG	Property	Units	40 °C	30 °C	20 °C
0.13	Total Cost	\$/MT CO ₂	39.9	37.3	36.0
	Annualized CAPEX	\$/MT CO ₂	20.1	18.6	17.9
	Energy Cost	\$/MT CO ₂	19.8	18.7	18.1
	Absorber Price	\$/MT CO ₂	4.8	4.6	4.8
	Capacity	mol CO ₂ /kg sol	0.55	0.72	0.89
0.19	Total Cost	\$/MT CO ₂	43.2	37.8	35.6
	Annualized CAPEX	\$/MT CO ₂	23.9	20.1	18.8
	Energy Cost	\$/MT CO ₂	19.3	17.7	16.8
	Absorber Price	\$/MT CO ₂	6.9	5.7	5.8
	Capacity	mol CO ₂ /kg sol	0.42	0.59	0.78
0.22	Total Cost	\$/MT CO ₂	N/A	39.0	36.1
	Annualized CAPEX	\$/MT CO ₂	N/A	21.6	19.7
	Energy Cost	\$/MT CO ₂	N/A	17.4	16.3
	Absorber Price	\$/MT CO ₂	N/A	6.6	6.7
	Capacity	mol CO ₂ /kg sol	N/A	0.48	0.69

6.6.6 CO₂ Removal

Figure 6-4 compares the total cost of CO₂ capture for 7 m MDEA/2 m PZ and 8 m PZ with 90% and 99% CO₂ removal, and Table 6-14 compares the cases at a lean equilibrium CO₂ partial pressure of 75 Pa. The absorber uses in-and-out intercooling, and the regenerator is the advanced flash stripper. For both amines the cost of increasing removal from 90% to 99% increases the total cost of CO₂ capture by less than 1%. Above a lean CO₂ partial pressure of 0.44 kPa 7 m MDEA/2 m PZ outperforms 8 m PZ. Below this pressure the capacity of 8 m PZ gives it an advantage over 7 m MDEA/2 m PZ. Above this pressure the capacity of 8 m PZ drops dramatically relative to that of 7 m MDEA/2 m PZ.

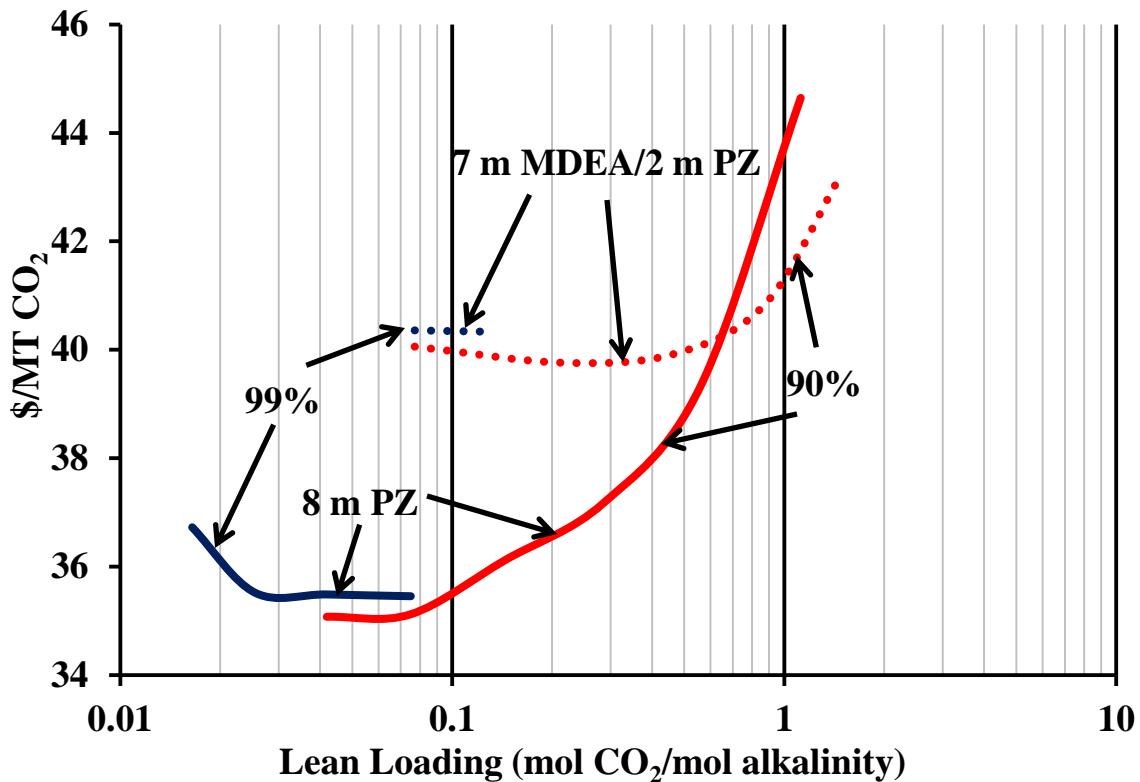


Figure 6-4: Total cost of CO₂ capture at 90% and 99% removal for 7 m MDEA/2 m PZ and 8 m PZ at 40 °C with an absorber with in-and-out intercooling and the advanced flash stripper. $\alpha\beta=1$ and COE=\$0.10/kWh.

Table 6-14: Cost of CO₂ captured for 7 m MDEA/2 m PZ and 8 m PZ with 90% and 99% removal with $L/L_{\min}=1.2$, in-and-out intercooling, 40 °C vapor and liquid feed, and a lean loading corresponding to a CO₂ equilibrium partial pressure of 75 Pa.

Amine	Property	Units	90%	99%
8 m PZ	Total Cost	\$/MT CO ₂	35.1	35.5
	Annualized CAPEX	\$/MT CO ₂	16.1	16.2
	Energy Cost	\$/MT CO ₂	19.0	19.3
	Absorber Price	\$/MT CO ₂	3.6	3.7
	Compressor Price	\$/MT CO ₂	4.1	4.1
	Capacity	mol CO ₂ /kg sol	1.44	1.37
7 m MDEA/ 2 m PZ	Total Cost	\$/MT CO ₂	39.8	40.3
	Annualized CAPEX	\$/MT CO ₂	18.7	19.0
	Energy Cost	\$/MT CO ₂	21.1	21.3
	Absorber Price	\$/MT CO ₂	4.2	4.3
	Compressor Price	\$/MT CO ₂	5.7	5.6
	Capacity	mol CO ₂ /kg sol	1.01	0.97

6.6.7 Sensitivity Analysis

The results presented in Figure 6-4 are dependent upon the assumed values of $\alpha\beta$ and COE. Increasing COE or $\alpha\beta$ will emphasize energy cost or annualized CAPEX, respectively, and it will affect the lean loading range in which 7 m MDEA/2 m PZ outperforms 8 m PZ. Table 6-15 considers the sensitivity of the results to values of $\alpha\beta$ and COE. The average marginal cost of 99% capture refers to the percent increase in total cost of capture required to go from 90% to 99%. The minimum pressure for 7 m MDEA/2 m PZ refers to the lean equilibrium CO₂ partial pressure at which 8 m PZ and 7 m MDEA/2 m PZ have equal total costs of CO₂ capture at 90% removal.

Table 6-15: Sensitivity of total cost of CO₂ capture to $\alpha\beta$ and COE

$\alpha\beta$	COE (\$/kWh)	Average Marginal Cost of 99% Capture	Minimum Pressure for 7 m MDEA/2 m PZ (kPa)
1	0.1	0.76%	0.44
1	0.2	1.01%	0.60
1	0.05	0.49%	0.31
2	0.1	0.49%	0.31
0.5	0.1	1.01%	0.60

Increasing the ratio of $\alpha\beta$ to COE shifts the point at which 8 m PZ and 7 m MDEA/2 m PZ have equal total costs of capture to higher lean equilibrium CO₂ partial pressures. This suggests that 7 m MDEA/2 m PZ benefits from capital intensive projects with inexpensive electricity. Consequently, regions with high costs of electricity will almost certainly opt for 8 m PZ.

Over the full range of combinations of $\alpha\beta$ and COE increasing the removal rate from 90% to 99% increases the total cost of CO₂ capture by 1% or less. The percent

increase is a function of the ratio of $\alpha\beta$ to COE, and it is fit by Equation 6-18 for ratio values between 4 and 40.

$$\% \text{ increase} = -0.37 \ln \left(\frac{\alpha\beta}{COE(\$ / kWh)} \right) + 1.6 \quad \text{Equation 6-18}$$

According to Equation 6-18 the marginal cost of increasing the removal rate from 90% to 99% will be zero when the ratio of $\alpha\beta$ to COE is ~ 77 (i.e. COE is effectively \$0/kWh). As the ratio approaches zero the marginal cost becomes the marginal increase in equivalent work (1.45%) and, thus, Equation 6-18 no longer applies.

6.7 CONCLUSIONS

- At high lean loading intercooling reduces the total cost of CO₂ capture by \$2/MT in 8 m PZ. At low lean loading the advantage of intercooling diminishes, and the adiabatic absorber is the optimum configuration at a lean loading of 0.20 mol CO₂/mol alkalinity.
- Decreasing absorber temperature for 7 m MDEA/2 m PZ at low lean loading from 40 °C to 20 °C decreases total cost of CO₂ capture by 9.3%.
- Increasing the CO₂ removal from 90% to 99% increases the cost of CO₂ capture by less than 1% for both 8 m PZ and 7 m MDEA/2 m PZ.
- 7 m MDEA/2 m PZ is less expensive than 8 m PZ for projects that are capital intensive with inexpensive electricity. 8 m PZ always does better than 7 m MDEA/2 m PZ at over-stripped conditions.
- The advanced flash stripper with intercooled absorber represents an improvement in both operating costs (5.8%) over the short stripper and capital costs (0.8%) over two

stage flash configurations reported in the 2012 DOE NETL Report for a supercritical pulverized coal power plant with 550 MW_e net capacity.

- The added power plant capacity required to avoid 90% of the CO₂ and maintain 550 MW_e net capacity was reduced to 141.9 MW_e, and the purchased equipment cost was reduced to \$167.5 MM.
- The main contributors to the capital cost of CO₂ capture and compression are the absorber, cross exchangers, reboiler, and compressor.
- When evaluating the impact of CO₂ avoidance on the cost of electricity more attention should be paid to the impact of assumptions relating purchased equipment cost to total capital requirement.

Chapter 7: Conclusions and Recommendations

7.1 CONCLUSIONS

Thermodynamic Modeling

- Model predictions for the heat of CO₂ absorption at 40 °C and an equilibrium CO₂ partial pressure of 1,500 Pa for 8 m PZ, 5 m PZ, 7 m MDEA/2 m PZ, and 5 m MDEA/5 m PZ are 70.5, 69.6, 70.7, and 74.5 kJ/mol CO₂, respectively.
- Model predictions for the CO₂ capacity at 40 °C between equilibrium CO₂ partial pressures of 500 Pa and 5,000 Pa for 8 m PZ, 5 m PZ, 7 m MDEA/2 m PZ, and 5 m MDEA/5 m PZ are 0.799, 0.573, 0.813, and 0.970 mol CO₂/kg H₂O + Amine, respectively. When normalized by viscosity to the 0.25 power these values are 0.787, 0.738, 0.846, and 0.904 mol CO₂/kg H₂O + Amine, respectively.
- The temperature dependence of the heat of absorption for 8 m PZ is the result of shifting towards generation of HCO₃⁻ and H⁺PZCOO⁻ at high temperatures. MDEA shows very little variation in the temperature dependence of the heat of absorption across operationally significant loadings. MDEA/PZ reflects both of these trends, with the effects balancing each other at a loading of 0.23 mol CO₂/mol alkalinity for 7 m MDEA/2 m PZ.

Kinetic Modeling

- The optimum viscosity normalized capacity, heat of absorption, and k_g' are achieved with 15 wt % PZ/ 35 wt % MDEA (5.4 mol % PZ/ 9.1 mol % MDEA).

- At the nominal lean condition (i.e. 500 Pa equilibrium partial pressure of CO₂) the four solvents evaluated in order from fastest to slowest CO₂ absorption rate are 5 m PZ, 8 m PZ, 5 m MDEA/5 m PZ, and 7 m MDEA/2 m PZ. At the nominal rich condition (i.e. 5,000 Pa equilibrium partial pressure of CO₂) 5 m PZ still has the fastest CO₂ absorption rate, but the other three solvents have converged to a similar CO₂ absorption rate that is 30% less than that of 5 m PZ.
- The regressed temperature dependence of the binary diffusivity of reactants and products ($T^{1.06}$) is comparable to Wilke-Chang predictions (T^1). The regressed viscosity dependence ($\mu^{-1.45}$) is greater than that predicted by Wilke-Chang (μ^{-1}).
- For all solvents at low loadings and temperatures the absorption rate of CO₂ is limited by reaction kinetics; at high loadings and temperatures the diffusion of reactants and products is limiting.

Process Modeling

- Increasing CO₂ removal in an adiabatic absorber from 90% to 99% for 7 m MDEA/2 m PZ at a lean loading of 0.07 mol CO₂/mol alkalinity increases packing area by 64% and equivalent work by 1%. Higher CO₂ absorption rates at the lean conditions avoid doubling the packing requirement, and a slight reduction in capacity induces the slight increase in equivalent work.
- Cooling an adiabatic absorber with 7 m MDEA/2 m PZ and a liquid flow rate that is 1.2 times the minimum increases capacity by 16-17% and packing area by 2-5X between lean loadings of 0.07 and 0.19 mol CO₂/mol alkalinity.

- The advanced flash stripper reduces equivalent work by 4-14% relative to the simple stripper. The most significant improvement is observed at low lean loadings.
- Absorber complexity directly addresses sensible heat losses, and stripper complexity directly addresses steam losses.

Economic Modeling

- Increasing the CO₂ removal from 90% to 99% increases the cost of CO₂ capture by less than 1% for both 8 m PZ and 7 m MDEA/2 m PZ.
- For all amines decreasing the lean loading decreases the total cost of CO₂ capture.
- At high lean loading intercooling reduces the total cost of CO₂ capture by \$2/MT in 8 m PZ. At low lean loading the advantage of intercooling diminishes, and the adiabatic absorber is the optimum configuration at a lean loading of 0.20 mol CO₂/mol alkalinity.
- Decreasing absorber temperature for 7 m MDEA/2 m PZ at low lean loading from 40 °C to 20 °C decreases total cost of CO₂ capture by 9.3%.
- 7 m MDEA/2 m PZ is less expensive than 8 m PZ for projects that are capital intensive with inexpensive electricity. 8 m PZ is always less expensive than 7 m MDEA/2 m PZ at over-stripped conditions.

7.2 RECOMMENDATIONS

Thermodynamic Modeling

- Expand the set of regressed experimental data to include over-stripped conditions.
- Add amines and amine blends to the Independence framework with a more diverse offering of CO₂ absorption rates, heats of absorption, and capacities. The current set

of amines is inadequate for determining the relative effects of these properties on process performance.

- Modify the set of experimental data used to regress MDEA/H₂O/CO₂ to include more recent and more accurate CO₂ solubility data.

Kinetic Modeling

- Examine in greater detail the effect of viscosity on binary diffusivities in concentrated amines and at elevated temperature.
- Modify the binary diffusivity calculation to differentiate between charged and uncharged species in the liquid phase.

Process Modeling

- The advanced flash stripper should represent the base case when developing new process configurations. For all amines, absorber configurations, and lean loadings it outperforms the simple stripper.
- Evaluate process performance at removal between 90% and 99%.
- Determine the effect of removal on process performance for 5 m PZ. The wider solubility window of 5 m PZ relative to that of 8 m PZ may allow for higher removal in pilot plant campaigns.

Economic Modeling

- Modify the method for estimating the price of the compressor by compiling a more diverse and detailed set of vendor quotes.
- Include the economics associated with water management in the calculated total cost of CO₂ capture.

- After expanding the set of amines represented by the Independence model determine the value of amine properties so that new amines can be screened on the basis of capacity, CO₂ absorption rate, and heat of absorption.

Appendix A: 5deMayo Thermodynamics

Table A-1: Regression results for PZ/H₂O

Parameter	Species	Value	Standard Dev.
NRTL 1	PZ-H ₂ O	-0.34	0.10
NRTL 1	H ₂ O-PZ	-8.23	1.78
NRTL 3	PZ-H ₂ O	0.17	0.018
HENRY 1	PZ-H ₂ O	28.2	0.96
(HENRY 2)/313	PZ-H ₂ O	-24.6	0.99
CPIG 1 (J/kmol.K)	PZ	-5.29x10 ⁵	1.24x10 ⁵
(CPIG 2)x313 (J/kmol.K)	PZ	1.10x10 ⁶	1.10x10 ⁵

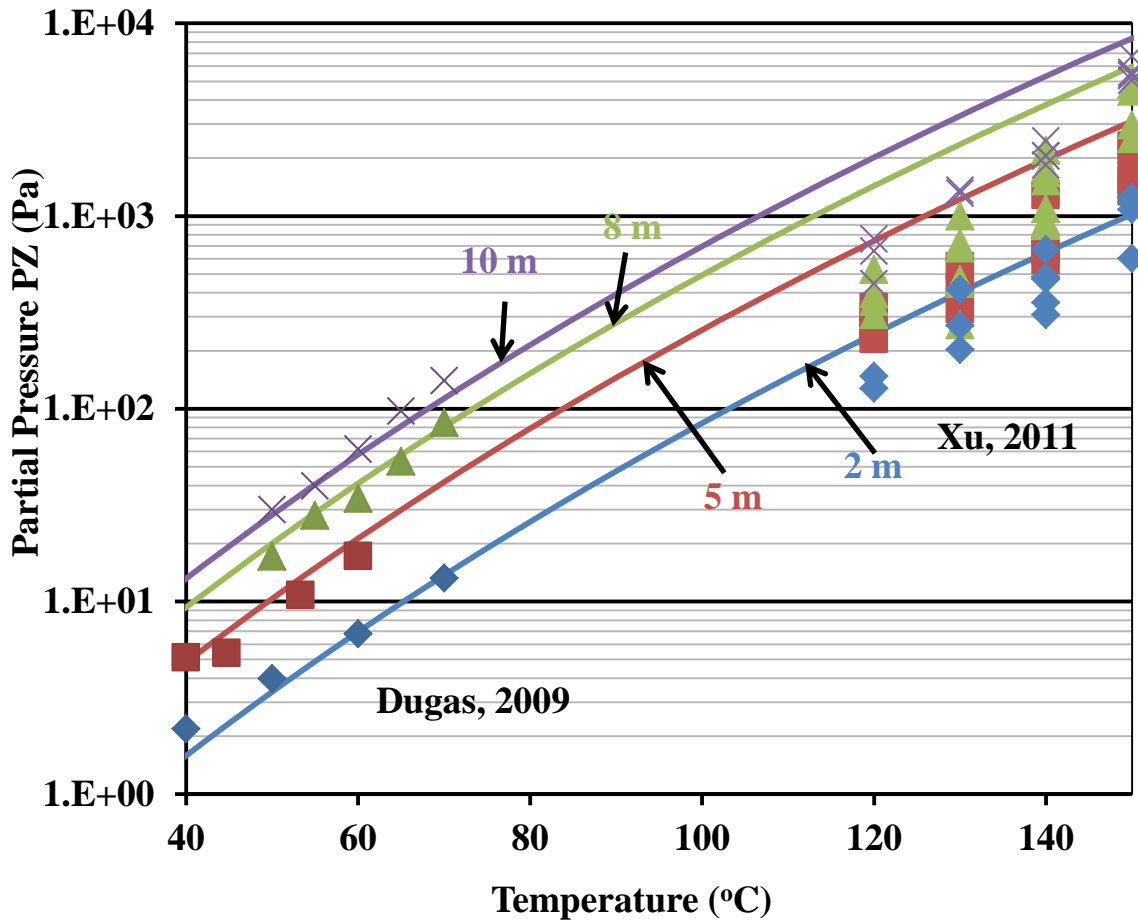


Figure A-1: Experimental data (points, Dugas 2009; Xu 2011) and model predictions (lines) for PZ volatility in 2-10 m PZ. High temperature data was omitted from the regression due to incompatibility.

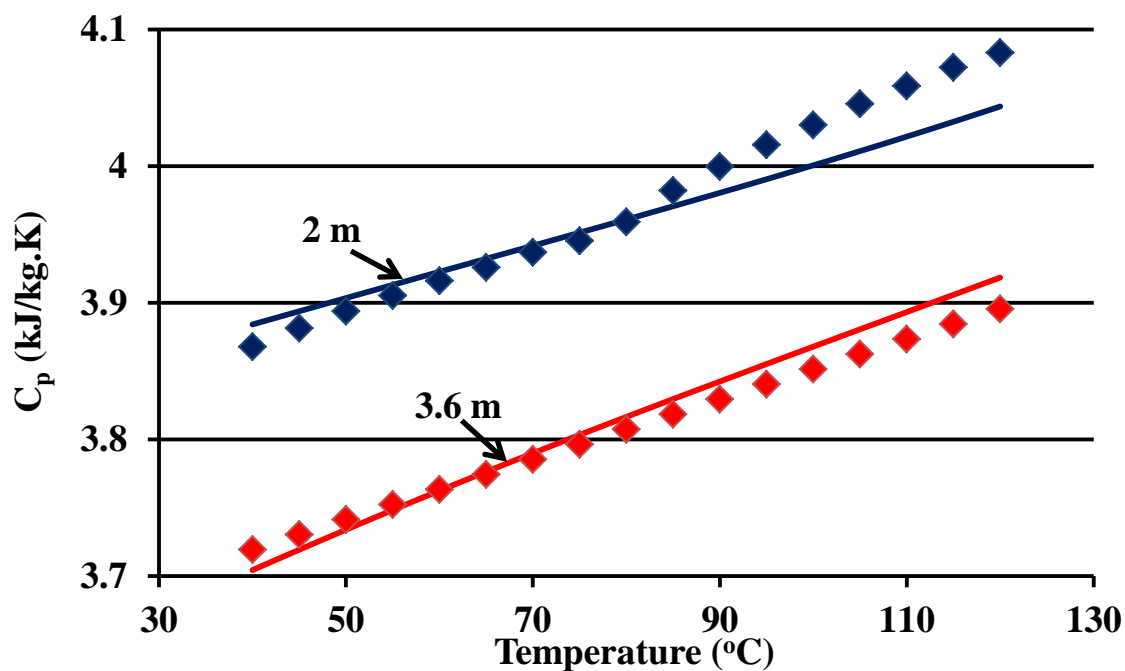


Figure A-2: Experimental data (points, Hilliard 2008) and model predictions (lines) for the heat capacity of 2 m PZ and 3.6 m PZ.

Table A-2: Regression results for PZ/H₂O/CO₂ Density and Viscosity

Parameter	Species	Value	Standard Dev.
IONMUB 1	PZH ⁺	3.29	0.466
IONMUB 1	PZ(COO) ₂ ²⁻	-11.7	3.15
MUKIJ 1	H ₂ O-PZ	714	121
MULIJ 1	H ₂ O-PZ	430	219
MULIJ 1	H ₂ O-PZ	659	194
MUKIJ 1	H ₂ O-H ⁺ PZCOO ⁻	91.9	11.5
MUKIJ 2	H ₂ O-H ⁺ PZCOO ⁻	-78.8	12.1
MULIJ 1	H ₂ O-H ⁺ PZCOO ⁻	98.0	19.7
MULIJ 2	H ₂ O-H ⁺ PZCOO ⁻	-81.2	20.3
RKTZRA 1	PZ	0.265	2.29x10 ⁻³
RKTZRA 1	CO ₂	0.168	0.032
RKTZRA 1	H ⁺ PZCOO ⁻	0.194	2.49x10 ⁻³
VCRKT 1	H ⁺ PZCOO ⁻	0.560	0.34
VCRKT 1	PZ	0.31	Fixed
VLCLK	PZH ⁺ -PZCOO ⁻	0.134	8.92x10 ⁻³
VLCLK	PZH ⁺ -HCO ₃ ⁻	0.427	0.036
VLCLK	PZH ⁺ -PZ(COO) ₂ ²⁻	0.470	0.034
VLCLK	PZH ⁺ -PZCOO ⁻	0.153	0.043
VLCLK	PZH ⁺ -HCO ₃ ⁻	-2.34	0.312
VLCLK	PZH ⁺ -PZ(COO) ₂ ²⁻	-0.967	0.181

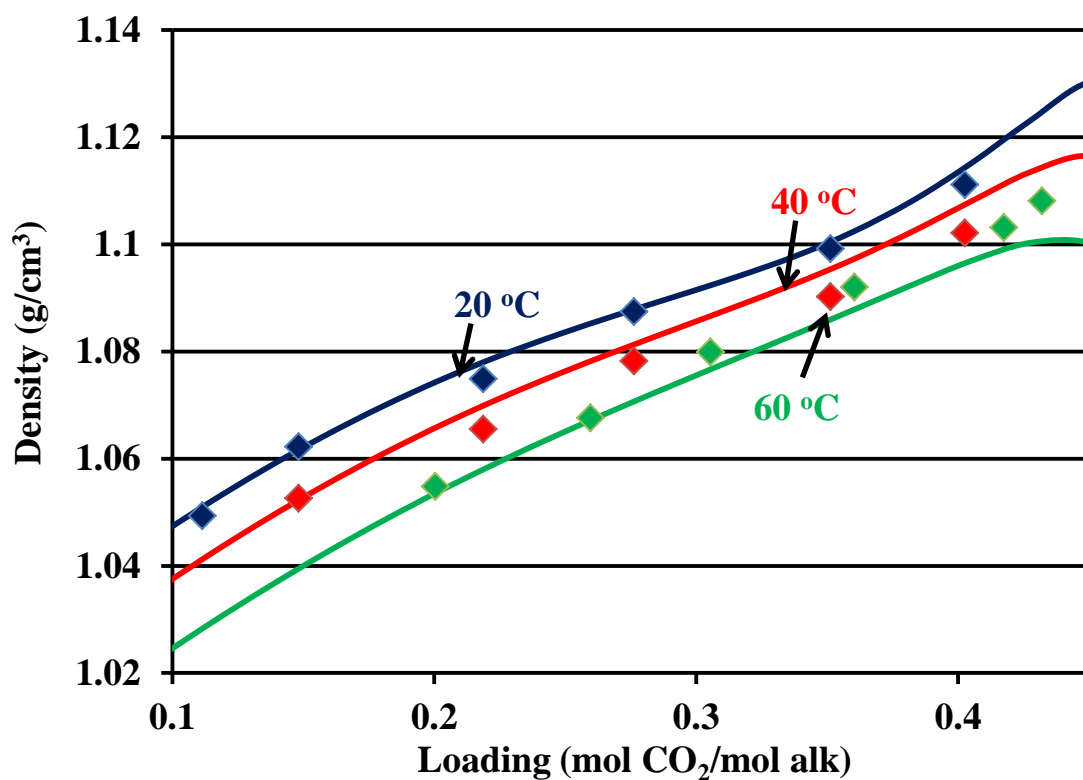


Figure A-3: Density of loaded 5 m PZ from 20-60 °C.

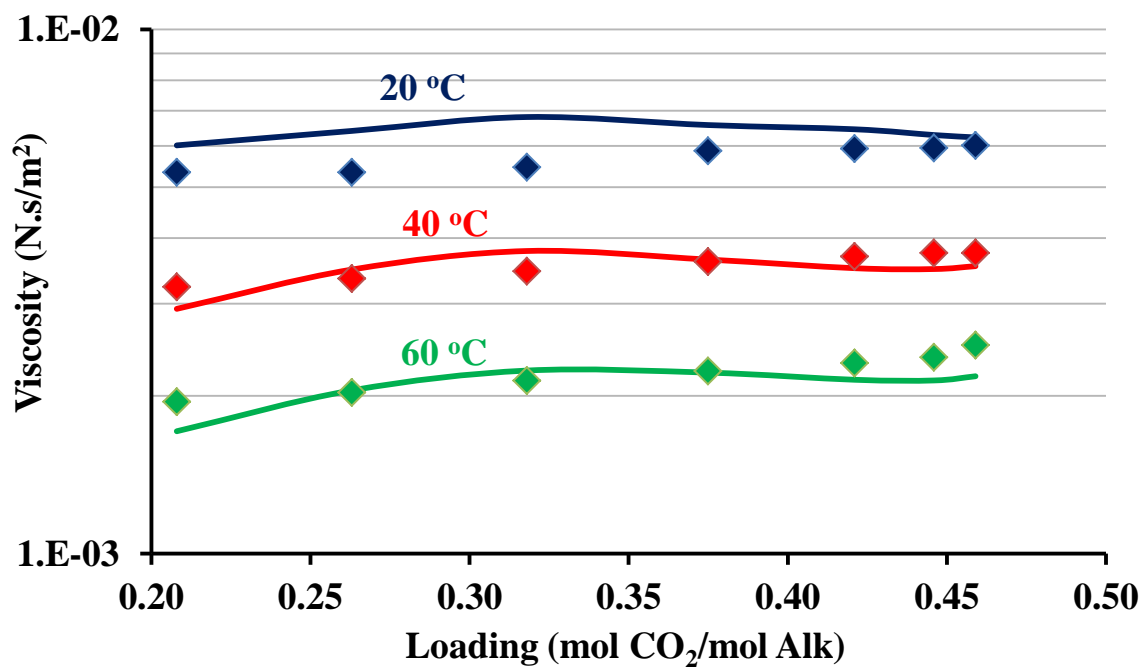


Figure A-4: Viscosity of loaded 5 m PZ from 20-60 °C.

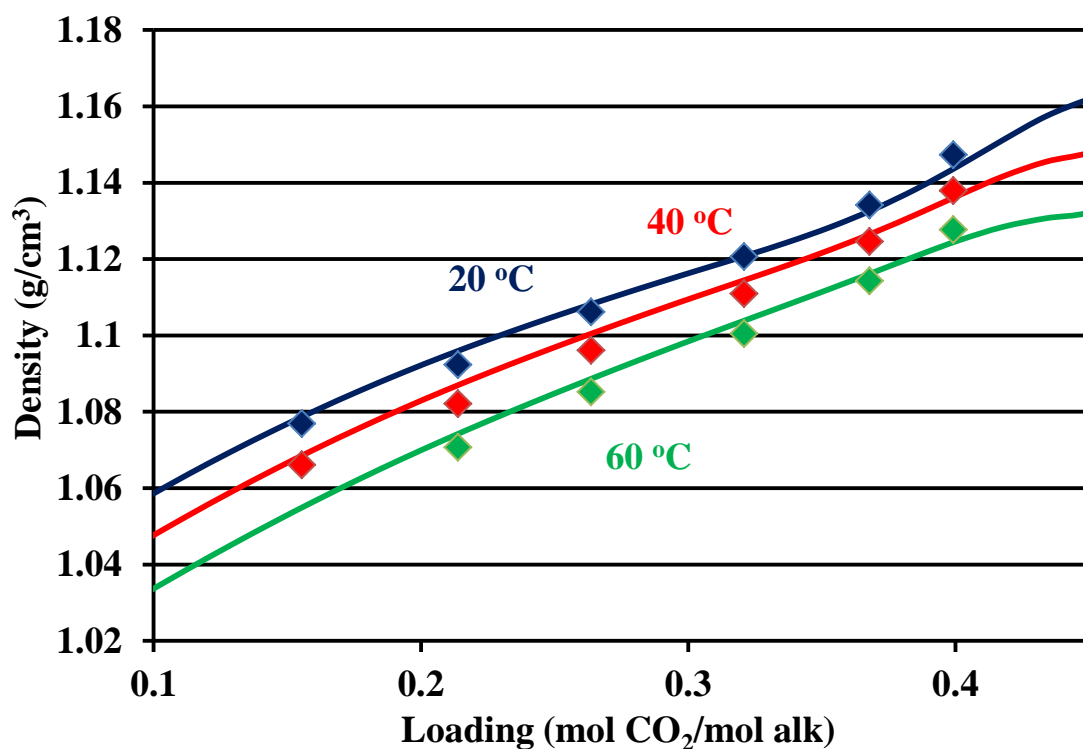


Figure A-5: Density of loaded 7 m PZ from 20-60 °C.

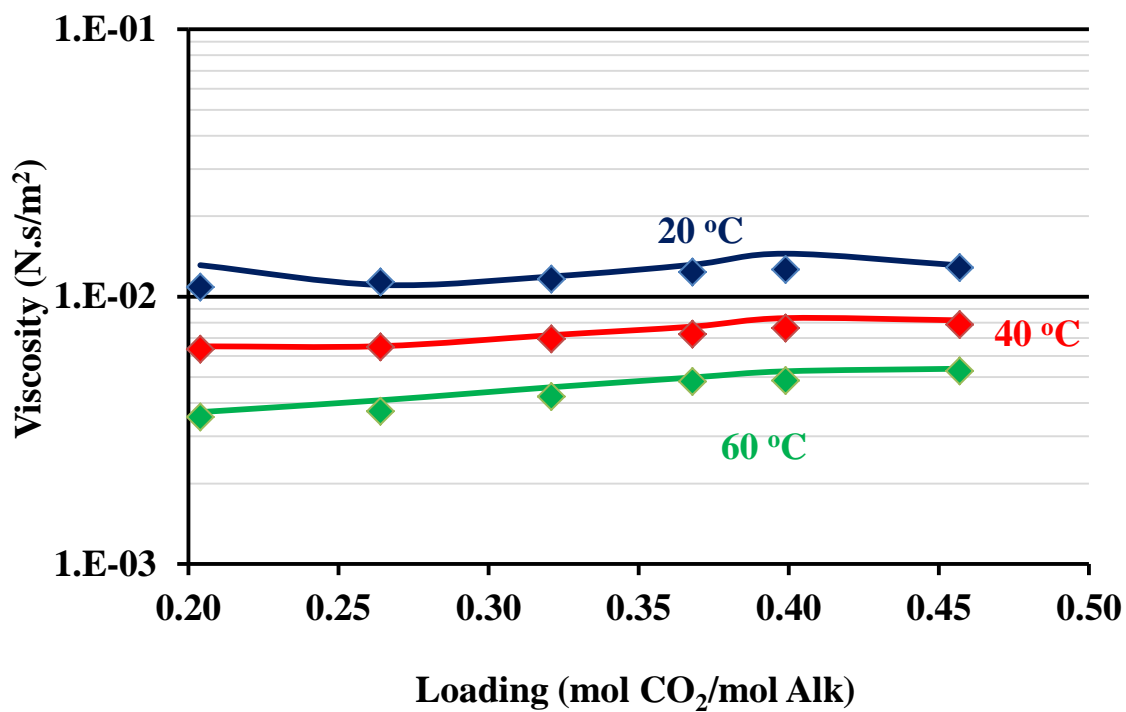


Figure A-6: Viscosity of loaded 7 m PZ from 20-60 °C.

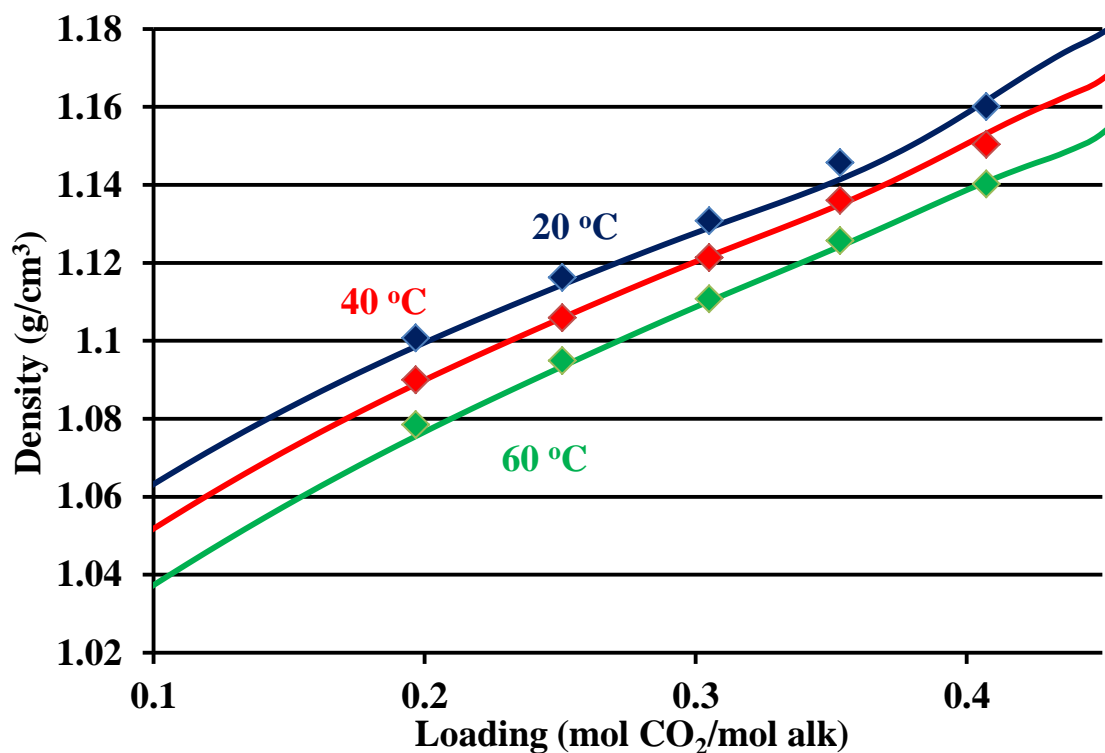


Figure A-7: Density of loaded 8 m PZ from 20-60 °C.

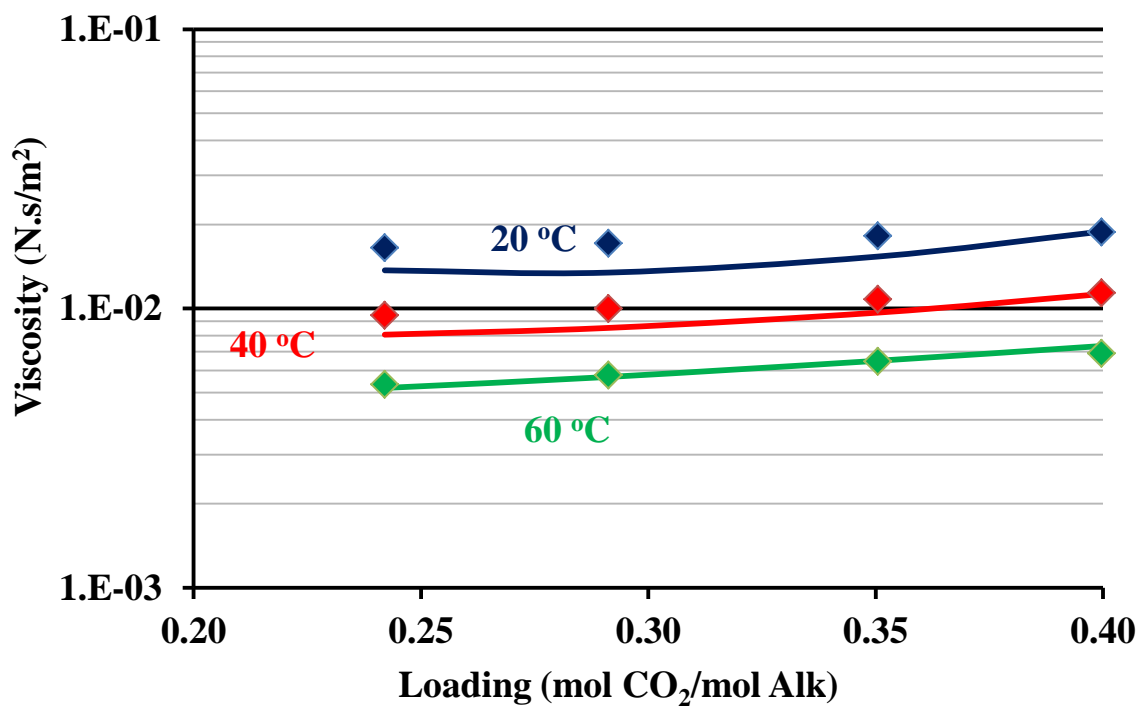


Figure A-8: Viscosity of loaded 8 m PZ from 20-60 °C.

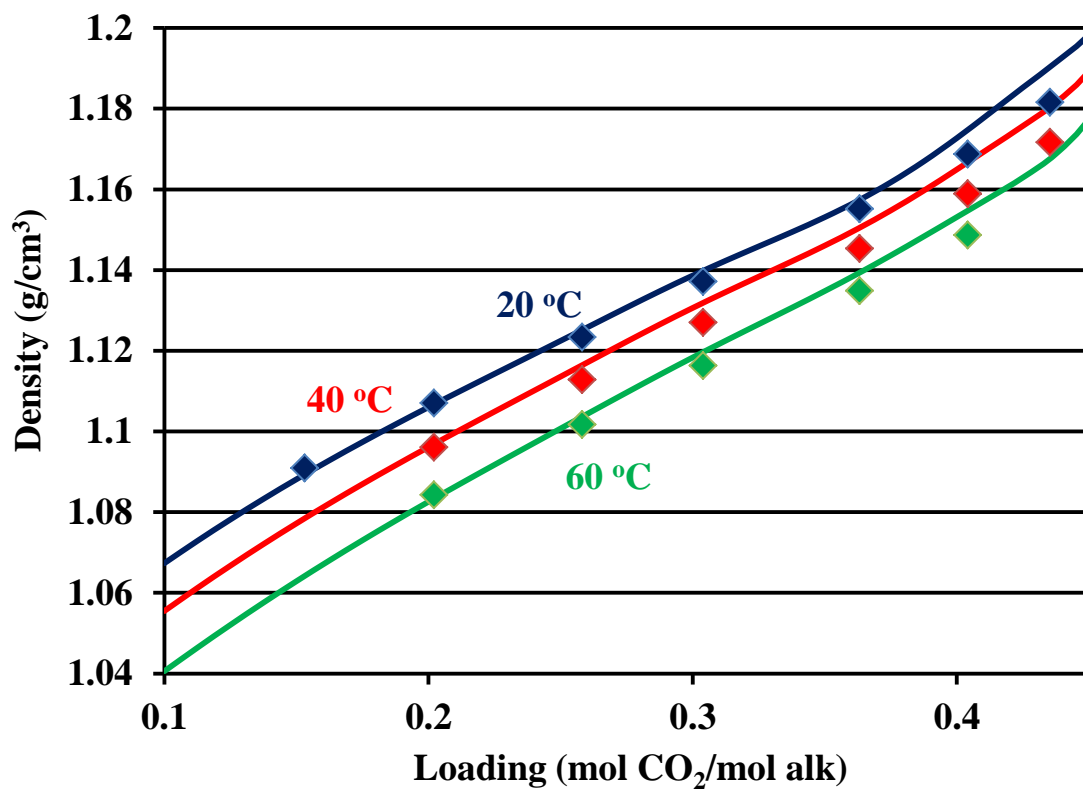


Figure A-9: Density of loaded 9 m PZ from 20-60 °C.

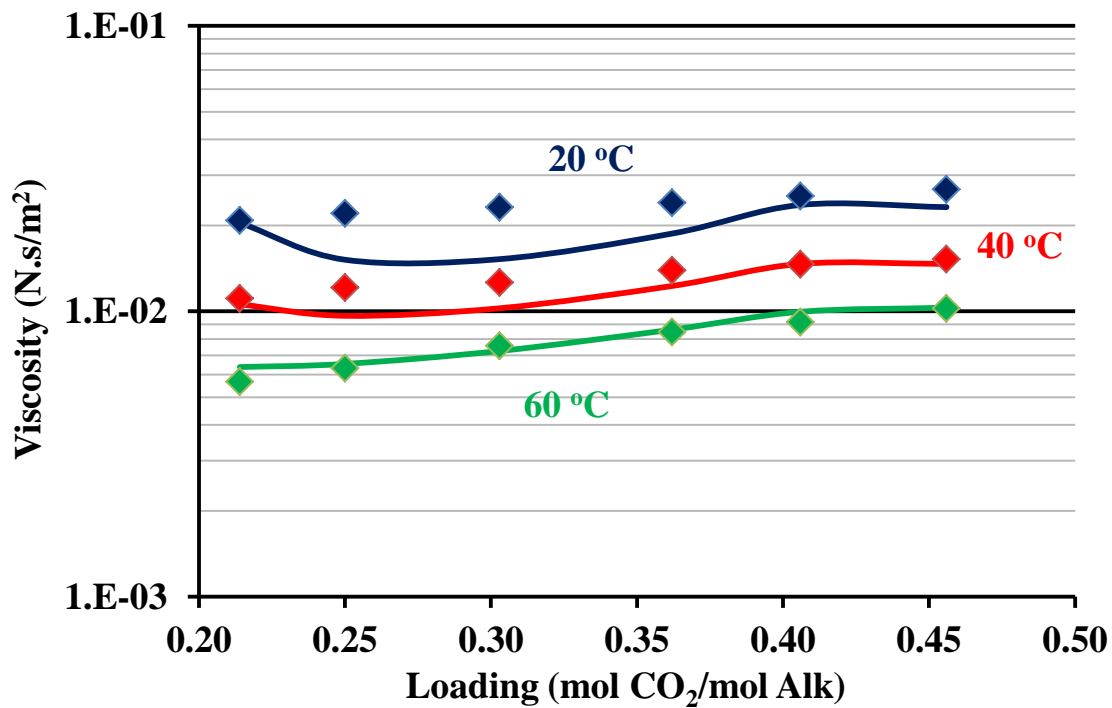


Figure A-10: Viscosity of loaded 9 m PZ from 20-60 °C.

Table A-3: Regression results for PZ/H₂O/CO₂

Parameter	Species	Value	Units
DGAQFM	H ⁺ PZCOO ⁻	-2.73x10 ⁸	J/kmol
DHAQFM	H ⁺ PZCOO ⁻	-5.2x10 ⁸	J/kmol
DGFORM	H ⁺ PZCOO ⁻	-2.16x10 ⁸	J/kmol
DHFORM	H ⁺ PZCOO ⁻	-5.2x10 ⁸	J/kmol
CPIG 1	H ⁺ PZCOO ⁻	77.3	J/kmol.K
CPIG 2	H ⁺ PZCOO ⁻	-2.49x10 ⁻⁵	J/kmol.K
DGAQFM	PZH ⁺	9.48x10 ⁷	J/kmol
DHAQFM	PZH ⁺	-1.0x10 ⁸	J/kmol
CPAQ0 1	PZH ⁺	-4.8x10 ⁵	J/kmol.K
CPAQ0 2	PZH ⁺	2120	J/kmol.K
DGAQFM	PZCOO ⁻	-2.32x10 ⁸	J/kmol
DHAQFM	PZCOO ⁻	-4.78x10 ⁸	J/kmol
CPAQ0 1	PZCOO ⁻	1.51x10 ⁵	J/kmol.K
CPAQ0 2	PZCOO ⁻	-0.025	J/kmol.K
DGAQFM	PZ(COO) ₂ ²⁻	-5.93x10 ⁸	J/kmol
DHAQFM	PZ(COO) ₂ ²⁻	-9.12x10 ⁸	J/kmol
CPAQ0/1	PZ(COO) ₂ ²⁻	1.19x10 ⁵	J/kmol.K
CPAQ0/2	PZ(COO) ₂ ²⁻	-0.0159	J/kmol.K
GMELCC	H ₂ O/(PZH ⁺ , HCO ₃ ⁻)	10.25	N/A
GMELCC	H ⁺ PZCOO ⁻ /(PZH ⁺ , PZCOO ⁻)	10.62	N/A
GMELCC	(PZH ⁺ , PZCOO ⁻)/H ⁺ PZCOO ⁻	-2.69	N/A
GMELCC	H ⁺ PZCOO ⁻ /(PZH ⁺ , PZ(COO) ₂ ²⁻)	7.16	N/A
GMELCC	(PZH ⁺ , PZ(COO) ₂ ²⁻)/H ⁺ PZCOO ⁻	-3.21	N/A
GMELCC	H ⁺ PZCOO ⁻ /(PZH ⁺ , HCO ₃ ⁻)	4.0	N/A
GMELCC	(PZH ⁺ , HCO ₃ ⁻)/H ⁺ PZCOO ⁻	-9.5	N/A
NRTL 1	H ₂ O-H ⁺ PZCOO ⁻	0.080	N/A
NRTL 1	H ⁺ PZCOO ⁻ -H ₂ O	0.080	N/A
(NRTL 2)/313K	H ₂ O-H ⁺ PZCOO ⁻	132	N/A
(NRTL 2)/313K	H ⁺ PZCOO ⁻ -H ₂ O	30.0	N/A
NRTL 3	H ₂ O-H ⁺ PZCOO ⁻	0.109	N/A
(NRTL 5)(ln313K)	H ₂ O-H ⁺ PZCOO ⁻	-0.525	N/A
(NRTL 5)(ln313K)	H ⁺ PZCOO ⁻ -H ₂ O	0.137	N/A

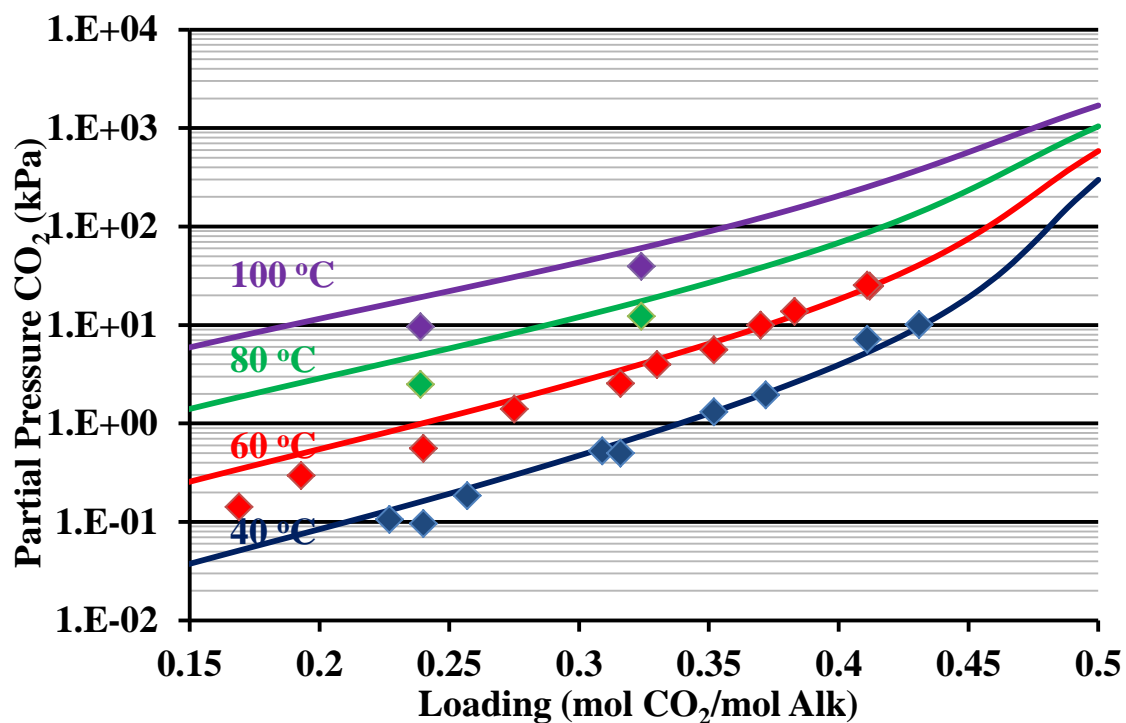


Figure A-11: Experimental data (points; Dugas 2009) and model predictions (lines) for CO₂ solubility in 2 m PZ from 40-100 °C.

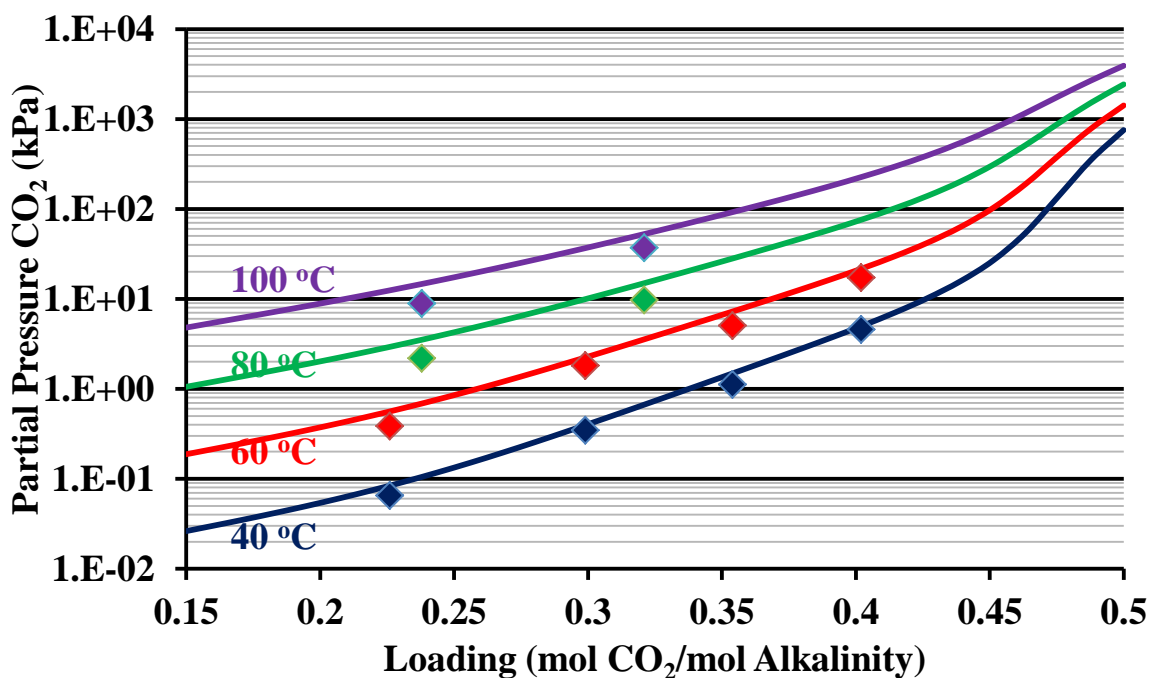


Figure A-12: Experimental data (points; Dugas 2009) and model predictions (lines) for CO₂ solubility in 5 m PZ from 40-100 °C.

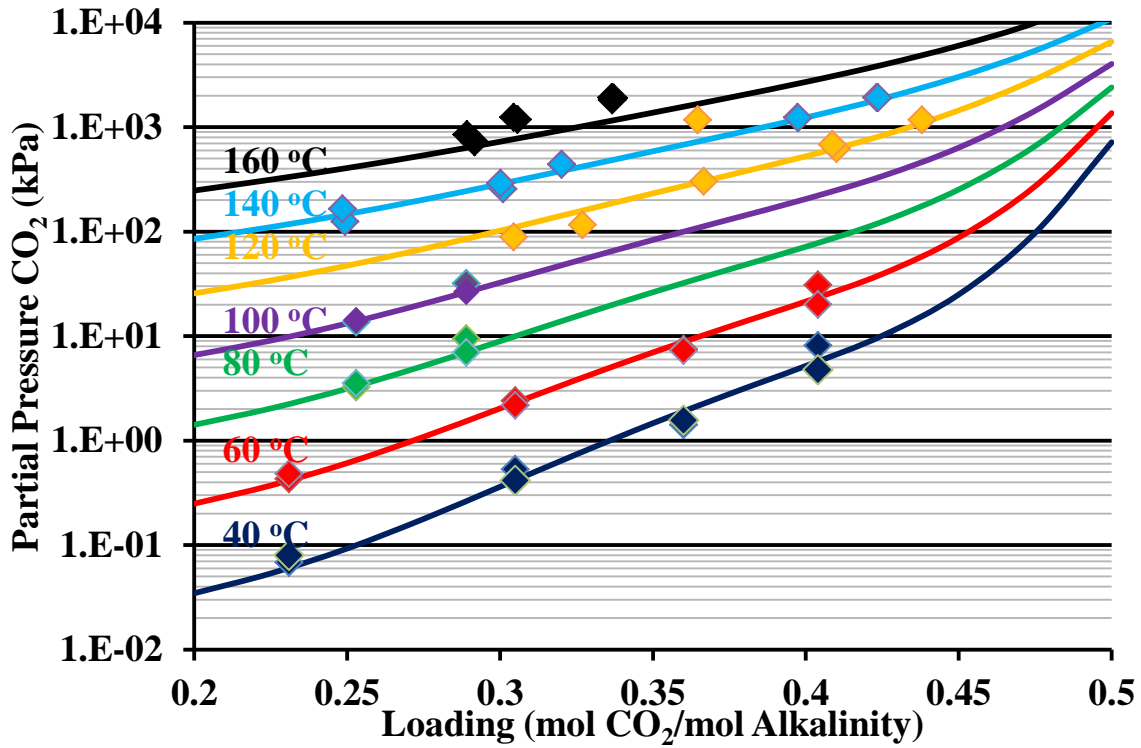


Figure A-13: Experimental data (points; Dugas 2009; Xu 2011) and model predictions (lines) for CO₂ solubility in 8 m PZ from 40-160 °C.

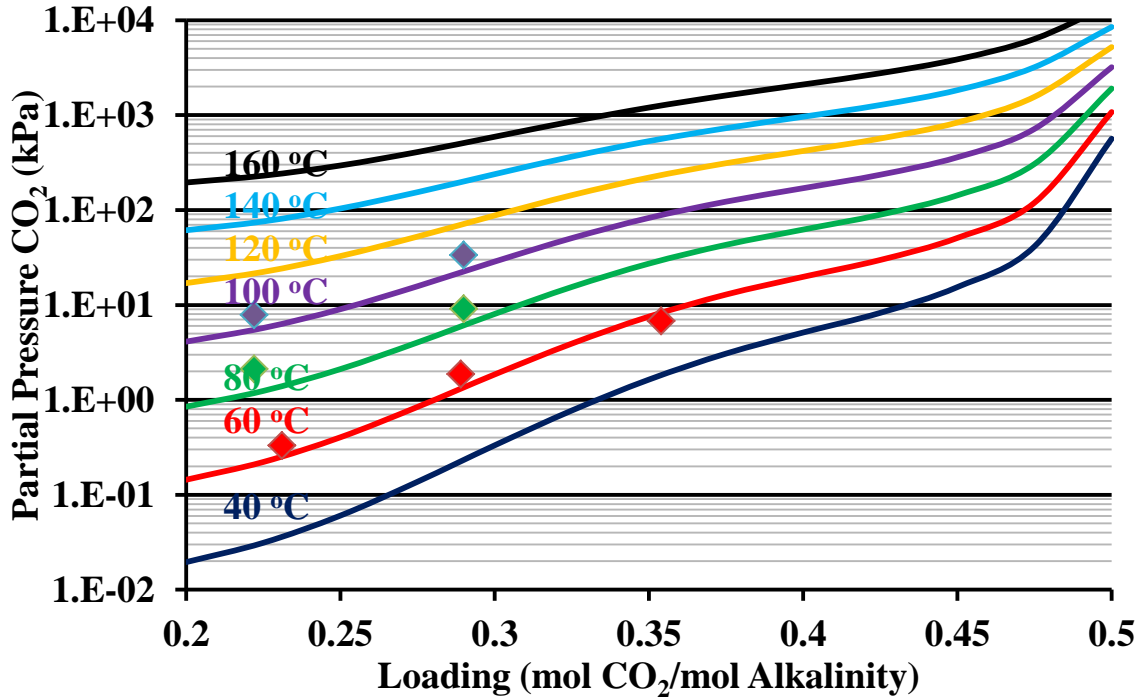


Figure A-14: Experimental data (points; Dugas 2009; Xu 2011) and model predictions (lines) for CO₂ solubility in 12 m PZ from 40-160 °C.

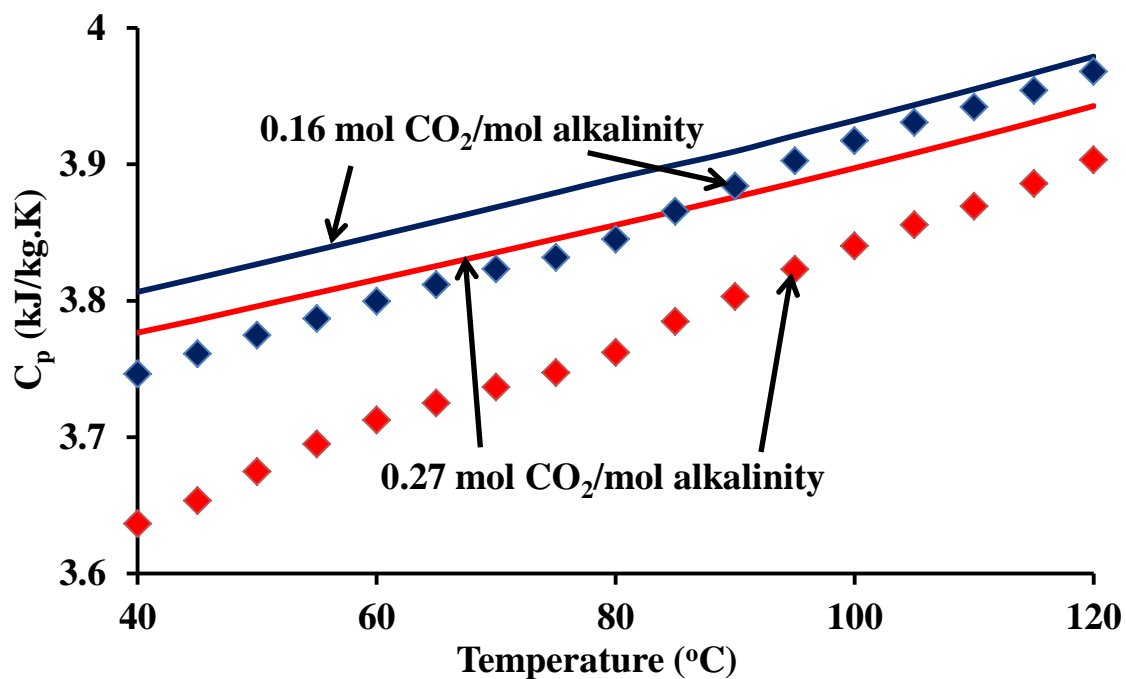


Figure A-15: Experimental data (points; Hilliard 2008) and model predictions (lines) for heat capacity of 2 m PZ at loadings of 0.16 and 0.27 mol CO_2 /mol alkalinity.

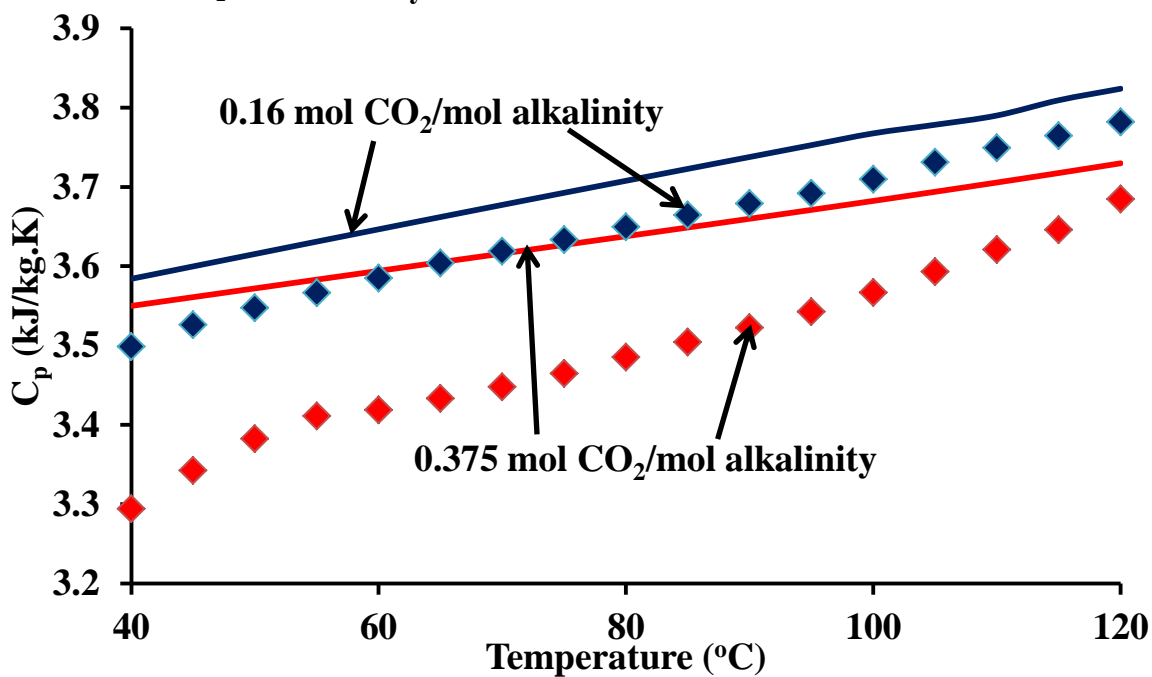


Figure A-16: Experimental data (points; Hilliard 2008) and model predictions (lines) for heat capacity of 3.6 m PZ at loadings of 0.16 and 0.375 mol CO_2 /mol alkalinity.

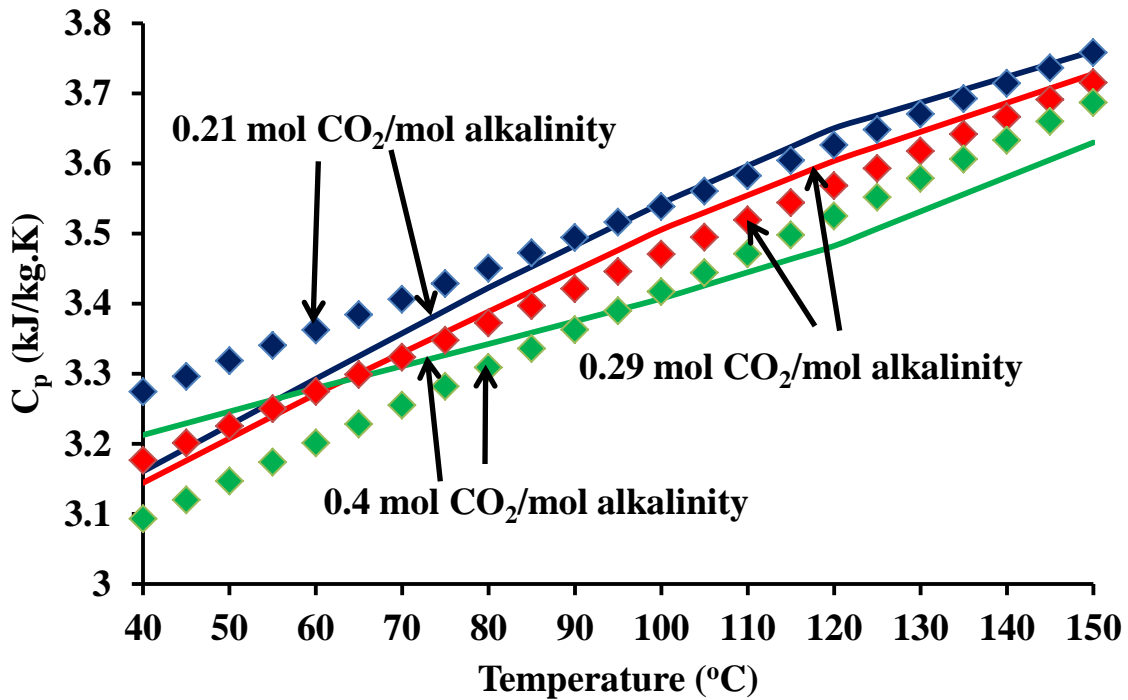


Figure A-17: Experimental data (points; Freeman 2011) and model predictions (lines) for heat capacity of 8 m PZ at loadings of 0.21, 0.29 and 0.4 mol CO₂/mol alkalinity.

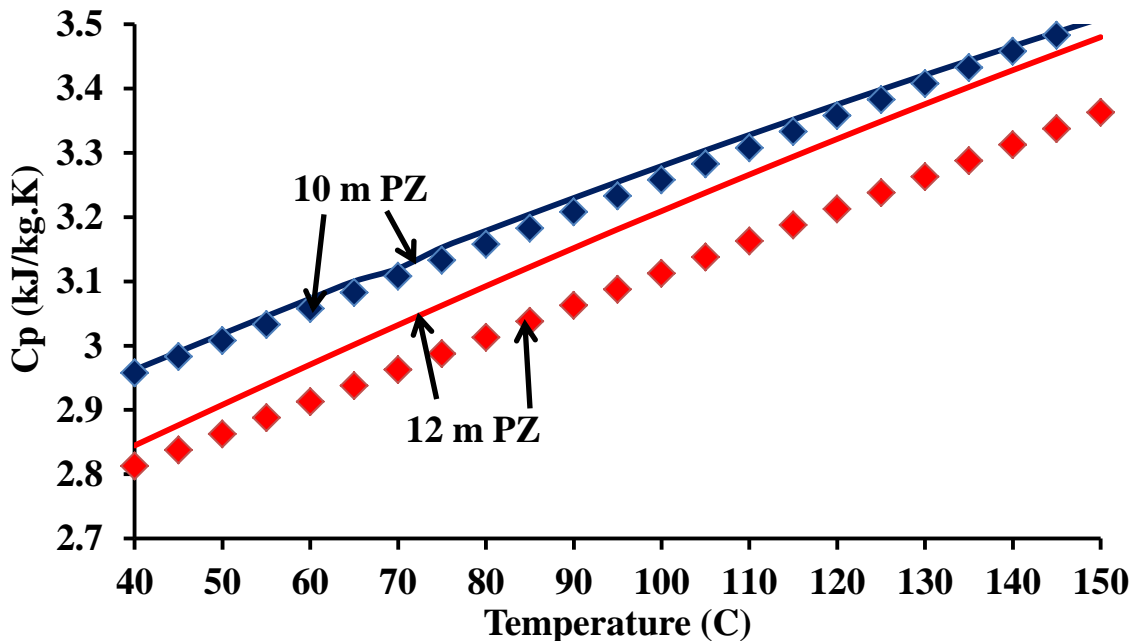


Figure A-18: Experimental data (points; Freeman 2011) and model predictions (lines) for heat capacity of 10 m PZ at a loading of 0.31 mol CO₂/mol alkalinity and 12 m PZ at a loading of 0.29 mol CO₂/mol alkalinity.

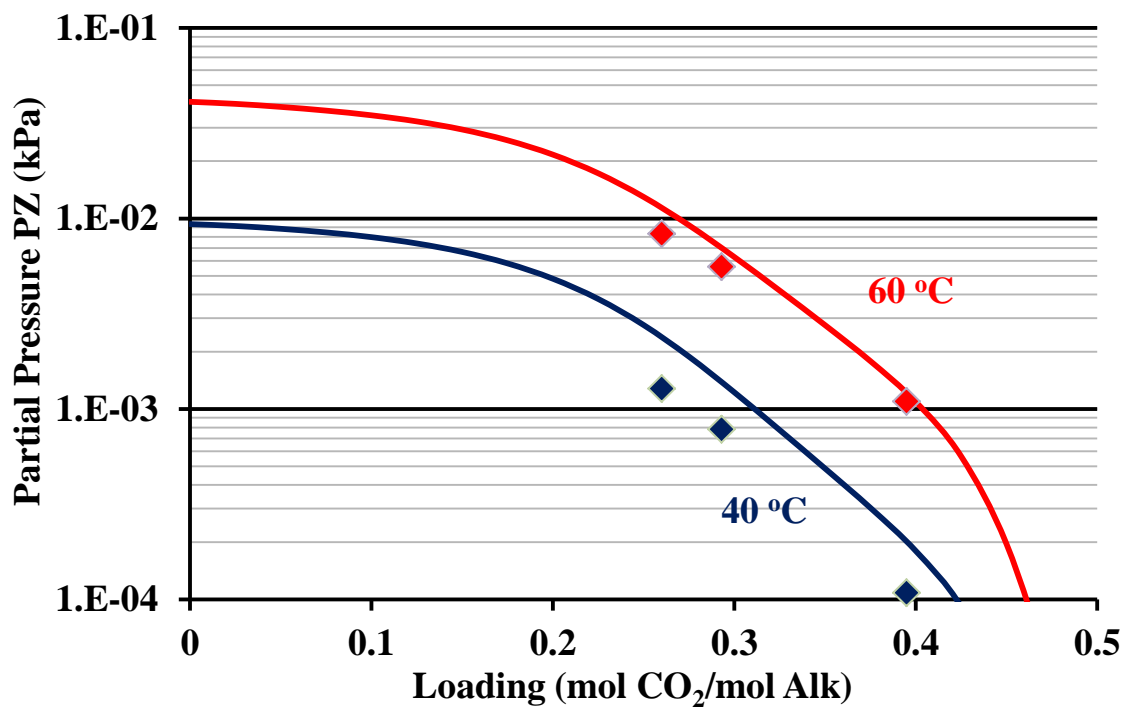


Figure A-19: Experimental data (points; Nguyen 2012) and model predictions (lines) for PZ volatility in loaded 8 m PZ from 40-60 °C.

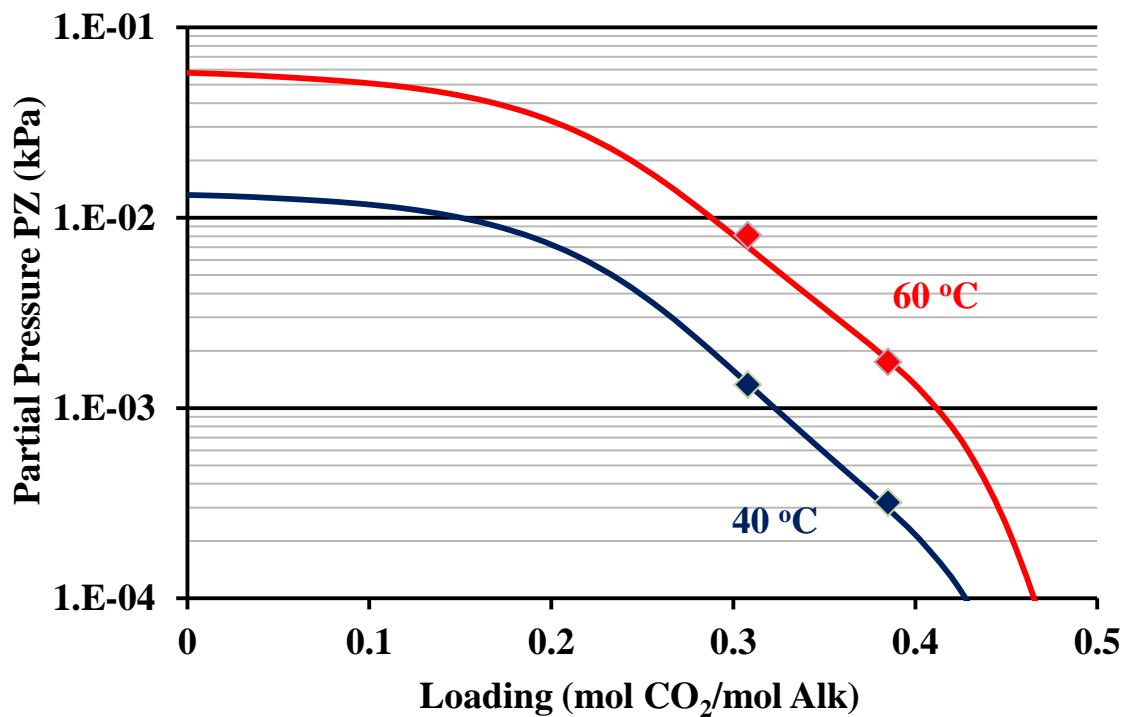


Figure A-20: Experimental data (points; Nguyen 2012) and model predictions (lines) for PZ volatility in loaded 10 m PZ from 40-60 °C.

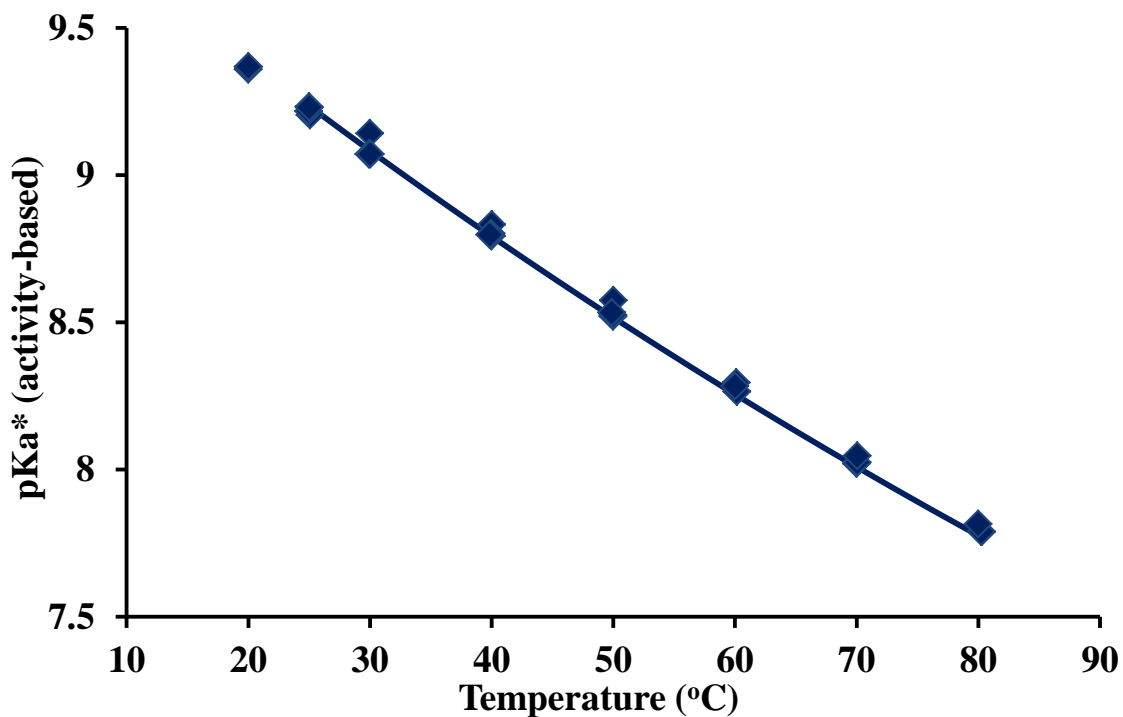


Figure A-21: Experimental data (points; Hetzer 1968) and model predictions (lines) for PZ pKa.

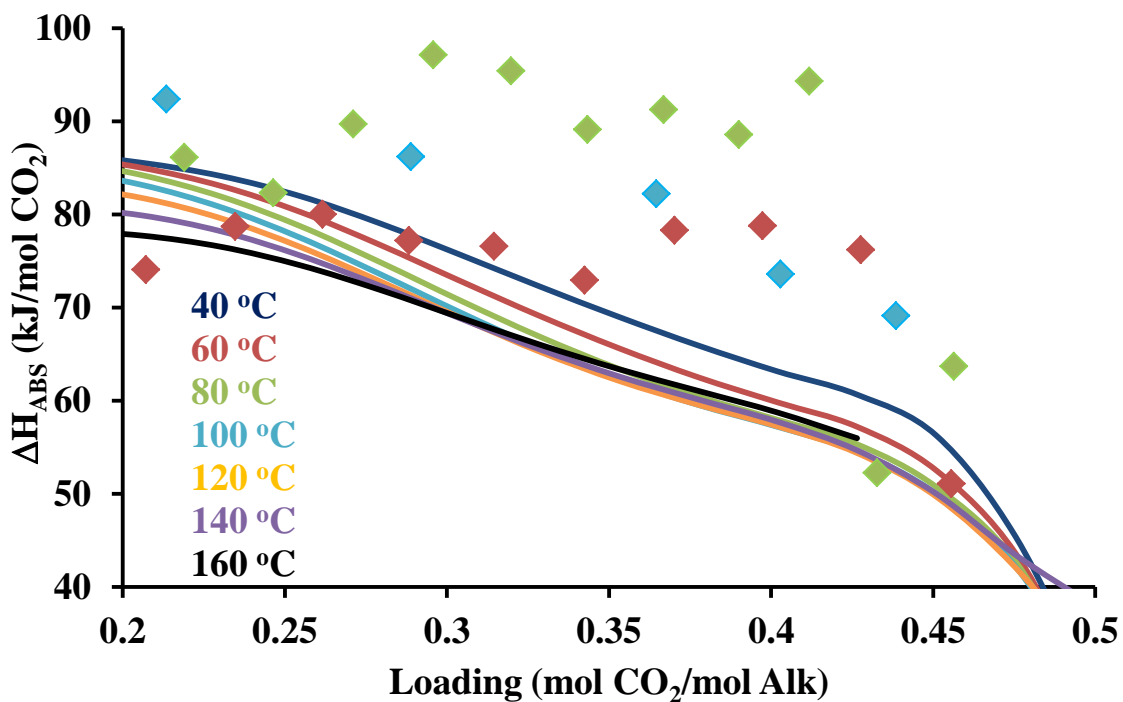


Figure A-22: Experimental data (points; Freeman 2010) and model predictions (lines) for heat of CO₂ absorption in 8 m PZ from 40—160 °C.

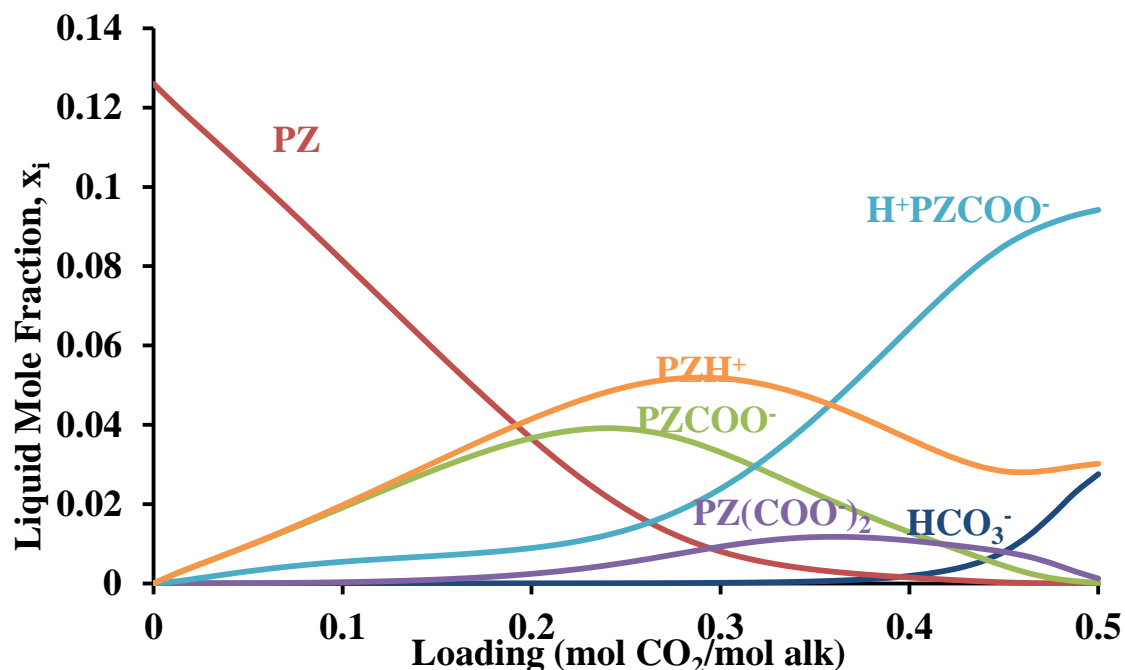


Figure A-23: Model predictions for liquid mole fraction in 8 m PZ at 40 °C.

Table A-4: Regression results for activity coefficient of CO₂.

Parameter	Species	Value
NRTL 1	PZ-CO ₂	-6.20
NRTL 1	CO ₂ -PZ	34.0
(NRTL 2)/313	PZ-CO ₂	8.70
(NRTL 2)/313	CO ₂ -PZ	-31.9
NRTL 3	PZ-CO ₂	0.20
NRTL 1	H ⁺ PZCOO ⁻ - CO ₂	-0.37
NRTL 1	CO ₂ -H ⁺ PZCOO ⁻	3.12
(NRTL 2)/313	H ⁺ PZCOO ⁻ - CO ₂	6.50
(NRTL 2)/313	CO ₂ -H ⁺ PZCOO ⁻	2.20
NRTL 3	H ⁺ PZCOO ⁻ - CO ₂	0.01
GMELCC	CO ₂ /(PZH ⁺ /PZCOO ⁻)	7.09
GMELCC	(PZH ⁺ /PZCOO ⁻)/CO ₂	-6.38
GMELCC	CO ₂ /(PZH ⁺ /PZ(COO) ₂ ²⁻)	3.93
GMELCC	(PZH ⁺ /PZ(COO) ₂ ²⁻)/CO ₂	-5.62
GMELCC	CO ₂ /(PZH ⁺ /HCO ₃ ⁻)	11.9
GMELCC	(PZH ⁺ /HCO ₃ ⁻)/CO ₂	-5.81
(GMELCD)/313	CO ₂ /(PZH ⁺ /PZCOO ⁻)	2.16
(GMELCD)/313	(PZH ⁺ /PZCOO ⁻)/CO ₂	4.12
(GMELCD)/313	CO ₂ /(PZH ⁺ /PZ(COO) ₂ ²⁻)	2.33
(GMELCD)/313	(PZH ⁺ /PZ(COO) ₂ ²⁻)/CO ₂	3.91

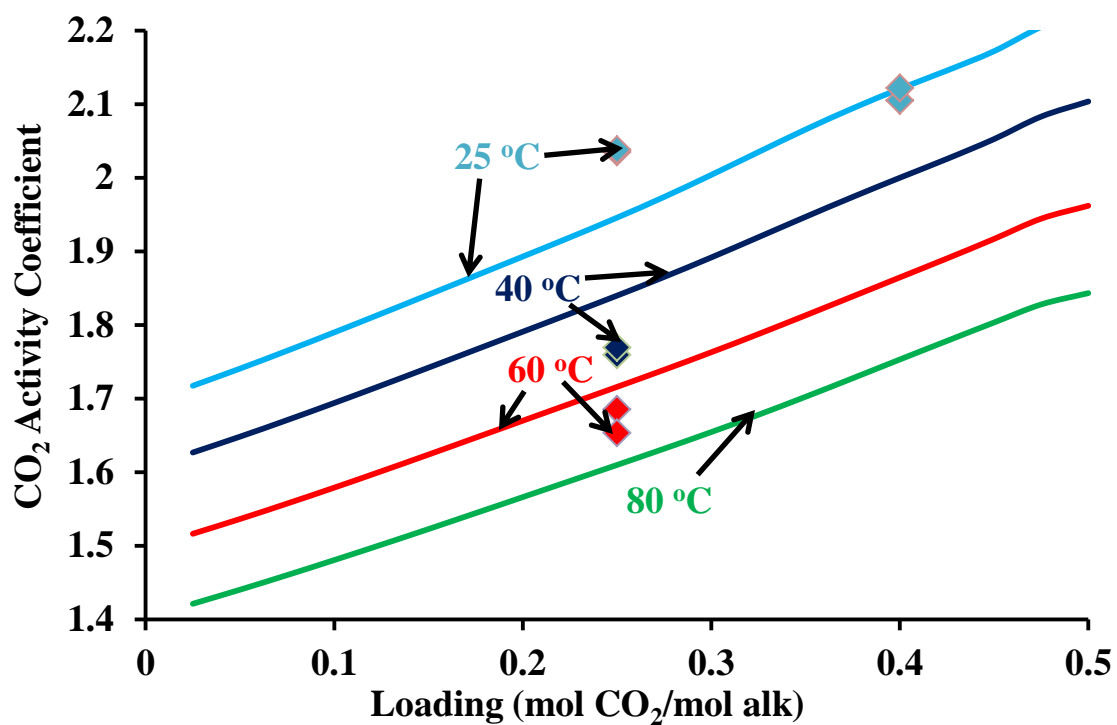


Figure A-24: Experimental data (points; Svendsen 2010) and model predictions (lines) for the activity coefficient of CO₂ from 25-80 °C.

Appendix B: Guy Fawkes Model

Table B-1: Regression results for PZ/H₂O

Parameter	Species	Value	Standard Dev.
NRTL 1	H ₂ O-PZ	-5.75	23.8
NRTL 3	PZ-H ₂ O	0.20	FIXED
HENRY 1	PZ-H ₂ O	29.0	1.02
(HENRY 2)/313	PZ-H ₂ O	-25.23	1.05
CPIG 1 (J/kmol.K)	PZ	-3.6x10 ⁴	FIXED
(CPIG 2)x313 (J/kmol.K)	PZ	2.27x10 ⁵	7.45x10 ³

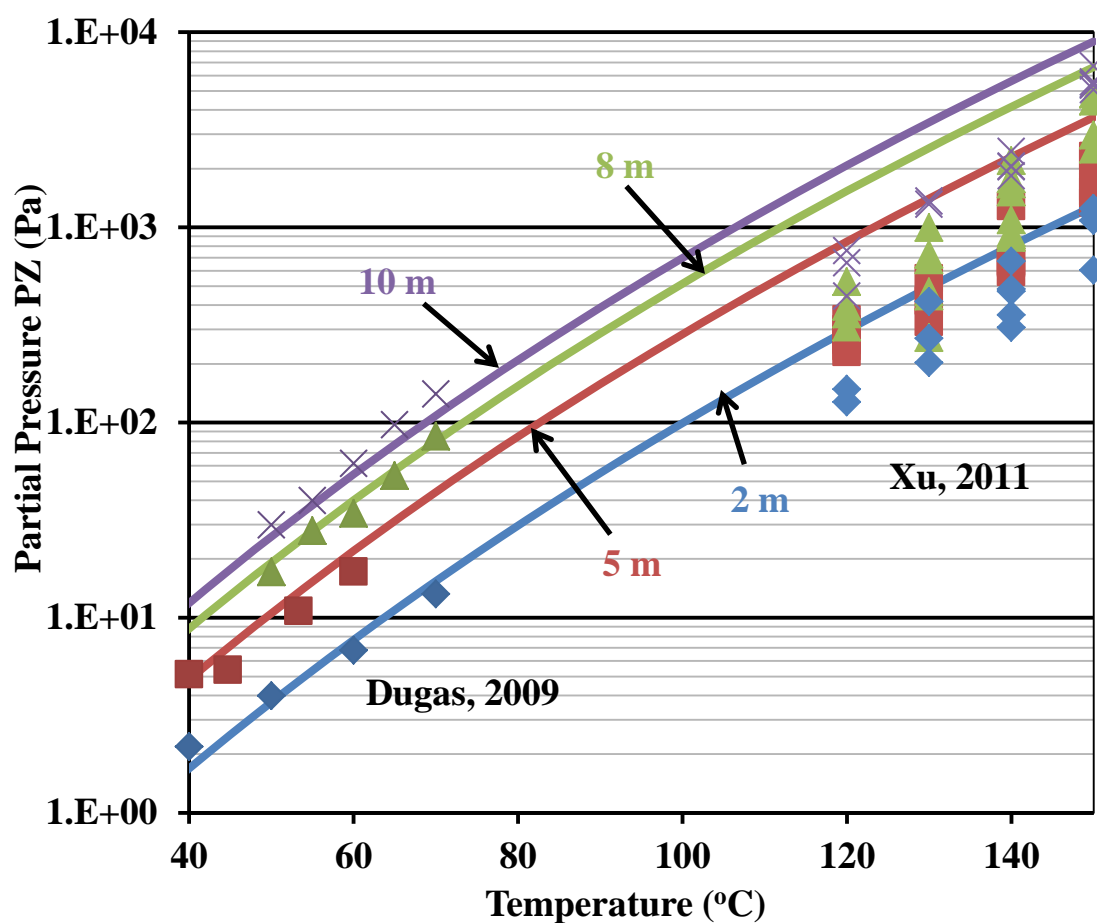


Figure B-1: Experimental data (points, Dugas 2009; Xu 2011) and model predictions (lines) for PZ volatility in 2-10 m PZ. High temperature data was omitted from the regression due to incompatibility.

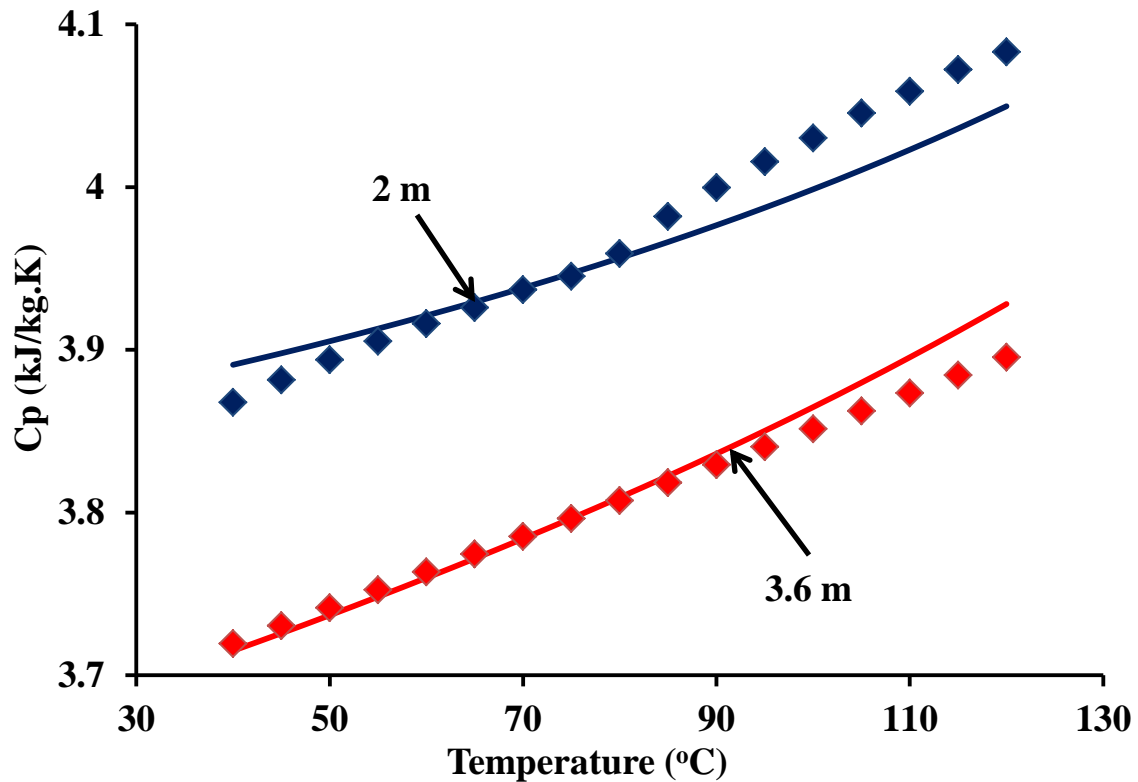


Figure B-2: Experimental data (points, Hilliard 2008) and model predictions (lines) for the heat capacity of 2 m PZ and 3.6 m PZ.

Table B-2: Regression results for PZ/H₂O/CO₂ Density (Reference Equation B-1)

Parameter	Value
A	2.68
B	-0.031
C	-0.073
D	2.10
E	1.55
F	-5.73x10 ⁻⁴

$$\rho = (E + FT) \ln(Ax_{CO_2} + Bx_{PZ} + C\alpha + D) \quad \text{Equation B-1}$$

- α = CO₂ loading
- x_i = component mole fraction
- T = temperature in K
- ρ = density in g/cm³

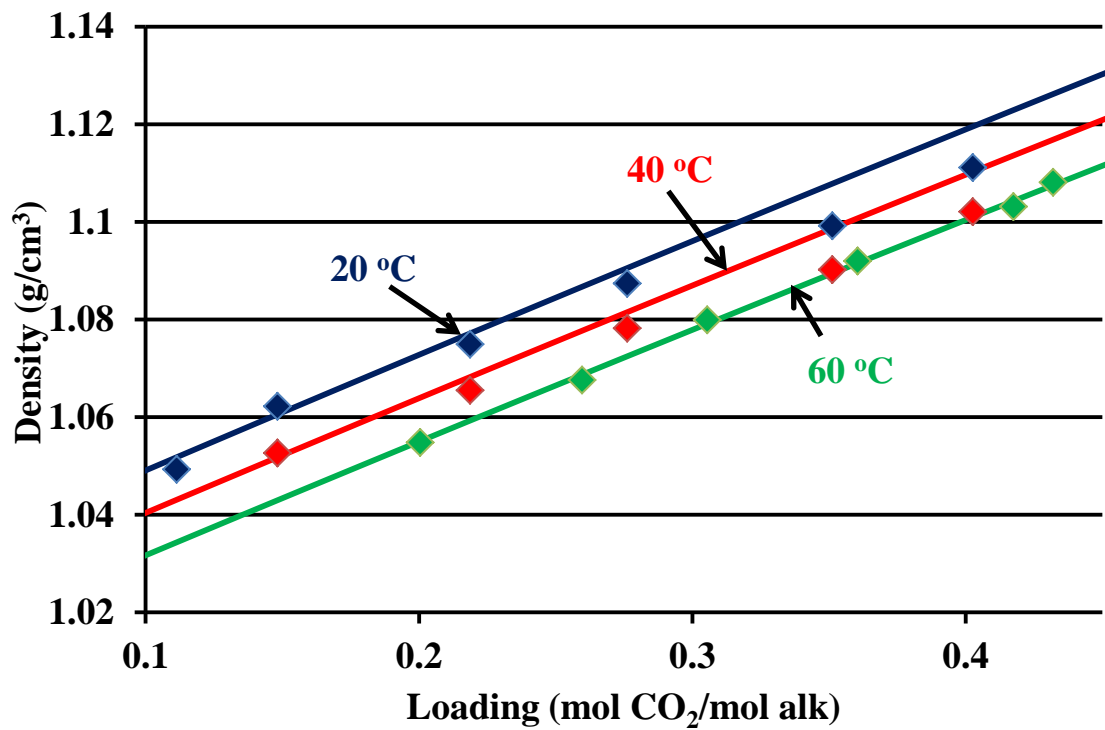


Figure B-3: Density of loaded 5 m PZ from 20-60 °C.

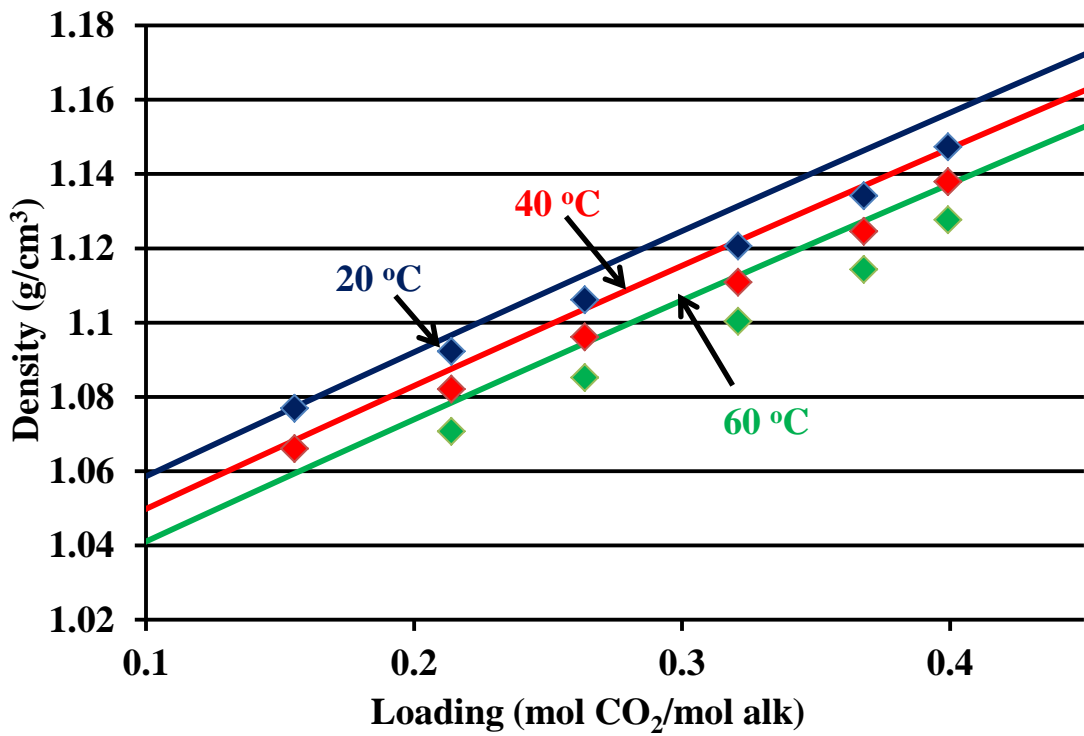


Figure B-4: Density of loaded 7 m PZ from 20-60 °C.

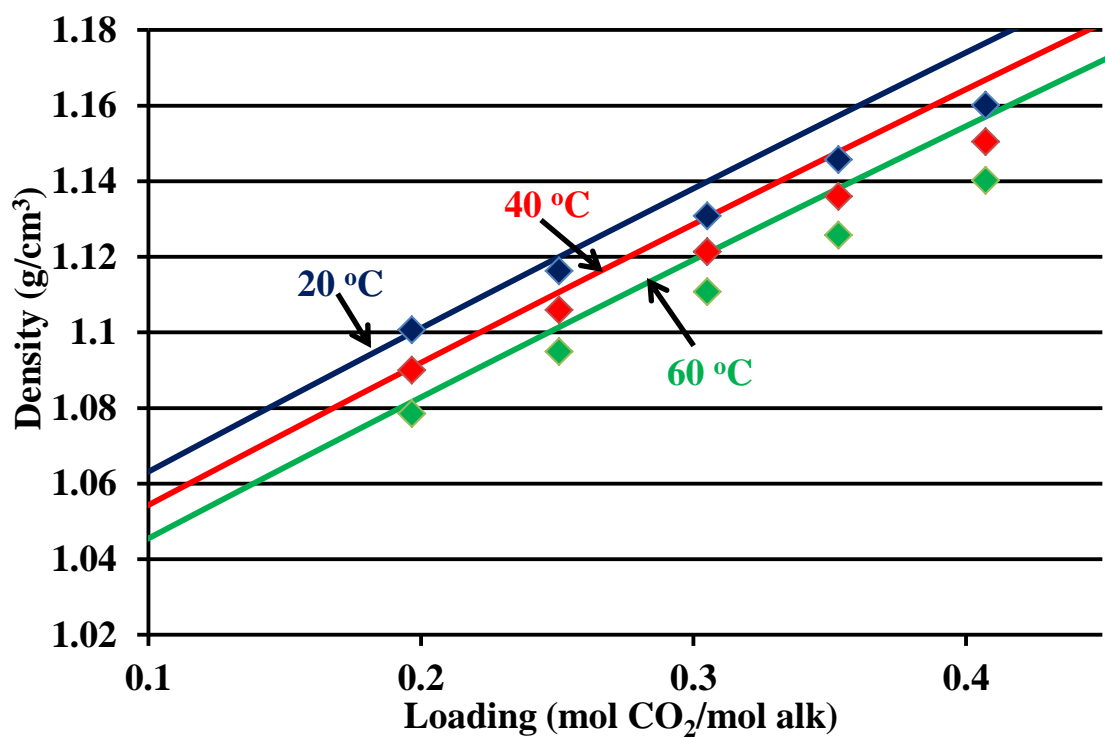


Figure B-5: Density of loaded 8 m PZ from 20-60 °C.

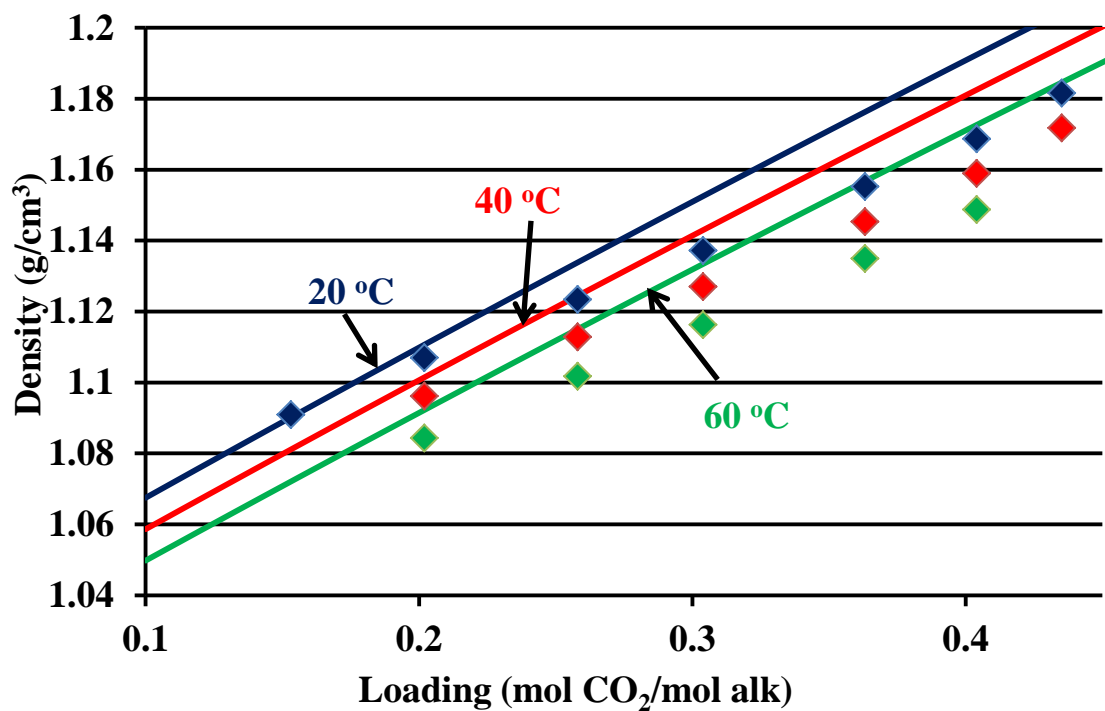


Figure B-6: Density of loaded 9 m PZ from 20-60 °C.

Table B-3: Regression results for PZ/H₂O/CO₂ Density (Reference Equation B-2)

Parameter	Value
A	-4.85x10 ⁻³
B	0.020
C	-0.041
D	0.184
E	2821

$$\mu = \left(A + Bwt_{PZ} + C\alpha + Dwt_{PZ}\alpha \right) \frac{\exp\left(\frac{E}{T}\right)}{\exp\left(\frac{E}{313.15}\right)} \quad \text{Equation B-2}$$

- α = CO₂ loading
- wt_i = component weight fraction
- T = temperature in K
- μ = viscosity in Pa.s

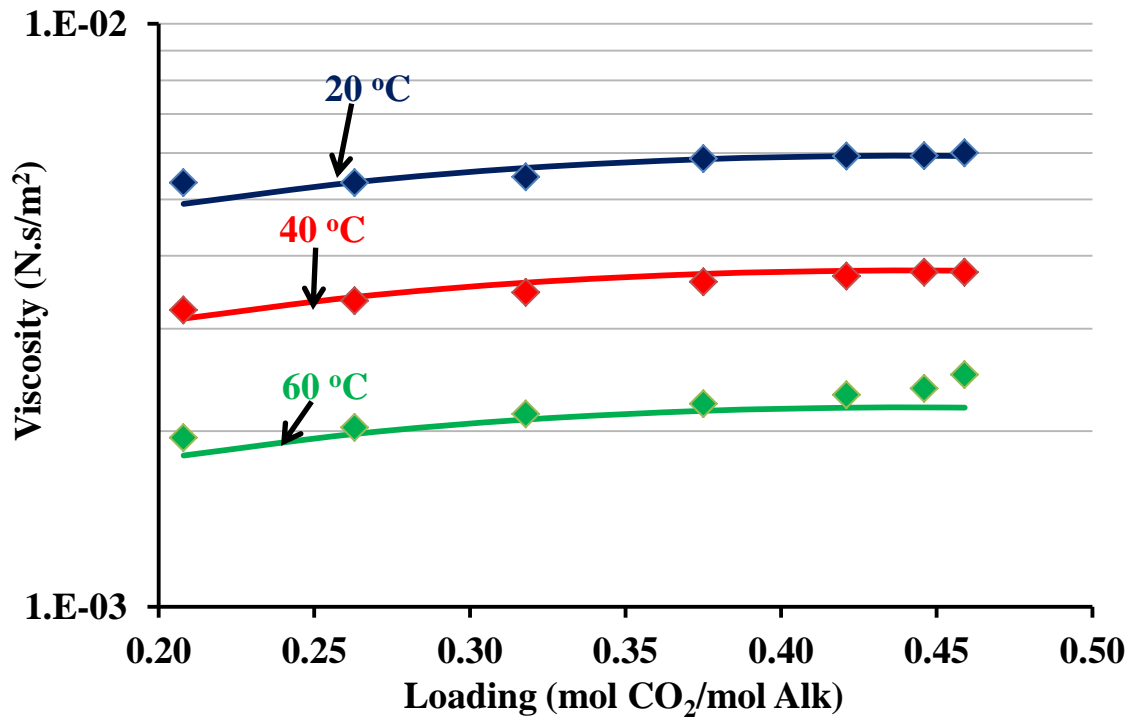


Figure B-7: Viscosity of loaded 5 m PZ from 20-60 °C.

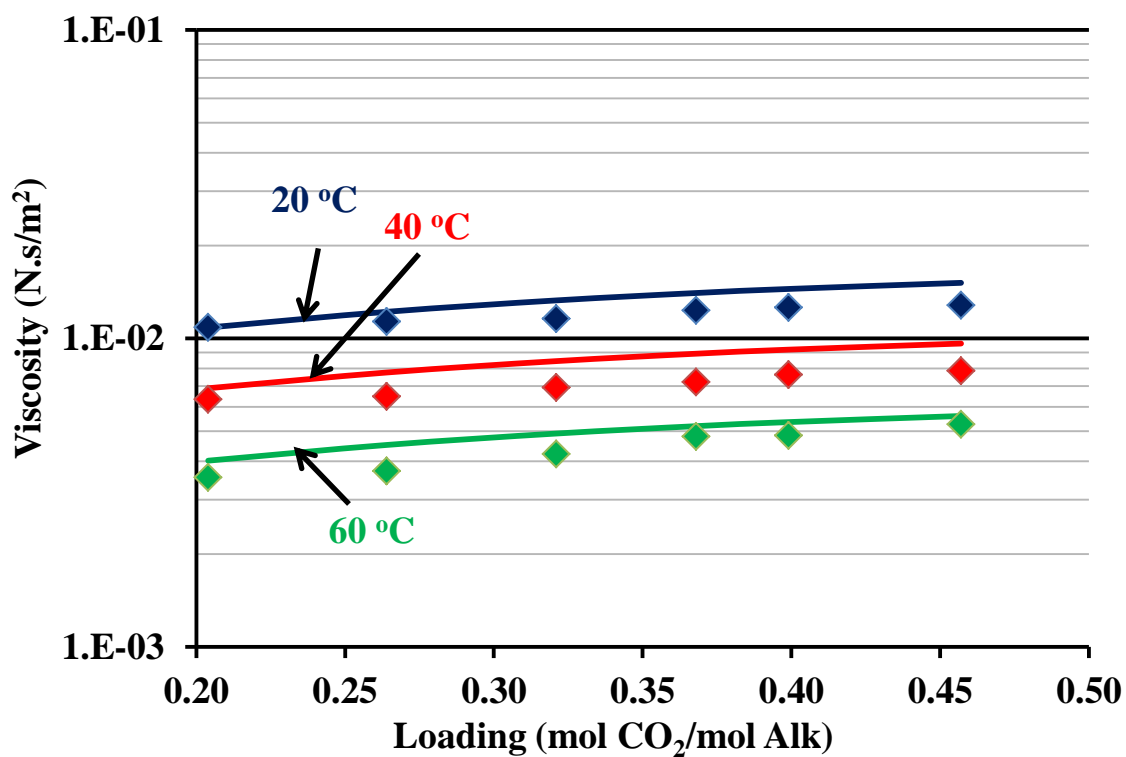


Figure B-8: Viscosity of loaded 7 m PZ from 20-60 °C.

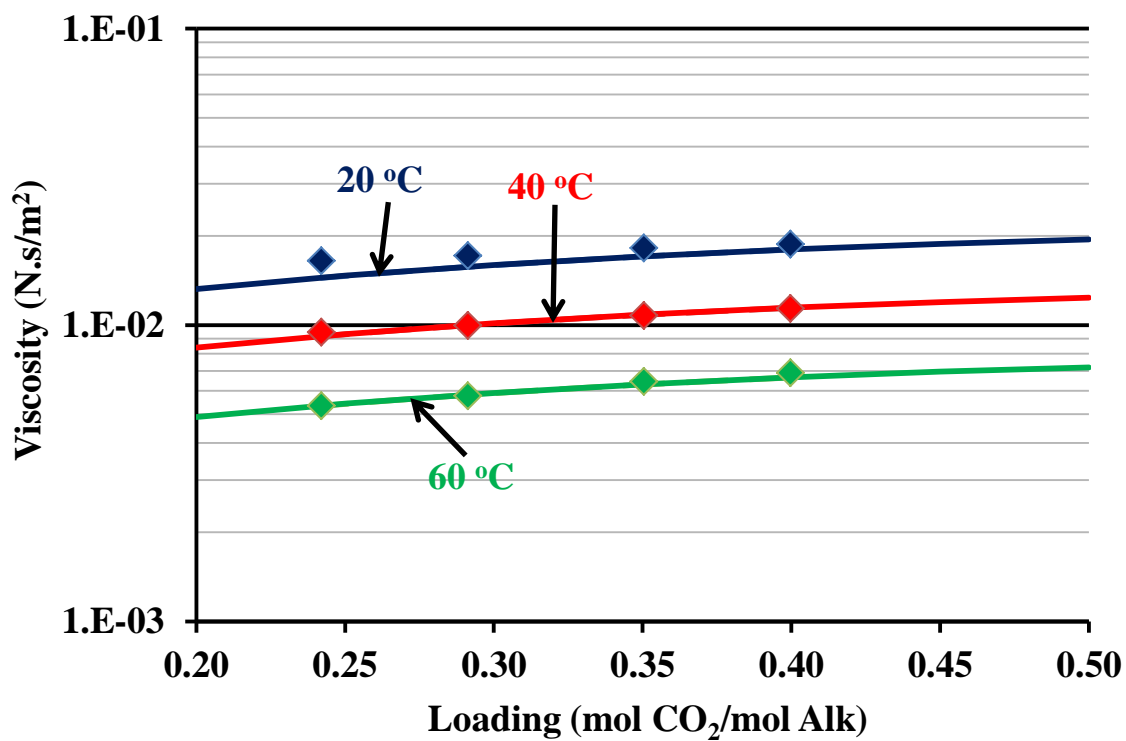


Figure B-9: Viscosity of loaded 8 m PZ from 20-60 °C.

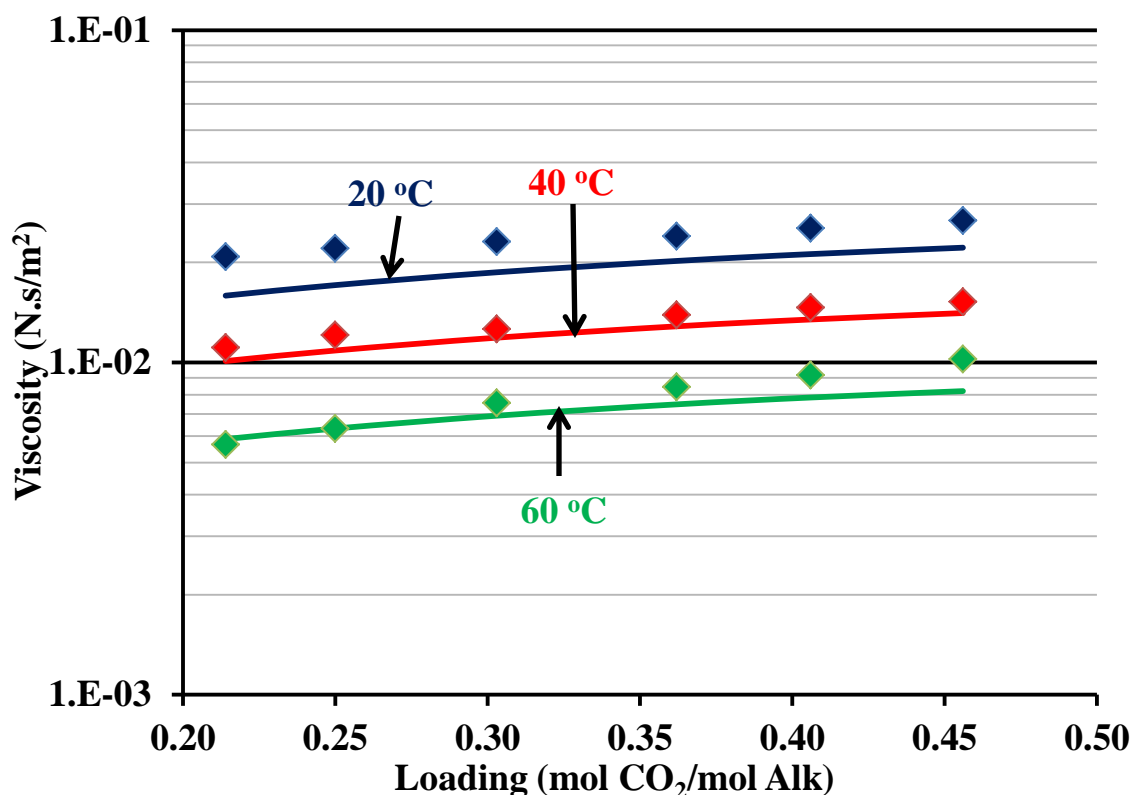


Figure B-10: Viscosity of loaded 9 m PZ from 20-60 °C.

Table B-4: Regression results for PZ/H₂O/CO₂

Parameter	Species	Value	St. Dev.	Units
DGFORM	H ⁺ PZCOO ⁻	-2.39x10 ⁸	N/A	J/kmol
DHFORM	H ⁺ PZCOO ⁻	-5.25x10 ⁸	N/A	J/kmol
CPIG 1	H ⁺ PZCOO ⁻	-2.55x10 ⁵	6.66x10 ⁴	J/kmol.K
DGAQFM	PZH ⁺	8.22x10 ⁷	N/A	J/kmol
DHAQFM	PZH ⁺	-9.2x10 ⁷	N/A	J/kmol
CPAQ0 1	PZH ⁺	2.21x10 ⁵	6.55x10 ⁴	J/kmol.K
DGAQFM	PZCOO ⁻	-2.19x10 ⁸	N/A	J/kmol
DHAQFM	PZCOO ⁻	-4.96x10 ⁸	N/A	J/kmol
CPAQ0 1	PZCOO ⁻	1.07x10 ⁵	2.65x10 ⁵	J/kmol.K
CPAQ0 2	PZCOO ⁻	604	700	J/kmol.K
DGAQFM	PZ(COO) ₂ ²⁻	-5.69x10 ⁸	N/A	J/kmol
DHAQFM	PZ(COO) ₂ ²⁻	-9.57x10 ⁸	N/A	J/kmol
CPAQ0/1	PZ(COO) ₂ ²⁻	-1.41x10 ⁵	N/A	J/kmol.K
CPAQ0/2	PZ(COO) ₂ ²⁻	4068	727	J/kmol.K
NRTL 1	H ₂ O-H ⁺ PZCOO ⁻	-12.6	3.15	N/A
NRTL 3	H ₂ O-H ⁺ PZCOO ⁻	0.238	0.117	N/A
(NRTL 5)(313K)	H ₂ O-H ⁺ PZCOO ⁻	13.0	3.25	N/A

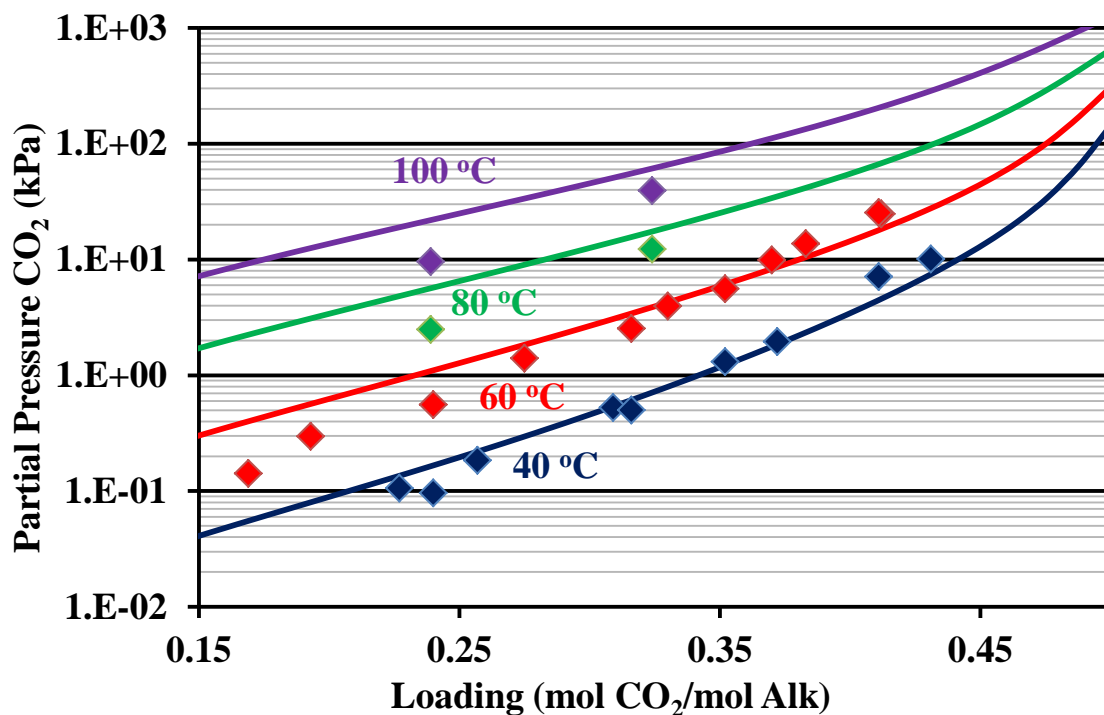


Figure B-11: Experimental data (points; Dugas 2009) and model predictions (lines) for CO₂ solubility in 2 m PZ from 40-100 °C.

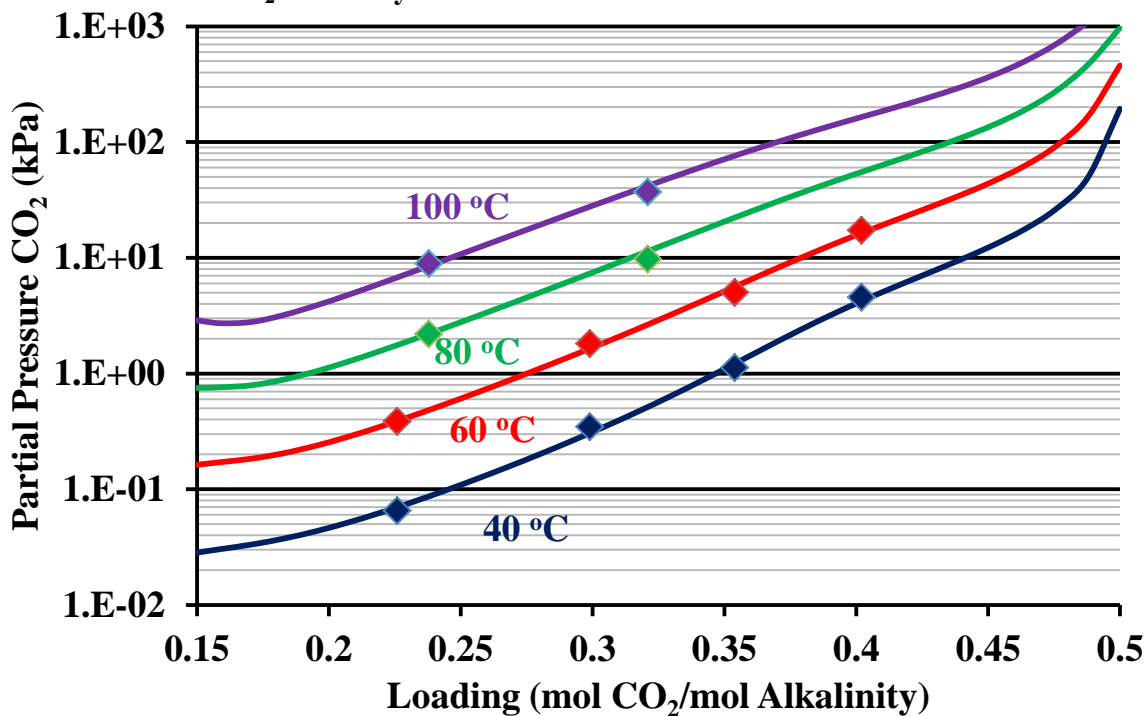


Figure B-12: Experimental data (points; Dugas 2009) and model predictions (lines) for CO₂ solubility in 5 m PZ from 40-100 °C.

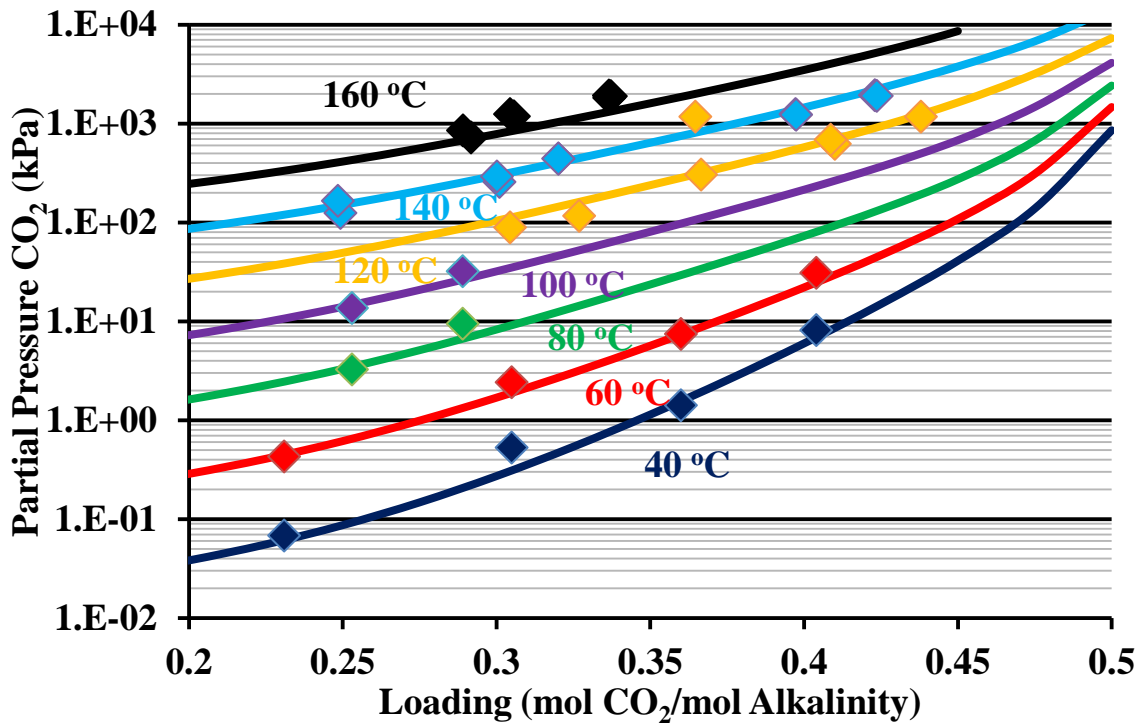


Figure B-13: Experimental data (points; Dugas 2009; Xu 2011) and model predictions (lines) for CO₂ solubility in 8 m PZ from 40-160 °C.

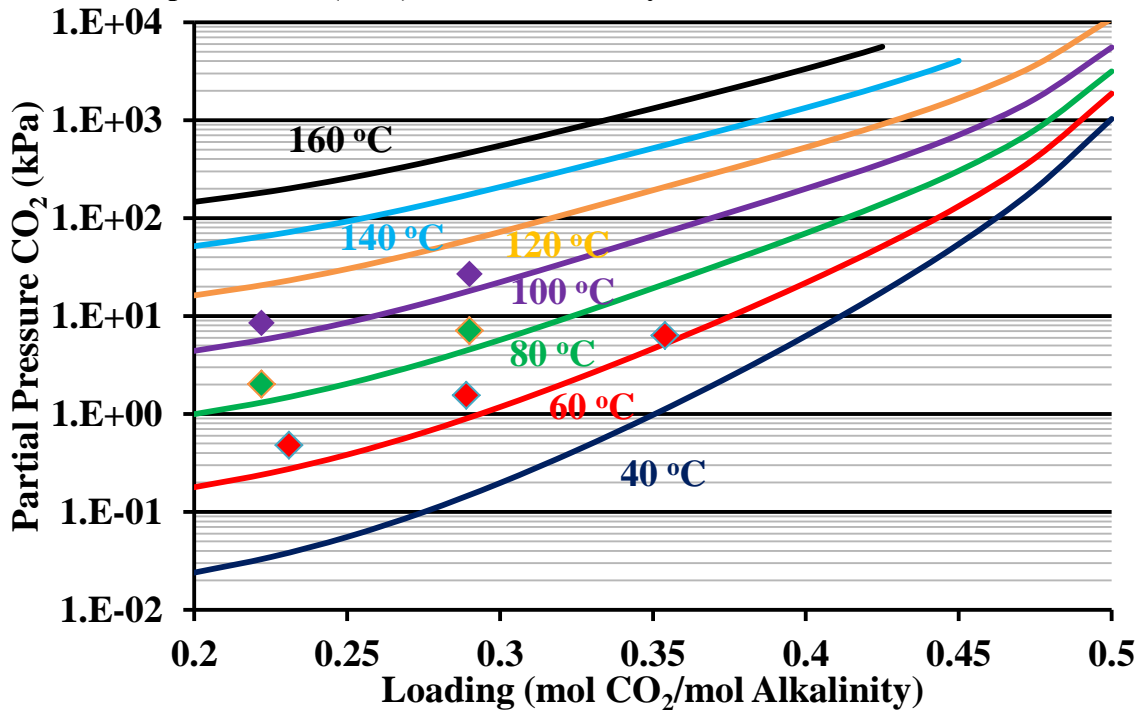


Figure B-14: Experimental data (points; Dugas 2009; Xu 2011) and model predictions (lines) for CO₂ solubility in 12 m PZ from 40-160 °C.

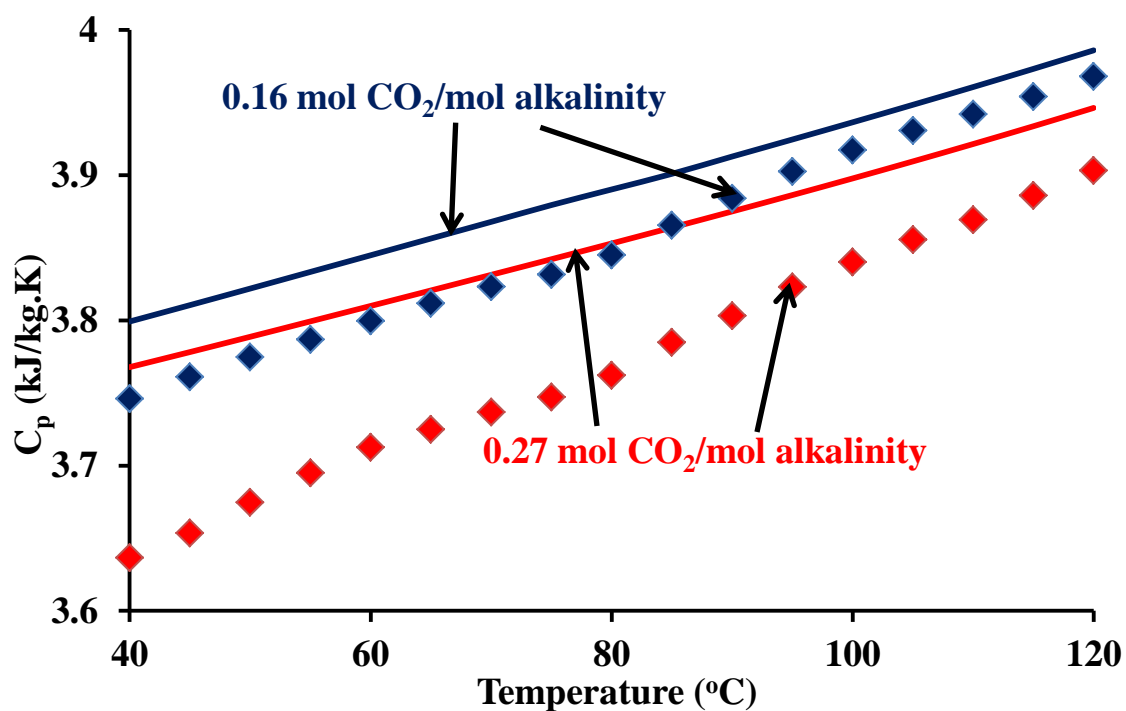


Figure B-15: Experimental data (points; Hilliard 2008) and model predictions (lines) for heat capacity of 2 m PZ at loadings of 0.16 and 0.27 mol CO₂/mol alkalinity.

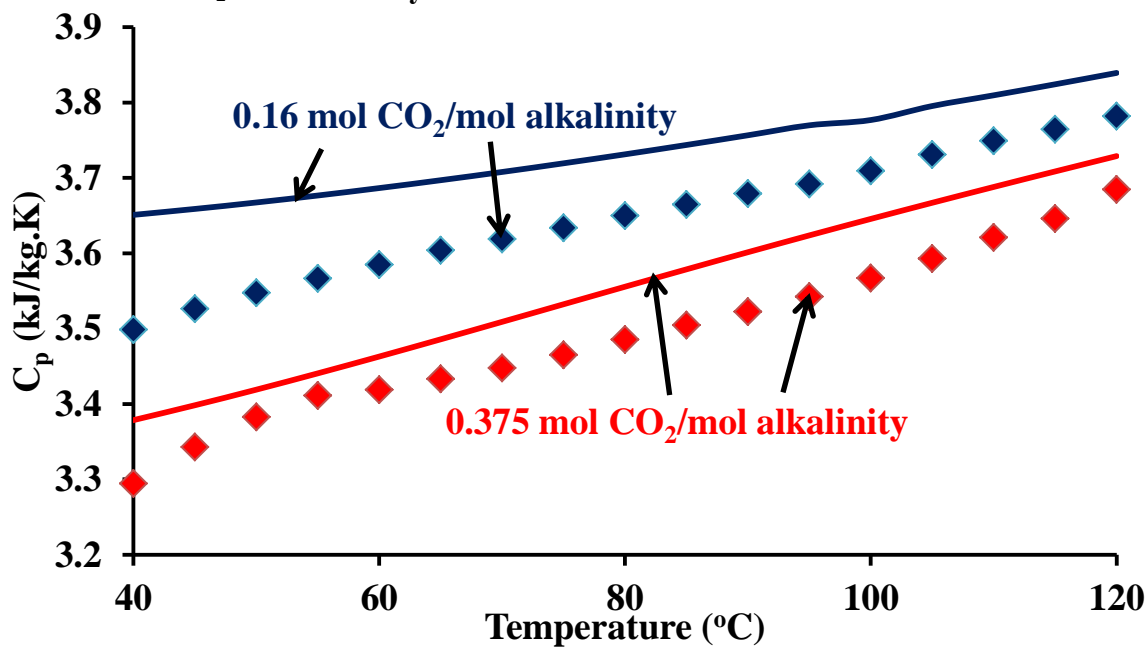


Figure B-16: Experimental data (points; Hilliard 2008) and model predictions (lines) for heat capacity of 3.6 m PZ at loadings of 0.16 and 0.375 mol CO₂/mol alkalinity.

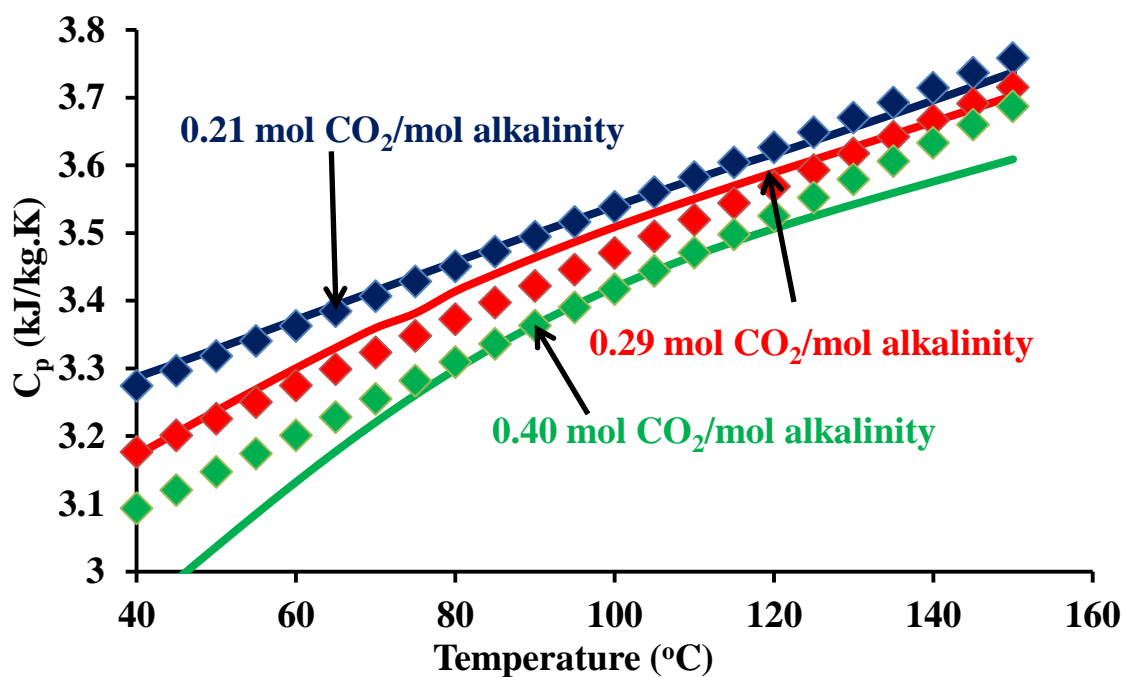


Figure B-17: Experimental data (points; Freeman 2011) and model predictions (lines) for heat capacity of 8 m PZ at loadings of 0.21, 0.29 and 0.4 mol CO₂/mol alkalinity.

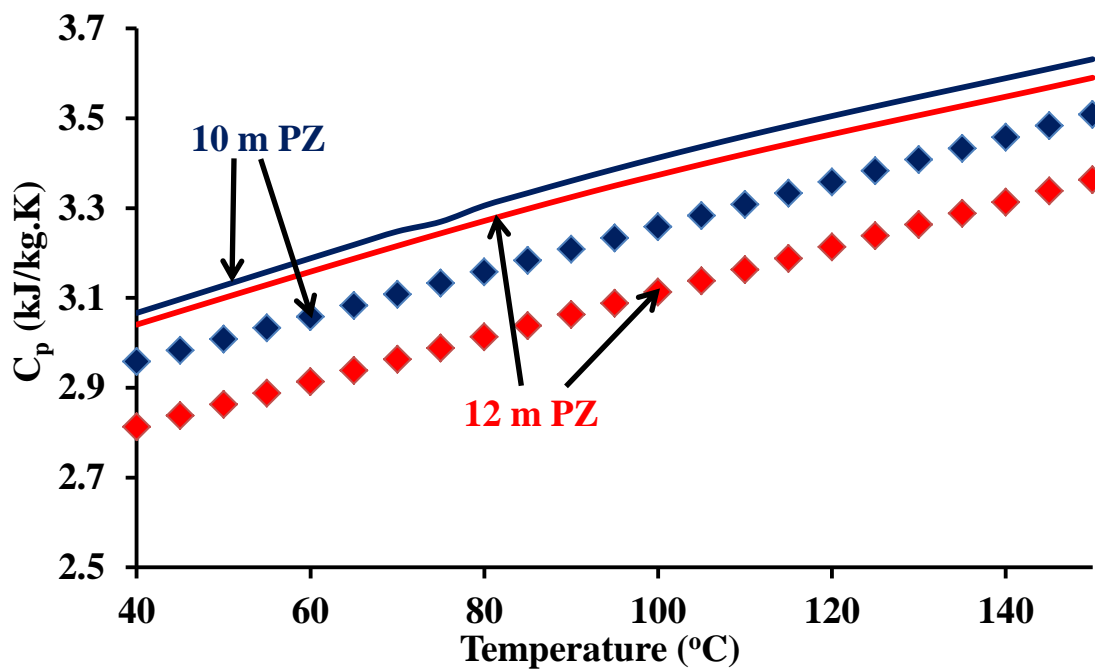


Figure B-18: Experimental data (points; Freeman 2011) and model predictions (lines) for heat capacity of 10 m PZ at a loading of 0.31 mol CO₂/mol alkalinity and 12 m PZ at a loading of 0.29 mol CO₂/mol alkalinity.

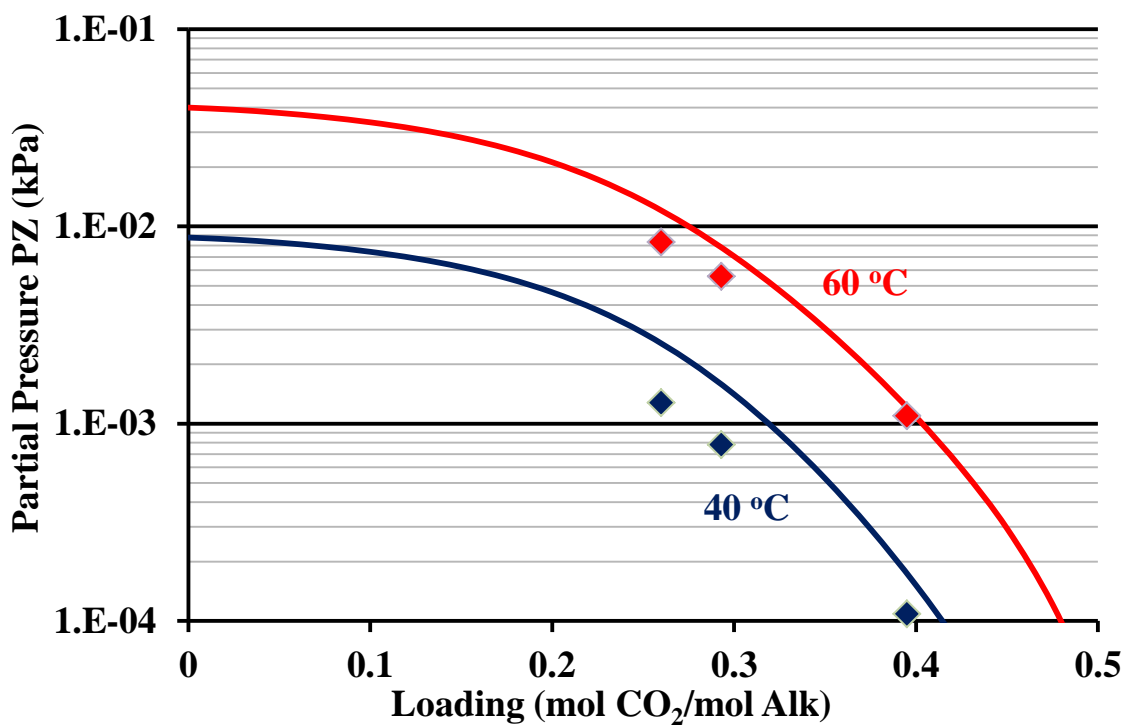


Figure B-19: Experimental data (points; Nguyen 2012) and model predictions (lines) for PZ volatility in loaded 8 m PZ from 40-60 °C.

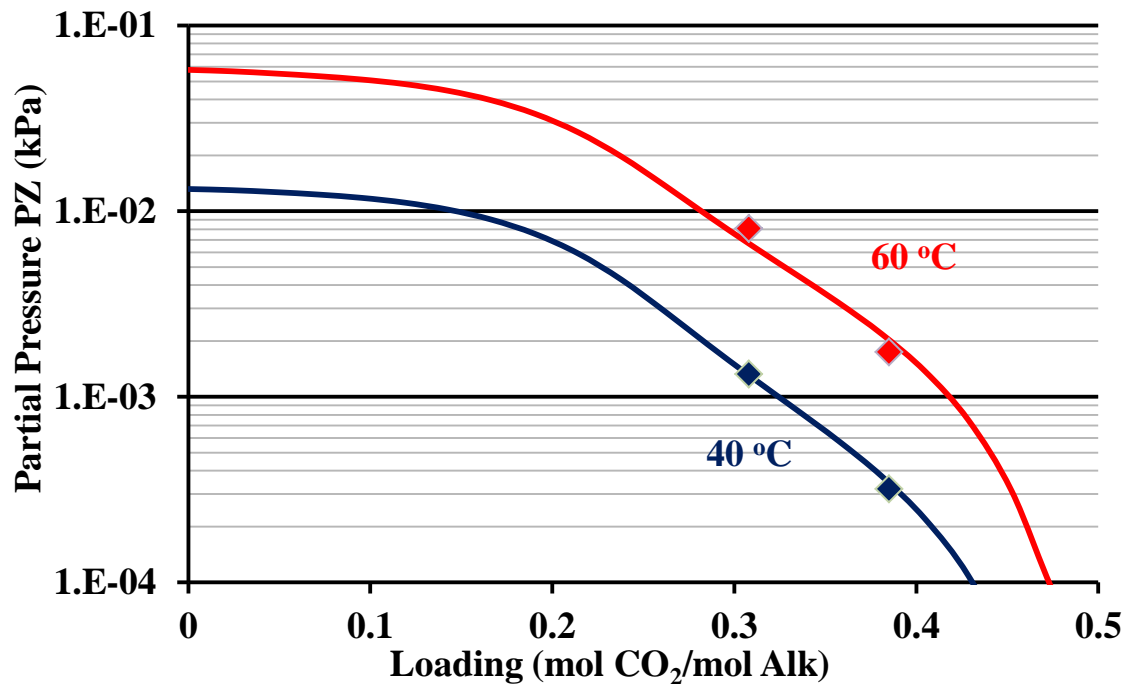


Figure B-20: Experimental data (points; Nguyen 2012) and model predictions (lines) for PZ volatility in loaded 10 m PZ from 40-60 °C.

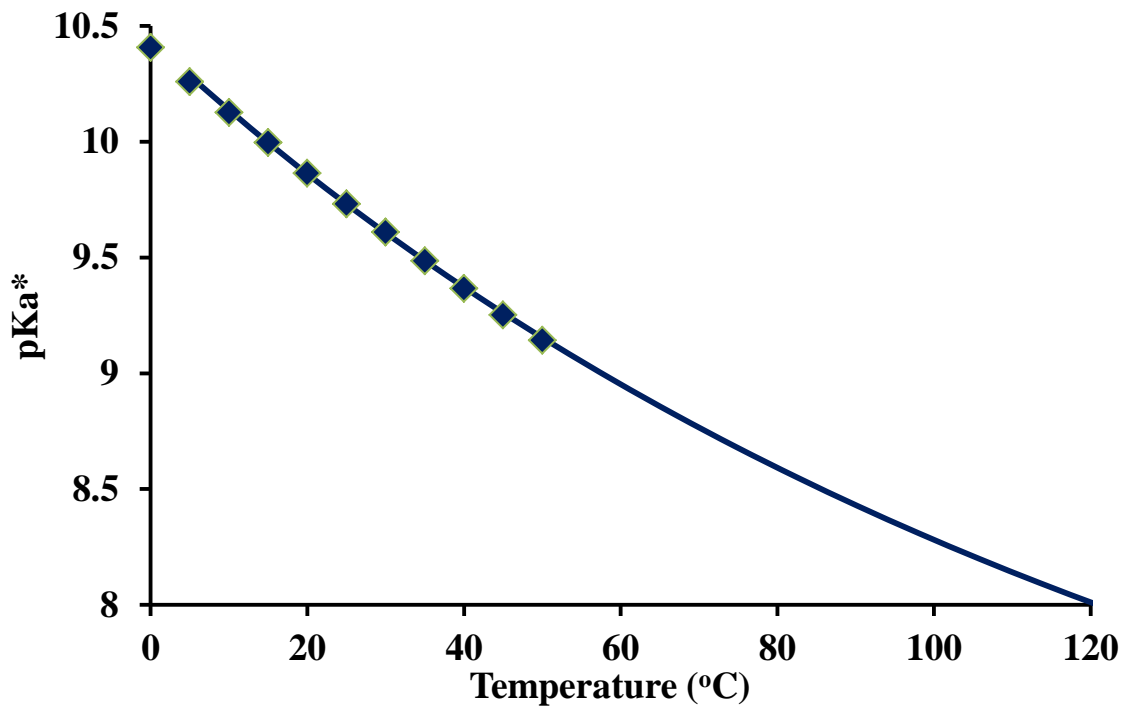


Figure B-21: Experimental data (points; Hetzer 1968) and model predictions (lines) for PZ pKa.

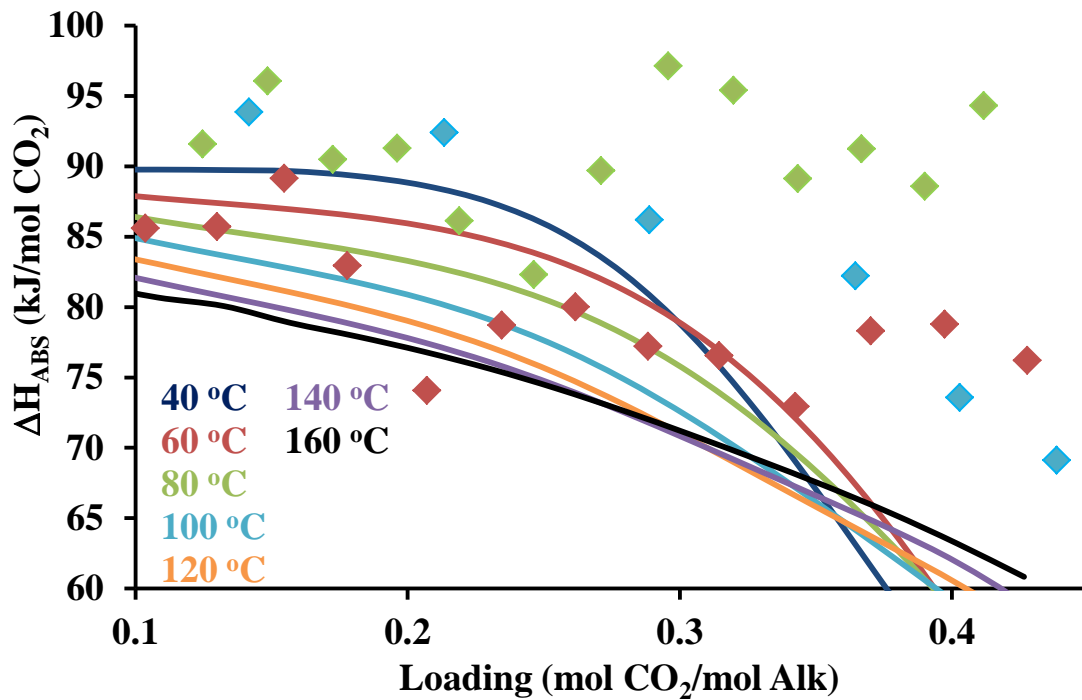


Figure B-22: Experimental data (points; Freeman 2010) and model predictions (lines) for heat of CO₂ absorption in 8 m PZ from 40—160 °C.

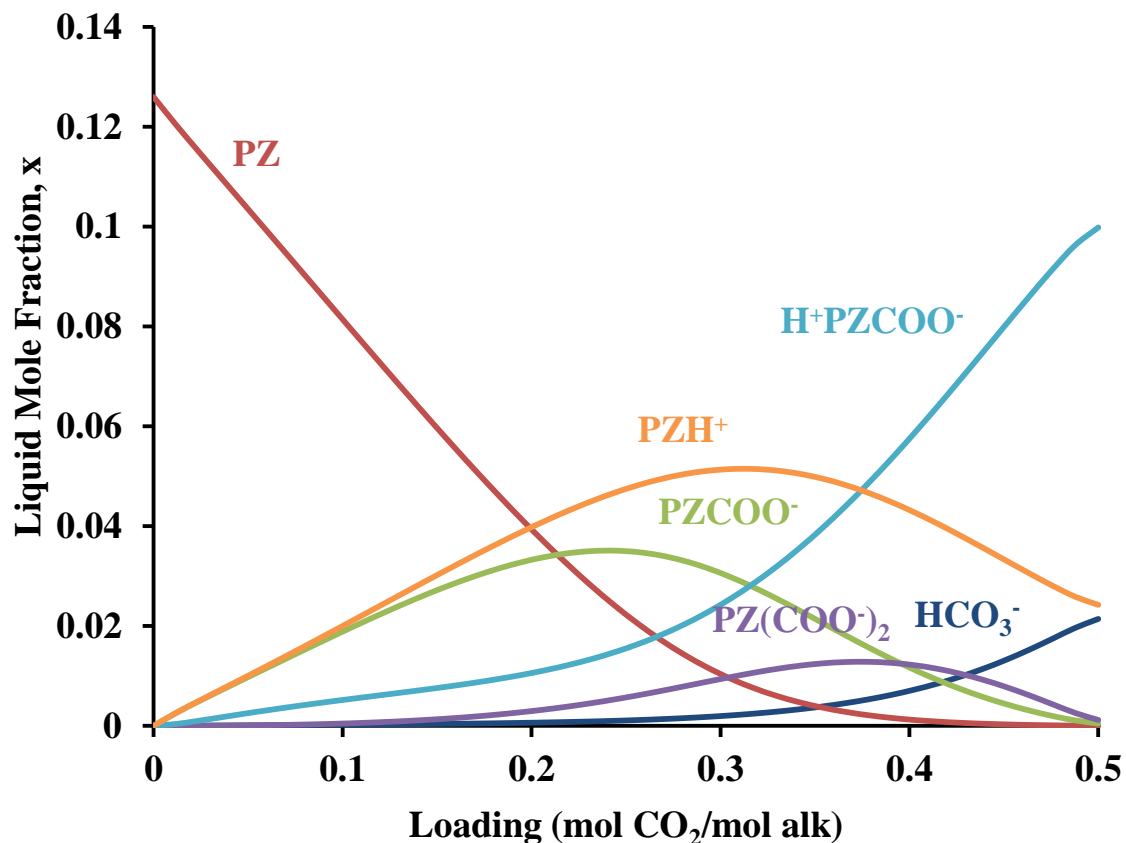


Figure B-23: Model predictions for liquid mole fraction in 8 m PZ at 40 °C.

Table B-6: Regression results for activity coefficient of CO₂.

Parameter	Species	Value	St. Dev.
NRTL 1	PZ-CO ₂	-8.60	0.475
(NRTL 2)/313	PZ-CO ₂	10.6	0.495
NRTL 3	CO ₂ -PZ	0.05	N/A
NRTL 1	H ⁺ PZCOO ⁻ -CO ₂	20.3	105
NRTL 1	CO ₂ -H ⁺ PZCOO ⁻	3.01	3.95
NRTL 3	H ⁺ PZCOO ⁻ -CO ₂	0.077	0.121
GMELCC	(PZH ⁺ /PZCOO ⁻)/CO ₂	-7.08	0.689
GMELCC	(PZH ⁺ /PZ(COO) ₂ ²⁻)/CO ₂	-8.88	1.70
GMELCC	(PZH ⁺ /HCO ₃ ⁻)/CO ₂	-4.15	0.926
(GMELCD)/313	(PZH ⁺ /PZCOO ⁻)/CO ₂	5.03	0.680
(GMELCD)/313	(PZH ⁺ /PZ(COO) ₂ ²⁻)/CO ₂	6.33	1.61
(GMELCD)/313	(PZH ⁺ /HCO ₃ ⁻)/CO ₂	0.786	1.37

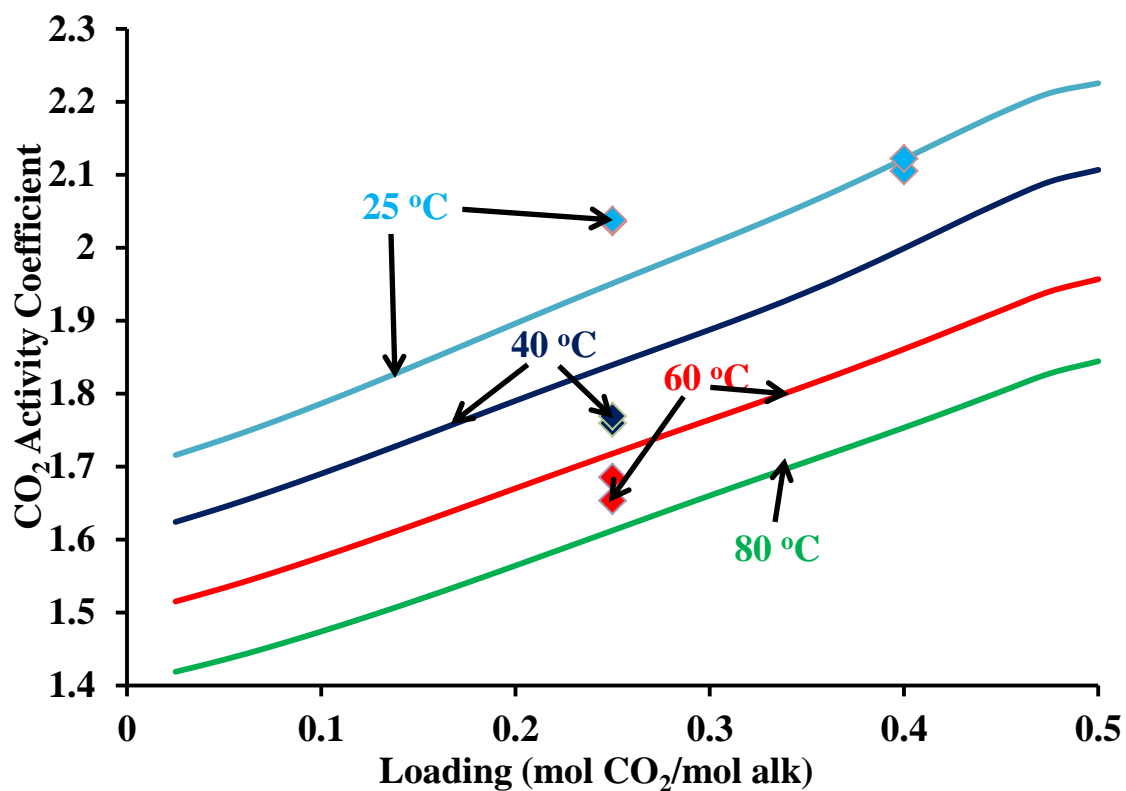


Figure B-24: Experimental data (points; Svendsen 2010) and model predictions (lines) for the activity coefficient of CO₂ from 25-80 °C.

Table B-7: Regression results for MDEA/H₂O

Parameter	Species	Value	Standard Dev.
NRTL 1	MDEA-H ₂ O	4.62	0.394
(NRTL 2)/313	MDEA-H ₂ O	-5.17	0.384
NRTL 3	MDEA-H ₂ O	0.20	FIXED
HENRY 1	MDEA-H ₂ O	56.0	1.08
(HENRY 2)/313	MDEA-H ₂ O	-42.6	0.761
(HENRY 4)x313	MDEA-H ₂ O	-12.3	0.413
CPIG 1 (J/kmol.K)	MDEA	5.99x10 ⁴	3.42x10 ⁴
(CPIG 2)x313 (J/kmol.K)	MDEA	1.03x10 ⁵	3.34x10 ⁴

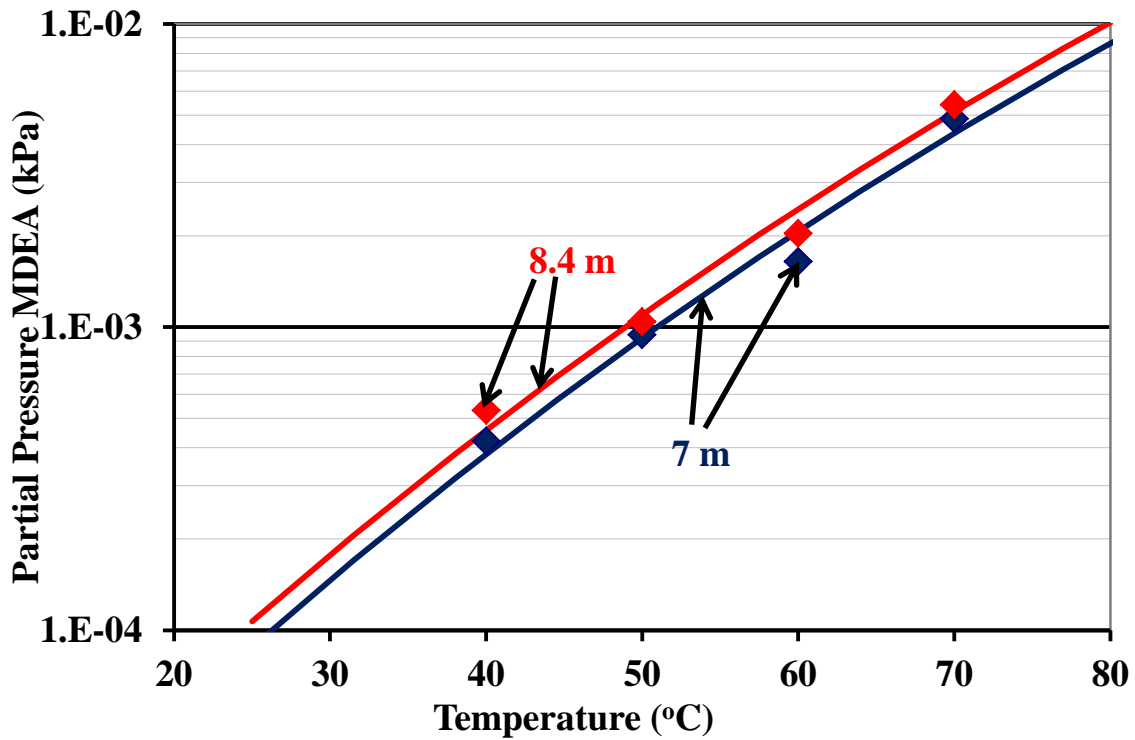


Figure B-25: Experimental data (Nguyen, 2012) and model predictions (lines) for MDEA volatility in 7 m and 8.4 m MDEA.

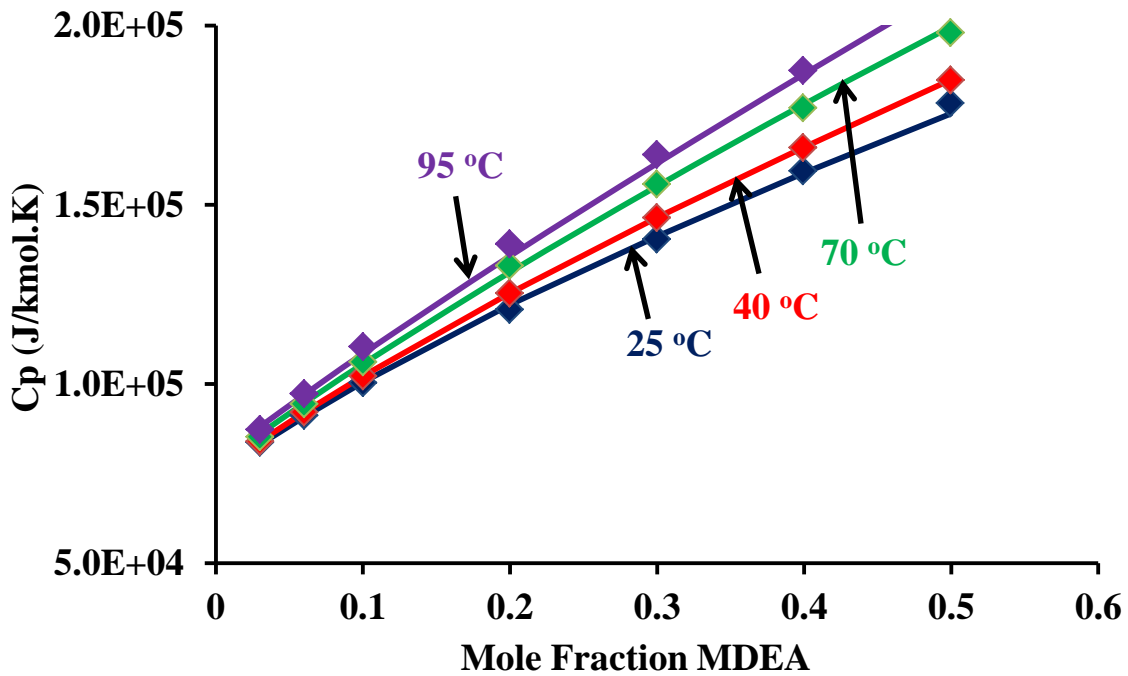


Figure B-26: Experimental data (Zhang, 2002) and model predictions (lines) for MDEA heat capacity from 25-95 °C.

Table B-8: Regression results for MDEA/H₂O/CO₂ Density and Viscosity

Parameter	Species	Value	Standard Dev.
IONMUB 1	MDEAH ⁺	0.512	N/A
MUKIJ 1	H ₂ O-MDEA	0.451	0.0319
MULIJ 1	MDEA-H ₂ O	-0.809	0.0955
RKTZRA 1	MDEA	0.249	1.75x10 ⁻⁴
VCRKT 1	MDEA	0.368	N/A
VLCLK 1	MDEAH ⁺ -HCO ₃ ⁻	0.107	1.42x10 ⁻³
VLCLK 2	MDEAH ⁺ -HCO ₃ ⁻	0.129	6.21x10 ⁻³

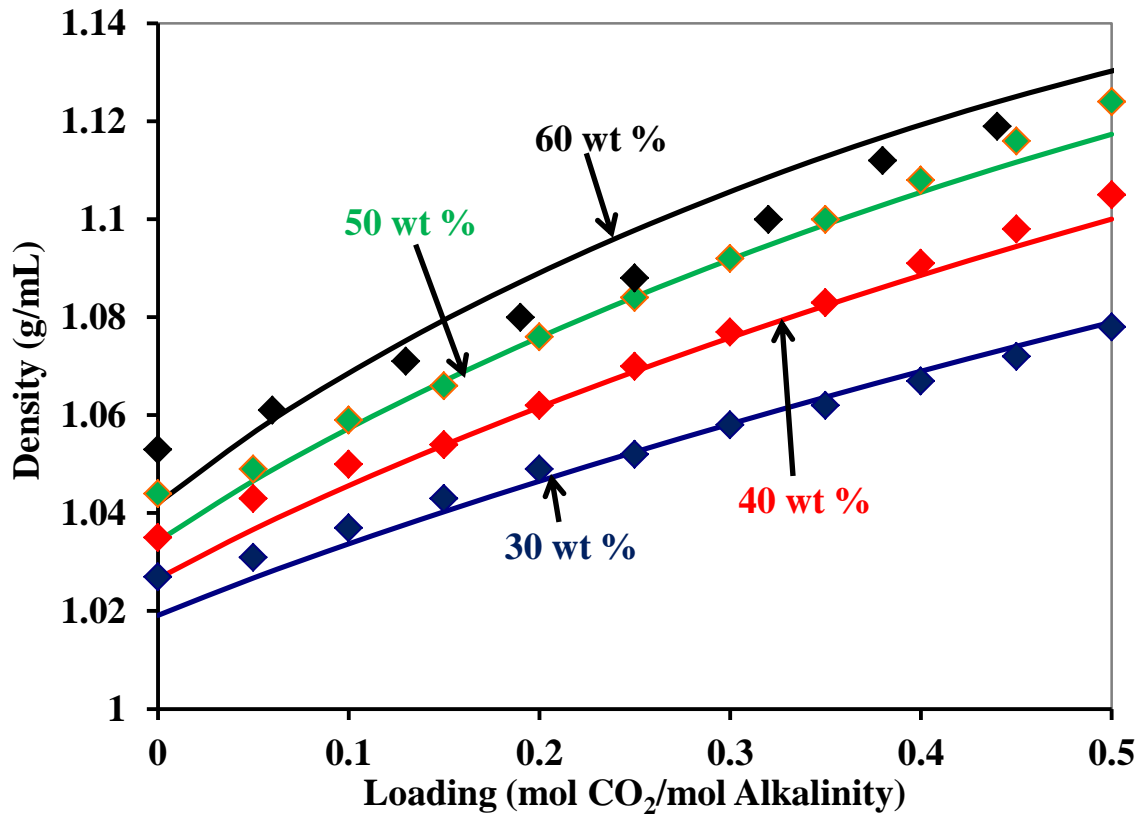


Figure B-27: Experimental data (Weiland, 1998) and model predictions (lines) for loaded MDEA density at 25 °C.

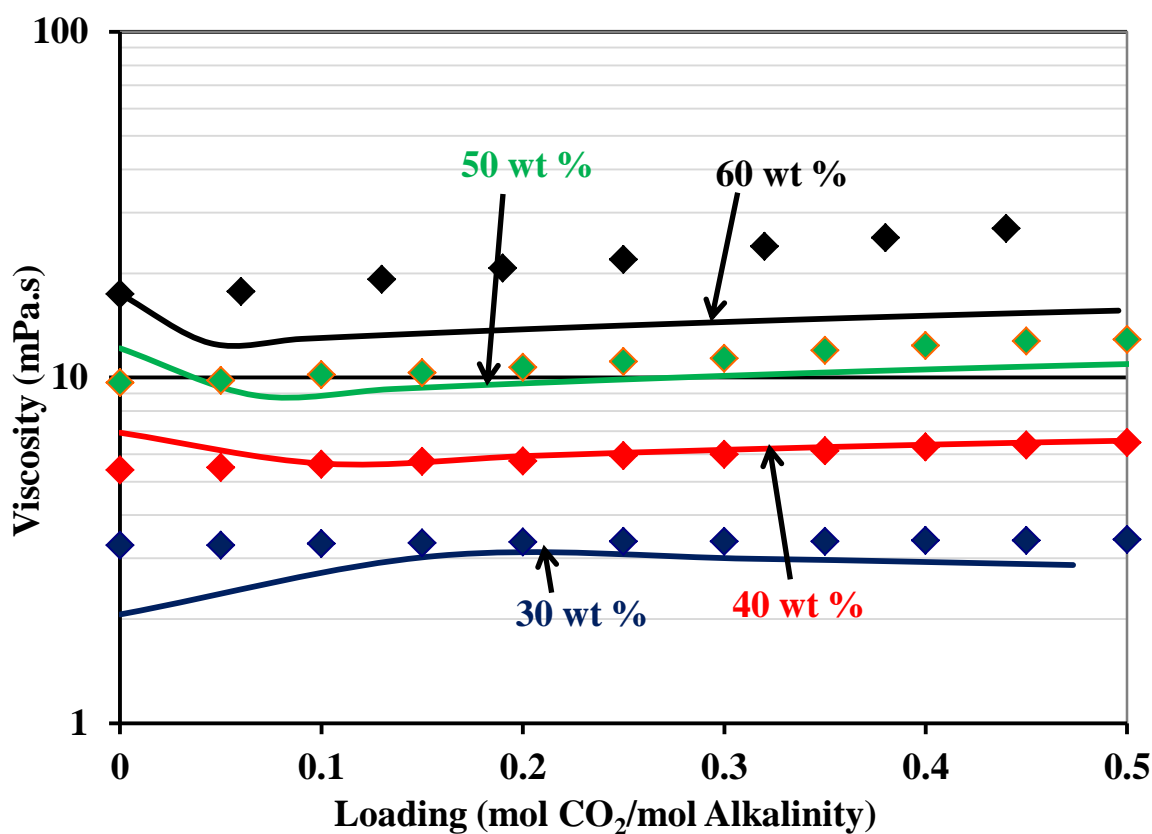


Figure B-28: Experimental data (Weiland, 1998) and model predictions (lines) for loaded MDEA viscosity at 25 °C.

Table B-9: Regression results for MDEA/H₂O/CO₂

Parameter	Species	Value	St. Dev.	Units
DGAQFM	MDEAH ⁺	-2.577x10 ⁸	N/A	J/kmol
DHAQFM	MDEAH ⁺	-4.99x10 ⁸	N/A	J/kmol
CPAQ0/1	MDEAH ⁺	3.4x10 ⁵	N/A	J/kmol.K
GMELCC	H ₂ O/(MDEAH ⁺ /HCO ₃ ⁻)	7.33	0.496	N/A
GMELCC	(MDEAH ⁺ /HCO ₃ ⁻)/H ₂ O	-3.16	0.244	N/A
GMELCC	MDEA/(MDEAH ⁺ /HCO ₃ ⁻)	24.1	2.26	N/A
GMELCC	(MDEAH ⁺ /HCO ₃ ⁻)/MDEA	-5.50	0.153	N/A
GMELCD/313	H ₂ O/(MDEAH ⁺ /HCO ₃ ⁻)	-0.795	0.0986	K
GMELCD/313	MDEA/(MDEAH ⁺ /HCO ₃ ⁻)	-15.7	1.96	K

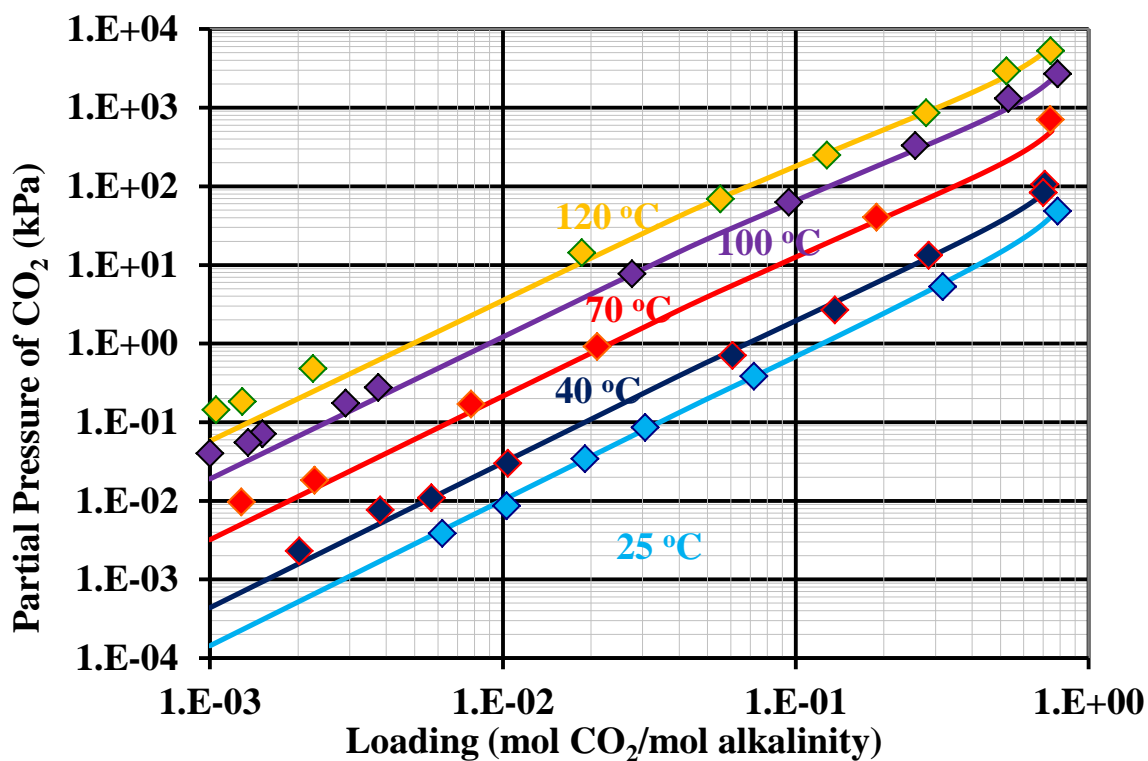


Figure B-29: Experimental data (Jou, 1982) and model predictions (lines) for solubility of CO₂ in 50 wt % MDEA from 25-120 °C.

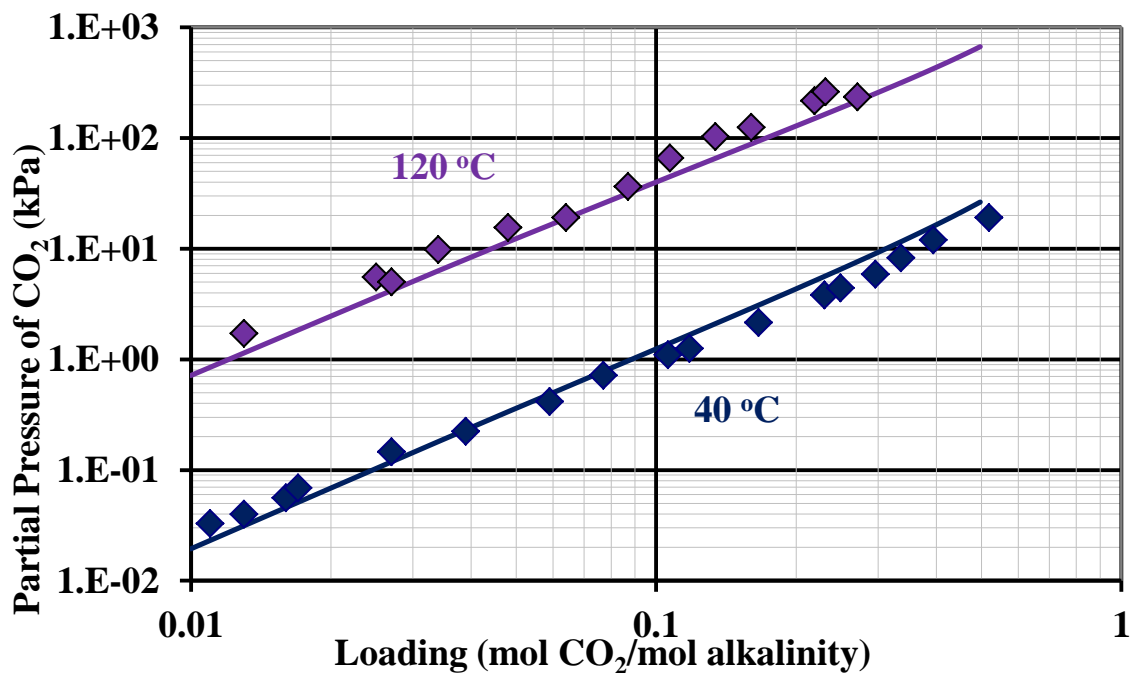


Figure B-30: Experimental data (Jou, 1993) and model predictions (lines) for solubility of CO₂ in 4.5 MDEA from 40-120 °C.

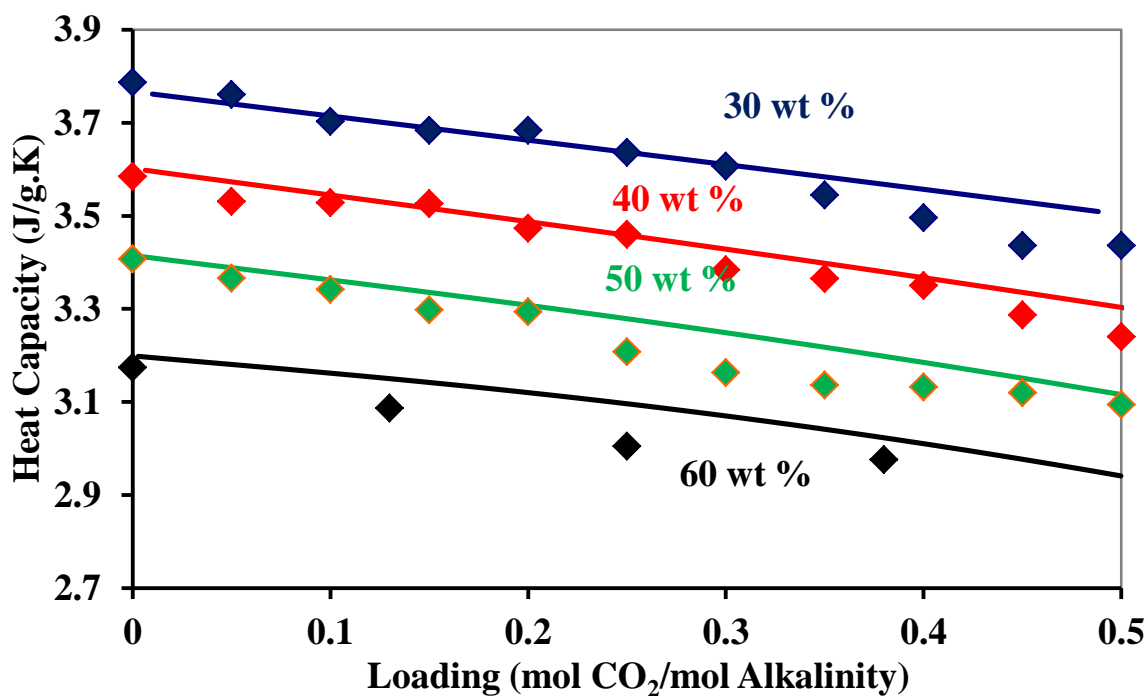


Figure B-31: Experimental data (Weiland, 1997) and model predictions (lines) for heat capacity of loaded 30-60 wt % MDEA at 25 °C.

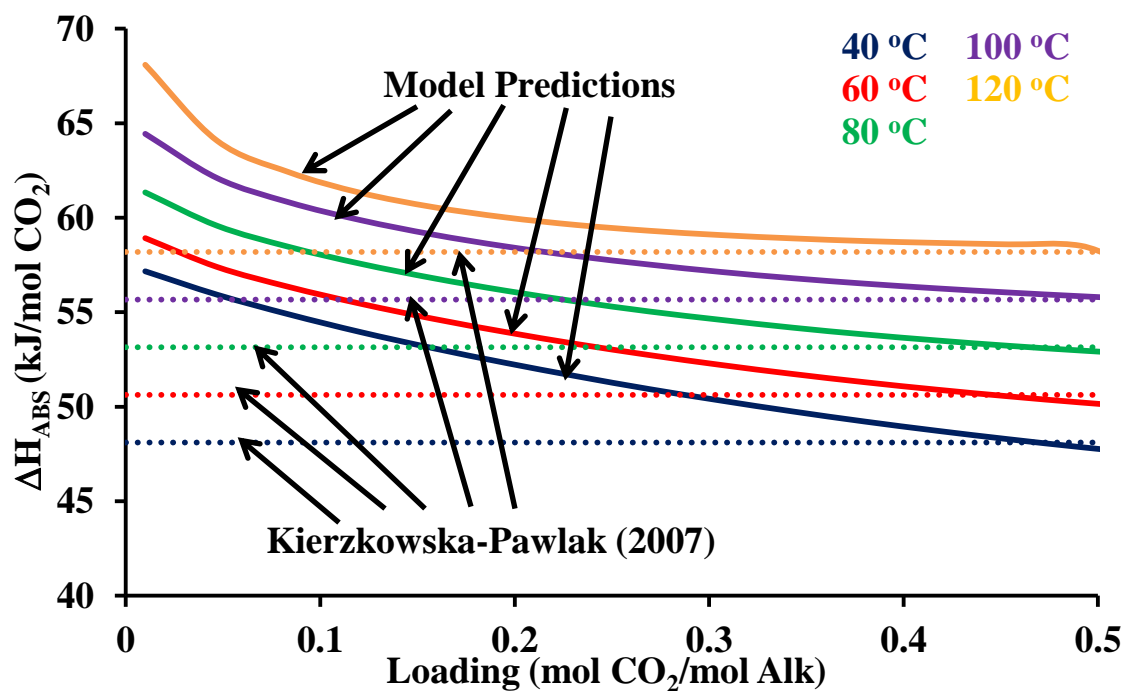


Figure B-32: Experimental data (Kierzkowska-Pawlak, 2007) and model predictions (lines) for heat of CO₂ absorption in 50 wt % MDEA from 40-120 °C.

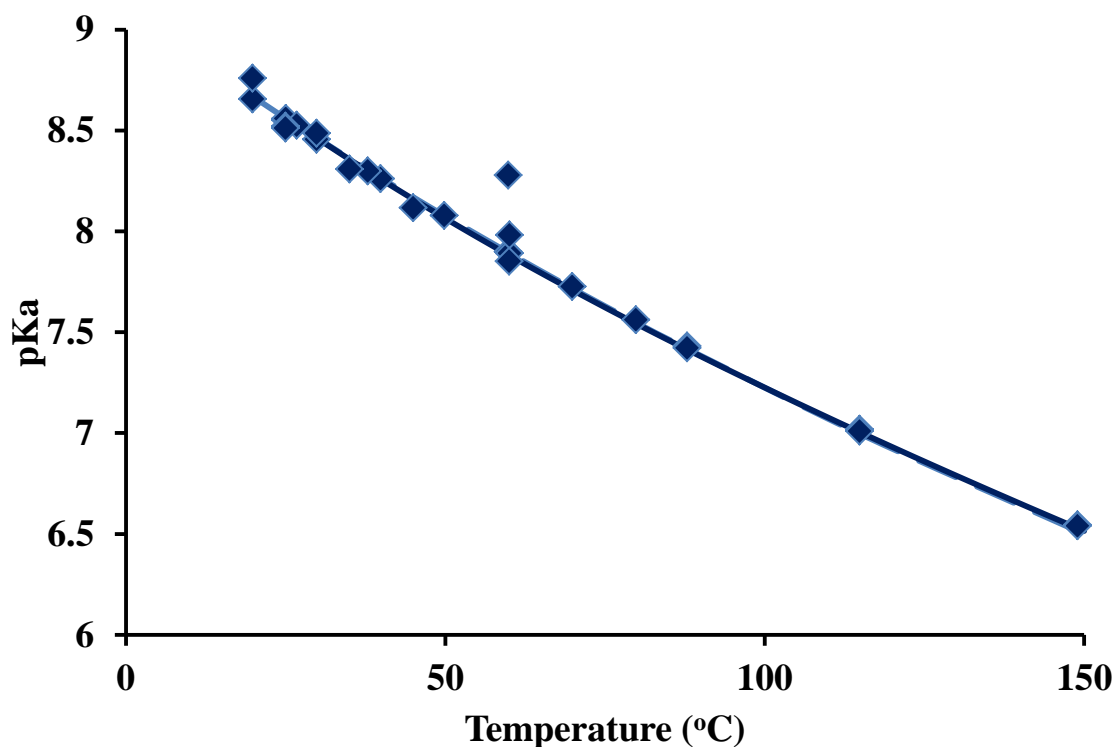


Figure B-33: Experimental data (Hamborg, 2007) and model predictions (line) for MDEA pKa from 20-150 °C.

Table B-10: Regression results for MDEA/PZ/H₂O and MDEA/PZ/H₂O/CO₂

Parameter	Species	Value	St. Dev.	Units
NRTL 1	PZ-MDEA	-2.84	0.10	N/A
NRTL 3	PZ-MDEA	0.2	N/A	N/A
GMELCC	(MDEAH ⁺ /PZCOO ⁻)/H ₂ O	-3.70	0.0433	N/A
GMELCC	(MDEAH ⁺ /PZ(COO) ₂ ²⁻)/H ₂ O	-4.33	0.0332	N/A
GMELCC	(MDEAH ⁺ /HCO ₃ ⁻)/H ⁺ PZCOO ⁻	0.208	0.987	N/A

Table B-11: Regression results for MDEA/PZ/H₂O/CO₂ Density (Reference Equation 4-1)

Parameter	Value
A	-1.01
B	-0.0428
C	0.606
D	2.45
E	1.35
F	-6.39x10 ⁻⁴
G	0.276
H	0.0799

Table B-12: Regression results for MDEA/PZ/H₂O/CO₂ Density (Reference Equation 4-2)

Parameter	Value
A	-0.0221
B	0.0579
C	0.0568
D	-0.0608
E	3526
F	-5.40×10^{-6}
G	-4.32×10^{-8}
H	-0.0106
I	0.196
J	0.0131

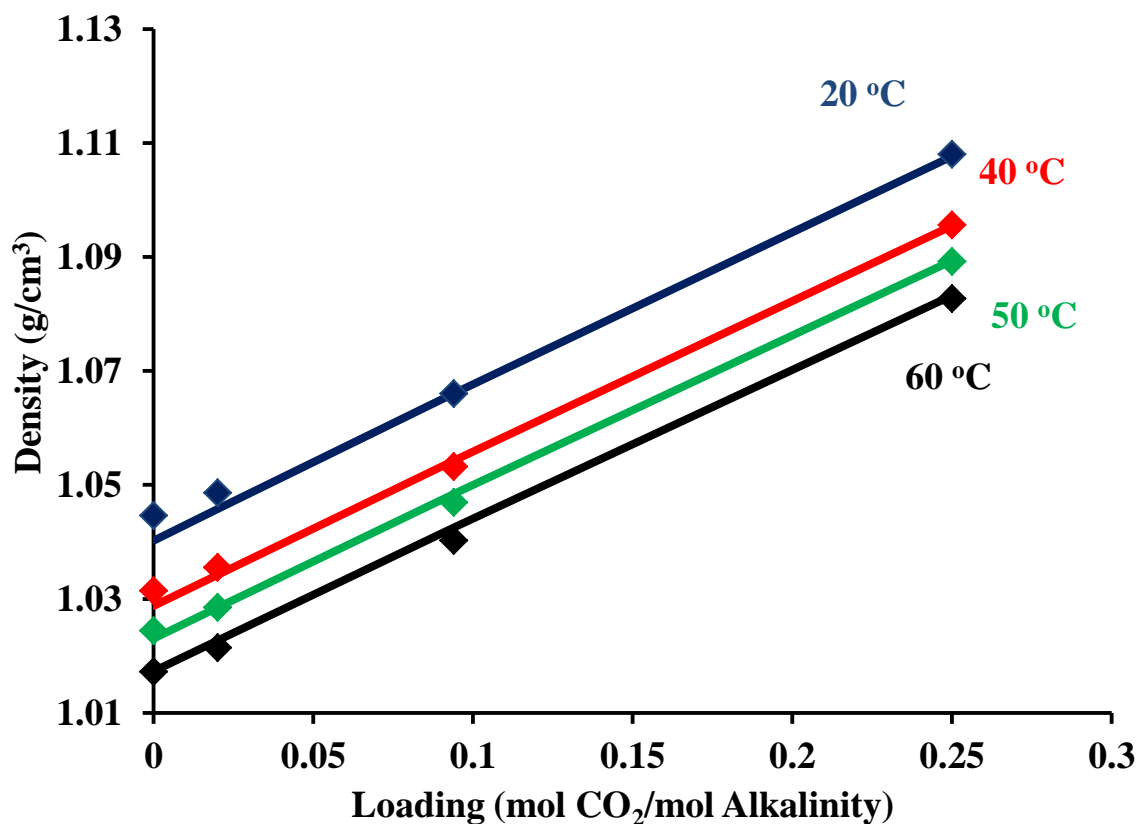


Figure B-34: Experimental data (This Work) and model predictions (lines) for loaded 7 m MDEA/2 m PZ density from 20-60 °C.

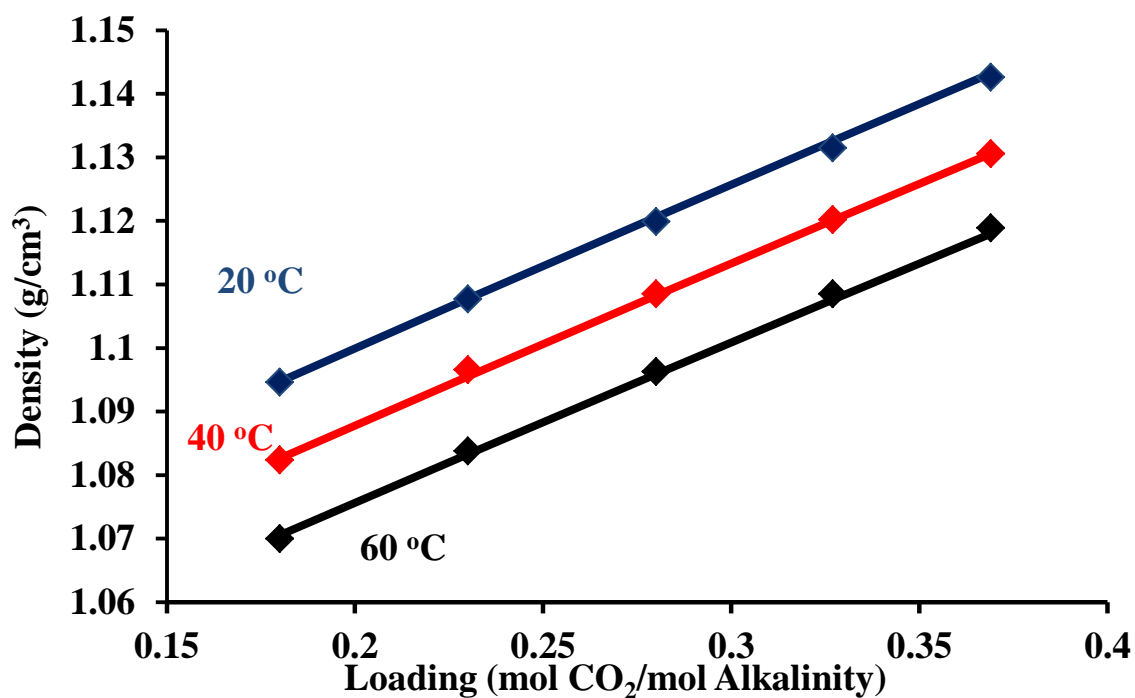


Figure B-35: Experimental data (This Work) and model predictions (lines) for loaded 5 m MDEA/5 m PZ density from 20-60 °C.

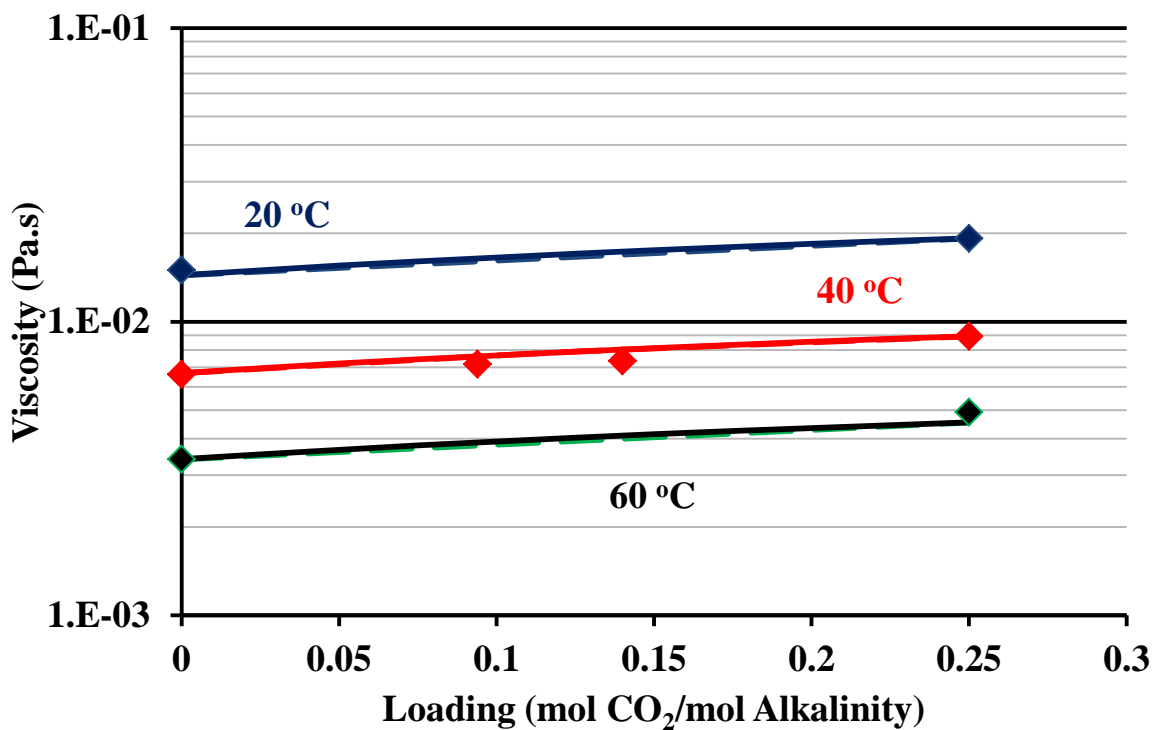


Figure B-36: Experimental data (This Work) and model predictions (lines) for loaded 7 m MDEA/2 m PZ viscosity from 20-60 °C.

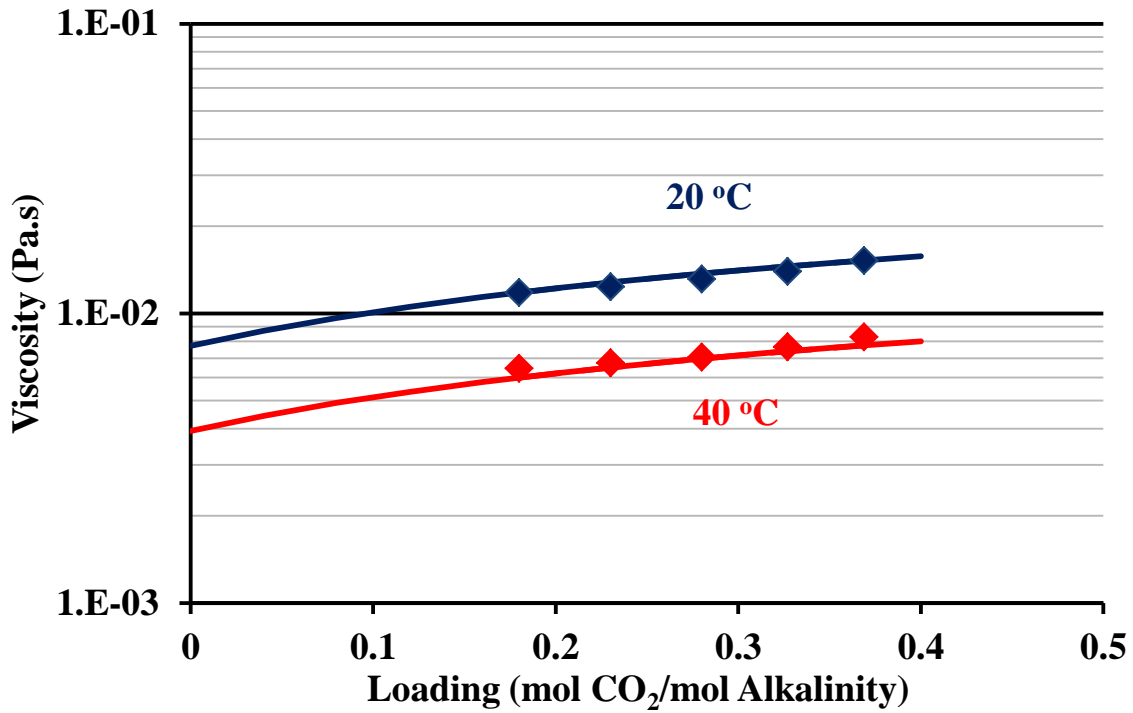


Figure B-37: Experimental data (This Work) and model predictions (lines) for loaded 5 m MDEA/5 m PZ viscosity from 20-40 °C.

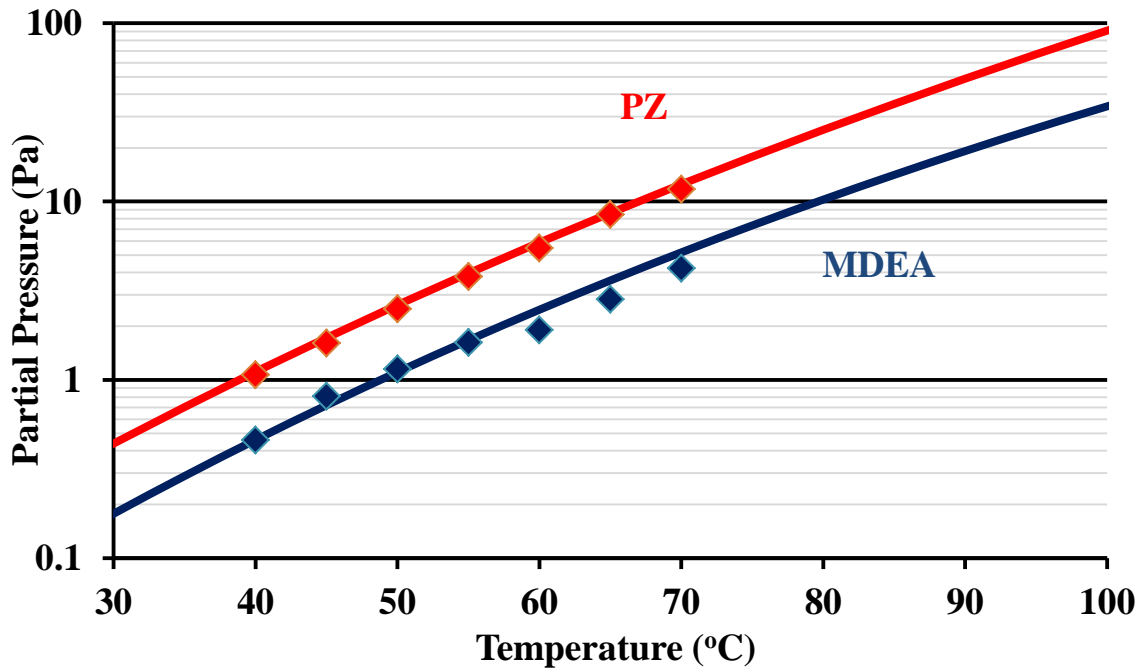


Figure B-38: Experimental data (Nguyen, 2012) and model predictions (lines) for unloaded amine volatility in 7 m MDEA/2 m PZ from 40-70 °C.

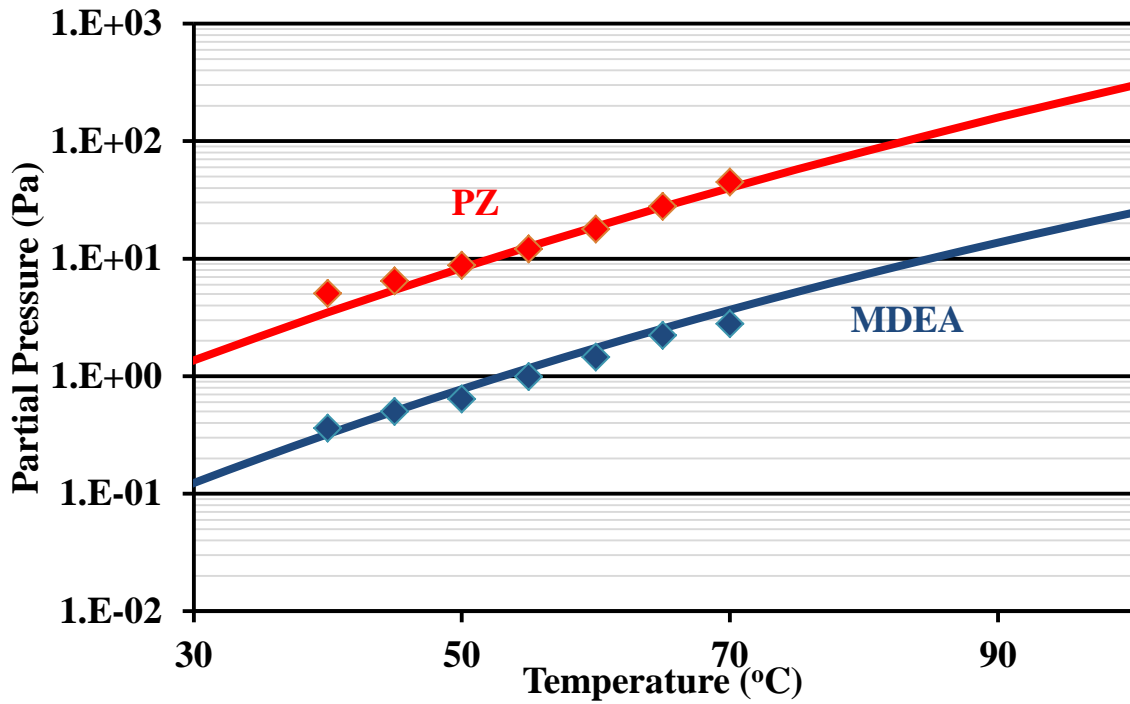


Figure B-39: Experimental data (Nguyen, 2012) and model predictions (lines) for unloaded amine volatility in 5 m MDEA/5 m PZ from 40-70 °C.

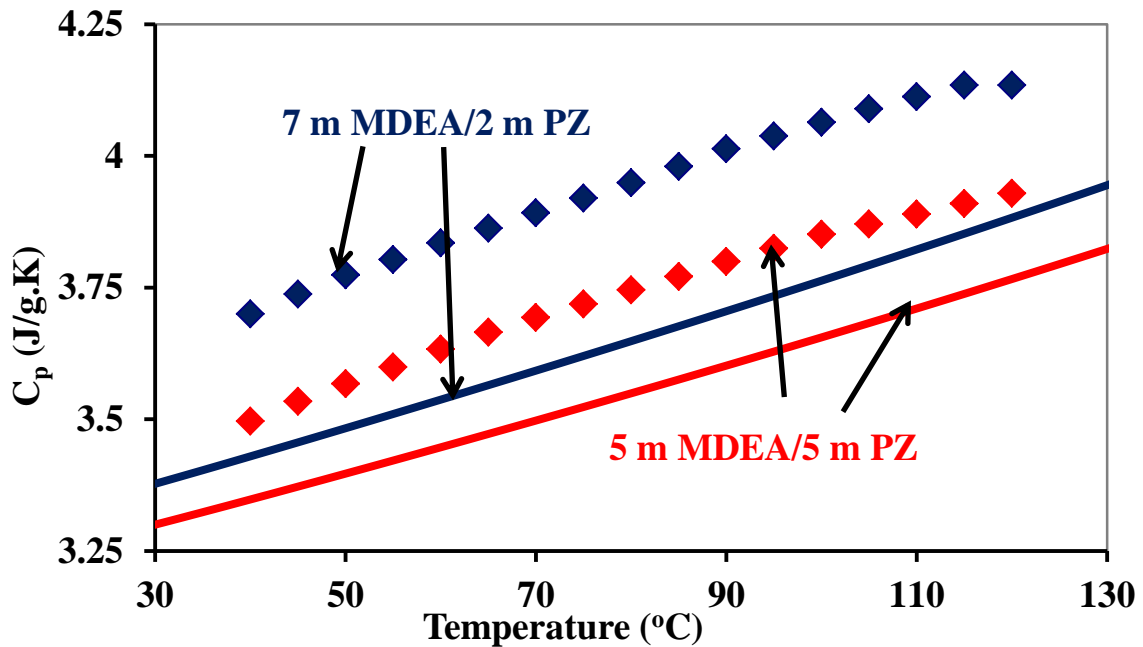


Figure B-40: Experimental data (Nguyen, 2012) and model predictions (lines) for heat capacity of 7 m MDEA/2 m PZ and 5 m MDEA/5 m PZ from 40-120 °C.

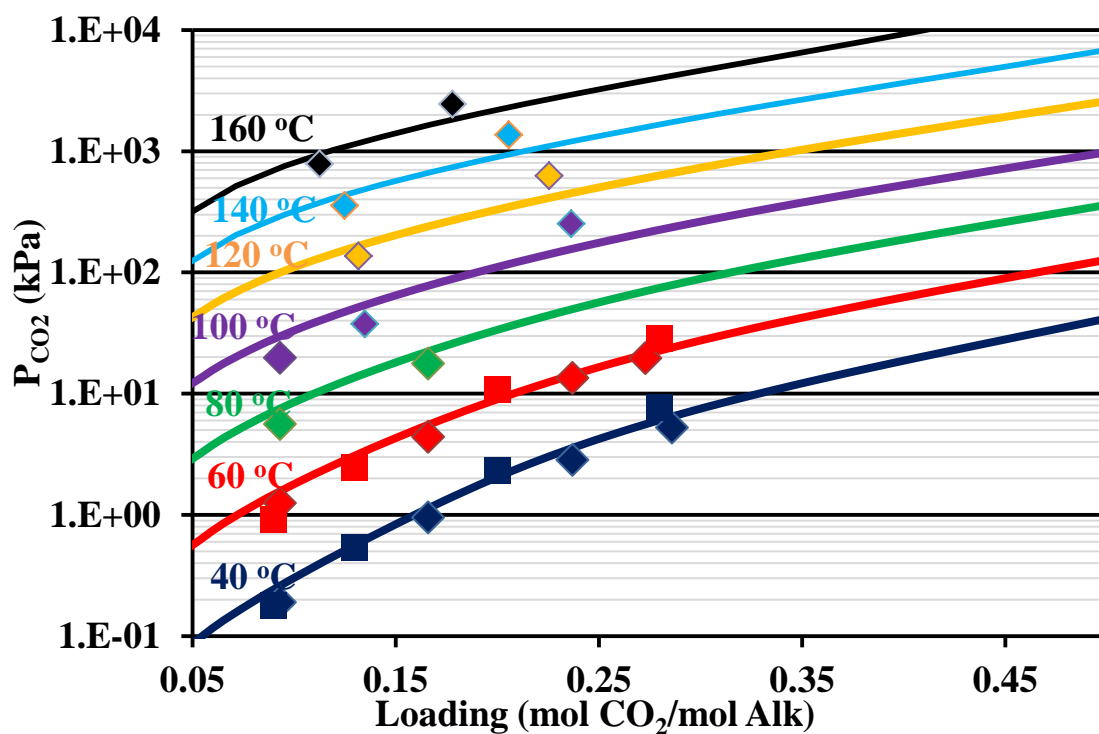


Figure B-41: Experimental data (Chen, 2011; Xu, 2011) and model predictions (lines) for solubility of CO₂ in 7 m MDEA/2 m PZ from 40-160 °C.

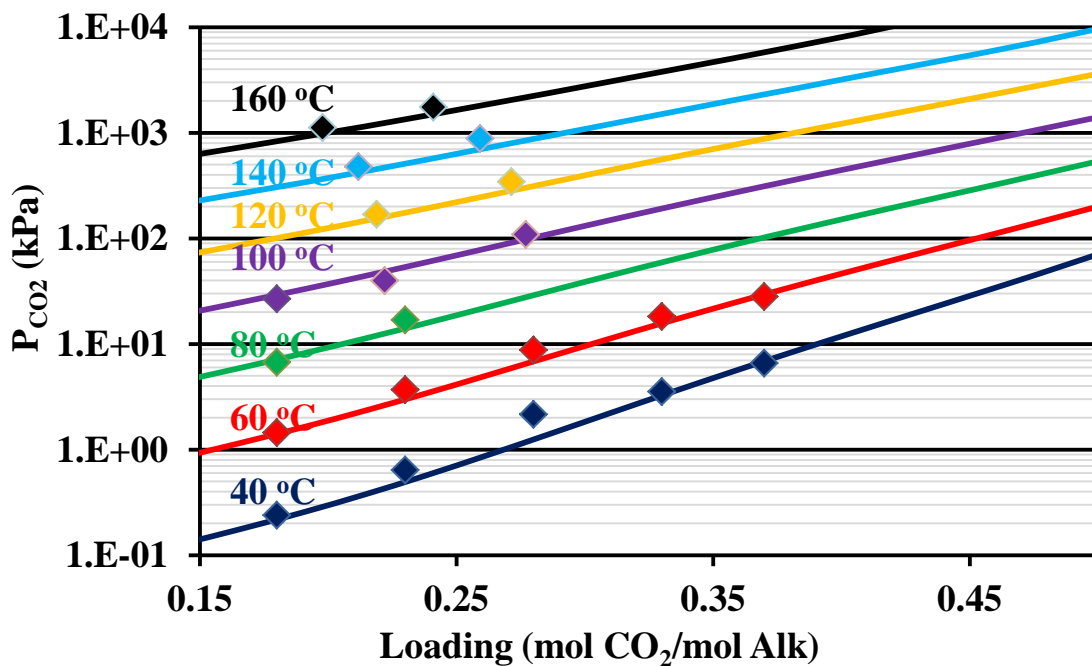


Figure B-42: Experimental data (Chen, 2011; Xu, 2011) and model predictions (lines) for solubility of CO₂ in 7 m MDEA/2 m PZ from 40-160 °C.

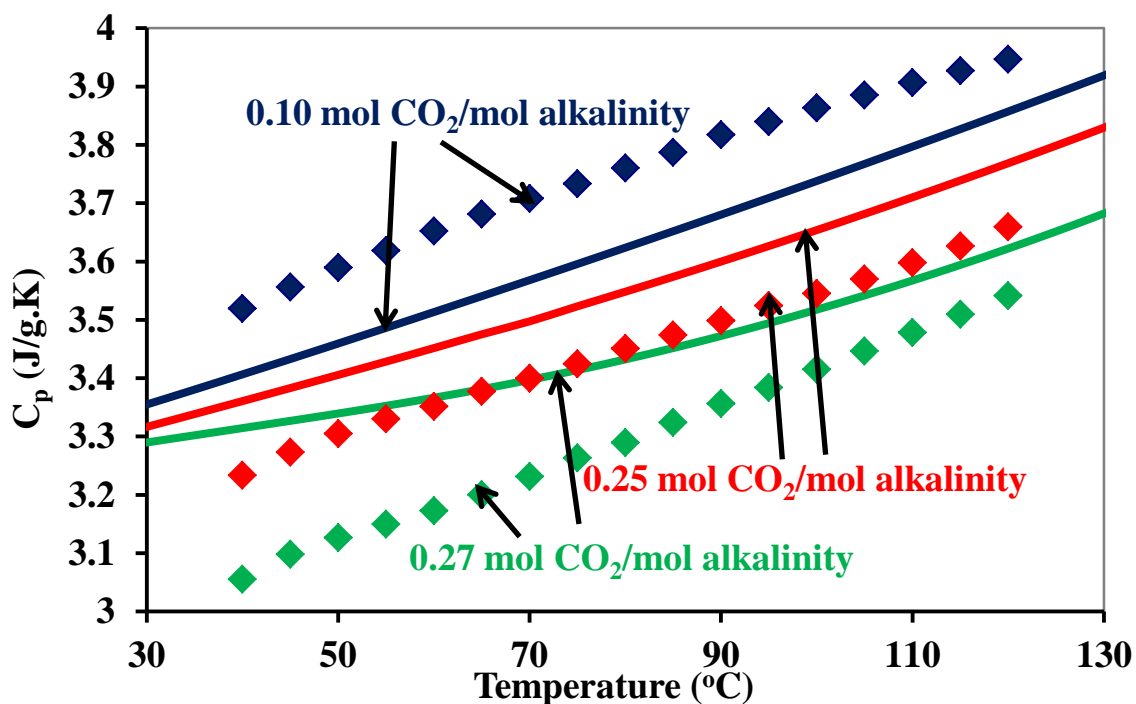


Figure B-43: Experimental data (Nguyen, 2012) and model predictions (lines) for heat capacity of 7 m MDEA/2 m PZ from 40-120 $^{\circ}\text{C}$.

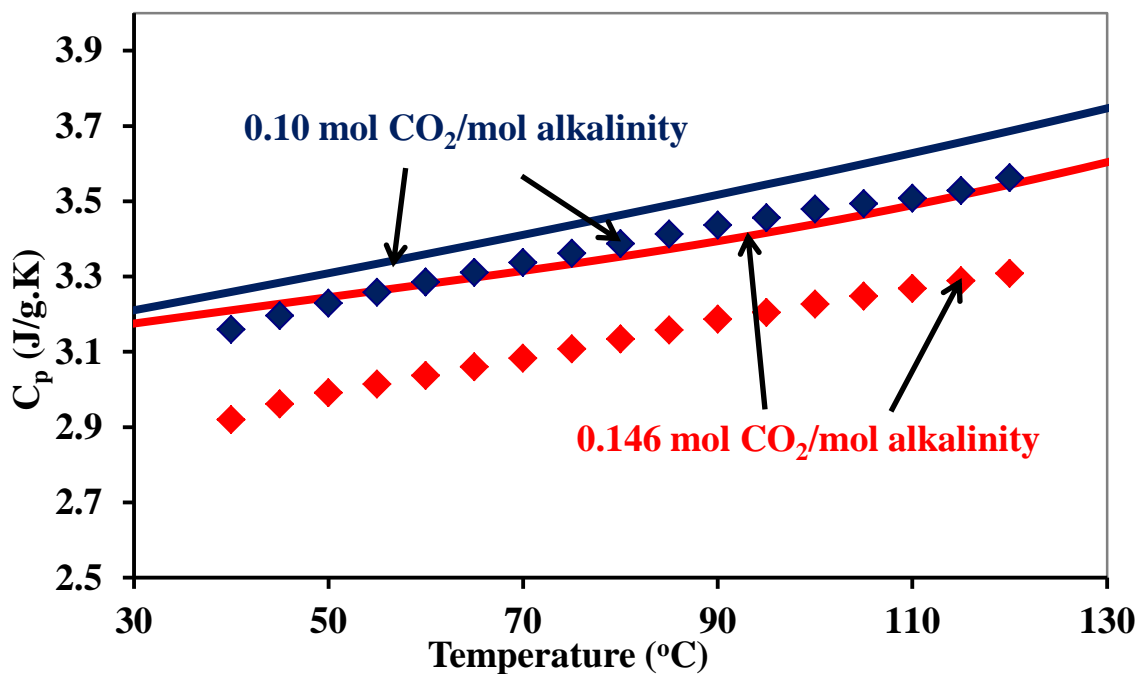


Figure B-44: Experimental data (Nguyen, 2012) and model predictions (lines) for heat capacity of 5 m MDEA/5 m PZ from 40-120 $^{\circ}\text{C}$.

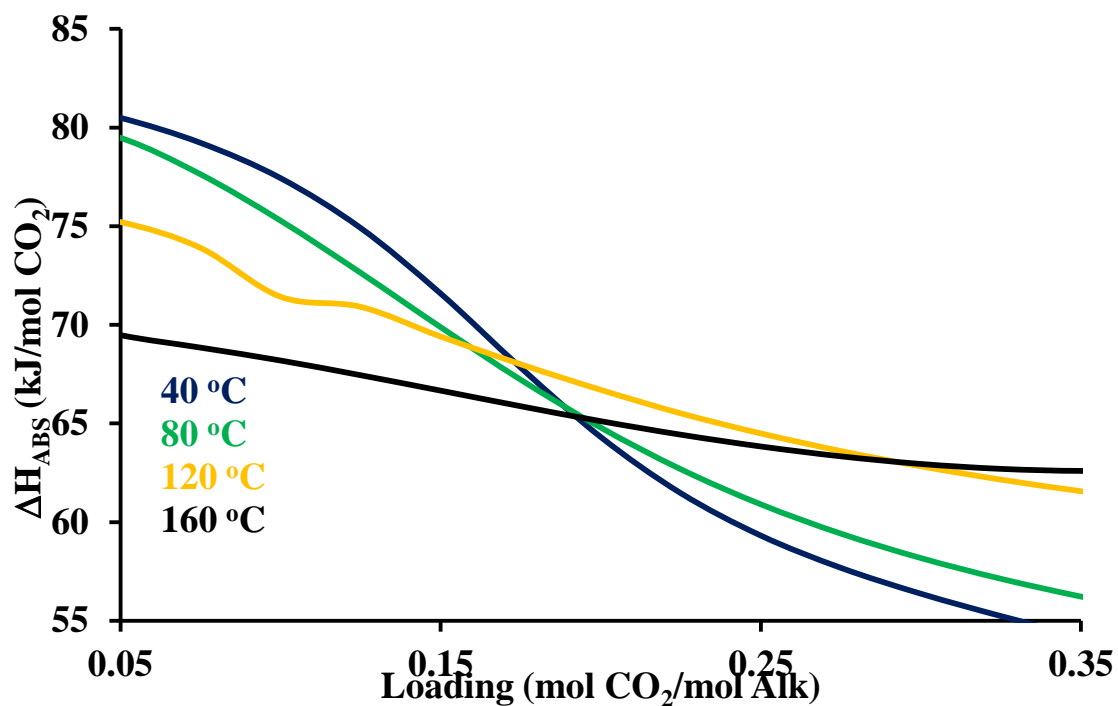


Figure B-45: Model predictions for heat of CO₂ absorption in 7 m MDEA/2 m PZ from 40-160 °C.

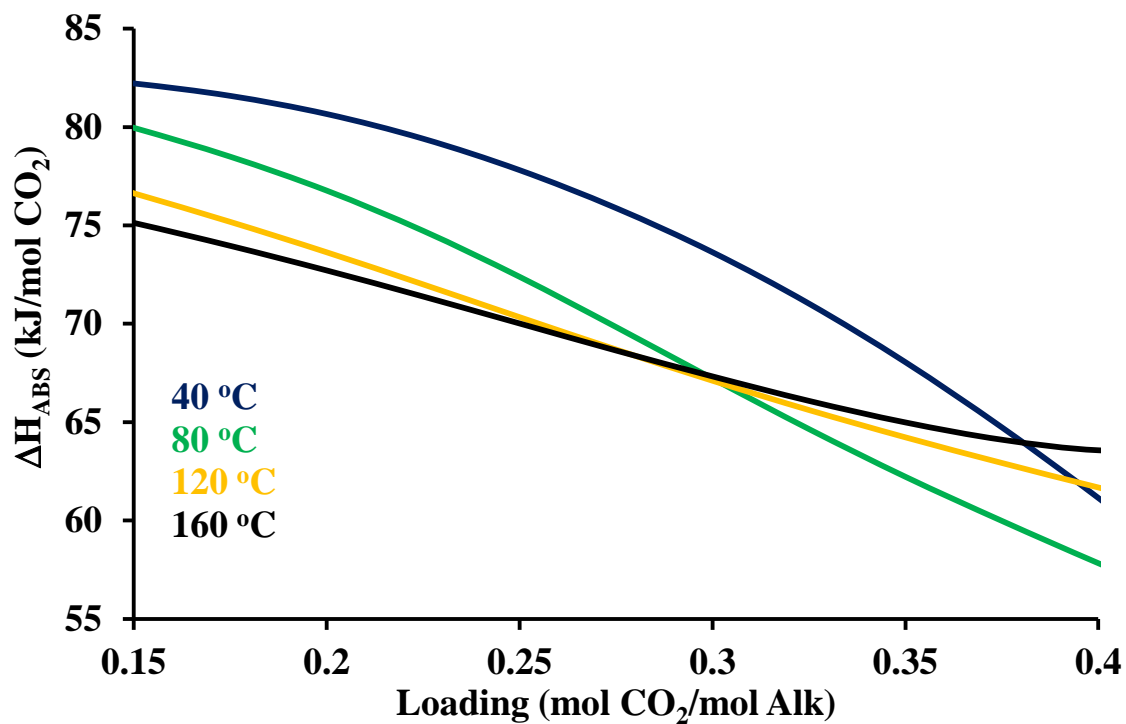


Figure B-46: Model predictions for heat of CO₂ absorption in 5 m MDEA/5 m PZ from 40-160 °C.

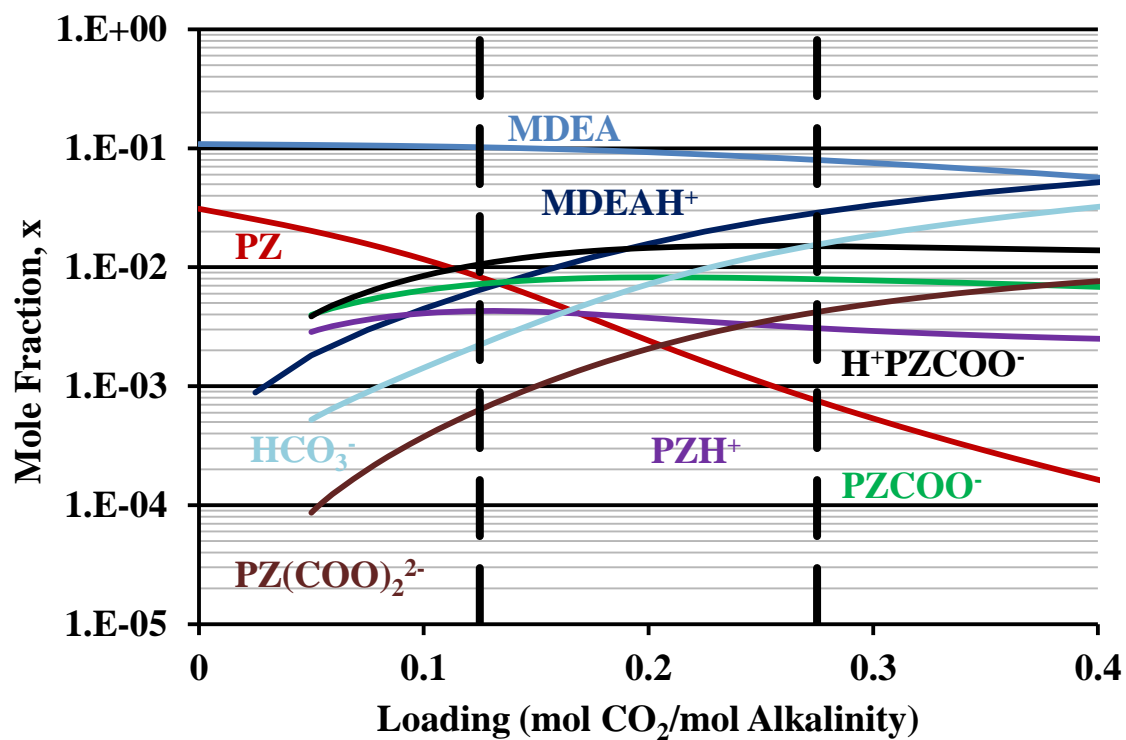


Figure B-47: Predictions for liquid mole fraction in 7 m MDEA/2 m PZ at 40 °C.

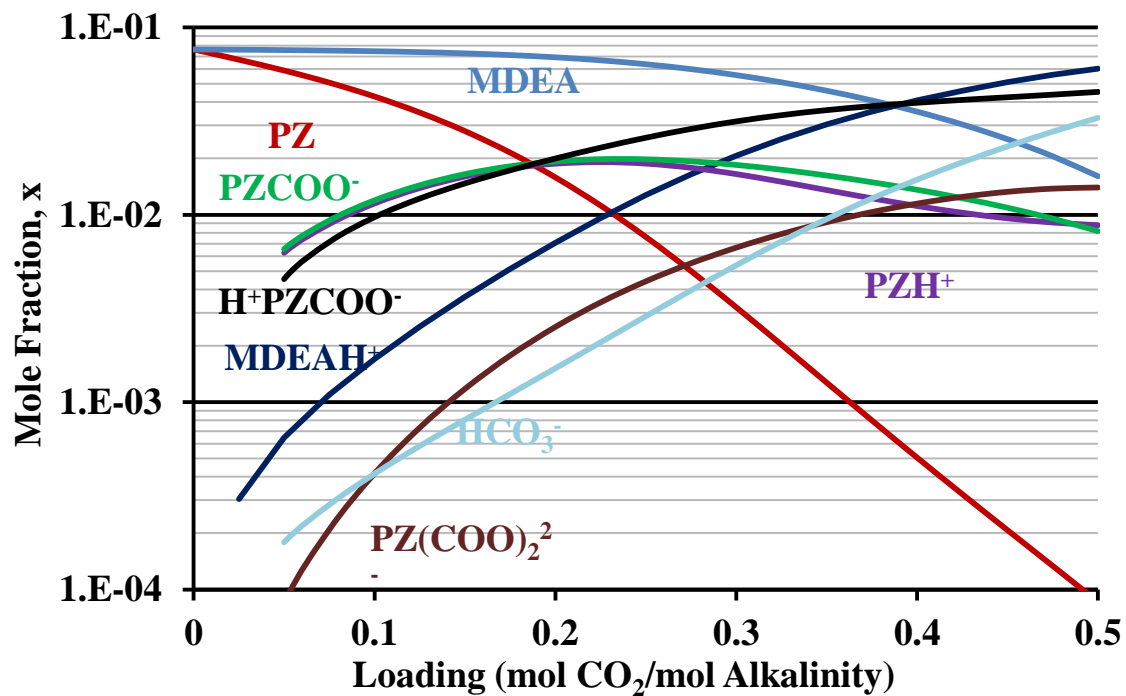


Figure B-48: Predictions for liquid mole fraction in 5 m MDEA/5 m PZ at 40 °C.

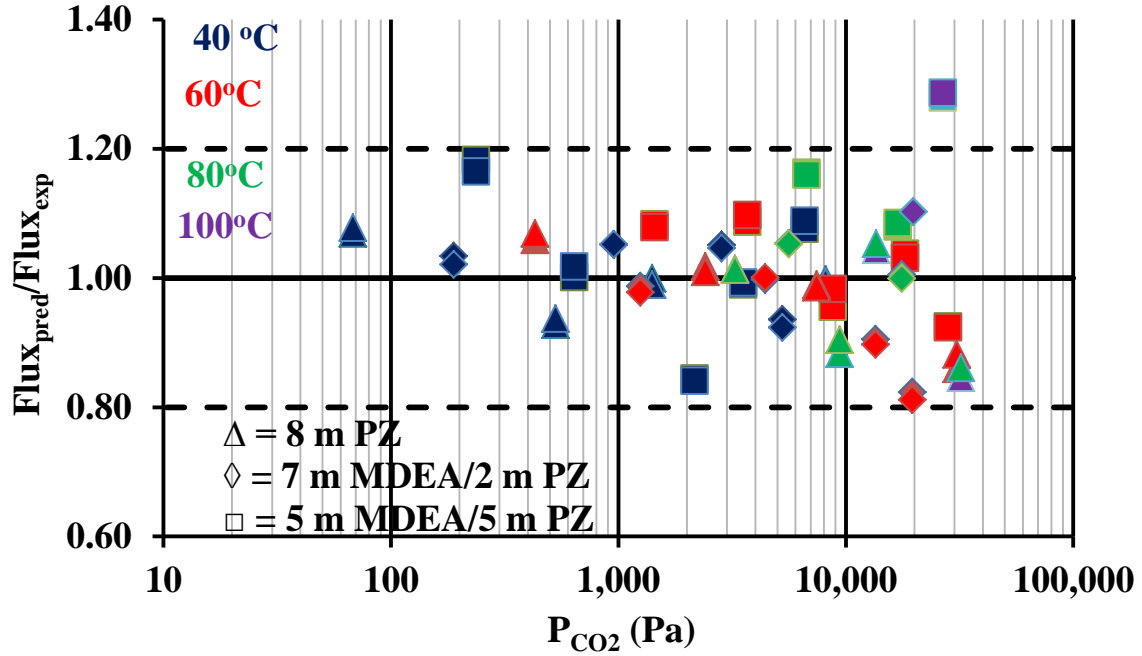


Figure B-49: Parity plot comparing experimental flux (Dugas, 2009; Chen, 2011) and predicted flux for 8 m PZ, 7 m MDEA/2 m PZ, and 5 m MDEA/5 m PZ from 40-100 °C.

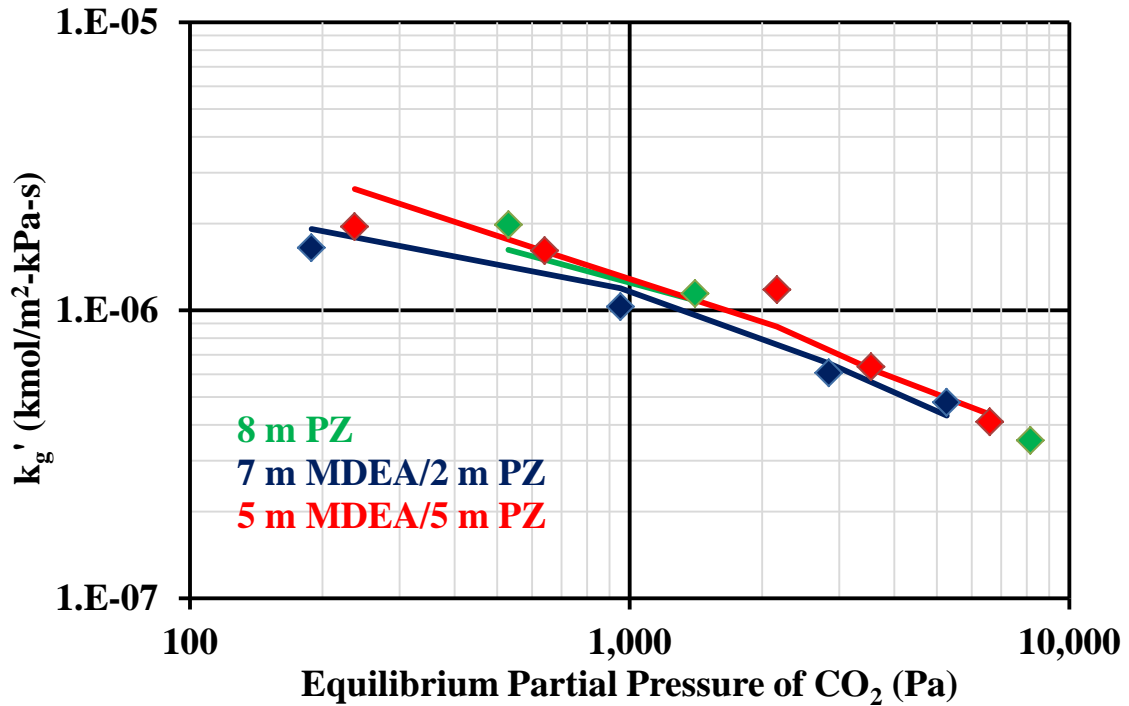


Figure B-50: Experimental (Dugas, 2009; Chen, 2011) and predicted (lines) k_g' for 8 m PZ, 7 m MDEA/2 m PZ, and 5 m MDEA/5 m PZ from 40-100 °C.

Appendix C: Density and Viscosity Data

Table C-1: Density of 7 m MDEA/2 m PZ and 5 m MDEA/5 m PZ from 20-60 °C.

Amine	T (°C)	Loading (mol CO ₂ /mol alk)	Density (g/cm ³)
7 m MDEA/2 m PZ	20	0	1.0446
		0.02	1.0486
		0.094	1.066
		0.25	1.108
	40	0	1.0314
		0.02	1.0355
		0.094	1.0532
		0.25	1.0956
	50	0	1.0244
		0.02	1.0285
		0.094	1.0469
		0.25	1.0892
	60	0	1.0172
		0.02	1.0214
		0.094	1.0402
		0.25	1.0827
5 m MDEA/5 m PZ	20	0.18	1.0946
		0.23	1.1077
		0.28	1.1199
		0.327	1.1315
		0.369	1.1426
	40	0.18	1.0824
		0.23	1.0966
		0.28	1.1085
		0.327	1.1202
		0.369	1.1306
	60	0.18	1.07
		0.23	1.0838
		0.28	1.0963
		0.327	1.1085
		0.369	1.1189

Table C-2: Viscosity of 7 m MDEA/2 m PZ and 5 m MDEA/5 m PZ from 20-60 °C.

Amine	T (°C)	Loading (mol CO₂/mol alk)	Viscosity (cP)
7 m MDEA/2 m PZ	20	0	15
		0.25	19.22
	40	0	6.612
		0.094	7.156
		0.14	7.336
	60	0.25	8.915
		0	3.402
5 m MDEA/5 m PZ	40	0.25	4.914
		0.18	11.79
		0.23	12.37
		0.28	13.13
		0.327	13.95
	60	0.369	15.24
		0.18	6.455
		0.23	6.735
		0.28	7.055
		0.327	7.651
		0.369	8.277

References

- Abu-Zahra MRM, Niederer JPM, Feron PHM, Versteeg GF (2007). "CO₂ capture from power plants Part II. A parametric study of the economical performance based on mono-ethanolamine." International Journal of Greenhouse Gas Control. 1(2007): 135-142.
- Alie C, et al. (2005). "Simulation of CO₂ capture using MEA scrubbing: a flowsheet decomposition method." Energy Conversion and Management. 46(3): 475-487.
- Appl M, et al. (1982). Removal of CO₂ and/or H₂S and/or COS from gases containing these constituents. U.S.P. Office. United States. BASF Aktiengesellschaft. 4336233.
- Aspen Technology Inc. (2011). "Rate-Based Model of the CO₂ Capture Process by MDEA using Aspen Plus." Documentation included with Aspen Plus V7.3.
- Aspen Technology Inc. (2011). "Rate-Based Model of the CO₂ Capture Process by Mixed PZ and MDEA Using Aspen Plus." Documentation included with Aspen Plus V7.3.
- Asprion N (2006). "Nonequilibrium Rate-Based Simulation of Reactive Systems: Simulation Model, Heat Transfer, and Influence of Film Discretization." Industrial and Engineering Chemistry Research. 45: 2054-2069.
- Austgen DM (1989). A model of vapor-liquid equilibria for acid gas-alkanolamine-water systems. The University of Texas at Austin. Ph. D. Dissertation.
- Bernal-Garcia JM, Ramos-Estrada M, Iglesias-Silva A, and Hall KR (2003). "Densities and Excess Molar Volumes of Aqueous Solutions of n-Methyldiethanolamine (MDEA) at Temperatures from (283.15 to 363.15) K." Journal of Chemical Engineering Data. 48: 1442-1445.
- Bisnoi S (2000). Carbon Dioxide Absorption and Solution Equilibrium in Piperazine Activated Methyldiethanolamine. The University of Texas at Austin. Ph. D. Dissertation.
- Bishnoi S, Rochelle GT (2002) "Absorption of Carbon Dioxide in Aqueous Piperazine/Methyldiethanolamine." AIChE Journal. 48(12): 2788-2799.
- Chen X (2011). Carbon Dioxide Thermodynamics, Kinetics, and Mass Transfer in Aqueous Piperazine Derivatives and other Amines. The University of Texas at Austin. Ph. D. Dissertation.

- Cullinane JT (2005). Thermodynamics and Kinetics of Aqueous Piperazine with Potassium Carbonate for Carbon Dioxide Absorption. The University of Texas at Austin. Ph. D. Dissertation.
- Derks PWJ, Hamborg ES, Hogendoorn JA, Niederer JPM, Versteeg GF (2008). “Densities, Viscosities, and Liquid Diffusivities in Aqueous Piperazine and Aqueous (Piperazine + N-Methyldiethanolamine) Solutions.” Journal of Chemical Engineering Data. 53: 1179-1185.
- Desideri U, Paolucci A (1999). “Performance modeling of a carbon dioxide removal system for power plants.” Energy Conversion and Management. 1899-1915.
- Department of Energy (DOE) National Energy Technology Laboratory (NETL). “Cost and Performance Baseline for Fossil Energy Plants Volume 1: Bituminous Coal and Natural Gas to Electricity”, Revision 2, November 2010, DOE/NETL 2010/1397.
- Dugas RE (2008). “Creation of an Aspen RateSep Absorber Model for the Evaluation of CASTOR Pilot Plant Data.” American Chemical Society, Division of Petroleum Chemistry. 53(1): 89-92.
- Dugas, RE (2009). Carbon Dioxide Absorption, Desorption, and Diffusion in Aqueous Piperazine and Monoethanolamine. The University of Texas at Austin. Ph. D. Dissertation.
- Edali M, Idem R, Aboudheir A (2010). “1D and 2D absorption-rate/kinetic modeling and simulation of carbon dioxide absorption into mixed aqueous solutions of MDEA and PZ in a laminar jet apparatus.” International Journal of Greenhouse Gas Control. 4(2010): 143-151.
- Ermatchkov V, Kamps APS, Maurer G (2003). “Chemical equilibrium constants for the formation of carbamates in (carbon dioxide + piperazine + water) from ¹H-NMR-spectroscopy.” Journal of Chemical Thermodynamics. 35: 1277-1289.
- Ermatchkov V, Kamps APS, Maurer G (2006). “Solubility of Carbon Dioxide in Aqueous Solutions of N-Methyldiethanolamine in the Low Gas Loading Region.” Industrial and Engineering Chemistry Research. 45: 6081-6091.
- Ermatchkov V, Maurer G (2011). “Solubility of carbon dioxide in aqueous solutions of N-methyldiethanolamine and piperazine: Prediction and correlation.” Fluid Phase Equilib. 302(1-2): 338-346.

- Fine NA, Goldman MJ, Nielsen PT, Rochelle GT (2013). "Managing n-nitrosopiperazine and dinitrosopiperazine." Energy Procedia. 37: 1678-1686.
- Freeman SA, Dugas RE, Van Wagener DH, Nguyen T, Rochelle GT (2010). "CO₂ Capture with Concentrated, Aqueous Piperazine." International Journal of Greenhouse Gas Control. 4:119-124.
- Freeman SA (2011). Thermal Degradation and Oxidation of Aqueous Piperazine for Carbon Dioxide Capture. The University of Texas at Austin. Ph.D. Dissertation.
- Fisher KS. "Advanced Amine Solvent Formulations and Process Integration for Near-Term CO₂ Capture Success", June 2007, Grant No: DE-FG02-06ER84625.
- Hamborg ES, Niederer JPM, Versteeg GF (2007). "Dissociation Constants and Thermodynamic Properties of Amino Acids Used in CO₂ Absorption from (293 to 353)K." Journal of Chemical Engineering Data. 52: 2491-2502.
- Hanley B, Chen CC (2012). "New mass-transfer correlations for packed towers." AIChE Journal. 58(1): 132-152.
- Hetzer HB, Robinson RA, Bates RG (1968). "Dissociation Constants of Piperazinium Ion and Related Thermodynamic Quantities from 0 to 50°." Journal of Physical Chemistry. 72(6): 2081-2086.
- Hewitt GF, Shires GL, Bott TR (1994). Process Heat Transfer. Boca Raton: CRC Press. Print.
- Hilliard MD (2008). A Predictive Thermodynamic Model for an Aqueous Blend of Potassium Carbonate, Piperazine, and Monoethanolamine for Carbon Dioxide Capture from Flue Gas. The University of Texas at Austin. Ph. D. Dissertation.
- International Energy Agency (IEA), 2011. CO₂ Emissions From Fuel Combustion: Highlights.
- IPCC, 2007: Summary for Policymakers. Climate Change 2007: The Physical Science Basis. Contribution of Working Group I to the Fourth Assessment Report of the Intergovernmental Panel on Climate Change. S. Solomon, D. Qin, M. Manning et al. Cambridge, UK and New York, NY, USA, Cambridge University Press.
- Jou FY, Mather AE, Otto FD (1982). "Solubility of hydrogen sulfide and carbon dioxide in aqueous methyldiethanolamine solutions." Industrial and Engineering Chemistry Process Design and Development. 21:539-544.

- Jou FY, Carroll JJ, Mather AE, Otto FD (1993). "The Solubility of Carbon Dioxide and Hydrogen Sulfide in a 35 wt% Aqueous Solution of Methyldiethanolamine." Journal of Chemical and Engineering Data. 71: 264-268.
- Kaganoi S (1997). Carbon Dioxide Absorption in Methyldiethanolamine with Piperazine or Diethanolamine: Thermodynamics and Rate Measurements. The University of Texas at Austin. M.S. Thesis.
- Kierzkowska-Pawlak H (2007). "Enthalpies of Absorption and Solubility of CO₂ in Aqueous Solutions of Methyldiethanolamine." Separation Science and Technology. 42(12): 2723-2737.
- Kim I, Hessen ET, Huag-Warbert T, Svendsen HF (2008). "Enthalpies of Absorption of CO₂ in Aqueous Alkanolamine Solutions from e-NRTL Model." GHGT-9. Washington D.C.: Elsevier, 2008.
- Ko JJ and Li MH (2000). "Kinetics of absorption of carbon dioxide into solutions of N-methyldiethanolamine + water." Chemical Engineering Science. 55: 4139-4147.
- Kohl, Arthur and Richard Nielsen (1997). Gas Purification: Fifth Edition. Houston, TX: Gulf Publishing Company.
- Kvamsdal HM et al. (2010). "Maintaining a neutral water balance in a 450 MW_e NGCC-CCS power system with post-combustion carbon dioxide capture aimed at offshore operation." International Journal of Greenhouse Gas Control. 4: 613-622.
- Leites IL, et al. (2003). "The theory and practice of energy saving in the chemical industry: some methods for reducing the thermodynamic irreversibility in chemical technology processes." Energy. 55-97.
- Liu GB, Yu KT, et al. (2006). "Simulations of chemical absorption in pilot-scale and industrial-scale packed columns by computational mass transfer." Chemical Engineering Science. 61(19): 6511-6529.
- Nguyen T, Hilliard MD, Rochelle GT (2011). "Volatility of aqueous amines in CO₂ capture." Energy Procedia. 4(2011): 1624-1630.
- Nguyen T (2012). Amine Volatility in CO₂ Capture. The University of Texas at Austin. Ph.D. Dissertation.
- Oyenekan BA (2007). Modeling of Strippers for CO₂ Capture by Aqueous Amines. The University of Texas at Austin. Ph. D. Dissertation.
- Pacheco MA (1998). Mass Transfer, Kinetics and Rate-Based Modeling of Reactive Absorption. The University of Texas at Austin. Ph.D. Dissertation.

- Pilling M (2008). Personal communication to Robert E. Tsai.
- Pilling M (2009). Personal communication to Robert E. Tsai.
- Plaza JM, Van Wagener DH, Rochelle GT (2008). "Modeling CO₂ Capture with Aqueous Monoethanolamine." GHGT-9. Washington D.C.: Elsevier.
- Plaza JM, Chen E, Rochelle GT (2009). "Absorber Intercooling in CO₂ Absorption by Piperazine-Promoted Potassium Carbonate." AIChE Journal. 56(4): 905-914.
- Plaza JM (2011). Modeling of Carbon Dioxide Absorption Using Aqueous Monoethanolamine, Piperazine and Promoted Potassium Carbonate. The University of Texas at Austin. Ph.D. Dissertation.
- Ralf G (2004). Mathematische Modellierung des MDEA Absorptionsprozesses. Rheinisch Westfali Technical University at Aachen. Ph.D. Dissertation.
- Rinker EB, Ashour SS, Sandall OC (1997). "Physical Property Data Important in Modeling H₂S and CO₂ Absorption into Aqueous DEA, MDEA, and Blends of DEA and MDEA." Gas Processors Association. RR-158.
- Rochelle GT, Fisher KS, et al.(2005). Integrating MEA Regeneration with CO₂ Compression and Peaking to Reduce CO₂ Capture Costs, DOE Final Report for Trimeric Corp.
- Samanta A, Roy S, Bandyopdhyay SS (2007). "Physical Solubility and Diffusivity of N₂O and CO₂ in Aqueous Solutions of Piperazine and (N-Methyldiethanolamine + Piperazine)." Journal of Chemical Engineering Data. 52:1381-1385.
- Sexton AJ. "Techno-Economic Analysis for CO₂ Capture by Concentrated Piperazine with Regeneration by High Temperature Two Stage Flash: Budget Period 1", June 2012, Cooperative Agreement No: DE-FE0005654.
- Sipocz N, Tobiesen A, Assadi M (2011). "Integrated modeling and simulation of a 400 MW NGCC power plant with CO₂ capture." Energy Procedia. 4: 1941-1948.
- Svendsen H, personal communication, November 11, 2009.
- Teng TT, Maham Y, Hepler LG, and Mather AE (1994). "Viscosity of Aqueous Solutions of N-Methyldiethanolamine and of Diethanolamine." Journal of Chemical Engineering Data. 39: 290-293.

- Tobiesen FA, Svendsen HF, Mejdell T (2007). "Modeling of Blast Furnace CO₂ Capture Using Amine Absorbents." Industrial and Engineering Chemistry Research. 46: 7811-7819.
- Tsai RE (2010). Mass Transfer Area of Structured Packing. The University of Texas at Austin. Ph. D. Dissertation.
- U.S. Department of Energy (USDOE), 2008. Annual Energy Outlook.
- U.S. Energy Information Administration (USEIA), 2011. Net Generation by Energy Source and Type of Producer.
- Van Wagener DH (2011). Stripper Modeling for CO₂ Removal Using Monoethanolamine and Piperazine Solvents. The University of Texas at Austin. Ph. D. Dissertation.
- Weiland RH, Dingman JC, Cronin DB (1997). "Heat Capacity of Aqueous Monoethanolamine, Diethanolamine, N-Methyldiethanolamine, and N-Methyldiethanolamine-Based Blends with Carbon Dioxide." Journal of Chemical Engineering Data. 42:1004-1006.
- Weiland RH, Dingman JC, Cronin DB, and Browning GJ (1998). "Density and Viscosity of Some Partially Carbonated Aqueous Alkanolamine Solutions and Their Blends." Journal of Chemical Engineering Data. 43: 378-382.
- Wilke CR and Chang P (1955). "Correlation of Diffusion Coefficients in Dilute Solutions." AIChE Journal. 1(2): 264-270.
- Xu GW, Zhang CF, Qin SJ, and Wang YW (1992). "Kinetics Study on Absorption of Carbon Dioxide into Solutions of Activated Methyldiethanolamine." Industrial and Engineering Chemistry Research. 31: 921-927.
- Xu Q (2011). Thermodynamics of CO₂ Loaded Aqueous Amines. The University of Texas at Austin. Ph.D. Dissertation.
- Zhang K, Hawrylak B, Palepu R, Tremaine PR (2002). "Thermodynamics of aqueous amines: excess molar heat capacities, volumes, and expansibilities of {water + methyldiethanolamine (MDEA)} and {water + 2-amino-2-methyl-1-propanol (AMP)}." Journal of Chemical Thermodynamics. 34: 679-710.

Vita

Peter Thompson Frailie, II was born in Ironton, OH on August 26, 1985. He graduated from Russell High School in May of 2004, and attended The University of Kentucky from 2004 to 2008 where he earned a B.S. in Chemical Engineering. While at UK he split his spare time between working in the laboratory of Dr. Dibakar Bhattacharyya and convening with fellow fellows at the Gaines Center for the Humanities. After graduation he immediately began graduate school at The University of Texas at Austin, where he worked for Dr. Gary T. Rochelle. He has accepted a full-time position with BASF in Houston, TX.

Permanent e-mail: pfrailie@gmail.com

This dissertation was typed by the author.